ENERGY RESEARCH CENTER

LEHIGH University

Bethlehem, PA

RECEIVED
AUG 25 1999
OSTI

ORNL/Sub/95-SU604/02

INVESTIGATION OF IRON ALUMINIDE WELD OVERLAYS

August 2, 1999

Final Report Prepared by
S.W. Banovic, J.N.DuPont, B.F. Levin, and A.R. Marder
Lehigh University
Energy Research Center
117 ATLSS Drive
Bethlehem, PA 18015

under 19X-SU604V

for

OAK RIDGE NATIONAL LABORATORY
Oak Ridge, TN 37831
Managed by
LOCKHEED MARTIN ENERGY RESEARCH CORP.
For the
U.S. DEPARTMENT OF ENERGY
under contract DE-AC05-96OR22464

99-500-01-04

This report has been reproduced directly from the best available copy.

Available to DOE and DOE contractors from the Office of Scientific and Technical Information, P.O. Box 62, Oak Ridge, TN 37831; prices available from (423) 576-8401.

Available to the public from the National Technical Information Service, U.S. Department of Commerce, 5285 Port Royal Rd., Springfield, VA 22161.

This report was prepared as an account of work sponsored by an agency of the United States Government. Neither the United States Government nor any agency thereof, nor any of their employees, makes any warranty, expressed or implied, or assumes any legal liability or responsibility for the accuracy, completeness, or usefulness of any information, apparatus, product, or process disclosed, or represents that its use would not infringe privately owned rights. Reference herein to any specific commercial product, process, or service by trade name, trademark, manufacturer, or otherwise, does not necessarily constitute or imply its endorsement, recommendation, or favoring by the United States Government or any agency thereof. The views and opinions of authors expressed herein do not necessarily state or reflect those of the United States Government or any agency thereof.

DISCLAIMER

Portions of this document may be illegible in electronic image products. Images are produced from the best available original document.

ORNL/Sub/95-SU604/02

INVESTIGATION OF IRON ALUMINIDE WELD OVERLAYS

August 2, 1999

Research sponsored by the U.S. Department of Energy,
Office of Fossil Energy
Advanced Research and Technology Development Materials Program

Final Report Prepared by
S.W. Banovic, J.N.DuPont, B.F. Levin, and A.R. Marder
Lehigh University
Energy Research Center
117 ATLSS Drive
Bethlehem, PA 18015
under
19X-SU604V

for

OAK RIDGE NATIONAL LABORATORY
Oak Ridge, TN 37831
Managed by
LOCKHEED MARTIN ENERGY RESEARCH CORP.
For the
U.S. DEPARTMENT OF ENERGY
under contract DE-AC05-96OR22464

Table of Contents

ABSTRACT

Conventional fossil fired boilers have been retrofitted with low NO_x burners in order for the power plants to comply with new clean air regulations. Due to the operating characteristics of these burners, boiler tube sulfidation corrosion typically has been enhanced resulting in premature tube failure. To protect the existing panels from accelerated attack, weld overlay coatings are typically being applied. By depositing an alloy that offers better corrosion resistance than the underlying tube material, the wastage rates can be reduced. While Ni-based and stainless steel compositions are presently providing protection, they are expensive and susceptible to failure via corrosion-fatigue due to microsegregation upon solidification. Another material system presently under consideration for use as a coating in the oxidation/sulfidation environments is iron-aluminum. These alloys are relatively inexpensive, exhibit little microsegregation, and show excellent corrosion resistance. However, their use is limited due to weldability issues and their lack of corrosion characterization in simulated low NO_x gas compositions. Therefore a program was initiated in 1996 to evaluate the use of iron-aluminum weld overlay coatings for erosion/corrosion protection of boiler tubes in fossil fired boilers with low NOx burners. Investigated properties included weldability, corrosion behavior, erosion resistance, and erosion-corrosion performance.

Weldability results were obtained by depositing single pass welds and multiple pass claddings of Fe-Al alloys on carbon steel substrates using the Gas Tungsten Arc (GTAW) and Gas Metal Arc (GMAW) Welding processes. For GTAW, commercially pure aluminum wire was fed into the weld pool of a low carbon steel substrate to produce the overlays. A composite wire, consisting of an aluminum core with low carbon steel sheath, was specially developed for this project and used for the GMAW process. By varying the welding parameters, a range of dilution levels was achieved that resulted in fusion zone compositions with 3 to 30 wt% Al. Under these processing conditions (no pre-heat or post-weld heat treatment), cracking of the Fe-Al claddings was directly

Research sponsored by the US Department of Energy, Fossil Energy Advanced Research and Technology Development Materials Program, DOE/FE AA 15 10 10 0, Work Breakdown Structure Elemement LU-2

related to the aluminum concentration within the deposit. Cracking of the overlays was seen to occur by both inter- and transgranular modes for deposits containing greater than 10 wt% Al. Below this composition limit, cracking did not occur. According to the Fe-Al phase diagram, this composition indicates the microstructural transition from the single phase region of disordered solid solution (α) to the two phase region of α + ordered Fe_3Al. The ordered structures of Fe_3Al and FeAl have been found to be more susceptible to environmental embrittlement, which has been seen to be the source of the cladding cracking problem.

The corrosion behavior of weldable Fe-Al alloys in environments indicative of low NO_x gas compositions, i.e., high partial pressures of sulfur [$p(S_2)$] and low partial pressures of oxygen [$p(O_2)$] was conducted in oxidizing/sulfidizing gases. Through an integrated experimental approach involving thermogravimetric techniques, post-exposure metallographic examination of the corroded samples, and detailed chemical microanalyses of the reaction scales, the effect of aluminum content, temperature, and gas composition on the corrosion behavior was observed. The binary alloys chosen ranged from 0-20 wt% Al, encompassing both weldable (10 wt% and below) and non-weldable compositions. These samples were exposed at 500-700°C in both reducing [$p(S_2) < 10^{-4}$ atm and $p(O_2) < 10^{-25}$ atm] and oxidizing atmospheres for various times up to 100 hours. Corrosion behavior of Fe-Al alloys was found to be directly related to the aluminum content of the alloy. According to which reaction product developed, the corrosion behavior was found to exhibit one, if not more, of three stages of behavior: inhibition, breakdown, and steady-state. The observance and/or duration of these stages was directly related to the aluminum content of the alloy and the exposure temperature.

The inhibition stage was characterized by growth of a thin, gamma alumina scale that suppressed excessive degradation of the substrate at all temperatures. Formation of this phase was promoted by increasing the aluminum content of the alloy (approximately 10 wt% and above). The growth of this scale did not allow for internal sulfidation of the alloy, within detection limits of the techniques used (approximately 1 μm). Localized mechanical failure of this initial passive scale, in combination with the inability to re-establish itself, was found to result in nodular growth of non-

protective sulfide phases across the sample face due to short circuit diffusion through the gamma alumina layer. This time period was labeled the breakdown stage as relatively fast weight gains replaced the transient low rates detected at early times. The morphologies observed were very complex as continued growth of the nodule did not depend solely upon the diffusion of species through the previously formed product, but rather, continued mechanical failure of the passive scale. This resulted in faster growth along a lateral direction with respect to the substrate surface instead of perpendicular to it. Typically found for short exposure times on the Fe-7.5 wt% Al alloys, the nodule morphology consisted of an outer scale of iron sulfide ($Fe_{1-x}S$) plates growing on top of an inner layer of iron sulfide and tau phase, a spinel-type compound ($FeAl_2S_4$). With the remnants of the initial gamma scale found between the outer and inner scale, it was concluded that these layers grew by iron diffusion outward and sulfur diffusion inward, respectively. The corrosion rate observed during development of these morphologies was directly related to the density of the nodules on the surface and the exposure temperature. The final period observed was the steady-state stage. This behavior was encountered from the onset of exposure for all Fe-5 wt% Al alloys tested, or upon coalescence of the nodular growths. After initially high corrosion rates, the weight gains were found to increase at a steady rate as subsequent growth occurred via diffusion through the continuous scale. The morphological development consisted of a continuous outer scale of iron sulfide plates and inner scale of iron sulfide and tau phase. Similar to the nodular growth, these layers grew via iron diffusion outward and sulfur diffusion inward, respectively. When compared to the low carbon steel reference sample, the addition of 5 wt% Al was found to decrease the growth rate of the outer iron sulfide scale by an order of magnitude at 700°C.

The solid particle erosion resistance of Fe-Al weld overlay coatings was evaluated at 400°C using 300 um alumina particles at a velocity of 40 m/s and impingement angles between 30° and 90°. Erosion resistance was evaluated by determining the steady state erosion rate and comparing the microstructure of the deposit before and after testing. Several other commercial overlay coatings (both Fe- and Ni-based) were also tested for comparison. In general, the steady state volume erosion rate was found to be related to the depth of plastic deformation of the material at the eroded surface. Materials which dissipate particle impact energy through plastic deformation were found to exhibit

low erosion rates. The depth of plastic deformation, or plastic zone size, for the Fe-Al alloys was found to be approximately 70 um deep. This resulted in the erosion rate for the Fe-Al alloys being comparable to other commercial overlays presently applied.

The erosion-corrosion behavior of the alloys was also conducted. After exposing iron-based alloys, with 0-12.5 wt% Al, in an oxidizing environment for a 100 hr exposure at 700°C, room temperature erosion testing was performed. Due to the thinness of the corrosion product that formed, as well as the large amount of material typically removed during erosion, the major mechanism for material degradation was found to be erosion.

The results from this study indicate that weldable compositions of Fe-Al alloys (10 wt% Al) show excellent corrosion resistance to aggressive low NO_x gas compositions and comparable erosion rates to commercially applied alloys in the service temperature range (below 600°C). With the potential promise for applications requiring a combination of weldability and corrosion resistance in moderately reducing environments, these alloys are viable candidates for further evaluation for use as sulfidation resistant weld overlay coatings.

1.0 INTRODUCTION

In order to comply with clean air regulations, conventional fossil-fired boilers are being retrofitted to reduce NO_x emissions produced during combustion [Urich, 1996; Stringer, 1990; Chou, 1984]. One design principle [Chou, 1984] suppressing NO_x formation is to delay the mixing of fuel and air to create a substoichiometric combustion gas, and thus, a concomitant change in operating conditions within the boiler. Prior to the low NO_x retrofit, water wall panel wastage was minimal due to adherent and protective iron oxide scales that formed on the low carbon and Cr-Mo steel tubes. Sulfur from the fuel was not problematic as it was converted in the oxidizing atmosphere to form SO_2 and SO_3, which are not very corrosive at furnace wall temperatures (450-600°C). However, with installation of low NO_x burners, H_2S is now generated from the sulfur, presently up to 600 ppm, creating a reducing atmosphere [Gabrielson, 1996]. As a result, less protective sulfide scales are forming instead of the oxides, leading to unacceptable degradation (up to 2.5 mm/yr) of the water wall tubes [Chou, 1984].

Weld overlay coatings are typically being applied in order to protect existing panels from the accelerated sulfidation attack. By depositing an alloy that offers better corrosion resistance than the underlying tube material, the wastage rates can be reduced. Through sponsorship of an electric utility consortium, research was initiated to evaluate commercially available stainless steel and nickel based weld overlay coatings for erosion and corrosion protection in these low NOx boiler environments. While these compositions are presently affording protection, they are expensive and susceptible failure via corrosion-fatigue due to microsegregation upon solidification. Recent research on the corrosion [DeVan 1988, 1989, 1992, 1993a, 1993b; McKamey 1991; Natesan 1995; Tortorelli 1992, 1994a, 1994b, 1996, 1998] and erosion [Levin, 1994, 1995] of iron aluminide weld overlays indicated these alloys are also excellent candidates for this application. These alloys are relatively inexpensive and do not exhibit microsegregation.

However, even with superior sulfidation resistance, Fe-Al alloys are not presently applied as weld overlay coatings in boilers. Above 10 wt% Al, these alloys are seen to readily crack during welding, due to hydrogen cracking susceptibility, when deposited without extensive pre-heat and post-weld heat treatments [Banovic, 1999]. This problem has been observed to increase with an increase in the aluminum content of the overlay [Banovic, 1999; Fasching, 1995; Maziasz, 1992;

David, 1989]. In addition, application of more weldable coatings, i.e., those with low aluminum, will not be implemented without detailed corrosion studies indicating the performance of the alloys in low NO_x gas conditions. Presently, this information is limited in the open literature [DeVan, 1993a; Kai, 1997a, 1997b]. Therefore, a program was initiated in 1996 through sponsorship of the Fossil Energy Advanced Research and Technology Development (AR&TD) Program to evaluate the feasibility of Fe-Al alloys as weld overlay coatings. The main objectives of this research were to: 1) develop wires for gas metal arc welding overlay applications and 2) identify overlay compositions with good sulfidation and erosion resistance that are readily weldable. The following sections will discuss in detail the results obtained through this investigation.

2.0 WELDING STUDIES

2.1 Wire Development

The deposition of weld overlays on boiler tube waterwalls often requires application of very large surface areas under field conditions. Thus, a high deposition rate process such as gas metal arc (GMA) welding may be necessary. Although iron aluminide consumables can be prepared in rod and powder form for use with gas tungsten arc (GTA) welding and plasma arc welding (PAW) processes, these processes typically operate at low deposition rates due to their inherently low thermal efficiency [DuPont 1995, 1996]. Therefore, a technique is required for fabricating spooled wire for the GMAW process. However, preparation of small diameter iron aluminide wires for GMAW is impractical due to the relatively low ductility of the phase.

A composite wire fabrication technique has been devised and implemented by Stoody Company of Bowling Green, KY, to produce various filler metal compositions of iron and aluminum. With this process, a commercially pure aluminum wire is wrapped in a low carbon steel sheath and drawn to the final diameter. Additional alloying elements (e.g., Cr and Zr) can be added between the aluminum core wire and steel sheath during the drawing process. A typical wire prepared by this technique containing 22 wt% Al - 8 wt% Cr - 0.4 wt% Zr - balance iron is shown in Fig 2.1. Six other wire compositions were also fabricated by this method for future studies on weldability, corrosion, and erosion resistance, with their compositions in Table 2.1.

2.2 Weldability

2.2.1 Introduction

Intermetallic iron aluminide alloys based on the ordered structures of Fe_3Al and FeAl show excellent resistance to oxidation and sulfidation in highly aggressive environments (McKamey, 1991; DeVan, 1993a, 1993b, 1992; Tortorelli, 1995, 1994a, 1994b, 1992). This outstanding resistance has been attributed to the formation of a dense, adherent surface scale of aluminum oxide (Al_2O_3) which is stable under a wide range of environments. In order to utilize their excellent corrosion resistance, and avoid problems due to poor high temperature strength (McKamey, 1991), the use of iron aluminide claddings has been considered. Recent work (DeVan 1993?) suggests that Al levels should be greater than approximately 9.6 wt% for severely reducing environments (e.g.,

800°C, $P_{S2} = 10^{-6}$, $P_{O2} = 10^{-22}$). In spite of the potential protection offered, these compositions have been seen to be susceptible to hydrogen (cold) cracking (Fasching, 1995; Maziasz, 1992; David, 1989) subsequent to deposition. A direct correlation between the severity of embrittlement and the amount of aluminum in the alloy (Woodyard, 1993; Sikka 1993) has been observed, specifically when the composition resides in the ordered regions of the Fe-Al phase diagram. Recent investigations (Maziasz 1992; David 1991) have cited the use of preheat and post weld heat treatments (PWHT) to alleviate some of the hydrogen cracking problem, thus allowing for higher aluminum content claddings to be deposited crack free. Regardless of these improvements, the use of such extensive treatments are usually not possible when coating large scale structures. However, applications exist in which the corrosion environments are not as severely reducing and lower Al contents, which exhibit good weldability, may provide useful protection. A typical example includes the waterwall structures of coal fired boilers operating with Low NO_x burners (Urich, 1996; Gabrielson 1996; Chou, 1984). These units often require cladding areas reaching up to 4,000 ft^2 where application of preheat and PWHT are not possible. These units operate under a moderately reducing environment where low Al claddings may provide adequate protection. Successful substitution of currently used stainless steel and Ni alloy claddings by Fe-Al claddings would be accompanied by reduced cost and elimination of the brittle martensitic region which develops in the partially mixed zones of the claddings presently in use (Gittos, 1992). Thus, the objectives of this portion of the research was to investigate the weldability and sulfidation resistance of Fe-Al claddings in order to identify cladding compositions which offer good weldability.

2.2.2 Experimental Procedure

Claddings were produced using the Gas Tungsten Arc (GTAW) and Gas Metal Arc Welding (GMAW) processes. For the GTAW process, a filler metal of commercially pure aluminum wire was directly fed into the weld pool. The substrates were A285 Grade C steel, 6 mm thick x 152 mm wide x 305 mm long. The filler metal feed speed and current were varied to produce different aluminum concentrations in the claddings. A constant travel speed of 2.0 mm/s was used for all GTAW experiments. Single and multiple pass deposits were produced under identical processing parameters using argon shielding gas. For the GMAW multiple pass welds, a range of values for

electrode tip to plate distance, electrode feed speed, and travel speed was used. The electrode tip to plate distance was varied in order to induce current variations within a fixed electrode feed speed. Two aluminum-cored, steel sheathed wires with different amounts of aluminum (13 and 27 wt%) were used as the consumable electrodes, and a shielding gas of Ar-2% O_2 was utilized. To simulate the external constraint encountered during welding, the steel plates were restrained by bolts placed in each of the four corners. Pre-heat and post-weld heat treatments were not conducted, but an interpass temperature for the multiple pass welds was maintained between 300-350°C. A dye penetrant technique was used to assess cracking of the claddings.

Samples were removed from the claddings using an abrasive cut-off wheel, mounted in cold setting epoxy, and polished to a 0.04 μm finish using colloidal silica. The samples were etched in a solution of 60 ml methanol, 40 ml nitric acid, and 20 ml hydrochloric acid. Microstructural characterization was performed using light optical microscopy (LOM) and scanning-electron microscopy (SEM). Electron probe microanalysis (EPMA) was conducted on a JEOL 733 SuperProbe equipped with wavelength dispersive spectrometers. The accelerating voltage and probe current were 15 kV and 15 nA, respectively. K_α x-ray lines were analyzed and counts converted to weight percentages using a $\phi(\rho z)$ correction scheme. Knoop hardness measurements were made with a LECO Hardness tester using a load of 100g held for 15 seconds.

2.2.3 Results and Discussion

2.2.3.1 GTAW Single Pass Deposits

A sample matrix was produced to obtain a wide range of aluminum contents and determine the maximum amount of aluminum which could be tolerated in the cladding without cracking. Filler metal feed speeds between 10 and 50 mm/sec were used while the current was varied between 250 and 300 A in 25 A increments. Voltages averaged around 14.5V. Single pass welds were first deposited to ensure that the microstructure and compositions of the claddings were not complicated by overlapping passes. Fig 2.2 shows the experimental matrix of the single pass deposits. The energy input was calculated using an arc efficiency of 0.67 for the GTAW process (DuPont, 1996). Each data point represents a cladding deposited and is labeled as either cracked or not cracked. For those that cracked, the number of cracks that occurred are located to the right of the symbols, with

M signifying more than 15. The numbers to the left of the symbols denote the amount of aluminum in the deposit (in wt%) as measured using EPMA. The samples located near the crack/no crack boundary exhibited reproducible cracking tendencies. Cracking of the welds was observed to occur soon after solidification as well as days after depositing the claddings.

All of the deposits produced with this range of processing conditions exhibit coarse columnar microstructures (Fig 2.3a). Cracking of the cladding was both inter- and transgranular (Fig 2.3b). As shown in Fig 2.3c, cracks in the deposits never propagated into the underlying substrate, but appear to be arrested at or near the interface. Composition traces across the columnar microstructures of three deposits prepared at a constant energy input and varying filler metal feed speeds are shown in Fig 2.4. The size of the partially mixed zone (PMZ) is seen to increase as the nominal aluminum content of the weld increases. A typical composition profile acquired across a single grain is shown in Fig 2.5. These results show that, beyond the partially mixed zone, the deposits exhibit a uniform distribution of alloying elements. These results indicate that good mixing occurs beyond the partially mixed zone and that localized concentration gradients, which typically develop due to microsegregation, are eliminated during solidification and post-solidification cooling. The elimination of localized concentration gradients, as seen in Fig 2.5, can be attributed to the relatively high diffusivity of Al in the BCC structure of disordered solid solution (α).

The size of the partially mixed zone generally increases with increasing filler metal feed rate. This indicates that the thickness of the stagnant boundary layer near the fusion line increases as the filler metal feed rate increases. However, beyond this point, the composition is uniform. For claddings with Al contents below 10 wt%, which exhibit good weldability, the partially mixed zone is small compared to the deposit thickness. These results are significant because they indicate there should be no regions near the surface of the deposits which are Al depleted and, thus, there should be no regions susceptible to localized corrosion.

Fig 2.6 shows a typical Knoop hardness trace across the fusion line of an Fe-Al alloy. No significant spike in hardness occurs near the fusion line indicative of a brittle interface layer, as commonly seen with stainless steel and nickel-alloy claddings (Gittos, 1992). During deposition of the superalloys, a composition gradient between the base metal and weld metal may form, leading to complex microstructures close to the fusion line. With relatively high cooling rates, the formation

of a martensitic layer, which is high in strength and low in ductility, is often observed in this area. Gittos and Gooch (1992) observed that this hard zone cracked during side bend tests, thus lending the possibility of the brittle interface layer being susceptible to cracking under thermal cycling conditions.

Fig 2.2 shows that the amount of aluminum in the deposit decreases with increasing energy input and decreasing wire feed speed. This trend is readily expected and can be interpreted based on the simple energy balance dilution model recently proposed by DuPont and Marder (1996). The dilution is essentially controlled by the relative melting rates of the filler metal and substrate. For a fixed filler metal feed rate (melting rate), the dilution increases (i.e, amount of Al decreases) with increasing energy input. In this case, the extra energy can not absorbed by the filler metal if the filler metal feed rate is fixed, so the substrate absorbs the extra energy. This results in an increase in the melting rate of the substrate and a concomitant increase in dilution. Conversely, for a given energy input, an increase in the filler metal feed rate results in a decrease in dilution (i.e., higher Al). Here, the filler metal consumes a larger portion of the total energy input and less energy is available to melt the substrate. As a result, the substrate melting rate decreases and dilution is reduced. It can be seen Fig 2.2 that a dilution level resulting in approximately 10 wt% Al in the cladding represents a boundary condition. Processing conditions below this boundary produced claddings with less than 10 wt% Al that did not crack under the current set of conditions, while claddings produced with parameters above the boundary exhibit greater than 10 wt% Al and were susceptible to cracking.

Previous studies (Fasching, 1995; David, 1989) have shown that iron aluminide claddings with ordered structures (i.e., Fe_3Al and FeAl) are susceptible to hydrogen-induced (cold) cracking due to environmental embrittlement enhanced by residual stresses from welding. Intrinsically, bulk iron aluminides have been observed to be quite ductile when tested in vacuum or dry oxygen atmosphere at room temperature (Liu, 1991, 1990, 1989). However, the ductility dramatically decreases when tested in atmospheres containing moisture. This is attributed to environmental embrittlement involving hydrogen generated from the chemical reaction between aluminum and water vapor (Speidel, 1977):

$$2Al + 3H_2O \rightarrow Al_2O_3 + 6H^+ + 6e^-. \qquad (2.1)$$

The atomic hydrogen is produced at the crack tip and then enters the lattice, propagating ahead of

the advancing crack and reducing the ductility of the alloy. This evolution and transport of hydrogen, when combined with the residual stresses which exist during and after welding (Wang), promote hydrogen cracking. Previous studies (David, 1991) have shown that pre-heat and post-weld heat treatments can be utilized to produce crack-free intermetallic alloys with aluminum concentrations around 15.9 wt%. However, under conditions where preheat and PWHT are not possible, the results in Fig 2.2 indicate that the Al content in the cladding should be below 10 wt%.

Other researchers (Woodyard, 1993; Sikka, 1993; Vyas, 1992) have observed a similar trend for bulk samples. For example, Sikka et al. (1993) have shown that a wrought Fe-Al alloy with 8.4 wt% Al, which has a disordered structure, exhibits a ductility (elongation) above 20% when tested in air. However, when the Al content is increased to 12 wt% and above, the ductility drops significantly to approximately 5 %. This trend is in good agreement with the weldability results presented in Fig 2.2. According to the Fe-Al phase diagram, those claddings that did not crack are located in the single phase, disordered α region. The ordered phase Fe_3Al is first observed approaching 10 wt% Al, leading to a dual phase, ordered Fe_3Al + disordered solid solution α deposit, and as seen in Fig 2.2, the onset of cladding cracking. It must be emphasized that these results should be considered tentative as the sensitivity to hydrogen cracking will also depend on, for example, the degree of restraint as affected by the substrate size. The small-scale results presented here are intended to serve as a guide for further research and subsequent practical applications. The reproducibility of these results to multiple pass deposits produced with both the GTAW and GMAW processes is discussed below.

2.2.3.2 GTAW Multiple Pass Claddings

Based upon the single pass results, a second experimental matrix of multiple pass claddings was produced using similar parameters, Fig 2.7. As found for the single pass welds, the cracking results were again related to the amount of aluminum in the claddings. Due to the 50% overlap of adjacent passes, the aluminum contents of the multiple pass cladding were higher than that of the corresponding single pass welds prepared at identical processing parameters. Microstructures for these samples were similar to those found for the single pass deposits, as seen in Fig 2.3, and cracking was again observed to occur in both inter- and transgranular modes. Electron microprobe

traces through the multiple pass cladding, conducted parallel to the coating-substrate interface, showed that the cladding was homogeneous on a macroscopic scale at these processing parameters, Fig 2.8. Again, cladding compositions on either side of the crack/no crack boundary for the matrix exhibited reproducible cracking tendencies.

2.2.3.3 GMAW Multiple Pass Claddings

Multiple pass claddings were deposited with the GMAW process using a range of currents between 260 and 370 A. Current variations were achieved by changes to both the electrode feed speed and electrode tip to plate distance. In addition, two aluminum-cored, steel sheathed wires with different amounts of aluminum (13 and 27 wt%) were used as consumable electrodes to alter the compositions of the deposits. Fig 2.9 shows the experimental matrix for the claddings produced. A value of 0.87 was used for the arc efficiency to calculate the energy input (DuPont, 1996). All deposits produced with the 27 wt% Al electrode resulted in claddings with more than 15 cracks (above dashed line in Fig 2.9). Use of this electrode resulted in deposits with higher aluminum contents, even when relatively high energy inputs were used. The dilution levels for both electrodes ranged between 40 and 50 %, which is much lower than the range attained for GTAW. Unlike the GTAW process, the GMAW current and electrode feed speed can not be changed independently under the current set of conditions. As a result, it is difficult to achieve a higher range of dilution levels. This made it difficult to produce claddings with compositions near 10 wt% Al. However, for the claddings produced under these conditions, the weldability results are in agreement with those of Fig 2.2 and 2.7, where claddings with less than 10 wt% Al could be deposited crack-free. Like the GTAW deposits, the cladding microstructures had coarse columnar grains and a uniform composition beyond the partially mixed zone (Fig 2.10).

2.3 Weldability Summary

Weldability results were obtained by depositing single pass welds and multiple pass claddings of Fe-Al alloys on carbon steel substrates using the Gas Tungsten Arc (GTAW) and Gas Metal Arc (GMAW) Welding processes. For GTAW, commercially pure aluminum wire was fed into the weld pool of a low carbon steel substrate to produce the overlays. A composite wire, consisting of an aluminum core with low carbon steel sheath, was specially developed for this project and used for the GMAW process. By varying the welding parameters, a range of dilution levels was achieved that resulted in fusion zone compositions with 3 to 30 wt% Al. Under these processing conditions (no pre-heat or post-weld heat treatment), cracking of the Fe-Al claddings was directly related to the aluminum concentration within the deposit. Cracking of the overlays was seen to occurred by both inter- and transgranular modes for deposits containing greater than 10 wt% Al. Below this composition limit, cracking did not occur. According to the Fe-Al phase diagram, this composition indicates the microstructural transition from the single phase region of disordered solid solution (α) to the two phase region of α + ordered Fe_3Al. The ordered structures of Fe_3Al and FeAl have been found to be more susceptible to environmental embrittlement, which has been seen to be the source of the cladding cracking problem.

2.4 Weldability Tables

Wire Number	Al (wt%)	Cr (wt%)	Mo (wt%)	C (wt%)	Zr (wt%)	B (wt% in ppm)
#1	13.2	0	0	0	0	0
#2	26.7	0	0	0	0	0
#3	21.3	0	0.4	0.1	0.25	25-50
#4	21.3	6.7	0.4	0.1	0.25	25-50
#5	10.5	0	0.4	0.1	0.25	25-50
#6	10.5	6.7	0.4	0.1	0.25	25-50

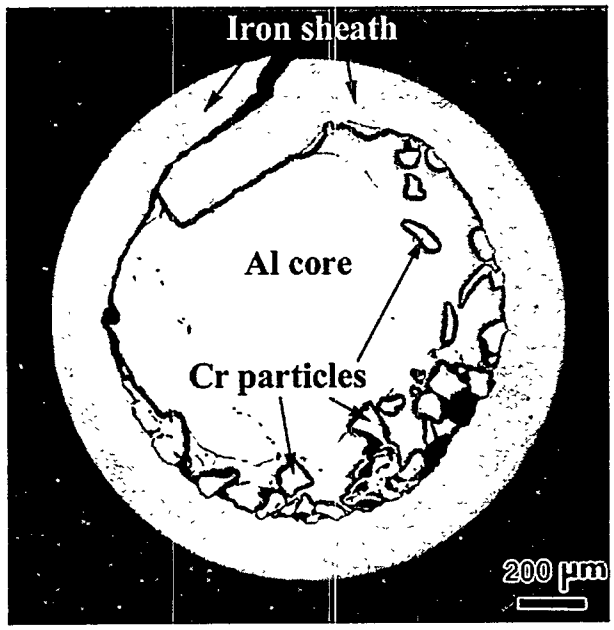

Figure 2.1: Typical cross-section of a composite wire specially developed for this project. This is an Fe-Cr-Al alloy.

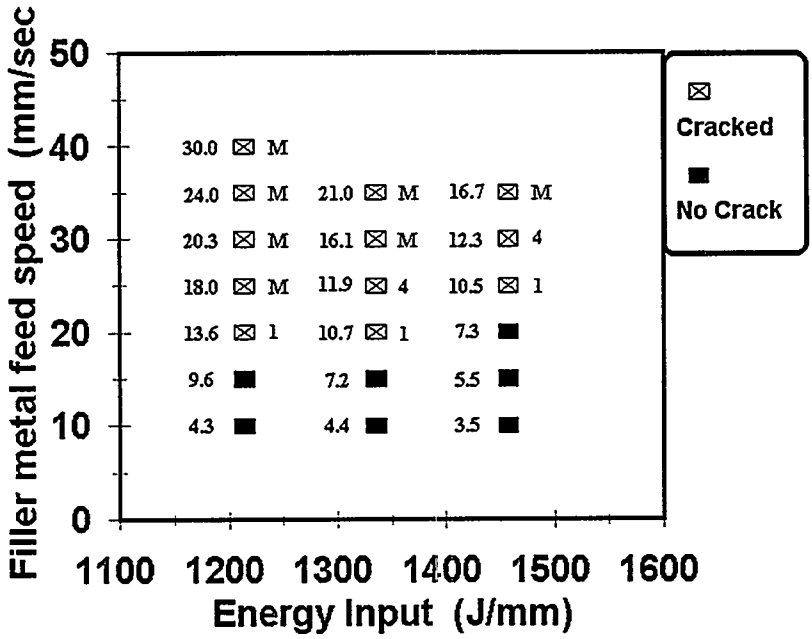

Figure 2.2: Sample matrix of single pass welds produced by GTAW. Each box represents a sample deposited at that processing condition and was subsequently labeled as cracked or no crack. Numbers to the right of the cracked data points signifies the number of cracks that occurred, with M being more than 15. The numbers to the left denote the wt% of aluminum in the deposit.

Figure 2.3: a) Typical columnar microstructure of GTAW cladding.

b)

c)

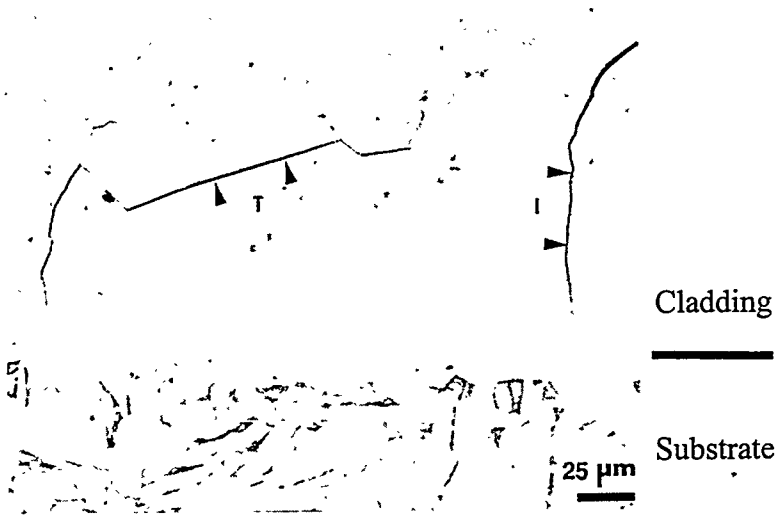

Figure 2.3: b) Cracking is seen to occur by both inter- (**I**) and transgranular (**T**) modes, and c) Cracking is arrested at the fusion line.

a)

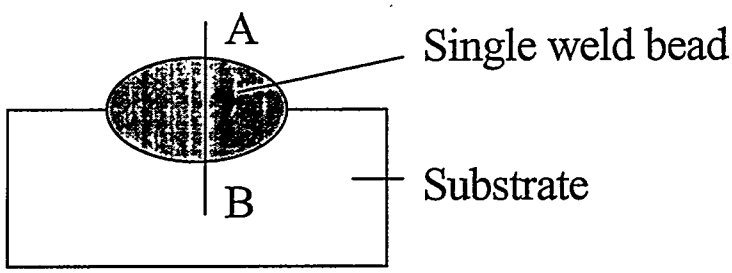

b)

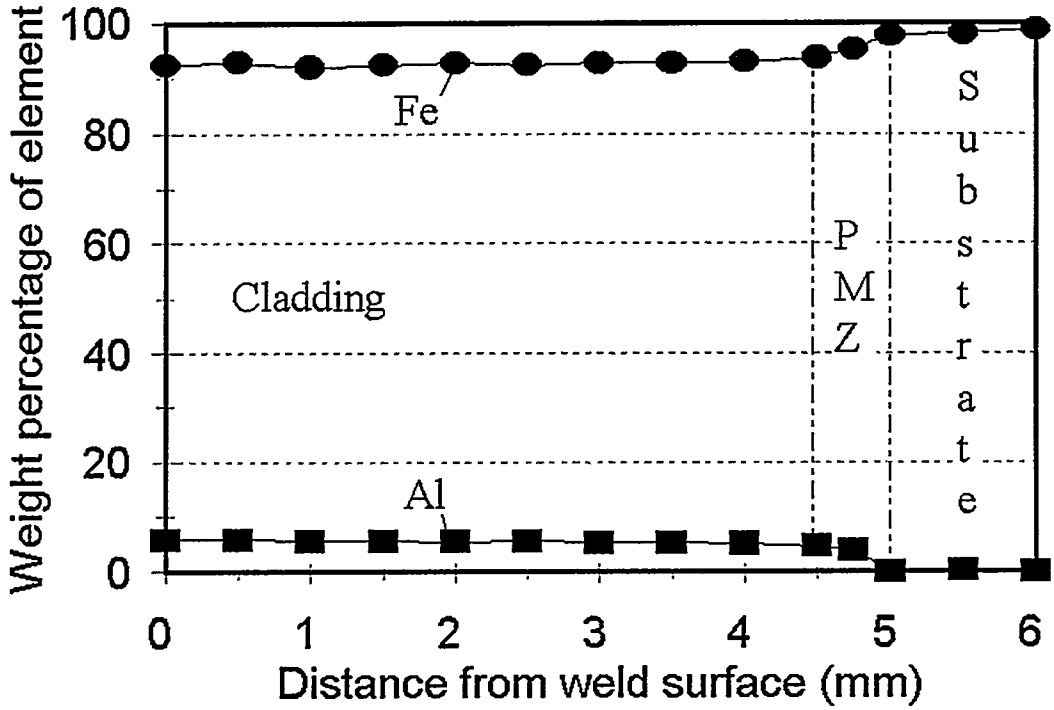

Figure 2.4: Composition EPMA traces through single pass GTAW deposits. Trace were conducted perpendicular to the deposit/substrate interface as seen in a). The size of the partially mixed zone (**PMZ**) is seen to increase as the nominal aluminum content of the weld increases: b) 5.5 wt% Al.

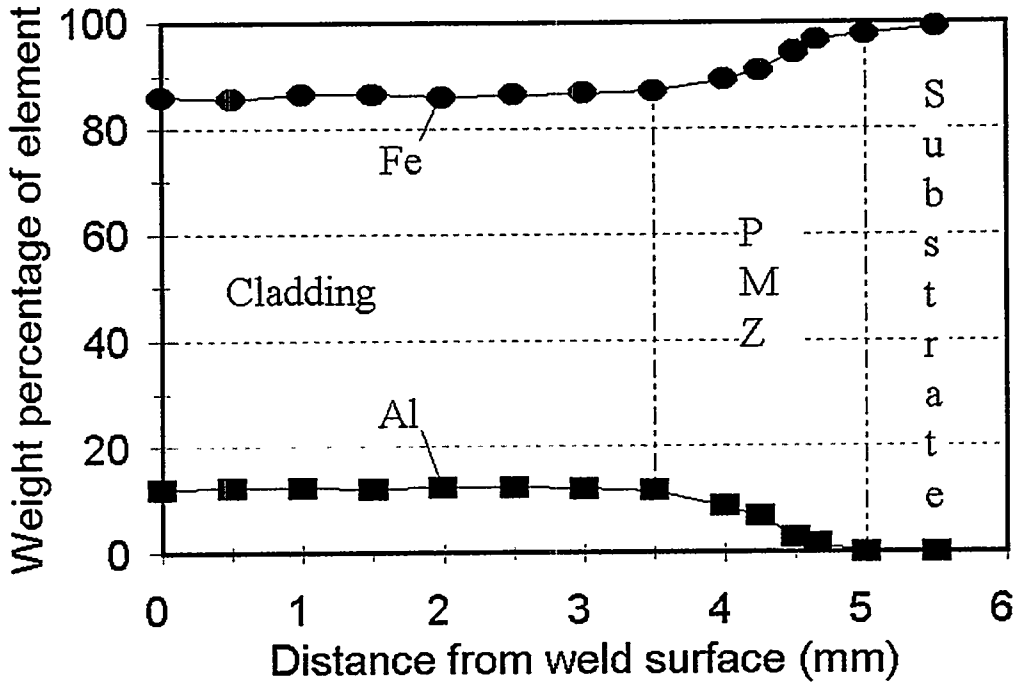

c)

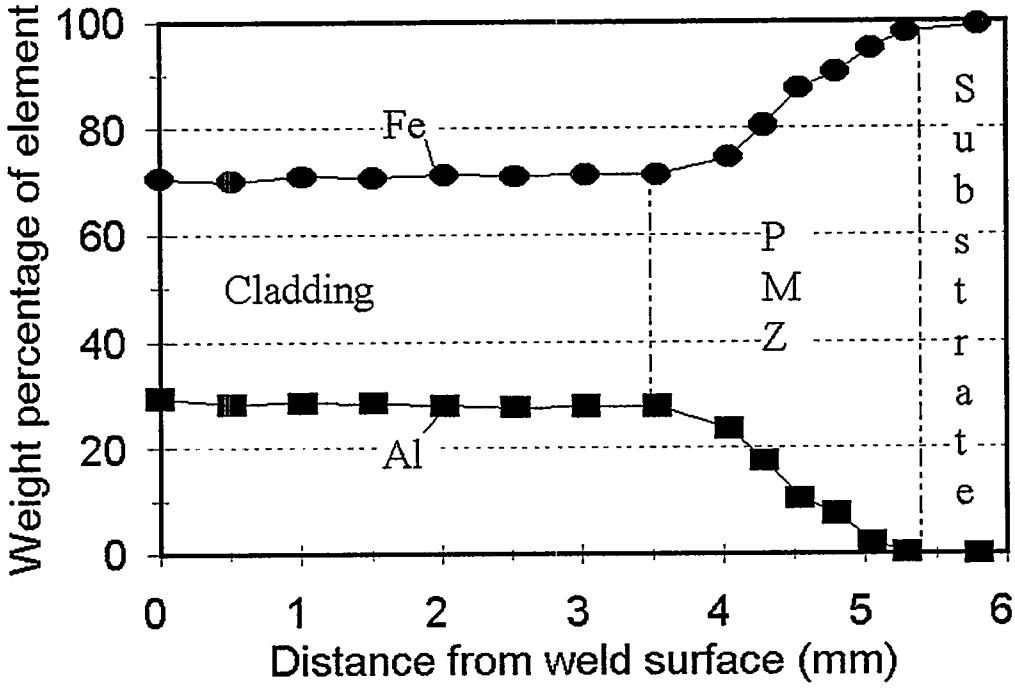

d)

Figure 2.4: Composition EPMA traces through single pass GTAW deposits. c) 12.3 wt% Al, and d) 28.4 wt% Al.

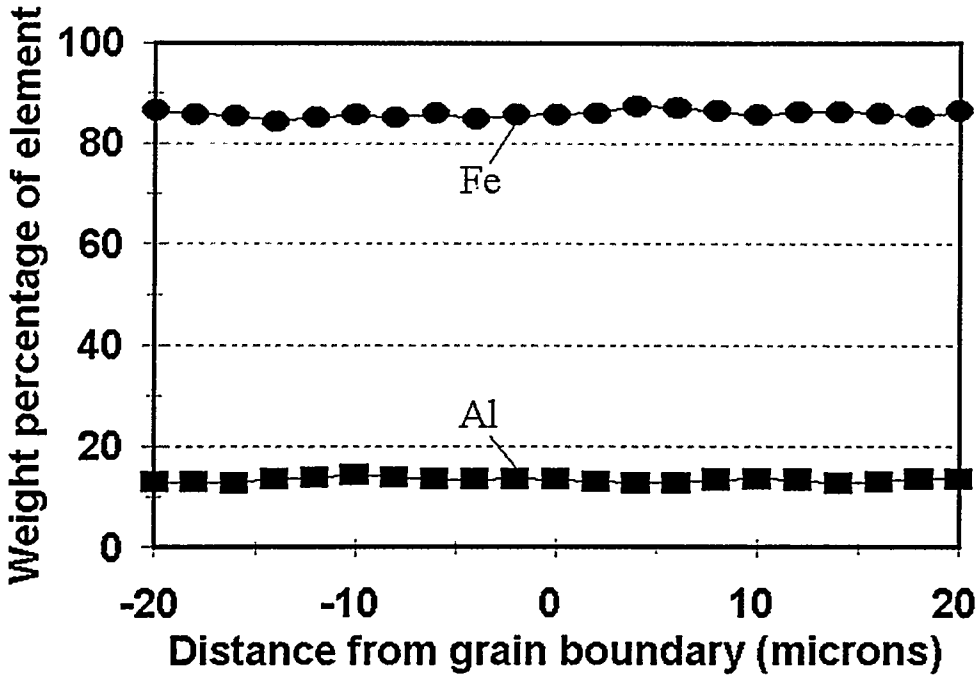

Figure 2.5: Composition EPMA trace across a grain boundary showing no localized concentration gradient.

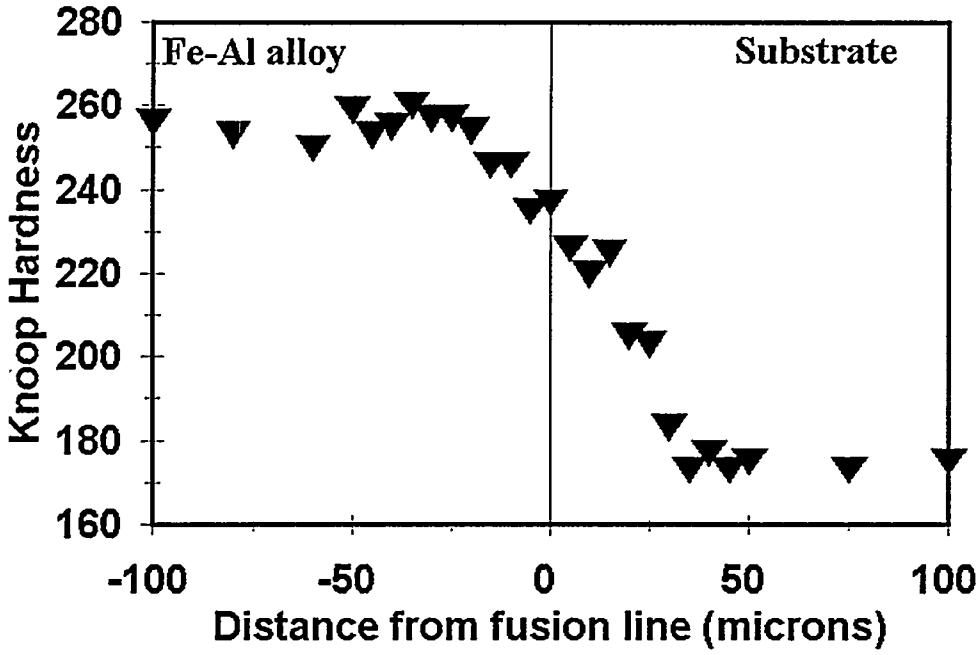

Figure 2.6: Typical Knoop hardness profile across the fusion line of a cladding with nominal aluminum content of 7.2 wt%.

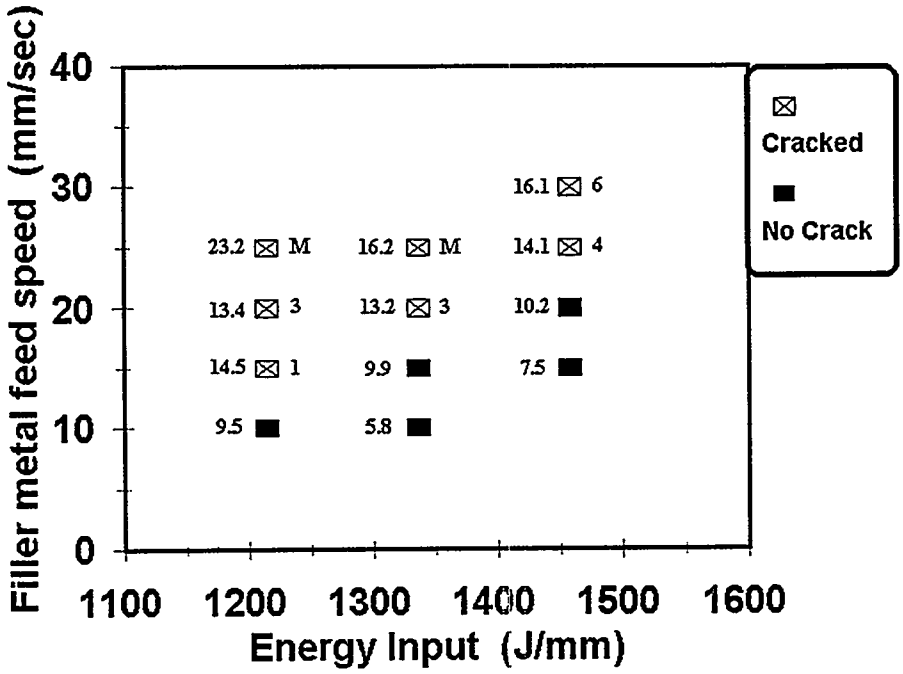

Figure 2.7: Sample matrix of GTAW multiple pass claddings. The symbols correspond to those in Figure 2.2.

a)

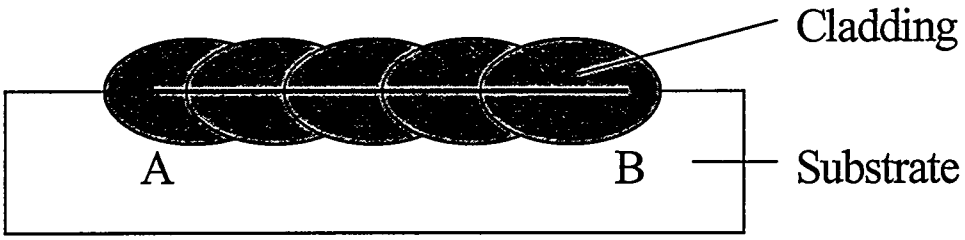

b)

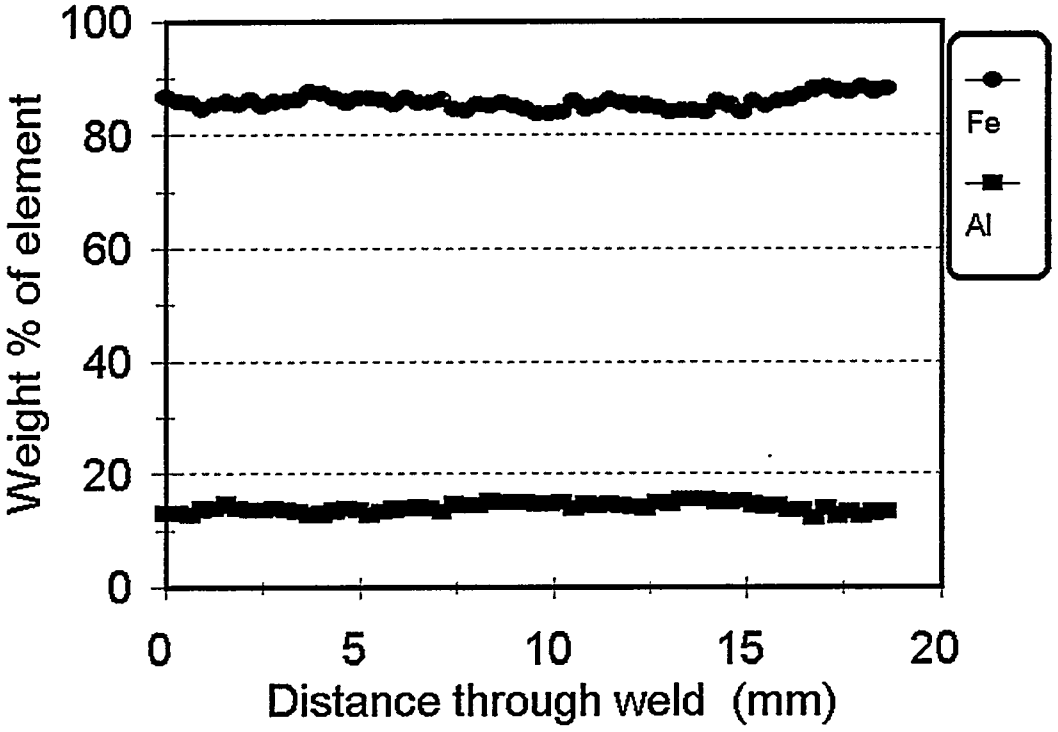

Figure 2.8: Typical composition EPMA trace through a multiple pass cladding showing the deposit is homogeneous on a macroscopic scale. Trace was conducted parallel to the coating/substrate interface as seen in a).

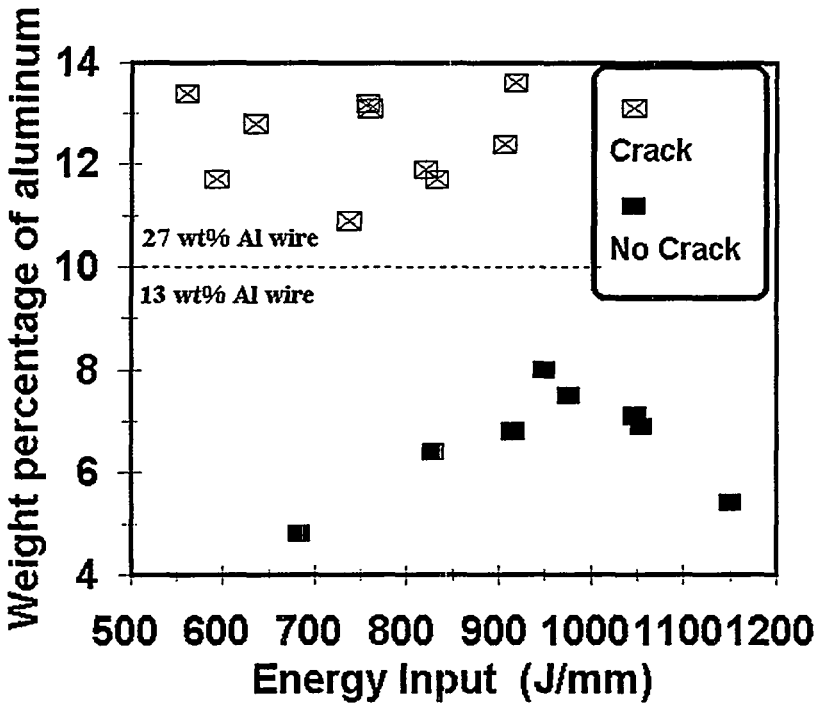

Figure 2.9: Sample matrix of multiple pass claddings produced by GMAW. The dashed line signifies the difference between the two types of aluminum-cored, steel sheathed wires. Above the line, the 27 wt% Al wire was used to produce the claddings, while below the 13 wt% Al wire was deposited. All samples that cracked had in excess of 15 cracks per deposit.

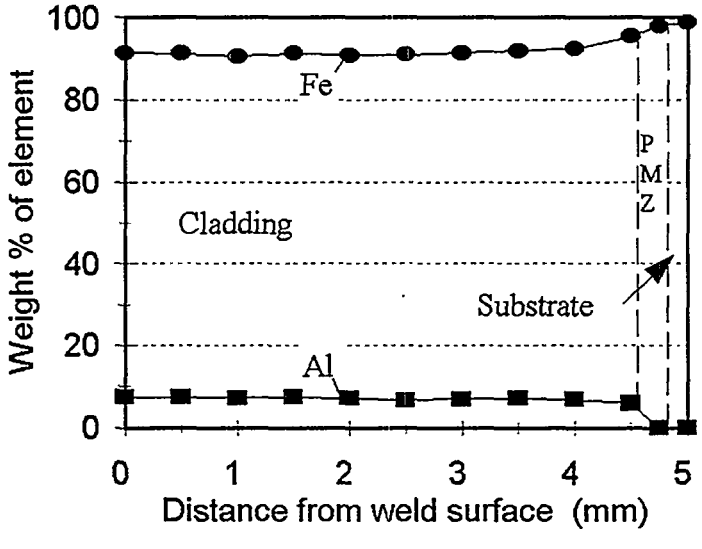

Figure 2.10: Typical probe trace through a multiple pass GMAW cladding. Trace was taken perpendicular to the coating/substrate interface.

3.0 CORROSION STUDIES

3.1 Oxidizing/Sulfidizing Environments

3.1.1 Introduction

This chapter reviews the corrosion behavior of iron-aluminum alloys (0-20 wt% Al) with respect to the alloy content and exposure temperature. These studies were carried out in Ar-H_2-H_2S-O_2 atmospheres ($p(S_2) = 10^{-4}$ and $p(O_2) = 10^{-25}$) at temperatures of 500-700°C for various times in order to observe scale development. Kinetic data was obtained using thermogravimetric techniques and corrosion morphologies investigated through microscopy and electron probe microanalysis analysis. The following sections will review and discuss these results.

3.1.2 Experimental Procedure

The materials used during this research were a series of iron based alloys with varying aluminum additions ranging from 0-20 wt%. All Fe-Al alloys were produced at Oak Ridge National Laboratory by arc melting high purity Fe (99.99 %) and Al (99.99 %) under argon and drop casting into a water cooled copper mold. The low carbon steel was obtained from Ryerson-Thypin Company as a rolled sheet. Table 3.1 lists the alloy book keeping designations and the actual compositions as determined by wet chemical analysis techniques. Characterization of the Fe-Al substrates also consisted of grain size measurements performed using a Donsanto digitizing pad interfaced with a Nikon Optiphot microscope. Substrate faces were ground to 600 grit with silicon carbide papers and polished to 0.05 um colloidal silica. Etching techniques consisted of placing the substrates in boiling water for 1 min and then immediate swabbing for 10-20 seconds with a cooled mixture of 60 ml of methanol, 20 ml of HCl, and 40 ml of HNO_3 [Fasching]. The length and width at half max were measured in order to calculate an aspect ratio for the columnar grains. No discernable difference in grain size was noted after a heat treatment at 700°C for 100 hours. Table 3.2 lists these values.

The experimental alloy compositions were chosen based upon previous weldability results [Banovic]. Using Gas Tungsten Arc and Gas Metal Arc welding processes, it was previously shown that cracking of Fe-Al overlays was directly related to the amount of aluminum in the deposit when applied without preheat and post-weld heat treatments. This crack/no crack boundary of approximately 10 wt% Al was found to be independent of both the welding process and parameters.

Therefore, compositions that were considered both weldable and non-weldable near this weight percentage were chosen for investigation.

As-cast alloys were used to study the high temperature sulfidation behavior instead of actual weld overlay material in order to eliminate the timely procedure of extracting a corrosion coupon from a deposited cladding. In addition, the aluminum depleted region near the overlay-substrate interface, produced due to poor mixing during the welding process, will be avoided. Prior research demonstrated that the corrosion products more readily formed on the specimen face that was located closer to the substrate due to the inhomogeneous composition in this area. This was found to result in higher corrosion rates of the specimen [Tortorelli 1994]. Furthermore, it was previously shown that the sulfidation behavior of Fe-Al weld overlays could be explained on the basis of what was known from cast alloys of equivalent compositions [Tortorelli 1994, 1996].

The high temperature corrosion behavior in environments containing oxygen and sulfur was characterized by three different methods: thermogravimetric techniques, long-term tube furnace, and short-term box furnace. Substrates, with approximate dimensions of 1.5 cm by 1.5 cm by 3 mm, were sectioned from the bulk using a high speed diamond saw. A 5/64" hole was then drilled into the top, middle portion for suspension purposes. Specimens were prepared immediately before insertion into the balance so as to eliminate the formation of a surface scale during storage. Many authors have observed an early transient or "induction" period related to the breakdown of a preformed oxide scale on metallographically prepared samples that were in storage at room temperature [Narita; Pryzbylski 1992a and 1992b; Strafford 1969]. By freshly abraiding the samples before the test, this occurrence can be eliminated. Typical corrosion samples were ground to 600 grit using silicon carbide papers with the corners and edges manually rounded off. Dimensions of the substrate, to the nearest hundredth of a mm, were then taken using a micrometer. As a final step, the samples were ultrasonically cleaned in soapy water, rinsed, and then ultrasonically cleaned in methanol. Weight of the sample was recorded to the nearest mg.

A Netzsch STA 409 high temperature thermogravimetric balance was used to measure weight gain as a function of time for a given temperature. The sensitivity of the balance is ± 1.25 micrograms on the lowest setting and the temperature accuracy is ± 1.0°C. A water jacket, maintained at 35°C ± 1°C, was employed to help reduce ambient temperature fluctuation effects on these measurement capabilities of the instrument.

As traces of oxygen from laboratory air will affect the results, a minimum of 6 vacuum/argon purge cycles of the testing chamber were performed after sample installation. The corrosive gas was metered through the testing chamber at a rate of 50 ml/min while a similar flow rate was used to meter ultra high purity argon into the base of the equipment. The balance was then allowed to purge for a minimum of 2 hours with the corrosive gas flowing through the chamber. After the balance was zeroed, a test was started using a typical temperature program as seen in Table 3.3. The isothermal hold at temperature was varied between 1 to 100 hours, with most samples being exposed for only 50 hours. Following the isothermal hold at room temperature, specimens were removed and weighed to the nearest mg.

Before normalizing the raw data by the surface area, it was corrected for the buoyancy force imposed on the sample by the corrosive gas at temperature. Buoyancy curves for each temperature were experimentally produced in a similar procedure to the corrosion testing described above with the exception that a piece of alumina, with similar volume to the corrosion coupons, was placed in the chamber. This test was conducted for 3 hours so as to obtain the steady state buoyancy force. This curve was then subtracted from the original data eliminating the effects of buoyancy. In addition, accuracy of the balance was periodically checked at room temperature using certified weights from Troemner, Inc.

Tests with durations of 100 hours were also conducted in a Lindberg tube furnace. Samples were prepared as above and suspended in an alumina crucible using alumina rods. No more than four samples were tested at a time. Samples were placed in the middle of the "hot zone" of the furnace and sealed by aluminum end caps. The hot zone for the furnace was determined by placing a thermocouple at known locations within the furnace while argon was flowing at temperature. Due to the flowing gas, the natural hot zone of the furnace was found to be shifted towards the exhaust end, and therefore, had to be corrected by placing the samples off center and closer to this end. Integrity of the tube and seals was checked prior to testing by pulling a vacuum on the system after sample insertion. An acceptable rate of vacuum loss was 0.5 torr/min. Vacuum/argon purge cycles were again conducted, typically 15-20 times. The tube furnace was then allowed to purge for a minimum of 8 hours with the corrosive gas flowing at a rate of 300 ml/min. The heat up of the furnace typically occurred in about 30 minutes while cool down to room temperature lasted about 5-6 hours.

The gas compositions and temperatures for the above experiments were chosen so as to produce a highly reducing environment that is indicative of low NO_x gas conditions [Chou; Urich; Gabrielson]. Previous research [Banovic 1999a, 1999b] in less aggressive gas compositions ($10^{-34} < p(O_2) < 10^{-27}$ atm and $10^{-11} < p(S_2) < 10^{-8}$ atm) showed that the lower aluminum content alloys performed well in the range of 500-700°C. A higher partial pressure for oxygen, $p(O_2)$, and sulfur, $p(S_2)$, were thus chosen and mixtures of Ar-H_2-H_2S-O_2-Ar gases determined so as to maintain equivalent partial pressures at different temperatures. Table 3.4 shows the gas compositions for each temperature and the corresponding $p(O_2)$ and $p(S_2)$ values. The $p(O_2)$ was determined using a solid state oxygen detector and the $p(S_2)$ was calculated using the SolGasMix program. Since the oxygen detector is limited by temperature (operable only above 600°C), it could not be used to directly determine the $p(O_2)$ at 500°C. Instead, numerous measurements were taken between 600-850°C and the value for 500°C extrapolated.

A bookkeeping designation system for the corrosion samples was also developed for easy reference. This system identified the alloy, temperature, and exposure gas. The samples were coded as follows: **TX.xYZ**. The **T** indicated that the sample was corrosion tested, the **X.x** designated the weight percentage of aluminum in the alloy (with possible values of *0, 5, 7.5, 10, 12.5, 15,* and *20*), **Y** indicated the temperature (with possible values of *5, 6,* and *7* for 500, 600, and 700°C), and **Z** signifying the exposure gas (with *2* indicating oxidizing-sulfidizing and *3* as oxidizing). Therefore, for a code of **T1072**, the alloy tested was Fe-10wt% Al at 700°C in an oxidizing-sulfidizing environment.

Macroscopic photographs were taken of the samples using an Olympus SZH10 Research Stereoscope interfaced with a SONY Color Video Printer in order to show the coloring of the corrosion product. These outer surfaces were then characterized using a JEOL 6300F scanning electron microscope with an Oxford (Link) energy dispersive spectroscopy (EDS) system capable of detecting light elements. Secondary electron images (SEI) of the surface morphologies were obtained using a working distance of 16mm with an accelerating voltage of 3.0 kV and a condenser lens setting of 7. When obtaining qualitative chemical information from the surface scales, the accelerating voltage was increased to 20 kV with a decrease in both the working distance (15mm) and condenser lens setting (5).

For samples with low weight gains and/or thin corrosion products on the surface, a fracturing technique using liquid nitrogen was employed to view the scale in cross-section. By notching the back side (approximately 4/5 of the thickness of the substrate) with a low speed diamond saw and submersing the specimen for a minimum of 3 minutes in liquid nitrogen, the samples easily broke. Cross-sectional micrographs of these samples were also taking using the JEOL 6300F with the same working conditions as used for the surface SEIs.

Samples that developed large amounts of corrosion product were mounted in cold setting epoxy. Shields were used to maintain edge retention between the epoxy and scale, as well as reduce rounding that occurs on the edges of the sample due to the preparation techniques. Subsequent grinding procedures to 1200 grit with silicon carbide papers was initial conducted using methyl alcohol (methanol) as a lubricant. It was hoped that this would eliminate the destruction of any underlying sulfide scale that may dissolve in water. It was later determined that 200 proof dehydrated ethyl alcohol (ethanol) offered better results. A final polishing step was conducted using 1.0 um diamond paste on a low nap cloth. Further polishing with any type of colloidal alumina or silica was avoided in order to eliminate any possibilities of contamination or pull-out of the scale.

All cross-sectional light optical micrographs (LOM) found in this study were taken using a Reichert-Jung MeF3 metallograph. SEI cross-sections were also obtained using the JEOL 6300F with similar parameters found above. Cross-sectional scale thicknesses were measured on both light optical samples and SEI micrographs using a Donsanto digitizing pad interfaced with a Nikon Optiphot microscope. A minimum of 20 lengths were taken per layer per sample on various planes. Quantitative chemical information was obtained using a JEOL 733 electron probe micro analyzer (EPMA) equipped with wavelength dispersive spectrometers (WDS). The accelerating voltage and probe current were 20 kV and 50 nA, respectively. K_{alpha} x-ray lines were analyzed and counts converted to weight percentages using a phi (rho z) correction scheme.

3.1.3 Results

3.1.3.1 Corrosion Kinetics

Exposure at 500°C

Fig 3.1 shows a plot of weight gain versus time for the alloys tested at 500°C. Additions of aluminum were found to decrease the overall corrosion rates of the samples with the low carbon steel

(LCS) reference having the highest weight gain. This specimen displayed linear kinetics over the 50 hour period (Table 3.5). Continuous weight gain data for the various exposure times of the 5Al sample can be found in Fig 3.2. Curves having similar behavior of initially rapid weight gain followed by what appeared to be steady state growth were found with good reproducibility. The time rate growth constant for the 50 hour exposure revealed behavior that was between diffusion and interface controlled. Fig 3.3 shows the kinetic behavior of the 7.5Al samples. Similar to the 5Al sample, the 50 hour exposure also had an initially high weight gain followed by somewhat linear growth. The n-value calculated showed that growth was nearly parabolic in nature. The 100 hr exposure was conducted in a tube furnace, therefore no continuous weight gain data could be obtained. However, the final weight gain was plotted on Fig 3.3 and did not appear to be in agreement with the sample exposed for the shorter time. (It was found that the chamber used to test the 100 hr sample was contaminated from previous experiments. These results were subsequently deleted from the analysis.) The 10Al and 12.5Al samples were also exposed for 100 hrs in a tube furnace and developed very little weight gain (0.1 mg/cm^2) as seen in Fig 3.1.

Exposure at 600°C

Fig 3.4 shows a plot of weight gain versus time for the alloys tested at 600°C. Again, the corrosion rates were found to decrease with additions of aluminum with the LCS sample displaying linear kinetics again (Table 3.6). Unlike the 500°C data, the 7.5Al sample obtained a higher final weight than 5Al. Exposure of the 5Al alloy for various times produced curves that were again similar, Fig 3.5. All exposures contained an initial period of high weight gain followed by a steady state regime of what appeared to be steady state growth. The time rate growth constant indicated behavior between diffusion and interface controlled. The 7.5Al alloy was exposed for 50 and 100 hours. The 50 hour sample was tested using thermogravimetric techniques and the kinetic data can be seen in Fig 3.6. An initial period of slow weight gain followed by an increase in the rate can be observed, which led to an n-value greater than 1. This has no physical meaning in terms of the mechanism for scale growth as 1 signifies interface control. The 100 hour sample was tested in a tube furnace with no continuous weight gain measurements being obtained. However, the final weight gain was plotted on the graph for comparison (Fig 3.6) and appeared to agree with an extrapolation of the 50 hour data. The 10Al and 12.5Al samples exhibited negligible weight gain

over the period of 100 hours. 50 hour exposures were tested in the balance and results plotted in Fig 3.7. A high degree of noise from the balance can be seen to affect the weight gain data. 100 hour exposures were conducted in a tube furnace and final weight gain plotted on the Figure. Again, an extrapolation of the 50 hour data showed good agreement between the samples.

Exposure at 700°C

Fig 3.8 shows kinetic results obtained at 700°C for the longest exposure time for each alloy. The effect of composition can be readily observed in the decreasing overall weight gains with increasing aluminum content. The low carbon steel sample was found to have weight gain that increased smoothly with time at a decreasing rate, Fig 3.9. However, when plotted on a logarithmic scale, two stages of growth could be observed, Fig 3.9b. An initial period of low weight gain, confirmed by the sample exposed for short time, was followed by a period of higher growth rates. Calculation of n-values indicated that the early period followed parabolic kinetics, whereas the later stage was closer to linear kinetics, Table 3.7.

Various exposure times for the 5Al sample showed good reproducibility in the results, Fig 3.10. There appeared to be two different regimes of high weight gain noted by the bend in the curve near 15 hours. The n-value calculated for the 50 hr time period was found to be above 1, which has no physical meaning in terms of the mechanism for scale growth.

Fig 3.11 shows the kinetic data for the 7.5Al samples. The samples exposed for 10 and 100 hours have similar initial behavior showing a high rate of weight gain, with the 100 hour corrosion rate reaching a steady state period at long times. Likewise, the weight gains for samples exposed for 20 and 50 hours are similar in shape to each other, however, have a different trend from that previously seen. Their weight gain was lower in the beginning followed by increased reaction at later times. Again, a value above unity was calculated for the growth rate time constant.

The weight gain data for the 10Al sample, tested at 2, 50, and 100 hours can be seen in Fig 3.12. Anomalous behavior was observed in the fact that the sample tested for 50 hours was found to have the highest weight gain. However, when compared to the weight gain of the lower aluminum samples, the amounts are considerably low. Plotting the kinetic data on a logarithmic scale indicated the existence of three regimes of weight gain for the 50 hour sample, Fig 3.12b. The initial stage of

negligible weight gain (points a-b) was followed by rapid growth (points b-c) that appeared to change over to a steady state period (points c-d). The 2 hour sample appeared to follow a similar trend of negligible weight gain for the short time, as does the 100 hour sample for the longer exposure times. The value for the time rate growth constant of section a-b was found to be negligible where as the other sections had values above 1.

The weight gain data collected for the 12.5Al alloys also revealed that the 100 hr sample had less weight gain than the 50 hr exposure, Fig 3.13. Again, the rates were negligible when compared to the previous low Al compositions tested. The sample exposed for 50 hours showed an initial period of negligible weight (points a-b) which was then followed by rapid growth (points b-c) when plotted on a logarithmic scale, Fig 3.13b. This type of behavior appeared similar to the first two stages observed for the 10Al sample at 50 hours. The n-values were similar to that calculated for the 10Al samples.

Higher aluminum content samples were also tested at 700°C. The kinetic data obtained for the 20Al sample can be seen in Fig 3.14. Negligible weight gain, with a high degree of noise from the balance, was found. While an error in the computer program did not allow for data collection during exposure of the 15Al sample, it's final weight change was measured after 100 hours and plotted on the figure also. Due to the similar final weight gain, it was assumed that the kinetic behavior of the 15Al sample was similar to the 20Al sample.

3.1.3.2 Corrosion Morphologies

During the course of exposure, the Fe-Al alloys were found to react with the corrosive environment and form products on their surface. The development of these products, in terms of the type and morphology, was found to have a large effect on the corrosion behavior of the alloys. The following section first describes the three general scale types observed (Figs 3.15-3.17) followed by their growth, with some modifications, on the individual alloys.

Type I Scale

This scale typically consisted of duplex layered, thick product growth that was continuous across the surface, Fig 3.15. The outer scale was found to be composed of iron sulfide in two

different morphologies: large plates and an outer interfacial layer containing minor quantities of aluminum (approximately 1 wt%). The inner scale was observed to be composed of two different regimes also: an inner interfacial layer of iron sulfide with minor quantities of aluminum (1 wt%) present and a mixed region of tau phase ($FeAl_2S_4$) plates and iron sulfide particles. For some samples, there appeared to be the remnants of an initial surface scale between the two interfacial layers. Fig 3.18a-3.18d displays macrographs that were characteristic of surface scales, depending upon the stage of development, related to this type of growth.

Type II Scale

This scale typically consisted of a continuous, thin scale of equiaxed grains of gamma alumina, Fig 3.16. Small sulfide platelets were found emerging from between the alumina grain boundaries but no corrosion product or ingress of sulfur was found in the substrate below the layer. Macrographs showing the coloring related to its formation can be found in Fig 3.18e-3.18g.

Type III Scale

This scale development was found to be a mixture of the Type I duplexed layer scale in the form of nodules dispersed across a scale of gamma alumina (Type II), Fig 3.17. Their location was generally random on the faces with a high density on the corners and edges. Fig 3.18h displays the characteristic appearance of its surface.

Exposure at 500°C

The low carbon steel sample was observed to develop a black surface scale that sparkled when rotated in light, Fig 3.18d. Fig 3.19a shows coverage by a continuous surface scale that was found to be badly cracked in the center. Higher magnification revealed the scale was composed of numerous plates of corrosion product in various orientations (Fig 3.19b) that contained Fe and S according to EDS analysis. Due to the growth of the plates, the outer scale appeared very porous as observed in cross-section using light optical microscopy (Fig 3.20). A bilayered scale was found consisting of the outer surface plates and an inner, fine grained region that had separated from the substrate, Fig 3.20b. These layers were 218 ± 21 um and 31 ± 5 um in thickness, respectively. The

scale, which had pulled away from the substrate, had linear interfacial attack into the alloy. EPMA results indicated that the scale was iron sulfide, with analysis of the substrate at the alloy-scale interface revealing no traces of sulfur, Table 3.8.

The 5Al samples at all times developed similar scales that were silver in color (Fig 3.18b) and reflected light. As the exposure time increased, the degree to which the samples sparkled also increased. Fig 3.21 shows SEI images of the samples at low magnification that have continuous surface scales. Higher magnification revealed that the surface was composed of thick hexagonal plates that contained iron and sulfur, Figs 3.22-3.26. The thickness of these plates was found to increase with time, Fig 3.27, with a time rate growth constant of 0.52.

Polished cross-sections revealed development of a Type I scale, Figs 3.28-3.32, with slight deviations from the general morphology as observed in Fig 3.15. The outer scale was composed of the large plates that were visible on the surface. Some porousness was observed near the inner scale-outer scale interface. EPMA data indicated the outer scale was a layer of iron sulfide, with non-uniform distribution of aluminum being detected throughout the base of the structure (Table 3.9). As an example, the area marked with an "**X**" in Fig 3.32a had approximately 0.4 wt% Al in solution, whereas the area marked with "**O**" had no aluminum present. The inner scale had linear interfaces with both the outer scale and substrate and was relatively uniform. No well defined interfacial regions could be observed, with the exception of the sample exposed for 25 hrs, Fig 3.31a. Higher magnification of the inner layer revealed a complex morphology of light particles in a dark phase matrix that was relatively compact. Fig 3.29b shows a good example of this. An EPMA scan of this region (approximately 10 square microns) placed the composition in a two phase region of iron sulfide and tau phase. Substrate near the alloy-scale interface was also analyzed with EPMA and indicated no sulfur and no depletion layer of either metallic element. Measurement of the individual constituents of the scale showed a general increase with time, Fig 3.33, with n-values between 0.6 and 0.7 being calculated for both the inner and outer scale.

The 50 hour exposure of the 7.5Al alloy produced a sample that had a dull gray surface scale, Fig 3.18a. The 100 hour sample was a darker gray that reflected in the light, Fig 3.18b. Low magnification SEI micrographs displayed two different types of surface scale, Fig 3.34. The 50 hour sample appeared to have a continuous and dense surface scale, whereas the 100 hour sample was

more porous. Closer examination of the 50 hour structure revealed ball like formations on the continuous surface scale, Fig 3.35. This scale was not like any other observed in this study and was found to contain iron, sulfur, and phosphorus. The porous scale of the 100 hour sample can be seen in Fig 3.36 as plates that have impinged upon growth, similar to the 1008 sample.

Cross-sectional analysis of these samples showed development of Type I scales. The 50 hour sample, Fig 3.37, had a continuous outer layer of iron sulfide with some phosphorous dissolved in solution. The inner scale showed characteristics of previous scales in terms of protrusions into the substrates and the appearance of a two or three phase microstructure. Unfortunately, good quantitative chemical data could not be obtained from this region, but did contain Fe, Al, S, and P. The 100 hour sample had blocky-type iron sulfide growths that grew on top of a continuous inner scale, Fig 3.38. Aluminum was again non-uniformly distributed along the base of the growths, Table 3.10. The inner scale was composed of dark plates and light gray particles, Fig 3.38c. Microprobe scans (approximately 5 square microns) of this area again placed the composition in a two phase regime of iron sulfide and tau phase.

The 10Al and 12.5Al samples both had a tanish color (Fig 3.18e) with the 12.5Al specimen having a purplish tint (Fig 3.18f). No appearance of corrosion products on their surfaces could be seen and the faces were still relatively shiny. Fig 3.39 shows the SEI micrographs at low magnification indicating very little corrosion product on the surface. Higher magnification revealed growth of a continuous, granular surface scale with platelets emerging from it, Fig 3.40 and 3.41, characteristic of Type II scale growth. The platelets contained significant amounts of iron, aluminum, and sulfur. The granular scale, which was similar for both alloys, had significant amounts of aluminum and oxygen with minor amounts of iron and sulfur, Fig 3.42. The average size of the particles was between 100-200nm. Cross-sectional analysis using fractured specimens indicated that the granular scale was about 100nm in thickness after 100 hours of exposure, Fig 3.43. Even after quenching to liquid nitrogen temperatures the scale appeared to have relatively good adhesion with the substrate.

Exposure at 600°C

The corrosion product formed on the 1008 sample was again faceted with a silver coloring that reflected light when rotated, Fig 3.18b. SEI images of the surface revealed a continuous surface

scale, Fig 3.44. A few larger particles can be observed growing on the corners of the sample in the shape of hexagonal plates. Higher magnification of the surface (Fig 3.44b) showed facets of non-uniform size with inter and transgranular cracking of the scale. Polished cross-sections revealed a bilayered scale, Fig 3.45. The outer layer was a relatively compact and uniform layer of columnar grains. The inner scale was composed of fine grains (Fig 3.45b) that had a linear interface with both the outer layer and the substrate. EPMA results (Table 3.11) indicated that the outer scale was iron sulfide. The inner scale was too fine to be analyzed by this technique, but was also assumed to be iron sulfide. Analysis of the substrate near the inner scale interface showed no presence of sulfur.

Characterization of the corrosion scales formed on the 5Al alloy revealed Type I scale development. The samples showed two different colorings of the surface scales. Before 30 hours of exposure, the surfaces had a matte gray finish, Fig 3.18a. Beyond this time period, the samples exhibited silver faces with black corners and edges Fig 3.18c. Some faceting was noted at 50 hours as the sample was rotated in the light. Fig 3.46 shows the SEI images of the sample surfaces that developed full coverage by corrosion products over the time period studied. The surface of the 1 hour sample was uniformly covered by a grainy scale (Fig 3.47) that contained iron and sulfur with small amounts of aluminum. By 5 hours, this scale had given way to the formation of thin platelets, Fig 3.48, that were randomly distributed across the surface. These platelets were observed to thicken with time (Figs 3.49-3.51) and advance out of the page. As seen for the LCS sample, the corner plate structures were observed to form sometime before 30 hours (Fig 3.46d).

Development of the corrosion products was also observed through cross-sectional analysis. Polished samples indicated the growth of a bilayered scale, Figs 3.52-3.56, that resembled that the 500°C samples very little. The outer scale consisted of both the initial grainy scale and the thin plates that emerged from it. The plates were determined by EPMA to be iron sulfide with minimal amounts of aluminum (<0.5 wt%) located near their base, Table 3.12. The other grainy particles were also iron sulfide with aluminum that was uniformly distributed through out the structure (approximately 1 wt %). A flat interface was found between the outer and inner scale for all exposures. The inner layer was relatively uniform in thickness, with the exception of the protrusion of dark plates into the substrate. The phases were too small to individually analyze via EPMA so a scan (approximately 2 square microns) of this layer was conducted. The composition placed it in

the two phase region of $Fe_{1-x}S$ and the spinel. Again, the plates were seen protruding into the alloy. EPMA analysis of these features also could not be conducted but EDS analysis indicated the presence of iron, aluminum, and sulfur. Analysis of the alloy around these needles (within detection limits of the probe, ~ 1 um) was conducted with no loss of either metallic element and no presence of sulfur. As time increased, the individual constituents of the scale were also found to increase, Figs 3.57. The n-values calculated for the growth of the inner and outer scales were 0.57 and 0.84, respectively.

Examination of the 7.5Al samples revealed Type III scale for short exposure periods that eventually developed into Type I scale at the later time. The 50 hr sample had a gray-tan coloring with coverage of dark, spotty growths (Fig 3.18h). The sample exposed for 100 hours was black, Fig 3.18d, with sparkling facets on the surface. This scale was somewhat friable as small flecks continually fell off with repeated handling. Fig 3.58 shows two completely different surface coverages for the samples. At 50 hours, the sample is covered with groupings of corrosion products, Fig 3.59. Unlike the sulfide plates observed on the 5Al samples, these sulfide plates (Fig 3.59b) are thick, being approximately 12.6 ± 3.0 um and contain iron and sulfur. Where these large sulfide phases were not found, the growth of sulfide platelets emerging from a granular surface scale was observed, Fig 3.60. The features of the surface scale (Fig 3.60b) were again on the order of 100-200 nm and contained high counts of aluminum and oxygen. The 100 hour sample had full coverage of the surface by large, thin plates (Fig 3.58b and 3.61) that have emerged from a surface coverage of thicker plates, Fig 3.61b. Both plates showed the presence of iron and sulfur. No indication of prior formations as that found on the 50 hr sample could be observed.

Cross-sectional analysis of the samples revealed Type III scale for the 50 hr sample and Type I for the 100 hr exposure. The outer sulfide scale was again iron sulfide with minor amounts of aluminum non-uniformly distributed in solution near the base (Table 3.13), Fig 3.62. Microprobe scans (approximately 5 microns square) of the inner scale (Fig 3.62b) indicated a composition in the two phase region of tau and iron sulfide. Analysis of the substrate below the granular scale and near the tau phase protrusions revealed no depleted area of metallic elements (Fe,Al) or the presence of sulfur. Fractured cross-sections showed the thin granular scale was just less than 100 nm and very adherent to the substrate, Fig 3.63. The cross-section of the 100 hour sample was also bilayered, but

observed to be continuous, Fig 3.64. The large iron sulfide plates can be seen to rise above the smaller sulfide scales. Again, very little aluminum was found non-uniformly distributed near the base of these features. Fig 3.64b-3.64d displays regions of the tau phase plates and iron sulfide particles of the inner layer. The remnants of a thin continuous scale can be observed in Fig 3.64b between the outer and inner scale (arrows). This was also observed, though not readily, in Fig 3.62a also where the nodules were found to grow. Finer detail of the inner phases can be seen in Fig 3.64c of the scale-alloy interface and Fig 3.64d of the inner scale.

The 10Al and 12.5Al samples had various colors associated with them. Both 50 hour exposure samples were found to be purple-tan (Fig 3.18f) and retained some of their shininess. The 100 hour samples were similar with the 10Al being blue-tan (Fig 3.18g) and the 12Al being primarily blue. Low magnification SEI micrographs reveal the growth of corrosion product nodules on the corners and edges of the 10Al samples, Fig 3.65. The size of these nodules averaged 241 ± 12 um and 634 ± 25 um for the 50 and 100 hour samples, respectively. The 12Al samples did not have any growths, Fig 3.66. Surface coverage was again found similar to the other samples with minimal scale growth and development of Type II scale. Figs 3.67 and 3.68 show characteristic micrographs of the sulfide platelet coverage and granular background scale for the 10Al and 12.5Al samples at various exposure times. The individual features (platelets and granular scale) can be seen to increase in size with time. Fractured cross-sections revealed the thin granular scales as being just under 100 nm for the 50 hour exposures and just over 100 nm for the 100 hour samples, Fig 3.69 and 3.70. Adhesion between the scale and substrate appeared good, even after the quenching in liquid nitrogen.

Exposure at 700°C

The LCS samples, which were tested for 1 and 50 hrs, had similar silver colored scales (Fig 3.18b). The faces of the samples were faceted which reflected light when rotated. SEI images of the samples revealed continuous surface scales (Fig 3.71) on both samples with large amounts of corrosion products on the corners and edges of the 50 hr specimen. These edge products were in the form of large hexagonal plates that were symmetrical, Fig 3.72. EDS analysis indicated the presence of Fe and S. Higher magnification of the faces revealed the facets as pyramidal-type structures of various sizes, Figs 3.73, similar to that observed at 600°C. The surface of the facets were relatively

smooth with some porosity found on the surface. Also noticeable in these Figures was inter and transgranular cracking across the surface. Light optical micrographs of polished cross-sections revealed a bilayered structure (Fig 3.74) as previously seen on the sample tested at 600°C. Both layers were porous, with the outer layer being columnar, as noted by the visible grain boundaries, and the inner scale fine grained, Fig 3.74b. The thicknesses for these layers was 372 ± 13 and 34 ± 5 um, respectively. EPMA results, Table 3.14, indicated that the scale was iron sulfide. Analysis of the substrate near the corrosion front did not find any presence of sulfur. For the large plates that were found to grow at the corners and edges, no significant difference in composition was noted with the exception of a slightly higher concentration of sulfur. Unfortunately, due to the brittle nature of the sulfide, the scale on the 1 hr sample crumbled before it could be mounted, thus eliminating the ability to view it in cross-section.

Examination of the 5Al samples revealed the development of Type I scale over the time period studied. With time, the color of the surface scale was found to change. Up to 45 minutes, the scale had a dull gray appearance (Fig 3.18a). Further exposure through 15 hours revealed faceted scales that had a silver color (Fig 3.18b). Beyond this time frame, samples obtained silver faces with corners and edges that were black (Fig 3.18c). SEI images of the samples at low magnification for the various times can be seen in Fig 3.75. The appearance of plates at the corners and edges of the samples, similar to the LCS sample, originated some time between 45 minutes and 5 hours. These plates (Fig 3.76) were found to increase in size as time increased and have the same type of morphology as those observed on the LCS sample.

Higher magnification of the surface revealed the development of a porous scale over this time period. For the earliest time of 7 min, coverage of the surface was uniform (Fig 3.77a) by very small platelet growths (Fig 3.77b) that were high in iron and sulfur with some aluminum, Fig 3.78. Increasing the exposure time to 45 minutes again showed uniform surface coverage (Fig 3.79a) that had some widespread, but patchy, growth of hexagonal platelets, Fig 3.79b and 3.79c. These platelets were found to contain Fe and S. The underlying scale was found to consist of uniform coverage by very small sulfide platelets, Fig 3.79d. These were also hexagonal in shape and contained iron, aluminum, and sulfur. After 5 hours of exposure, the platelets observed in Fig 3.79b have now grown large enough that they are the only structural features observable across the sample,

Fig 3.80, and 15 hours of exposure led to their thickening and start of coalescence, Fig 3.81. After 50 hours of exposure, a continuous scale has formed across the surface of the sample, Fig 3.82. However, instead of the smooth surface appearance of the LCS sample, the 5Al sample appeared to have both macro- and microporosity, Fig 3.82b. The larger voids seemed to have formed due to the impingement and thickening of individual platelets with different growth directions. EDS analysis again indicated only iron and sulfur were present. Inter and transgranular cracking observed for the 1008 sample was also found.

Development of the corrosion scale was also observed by viewing the cross-sections of the 5Al samples. For ease of discussion, the cross-section of the 50 hour sample will first be described due to its advanced stage of growth which facilitated the collection of quantitative chemical information. Fig 3.83 shows a polished light optical micrograph of a bilayered scale. The outer scale was composed of the impinged and thickened plates observed in the surface micrographs that had the appearance of being somewhat columnar due to the growth of the plates. However, it was not as compact as the LCS sample. The openness of the structure can be attributed to the fact that the plates were observed to be thicker at the top than at the bottom. EPMA data indicated that the large plates were iron sulfide with minor quantities of aluminum dissolved in solution near their base, Table 3.15. Filling in some of the voids at the interface between the outer and inner scales were smaller sulfide platelets, Fig 3.83b, having a similar composition to the larger ones with the exception of the amount of aluminum present (approximately 1 wt%). In localized areas, these platelets were found to grow together to form a continuous layer where aluminum was randomly distributed in the structure (between 0.2-0.8 wt%). The lower values were typically associate with the base of a large plate. In addition, the plates found growing on the corners and edges (Fig 3.76) were also analyzed and showed no discernable difference in composition from that of the outer surface scale.

The inner scale displayed a relatively flat interface with both the outer scale and the underlying alloy, Fig 3.83. An SEI micrograph of this area revealed that it was a porous, two phase region of dark gray plates and light gray particles, Fig 3.84. The light gray particles were found to have high counts of iron and sulfur with low counts of aluminum. Exact compositions could not be obtained due to their size, but from their coloring and EDS analysis, were assumed to be iron sulfide.

The dark plates were found to have various orientations and lengths with many of them penetrating into the alloy. At higher magnifications, light colored striations in the tau phase plates can be observed, Fig 3.84b. The overall composition of the plate indicated that it was the tau phase. The colored striations were too small to analyze individually. Quantitative chemical information was also obtained by scanning a broad area (approximately 25 square microns) of this inner layer to gain the overall composition of the two phases. The results placed it in a two phase region of tau and iron sulfide.

At the inner scale-outer scale interface (top of Fig 3.84a), the development of needles and large particles of iron sulfide can be seen. This morphology gives the appearance that the inner interfacial layer of iron sulfide was formed from the transformation of the tau phase plates. Attack at the alloy-scale interface (bottom of Fig 3.84a) showed the protrusion of tau phase plates into the substrate. Again, quantitative chemical information could not be obtained from the tips due to their size, but EDS analysis showed high counts of aluminum, iron, and sulfur indicating the possible continuation of the tau phase. Un-affected base metal near the protrusions showed no presence of sulfur and typical amounts of aluminum and iron when compared to the alloy at far distances.

The exact shape of the two inner scale phases was determined by polishing face down on the sample, in addition to reviewing the results of the cross-sectional morphologies. Fig 3.85 shows the various planes that were analyzed from the scale. The middle of the inner scale (plane #1) revealed the plate morphology of the tau phase and the particle nature of the iron sulfide, Fig 3.86. Again, the porousness of the layer and the striations of the tau phase can be seen. Closer to the alloy-scale interface (plane #2), the attack of the corrosion products into the substrate can be viewed, Fig 3.87. EPMA data for the un-attacked alloy (arrows in Fig 3.87b) near the plates showed no amount of sulfur present and the EDS data for the light color particles showed high counts of iron and sulfur with low counts of aluminum. Further polishing led to the removal of the inner mixed layer, with the substrate and plate protrusion left to be observed (plane #3), Figure 3.88. The tau phases can be seen to attack the substrate both in the grains and grain boundaries. Analysis of numerous grains revealed a crystallographic orientation of the plates with the substrate. Most grains displayed only four growth orientations (Fig 3.88b), while some had six directions due to a few plates being oriented in a slightly different manner (Fig 3.88c).

With an understanding of the phases present in the corrosion scale, Figs 3.89-3.93 display the 5Al samples at various times showing the development of the scale in cross-section. The constituents of the scale were found to lengthen with time and Fig 3.94 shows this relationship. Calculated n-values for the inner and outer scale were 0.61 and 0.63, respectively.

Examination of the 7.5Al samples revealed formation of Type III scale for short exposure periods that eventually developed into a Type I scale at the longest time. For the short exposures (50 hours or less), a grayish-purple surface scale with coverage by dark growths was observed to form, Fig 3.18h. Fig 3.95 shows SEI micrographs of the samples. The formation of corrosion product nodules across the surface (Fig 3.95a-3.95c) can be observed, with a large amount of the coverage located on the corners and edges of the samples. The 10 hour sample appeared to have a higher density of nodules on the surface compared to the 20 and 50 hour exposure samples which may explain the initial higher weight gain observed in Fig 3.11. In addition, growth of the corner plates, as previously observed on the 5Al samples, can already be observed after 10 hours of exposure.

Fig 3.96 shows the nodules have similar appearance regardless of the exposure time, however, their diameter size was related to this variable, Fig 3.97. Linear growth was found as the n-value was calculated to be 0.95. The 10 and 20 hour samples were relatively uniform in size, while nodules with larger deviations in diameter were observed on the 50 hour sample. This was due to the impingement with other nodules that impeded further growth (Fig 3.96c). Cross-sectional analysis showed that the nodules consisted of an outer and inner scale, with no discernable scale development between the growths, Fig 3.98. The overall appearance had a lenticular shape with further analysis revealing similar phases and morphologies to those observed for the 5Al specimens. Both the nodules and these phases can be viewed developing over time, as seen in Figs 3.99-3.101. The outer scale again consisted of iron sulfide plates (Table 3.16), with various growth directions, and smaller iron sulfide platelets near the inner scale-outer scale interface having some dissolved aluminum (~1 wt%). The inner scale again was composed of the tau phase plates and iron sulfide particles that grew with a growth rate time constant (n) of 0.63. A scan of this layer indicated a composition in the two phase tau-iron sulfide region. In the substrate directly below the areas of the nodule free regions, EPMA analysis did not indicated the presence of sulfur or the depletion of either metallic element. The same can be said for the substrate located next to the protruding tau phase plates.

Higher magnification of the nodule-free regions revealed surface coverage by a granular scale with small growths emerging from it, Fig 3.102. Note that the preparation marks from the 600 grit papers can be seen in the background signifying the absence of thick scale growth in this region (best observed in Fig 3.102c). The size of the platelets growing on the surface inhibited direct analysis of individual particles, however, a cluster of platelets were analyzed with EDS indicating the presence of iron, aluminum, and sulfur. The size and density of these sulfide particles did not appear to have a dramatic change with time. The same can be said for the granular background scale (Fig 3.103) in terms of size of the grains (constant between 100-200 nm). Analysis of this scale by EDS indicated high counts of Al and O with minor peaks of iron and sulfur. Fractured cross-sectional micrographs were obtained for the 50 hour sample in this area. As can be seen from Fig 3.104, a thin scale has formed with the sulfide platelets growing on top. This scale is roughly 100nm thick and appears to be uniform. Even after the fracturing at liquid nitrogen temperatures, good scale retention is observed.

At the longest exposure (100 hr), the surface scale was entirely black, Fig 3.18d. Higher magnification revealed no indication of the nodule growths as a continuous surface scale was observed, Fig 3.95d, with the growth of large sulfide plates, Fig 3.105. Both fractured cross-sections (Fig 3.106) and polished cross-sections (Figs 3.107 and 3.108) of this scale were obtained showing that a Type I morphology has now developed from the coalescence of the initial nodular growth. Higher magnification of the inner scale, Fig 3.106c and 3.108a, showed the individual particles of iron sulfide and the plates of tau phase. The loose packing of the iron sulfide particles between the tau phase plates from the fractured cross-section helps to verify the porosity observed in the polished cross-sections. The formation of the inner interfacial iron sulfide layer can be observed to form in Fig 3.107 and 3.108a. Higher magnification of the inner scale-outer scale region show that a thin, continuous scale was found between these layers, arrows in Fig 3.108b. This scale was also found to form on the nodules at the shorter exposure times, with it continuing on to the surface in the nodular free region.

The 10Al samples revealed Type II scale with localized formation of corrosion nodules at the corners and edges of the sample. These samples had various colors associated with their surface scales. The 2 hour and 50 hour sample both were tanish in color (Fig 3.18e), while the 100 hour

sample had a bluish tint (Fig 3.18g). All three were still relatively shiny. Fig 3.109 shows the SEI images at low magnification. At 2 hours, very little corrosion product can be seen on the surface. At 50 hours, large amounts of corrosion product was found on the corners and edges in the form of nodules, similar to those observed on the 7.5Al sample. The 100 hour sample had only a few isolated growths. The size of the nodules was not observed to increase dramatically with time, Fig 3.97, and it can be seen that for a given time, the nodules were of similar size regardless of alloy content.

The surfaces were uniformly covered with the granular scale and small sulfide particles (Fig 3.110) that were previously observed in the nodule free region of the 7.5Al sample. As time increased, the density and thickness of the platelets can be seen to increase from 2 to 50 hours, but with no apparent change afterwards at 100 hours. Their size and density is similar to that observed on the 7.5Al sample. The growth of the platelets from the granular surface scale can be more clearly seen in Fig 5.111. It appeared that the sulfides have grown in the grain boundaries of the granular scale. The particles in the granular scale appear similar, Fig 3.112, and again have high counts of aluminum and oxygen as indicated by EDS.

Cross-sectional analysis of the sulfide nodules found on the surface of the 50 hour sample revealed a similar appearance to those found on the 7.5Al samples, Fig 3.113. An outer scale of large and small iron sulfide plates was seen growing on top of an inner layer of tau phase plates and iron sulfide particles. EPMA data for the phases can be found in Table 3.17. Again analysis beneath the thin granular scale revealed no sulfur penetration and no depletion of either aluminum or sulfur. Since very few nodules were found on the 100 hour sample, a cross-section could not be obtained for comparison, but would most-likely have similar phases and morphologies.

The fracturing technique was again used to observe the thin, granular scale in cross-section for the various times, Fig 3.114. These scales were uniform and displayed no spallation from the substrate with the thickness of the alumina scale increasing as a function of time, Fig 3.115. As seen in Fig 3.116, the growth of a sulfide platelet through the thin granular scale was also observed. The corner of the 50 hr sample was also investigated, Fig 3.117. It appeared that the alumina scale growth in this region was enhanced, with the scale having a thickness of approximately 680 nm compared to 110nm found in the sample face.

The 12.5Al samples had similar coloring to the 10Al samples with the surfaces having a tanish-purplish coloring for all times (Fig 3.18f). SEI micrographs show the formation of corrosion products on the surfaces, Fig 3.118. As seen for the 10Al samples, the 2 and 100 hour samples had virtually no growth on the corners or edges, whereas the 50 hour sample has some growth in these areas. The surfaces were again covered with the granular scale and small platelets, Fig 3.119. Similar to the 10Al samples, no apparent growth of the sulfide platelets was observable after 50 hours. The same can be said for the granular scale, Fig 3.120. Cross-sectional analysis of the fractured specimens again showed similar results to that of the 10Al sample where growth of the thin scale occurred, Fig 3.121. Scale adhesion was again good with no discernable difference in scale thickness between alloy contents (Fig 3.115).

Both the 15Al and 20Al samples were observed to have a bluish tint associated with their surface scales that was again relatively shiny, Fig 3.18g. SEI micrographs showed that very little, if any, corrosion products formed on the sample, Fig 3.122. Higher magnification revealed that less corrosion product formed on these samples than previously seen for the lower aluminum contents, Fig 3.123, with 20Al having the least amount. Sulfide platelet growths were localized and typically associated with the preparation marks. The background scale is less granular than previously seen. It appeared more devoid of structure with only a few noticeable granules, Fig 3.124. Fractured cross-sectional analysis revealed the thin granular scale that formed, Fig 3.125. Again the scale is uniform at approximately 150nm (Fig 3.115) with some separation from the substrate.

3.1.4 Discussion

The corrosion behavior of Fe-Al alloys in the oxidizing/sulfidizing environment was found to be directly related to the aluminum content of the alloy, which influenced the type and morphology of corrosion product that formed during high temperature exposure. These growths were typically in the form of a surface scale, or scales, that developed with time. According to which reaction product developed, the corrosion behavior of the alloys was found to exhibit one, if not more, of three stages of behavior: inhibition, breakdown, and steady state. The duration of these stages was directly related to the aluminum content of the alloy and the exposure temperature. Fig 3.126 shows a schematic indicating these regions. The following sections will discuss the three

stages of corrosion behavior with respect to the aluminum content of the alloy and the exposure temperature in the oxidizing/sulfidizing environment.

3.1.4.1 Inhibition Stage

Additions of aluminum were found to decrease the corrosion rates by promoting the formation of slower growing surface reaction products on the alloy during exposure. This was generally observed from the weight gain data obtained during corrosion testing. Fig 3.127 shows this relationship. Since a single scale growth mechanism could not be determined for the alloys in general (see calculated n-values in Results section), the final weight gain normalized by exposure time was found to be the clearest manner to interpret the collective data. Alloys with ideal corrosion protection were richer in aluminum and found to initially form and maintain a Type II scale. These scales were composed of tightly packed, equiaxed grains containing high amounts of aluminum and oxygen. While definitive identification of the scale could not be made, enough evidence suggests that it is gamma alumina in terms of 1) the EDS analysis, 2) the temperature regime in which it has formed, 3) the color of the scale [Hagel], and 4) its protective nature (weight gain and thickness). DeVan (1988) also observed protective behavior from formation of a gamma scale in similar mixed environments on iron aluminide compositions. This scale formed due to preferential oxidation of the aluminum on the alloy surface and the results from this study indicated that formation was promoted through increasing the aluminum content of the alloy.

In order for protective behavior to occur, a continuous and defect free scale of alumina must form upon initial exposure. According to super-imposed thermostability diagrams for iron and aluminum, the location of the testing environment was found to lie in a region of alumina and iron sulfide, Fig 3.128, regardless of temperature. These are the two phases that will be stable on the Fe-Al alloy surface at initial exposure. During the very early stages of reaction, it is expected that both phases will nucleate on the surface due to thermodynamic considerations. Whether a continuous, protective scale will form is dependent upon the distribution of its nuclei, as well as the relative diffusion rates of cations in the alloy and scale [Hindam]. Since the sulfide products typical grow faster due to their highly defective structures, it is imperative that alumina nuclei have widespread and dense coverage of the surface to cutoff growth of the non-protective phases. This study showed

that by increasing the amount of aluminum in the alloy, the probability of forming a continuous scale of alumina was improved. This may be due to the decreased distance between adjacent alumina nuclei on the surface at early times, thus requiring less lateral growth, and concurrently less time, to obtain full surface coverage. Other studies have shown that at a given temperature, a certain composition must be possessed in order to form a protective alumina scale in both oxidizing [Boggs; Hagel; Prescott 1992b; Tomaszewski 1978; Wallwork] and oxidizing-sulfidizing [Devan 1988, 1992, 1993a, 1993b; Tortorelli 1992, 1994a, 1996] environments. It is clear that these results were further substantiated by this study.

Exposure temperature was also found to have an effect on the duration of the inhibition period. As the temperature increased, the length of time spent in the inhibition period decreased. Reasons for this behavior will more appropriately be discussed in the next section concerning the initiation of the breakdown stage.

The protectiveness of the gamma alumina scale manifested itself in three ways: 1) low weight gains/ thinness of scale, 2) lack of sulfur ingress, and 3) slow rate of cation diffusion. While it is intuitive that lower weight gains indicate a protective scale, it is also important to note the thinness/thickness of the scale that is providing protection at temperature. Alumina scales observed to grow on the weldable compositions at 600°C attained 100 nm of growth over the 100 hour exposure period, yet were able to maintain less than 0.5 mg/cm^2 in weight gain. Other forms of alumina, such as alpha, provide protection at higher temperatures (typically above 1000°C), but have a tendency to become much thicker over time even though their weight gains are also relatively low. At exposure temperature, these scales can grow to a thickness of 8 um within 100 hours [Pint]. Preferential aluminum removal through this type of thick scale growth depletes the alloy of this element at a relatively fast rate. This rate of aluminum consumption is critical when considering these alloys for use as protective coatings, as the weldable compositions considered here have relatively low aluminum reserves to begin with.

The effectiveness of a coating can be defined by the oxidation lifetime or the amount of time over which a protective scale will provide protection for the underlying substrate. This concept was studied and modeled by Quadakkers et al. (1994a and 1994b) and recently reviewed by Tortorelli and Natesan (1998). The time frame for protection has been found to be a function of the total

amount of aluminum available for reaction (at the surface and in reserve) and the rate at which it is consumed. Oxidation lifetime of an alloy ends when the aluminum content falls below a composition such that formation of the alumina scale is not possible and the development of less protective products can occur leading to breakaway corrosion. A major cause leading to aluminum depletion can be through thermal cycling where repeated spallation and re-growth of the alumina scale can readily deplete the alloy of aluminum [DeVan 1992, 1993b; Tortorelli 1993, 1996].

The use of Fe-Al alloys as protective weld overlay coatings will automatically limit the reservoir of aluminum due to the thickness of the deposited overlay. Therefore, it is natural to think that increasing the amount of aluminum in the deposit will further increase the oxidation lifetime of the coating. However, it has been shown that a limit (approximately 10 wt% Al) is imposed on the system in order to produce sound coatings deposited under conditions typically utilized in practice [Banovic]. Therefore, the other alternative to increasing oxidation lifetime of weldable compositions is by reducing the rate at which aluminum is consumed. Through this study, it was shown that the rate of consumption at temperature (500-700°C) was very low due to the thickness (thinness) of the protective scale. In addition, this thinness may be beneficial in that large growth stresses, which could enhanced spallation of the scale, may not have developed. While thermal cycling of the specimens was not conducted, at no time was the scale ever observed to crack, spall, or flake off, even after fracturing in liquid nitrogen temperatures, which suggests a somewhat adherent scale. Therefore, the thinness of the scale over extended periods of time, combined with the lack of spallation, results in a very low rate of aluminum consumption and may suggest a potential long oxidation lifetime for the weldable alloys at service temperatures (below 600°C).

While the scale was able to maintain low weight gains for extended periods of time, it was also protective in the fact that internal sulfidation was not encountered. Microprobe traces near the alloy-scale interface did not find an increase in sulfur in the alloy when compared to far distances into the substrate. This suggests that the scale was somewhat dense and impervious to inward diffusion of the anion, and may be related to the fact that gamma primarily grows via an outward cation diffusion mechanism [Prescott 1992a and 1992b]. It will be shown that sulfur penetration can be disastrous to the protective scale due to the formation of sulfide phases beneath its surface which can lead to mechanical degradation of the passive layer.

While the gamma scale was impermeable to sulfur, the diffusion of iron outward was readily observed on the surface in the form of the small sulfide platelets (e.g. Fig 3.110). These platelets are found to grow from between the grain boundaries which suggests a weakness in the scale. However, the sulfide platelets tend to stop growing after a certain time (roughly 50 hours) implying that the scale may have been able to inhibit iron diffusion outward at longer exposures. Concerning this type of outward iron diffusion, the aluminum content of the alloy was found to play a major role in the integrity of the scale. This can clearly be shown for samples at 700°C. The 15Al and 20Al samples are found to have very limited growth of the sulfides across their surfaces, Fig 3.123, whereas the lower aluminum content alloys have thicker and more dense coverage of the platelets, Fig 3.110c and Fig 3.119c.

Similar trends were found at the lower temperatures, however, the amount of product on the surface and the morphology of the sulfide platelets was observed to be different. With lower temperatures and less energy for diffusion, the sulfide platelets found at 500°C were observed to be more plate-like with planar aspect ratios closer to one (Fig 3.40b and 3.41b). With higher temperatures, the morphology of the sulfide platelets are more elongated with a thin base and "flowering" top (Fig 3.110c and 3.119c). This may be due to increased diffusion of iron through the alumina scale, as well as enhanced diffusion along certain crystallographic directions in the iron sulfide at higher temperatures.

3.1.4.2 Breakdown Stage

The ability of the alumina scale to maintain the overall passive nature was found to decrease as the aluminum content of the alloy decreased. This was primarily due to the mechanical breakdown of the alumina scale, in combination with the inability to re-establish itself. Ensuing growths typically took the form of localized nodules of corrosion product (Type III scale). The shape of the continuous weight gain data curves and the remnants of the initial surface scale between the two interfacial layers suggests this short circuit diffusion mechanism. This loss of protection was most notable in sample T1072 exposed for 50 hours, Fig 3.12. Even though a continuous and protective scale initially forms for the first 2 hours, resulting in low weight gains, mechanical failure in the highly stressed corners and edges of the alumina scale led to fast growth of the sulfide in this

area (Fig 3.109b) and the observance of the breakdown stage. The ability of the alloy to resist nodule formation was highly dependent upon aluminum content. This can readily be observed through exposures at 700°C. The 15Al and 20 Al samples did not develop massive nodule formations for the extended times. However, as the aluminum content decreased, the time to nodule formation, or conversely, the length of inhibition stage, also decreased (5 hours for 12.5Al, 2 hours for 10Al, and relatively short time for 7.5Al). This was again attributed to the inability of the alloy to re-establish the alumina scale due to low Al contents.

From literature, there appears to be a lack of understanding in the principles of nodule nucleation and growth [Boggs; Patnaik 1985a; Quan; Sakiyama; Smith 1987c; Tomaszewski 1983]]. (This will further be discussed in Section 6.) Available mechanisms [Boggs; Quan; Patnaik 1985a] for this type of growth in sulfur containing environments are based primarily upon scale disruptions or mechanical failures in an initially formed passive layer that cannot re-establish itself. This was easily observed by growth of iron sulfide platelets occurring in the alumina grain boundaries and not through the lattice of the scale itself. While the grain boundaries may qualify as a defect in the scale, the need to quantify the severity of the defect is important. This type of corrosion product development did not appear to be deleterious to the integrity of the scale, as no sulfur was found to penetrate the alloy beneath these growths and weight gains still remained negligible. Therefore, for growth of corrosion nodules to occur, a massive event must take place in which the mechanical integrity of the scale degrades and re-establishment cannot occur. The possible early stage of this may be observed in Fig 3.116, where a thick platelet can be seen growing through the alumina scale. Other platelet formations were not likely to have this type of "through thickness" growth, as Fig 3.116 was the only one found of its kind.

The ability of the initial oxide scale to re-establish itself was primarily related to the aluminum content of the alloy. As previously discussed, the formation of the alumina scale will deplete the alloy near the surface due to selective oxidation. Characteristics of this depletion region depend upon a number of factors including original alloy content, relative diffusivities in the alloy and scale, and exposure temperature. These three factors will dictate how quickly the aluminum is removed from the alloy, and its extent into the alloy, and the ability to replenish or maintain the area with further additions of aluminum from the bulk. From the discussion above, this will have a large

bearing on the alloys protective nature and oxidation lifetime. When the aluminum content was high enough, mechanical failures were readily healed. Thus, the formation of gross sulfide phases, and the observance of the breakdown stage, was not seen for these alloys over the 100 hour exposure. An example of this is for the 10Al and 12.5Al samples at low temperatures and for the 15Al and 20Al at 700°C. These latter alloys are iron aluminide compositions and have typically exhibited very long oxidation lifetimes due to their large reservoirs of aluminum [DeVan 1988, 1989, 1992, 1993a, 1993b; Kai 1997a, 1997b; Natesan 1995; Tortorelli 1992, 1993, 1994a, 1994b, 1996, 1998]. This has been observed to hold even after repeated scale spallation during thermal cycling at high temperatures [DeVan 1992, 1993b; Tortorelli 1993, 1996].

However, when the content of aluminum at the alloy-scale interface was insufficient to ensure re-establishment of the original scale, growth of the fast growing iron sulfide phases occurred in the fracture site due to an anion short circuiting mechanism. This was primarily found on the 7.5Al samples for short exposure times and on the 10Al and 12.5Al alloys exposed at 700°C. For the 7.5Al samples, no aluminum depletion region was observed beneath the initial oxide within detection limits of the equipment. Since diffusion in alumina scales is much slower than in the alloy and the rate of aluminum consumption is very low, it could be expected that a depletion layer may not be found as Al from the bulk readily diffuses to the surface. However, with mechanical failure of the scale, sulfur is now able to permeate the protective layer by means of a short circuiting mechanism. The local equilibrium (in terms of $p(O_2)$ and $p(S_2)$) in the alloy beneath the scale has now changed from that previously observed at the gas-scale interface and fast growing sulfide phases may now be promoted. Therefore, it appears that the initial surface activity of aluminum for the 7.5Al samples was high enough to form a protective scale, but not to suppress formation of the sulfide phases below it upon scale fracture.

It is important to note here that while nodular formation on the alloys occurs by the same mechanism (mechanical failure and inability to re-establish), the reasons for the latter half of the mechanism may be different. As previously discussed, the 7.5Al samples have nodules dispersed across their faces due to the inability to heal the mechanical break of the passive scale. This inability was related to the low aluminum content of the alloy. However, for the 10Al and 12.5Al samples, nodule growth typically occurred only in the regions near the corners and edges. These areas were

found to grow thicker alumina scales (Fig 3.117c) relative to the rest of the surface (Fig 3.114b). This may lead to a higher depletion rate of aluminum in this area and further decrease the probability of the scale re-establishing itself upon breakdown. Therefore, for these alloys, it may be the sample geometry that brought about the observance of the breakdown stage, and not the lack of protection afforded by the alloy.

Growth of the nodules was seen to occur by counter-diffusion of sulfur inward and iron outward in combination with the continuous lateral degradation of the passive scale. The resulting morphologies were observed to be very complex as the corrosion product growth is no longer solely a uniform process of ion diffusion, but now contains an element of lateral growth across the surface. This was substantiated by comparing the growth of the nodule diameters to the corrosion product penetration into the scale. Assuming that when the scale initially breaks down (Fig 3.129b), sulfur is allowed access to the underlying substrate. If growth of the nodules occurs exclusively through a diffusional process, then the lateral growth should be on the same order of magnitude as the perpendicular penetration. From the n-values calculated, this type of comparison cannot even be made as growth of the nodule diameter was linear (n = 0.95) and the tau phase development was parabolic (n = 0.63). It can also be noted that as the sulfide products grow underneath the scale, differences in phase volume caused expansion beneath the outer FeS layer and the nodule was found to expand outward into the gas (Fig 3.129c, 3.98 and 3.101). This may place additional stresses within the protective scale and lead to further failure with the nodules spreading until their eventual coalescence at long times, Fig 3.129d. Upon forming a continuous surface scale, a steady state corrosion rate was observed as diffusion through the scale, and not lateral mechanical breakdown, was the dominating growth mechanism. This can clearly be seen in Fig 3.11 for the 100hr sample. After the initial high weight gain associated with lateral growth, an n-value of 0.67 was calculated for the data obtained after 20 hours.

3.1.4.3 Steady State Stage

As the aluminum content of the alloy was further decreased to 5 wt%, the formation of alumina, and either of the first two corrosion stages, was never directly observed. Instead, thick scale growths accompanied by relatively high weight gains were observed (Type I scale). Even at the

shortest time, oxygen (indicating oxide nuclei) was not detected in the spectra, Fig 3.78. As previously discussed, the very early stages of reaction would expect to find the formation of alumina and iron sulfide nuclei on the surface due to thermodynamic considerations. However, it appears that due to lack of coverage and the faster kinetics of the sulfide phase, the initial oxide nuclei are soon buried under the sulfide platelets. This would then eliminate any possibility for formation of a continuous alumina layer to provide protection. Another possible explanation for the lack of an oxygen k_{alpha}-peak (E = 0.525 keV) may be that it was small and eclipsed by the larger Fe l-peak (E = 0.615 keV) in the spectra.

Even though the protective alumina scale was not observed to form, small additions of aluminum lead to the development of slower growing reaction products, when compared to the LCS sample, which reduced the overall weight gain (Fig 3.127). The slower growth of the scales was attributed to the impeding of iron diffusion outward through both developing layers (inner and outer scale). This can clearly be shown by observing the scales formed on the LCS and 5Al alloys at 600 and 700°C. (These two temperatures are discussed together as formation of the scales are similar. References to results will focus on the more developed samples exposed for 700°C, however, the arguments and trends presented apply to both exposures. Samples for 500°C will be discussed separately due to different morphological development.)

Many similarities and differences can be observed between the LCS and 5Al sample. Both samples developed "bilayered" outer FeS scales consisting of an inner fine grain and outer columnar region (Fig 3.74 for LCS and Fig 3.83 for 5Al). Growth of these bilayered scales was typical for iron, based upon observations in the literature [Danielewski; Fryt 1979a; McKee; Narita 1974;Orchard]. Initially, iron sulfide will nucleate equiaxed grains in random directions on the surface. At longer times, columnar development was observed due to preferential growth of favorably oriented equiaxed grains [Condit; Fryt 1979b]. At this exposure temperature, iron sulfide has a hexagonal crystal structure which would mean this preferred direction could either be along the *a*- or *c*-axis. Narita and Nishida (1974) have shown that the growth texture of the iron sulfide scale changes with sulfur pressure. At the low pressures ($p(S_2)$ below 10^{-3} atm), sulfide crystals grow preferentially along the *a*-axis. Above this pressure, growth occurs along the *c*-axis [Danielewski]. The appearance of the corner plates (Fig 3.72) and the pyramidal structures on the

surface (Fig 3.73) would suggest the major growth axis for these scales being in the *a*- direction of the hexagonal crystal, i.e., {102}. These results are in accordance with other authors [Fryt 1979a; McKee] for this sulfur pressure and temperature range.

For the 5Al sample, scale development also began with the nucleation and growth of randomly oriented iron sulfide grains on the surface (Fig 3.77a). With time, iron sulfide grains that were oriented in a favorable direction had preferential growth (Fig 3.79b) which ultimately resulted in an outer layer of thick "columnar" grains (Fig 3.82c). However, where the LCS sample developed a relatively dense scale from the widespread growth and impingement of the hexagonal plates at an early stage, the 5Al sample was found to be very porous due to what appears to be a decreased number of favorably oriented grains emerging from the fine grain layer (Fig 3.79b and 3.90a). These few plates, again showing growth along the *a*-axis, impinge at later times to form a continuous, yet porous, surface scale (Fig 3.83). Therefore, it appears that the addition of aluminum has resulted in a fewer number of favorably oriented grains being able to grow, or conversely, that it has inhibited the other equiaxed grains from growing.

From literature, the formation of these outer plate-like structures have been observed on many different Fe-based alloys in both sulfidation [Narita 1984; Przybylski 1992a and 1992b; Quan] and oxidation/sulfidation environments [DeVan 1989; Kai 1997b; Wang; Yurek]. Pryzbylski et al. (1992b) suggested that the development of iron sulfide plates on an Fe-based alloy are influenced by the growth of the inner scale corrosion products. Sulfidizing FeCrAl alloys at 700°C, the authors observed a similar type of scale formation to that found here with outer FeS plates and an inner mixed scale of iron, aluminum, and chrome sulfides in needle and plate-like forms. It was surmised that the crystallographic properties of the inner sulfide plate growths, and subsequent diffusion through them, lead to the growth of the outer scale in such a manner. However, the inner scale needle and plate-like morphology can also be found in similar systems (materials and exposures) resulting in a dense outer scale [Kai 1997b; Patniak 1985a; Smith 1987a and 1987b]. In addition, there appeared to be no type of orientation of the outer sulfide plates when viewed from the surface, Fig 3.82, in relation to the underlying crystallographic growth found for the tau phase plates for this study (Fig 3.88). Therefore, this hypothesis was not universally observed. Attempts were also made to correlate alloy composition, partial pressures of gaseous species, temperature, or inner scale

morphology to the growth of these outer plate structures from the literature, but no significant trends were revealed. Therefore, another mechanism must be leading to this type of growth.

Strafford and Manifold (1969) have observed slower diffusion rates of iron in iron sulfide due to the incorporation of aluminum (again approximately 1 wt%) in the scale during sulfidation experiments in this temperature range. Providing that the aluminum was substitutionally found in the FeS, they surmised that creation of localized strain fields in the FeS lattice may have occurred due to the incorporation of the Al ions into the structure. These strain fields may act as sinks for cation vacancies, and hence slow down the vacancy diffusion rate which in turn will reduce the cation diffusion rate outward. From this study, it was readily found that iron sulfide grains which grew and thickened with time contained very little aluminum at their bases. For iron sulfide plates with higher amounts (closer to 1 wt% Al), they were found either incorporated into the slow developing outer interfacial layer or were much slower growing (Fig 3.83b). Therefore, it may be due to the amount of aluminum, or lack there of, that is dissolved in solution in the outer interfacial layer that effects the morphology of the outer sulfide scale. By retarding the growth of the initial equiaxed grains, the development of the porous outer scale was found.

Aluminum may also be impeding the diffusion of iron in iron sulfide by creating a larger energy barrier to ion movement. Above 320°C, the c/a lattice parameter ratio for iron sulfide is nearly 1.63 [Condit], the same as that for ideal close packing of anions. On a hard-sphere ionic model with S^{-2} having a radius of 184 pm and residing on the hexagonal lattice sites, the radii of interstitial ions would therefore be 76 pm and 41 pm, for octahedral and tetrahedral sites respectively. Thus, iron ions (Fe^{+2} with radii equaling 76 pm) are more than likely found in the octahedral cites and when incorporated, aluminum may reside in either. In order for iron to move through the lattice, thermal oscillations of the sulfur ions must occur before a jump to a vacant site can take place. This has an associated activation energy for this process. However, aluminum incorporation into the lattice may reduce the amount of oscillation by the sulfur ions and create a larger energy barrier for the iron ions to get through, thus slowing down these rates and the overall growth of the scale.

The reduced rate of iron diffusion through this region can also be seen in the formation of the inner interfacial layer of iron sulfide. From Fig 3.84a and 3.92b, it appears that the tau phase

plates are "transforming" to iron sulfide. However, this is highly unlikely as diffusion of aluminum out of the tau phase structure would be necessary. This would require aluminum to diffuse up a concentration gradient (inward towards the alloy) as it is not found in large amounts in the FeS interfacial layers. Instead, another possible scenario is presented. It is probable that with decreased diffusion of iron outward through the interfacial layer, iron is "accumulating" in this region. It then manifests itself by forming iron sulfide with the inwardly diffusing sulfur. As both the tau phase and iron sulfide have the same hexagonal crystal structure, the FeS was found to grow epitaxially on the tau phase plates. Therefore, an inner layer of FeS was found to form at the inner scale-outer scale interface in the form of plates that may coalesce at longer times to form a continuous layer.

The growth of the tau phase plates was also observed to penetrate the alloy, suggesting that sulfur was diffusing inward. As the inner scale was porous (due to iron diffusion outward), it is believed that sulfur was able to easily penetrate the scale and diffuse along the phase boundaries between the tau phase plates and the alloy for further development at the corrosion front. This was in agreement with n-value calculations from measured cross-sectional lengths that reside between 0.5 and 1 suggesting a mixture of diffusion and linear kinetics for the growth of the inner layer for all samples. Since these plates are not isolated from the inner layer, further growth of them is not required through sulfur diffusion in the alloy, and none was found in the substrate ahead of the corrosion front.

Aluminum was also found to diffuse, however, in a more local manner. This can be observed in the formation of iron sulfide particles residing in between the tau phase plates. These particles were formed as aluminum diffused in order to create the tau phase. As no depletion layer was observed at the alloy-scale interface and the solubility of aluminum in the interfacial layers is limited, the aluminum from the attacked matrix was bound in this region and located in the tau phase plates.

Attempts were made to determine the mechanism for scale growth using the thermogravimetric data. However, upon first endeavors with the simplest case (LCS sample), problems were encountered. It has been well documented that the growth of iron sulfide from the sulfidation of iron is controlled by bulk cation diffusion through the scale [Condit; Danielewski; Fryt 1979a, 1979b; McKee; Narita 1974; Orchard]. This mechanism has been well supported through kinetic measurements [Condit; Fryt 1979a] and verified via chemical diffusion studies on FeS

crystals [Condit; Fryt 1979b]. Combined, these works show that the growth of a (relatively) compact sulfide scale is primarily due to the outward iron ion diffusion through the defective metal lattice and that short circuit paths, such as grain boundaries, will not affect the process at these temperatures. This was also proven by McKee and Druschel (1983) who observed similar diffusion rates for various scale grain sizes at 700°C. While crystallography does have an effect on the iron diffusion rates [Condit; Fryt 1979b], $D_{c\text{-}axis}/D_{a\text{-}axis} = 1.86$, the role of sulfur diffusion in scale development was negligible with its rate being nearly four orders of magnitude lower than diffusion of iron in FeS at 900°C [Condit]. Therefore, the growth of the scale should have a $t^{1/2}$ dependence.

Recalling the corrosion kinetic section above, the n-value calculated from the thermogravimetric data for the 50 hour LCS sample at 700°C was found to be 0.86. This value indicated a mixture of linear and parabolic behavior; results which deviate from published literature. Analysis of the cross-sectional microstructure (Fig 3.74) did not indicate any abnormalities in the growth of the scale signifying a change in growth mechanism (i.e., large degree of porosity or non-uniform thickness). However, one difference that was noted was the growth of the plates at the corners and edges of the 50 hour sample (Fig 3.71b). For the 1 hour sample, with an n-value very close to 0.5, the sample did not obtain the plate growth at the corners and edges. In addition, the initial period for the 50 hour sample also followed parabolic kinetics, where after the n-value increased to a value closer to linear rates (Table 3.5). Therefore, it is believed that the growth at the corners and edges of the sample, which apparently occurs sometime after 1 hour, has added error to the kinetic data which ultimately did not allow for determination of the scale growth mechanism through this manner.

However, the question still remains as to why other authors did not encounter this problem. This difference arises from the fact that others tested samples at various times and then measured scale thicknesses [McKee] or that the exposure times were very short [Danielewski; Fryt 1979a]. In an effort to substantiate the growth of this study's FeS scale via cation diffusion, scale measurements were made. Again, measurements of the short exposure sample could not be made due to its crumbling. However, taking the total thickness observed for the 50 hour sample (406 um) and assuming parabolic diffusion with the y-intercept = 0, a k_p value of 1.0×10^{-8} cm^2/sec was calculated. This diffusion rate was very close to measurements observed for other studies [Fryt

1979a] under similar conditions, Fig 3.130, indicating that iron cation diffusion was the mechanism for scale growth. This type of analysis was also conducted for the 600°C LCS sample that had an n-value of 1.0. As can be seen from Fig 3.130, similar results were found (k_p value of 1.5×10^{-9} cm^2/sec).

In terms of determining the kinetics of the 5Al alloy exposed at 700°C via the thermogravimetric data, problems were encountered similar to the LCS sample as growths of iron sulfide plates at the corners and edges were observed. In addition, the assumptions pertaining to Wagner's law of oxidation, necessary for this type of analysis, were violated (single diffusing specie through a dense, continuous single phase scale). Therefore, thickness measurements of the outer scale were made (Fig 3.94) and compared to the LCS sample as near parabolic kinetics were observed for the 5Al samples. It was found that aluminum additions decreased outer FeS scale growth by over an order of magnitude at 700°C (LCS $k_p = 1.0 \times 10^{-8}$ cm^2/s compared to 5Al $k_p = 2.5 \times 10^{-9}$ cm^2/s). This was a similar outcome to that of Strafford and Manifold (1969). From these results, it can clearly be seen that in determining the corrosion behavior of a material, the kinetic data obtained from the thermogravimetric balance and the scale morphology has to be carefully correlated. Further, these result suggests that analysis of the continuous weight gain data to obtained the growth mechanism may not be appropriate when Wagner's assumptions are not met.

The effect of temperature for this stage had a much larger effect on the corrosion behavior than previously seen for the first two. Whereas decreased corrosion rates were observed in going from samples exposed at 700 to 600°C (Fig 3.127), exposure at 500°C produced higher weight gains and thicker scales than at 600°C. This was unexpected as diffusional processes are thermally activated, and thus, should decrease in magnitude as the temperature decreased. Therefore, another mechanism may be controlling the growth of the sulfide scale in this temperature regime.

The increased rate at 500°C may be attributed to the amount of aluminum in solution in the iron sulfide near the interfacial regions. As seen from the results section, the amount of Al in solution at 500°C was maximum at 0.5 wt%. This composition allowed for faster growth at the higher temperatures. The large columnar grains were able to grow when the aluminum content of their bases were very low, and slow growth was found for grains that contained approximately 1 wt% of Al. From the microprobe analysis data for the 5Al samples at 500°C, it can be seen that the

aluminum content near the interfacial regions was very low across the whole base. It is possible then, that more grains with preferred orientations were allowed to grow, and at a faster rate than previously seen at 600°C, due to the lack of aluminum in the iron sulfide structure resulting in a higher weight gain even though the temperature was lower.

Interesting to note, at 500°C the maximum amount of aluminum found in solution for the iron sulfide was just below 0.5 wt%, while the two higher temperatures observed upwards of 1 wt%. According to the ternary phase diagram supplied by Patnaik and Smeltzer (1984), these values are relatively high as they quote 1.0 at% (0.5 wt%) as a maximum at 900°C. Their diffusion couple study was conducted using Fe-Al alloys and bulk crystals of iron sulfide. However, Strafford and Manifold (1969 and 1972) have observed 1 wt% in solution for similar temperature regimes, and have found up to 4 wt% in solution for growth of FeS scales on Fe-Al alloys at 1000°C. These results may suggest that thermally grown iron sulfide can dissolve more aluminum in solution than can synthesized, bulk phases.

Another change observed in the microstructure at the lower temperature was the increased density of the scale. This may be attributed to the increased diffusion along the *c*-axis, or conversely, decreased diffusion along the *a*-axis (relative to that observed at higher temperatures). It was previously shown that diffusion along the *a*-axis was preferred at this sulfur pressure. However, it also appears that temperature may have an effect on the diffusivities along the different axises. At the higher temperatures, it appears that diffusion along the *a*-axis was enhanced whereas at the lower temperatures the growth along both axises were more comparable.

3.1.5 Summary

The corrosion behavior of Fe-Al alloys was investigated in an oxidizing/sulfidizing environment in the temperature range of 500-700°C. The weight gain was found to be related to the type and morphology of the corrosion products that formed, typically as surface scales, during exposure. Three stages of behavior were found that were associated with the formation of the reaction product developed. The duration of these stages was directly related to the aluminum content of the alloy and the exposure temperature.

The inhibition stage was characterized by Type II scale growth consisting of a thin, gamma alumina scale that suppressed excessive degradation of the substrate. Due to slow cation diffusion through the scale, very low weight gains were found. Formation of gamma was promoted by increasing the aluminum content of the alloy. However, increasing the temperature was found to decrease the amount of time spent in the inhibition stage due to non-protective sulfide growth at the corners and edges of the sample. This may be relate to a limitation of the corrosion test in terms of sample geometry, and not indicative of the protectiveness of the scale.

The breakdown stage was associated with mechanical failure of an initially formed gamma alumina scale and the inability to re-establish its protectiveness. This typically occurred for alloys with medium aluminum contents (7.5 wt%) whose protection was brief due to short circuit diffusion through the passive layer and resulting nodular growth (Type III scale). Extremely rapid weight gains were often associated with this stage as continued growth did not depend solely upon diffusion of a species through the previously formed product, but rather, the further mechanical deterioration of the passive layer. This lead to faster growth along a lateral direction with respect to the substrate surface instead of perpendicular to it. Remnants of the initial passive scale were found between the inner and outer layer resulting in the conclusions that the inner scale grew due to sulfur penetration inward and the outer layer grew due to diffusion of iron cations outward. The large network of internal surfaces and phase boundaries within the nodule interior would be expected to support a rapid diffusional process.

The steady state stage was characterized by initially high corrosion rates which then typically leveled off as continued growth occurred via a diffusion mechanism through the thick surface scale. Found on the low Al alloys, these scales were usually continuous and bilayered. Attempts at determining the mechanism for scale growth via the continuous weight gain data failed due to the fact of the scales being multi-layered and multi-phase, as well as having enhanced growth on the corners and edges of the sample. Instead, cross-sectional analysis of the corrosion scales showed that low aluminum additions (5 wt%) to iron decreased the diffusion rate of iron outward by an order of magnitude at 700°C.

3.2 Oxidizing Environments

3.2.1 Introduction

This section reviews the corrosion product morphologies formed on Fe-Al alloys in an oxidizing environment. These samples were exposed to flowing zero grade air in a box furnace at temperatures of 500-700°C for 50 hours. For selected samples, characterization was also conducted using thermogravimetric techniques to obtain continuous weight gain data. Discussion of the mechanisms for nodular growth, in both oxidizing and reducing environments, will be related to the findings of this study.

3.2.2 Experimental Procedure

Qualitative oxidation studies were conducted using a Fisher Scientific box furnace. These experiments were performed in order to observe similarities in the growth of reaction products during high temperature exposure in dissimilar environments (oxidizing versus reducing). For these studies, only one face of the sample was ground to 600 grit and cleaned as described above. The furnace was brought to temperature with zero grade compressed air flowing through the chamber for a minimum of 2 hours. Samples were then placed in the furnace, prepared side up, and held for 50 hours. They were subsequently removed and allowed to cool. The temperature was monitored using a thermocouple located next to the samples. Characterization techniques were similar to that found in Section 3.1.2.

3.2.3 Results

3.2.3.1 Box furnace morphologies

Exposure at 500°C

Figure 3.131 shows the surfaces at low magnification. The 5Al sample was dull gray in appearance (Fig 3.132a) and the 7.5Al sample was tan with dark growths (Fig 3.132b). The 10Al and 12.5Al samples were blue-purplish in color with no signs of growth (Fig 3.132c).

Higher magnification of the 5Al sample surface revealed full coverage by a scale that had needle like projections growing from its surface, Fig 3.133. Cross-sectional analysis of the sample showed a tri-layered structure consisting of an outer light gray scale, middle gray scale that was

discontinuous, and an inner dark gray scale, Fig 3.134. Some porosity was noted at the interface between the two inner scales. EPMA identified the light gray scale as Fe_2O_3 and the inner dark gray layer as having a composition that placed it in the three phase region of Fe_2O_3-Fe_3O_4-Al_2O_3 on the ternary phase diagram, Table 3.18. The middle gray scale was too small for analysis, but will later be identified as Fe_3O_4. Microprobe analysis of the substrate beneath the scales revealed a similar composition as that found at far distances into the alloy.

The 7.5Al sample was found to have the same type of scale as observed on the 5Al sample, except that it had only partial coverage of the surface, Fig 3.135. These corrosion products were found to be aligned with the 600 grit preparation marks. In areas where thick corrosion product did not form, the surface scale was granular (Fig 3.136a) and had a thickness of about 50 nm, Fig 3.136b. Polished cross-sections revealed the tri-layered scale, in the form of nodules (Fig 3.137), with similar compositions to that previously seen, Table 3.18. Analysis of the substrate under the nodules, as well as directly under the nodule free region had similar chemistry to that of the alloy.

For the 10Al and 12.5Al samples, a similar surface scale was found as that on the 7.5Al sample in areas lacking thick scale growth, Fig 3.138. The cross-sections also revealed a similar thickness with high counts of aluminum and oxygen according to EDS analysis.

Exposure at 600°C

Figure 3.139 shows the SEI micrographs at low magnification for all samples tested at 600°C. The 5Al alloy had full coverage of the surface by a dull gray scale, Fig 3.132a, while the 7.5Al sample was tan with dark growths across its surface, Fig 3.132b. The 10Al and 12.5Al alloys were blue-purplish in color with no signs of surface growth, Fig 3.132c.

Carefully inspecting the surface of the 5Al sample, the location of the grain boundaries of the underlying substrate can be seen through the scale, Fig 3.139a and 3.140a. The surface also had a bubbled appearance which may indicate some type of nodular formations as precursors to full coverage. Higher magnification of the surface revealed a porous scale with needles growing out, Fig 3.140b. Polished cross-sections of these regions confirmed the prior formation of nodules, Fig 3.141a, as tri-layered structures with an internal oxidation zone. Full coverage was obtained through coalescence of the outer, light gray scale of Fe_2O_3. An inner layer of Fe_3O_4 also appeared somewhat

continuous. The third, dark gray layer penetrating into the substrate was found to have a composition that resided in a mixed scale regime, similar to that found above, on the ternary phase diagram, Table 3.18. Beneath these scales was found an internal oxidation layer (Fig 3.141b) whose composition was found to be in the two phase region of alpha iron and alumina (Table 3.18). The substrate below the precipitate region was not found to differ from alloy compositions.

Examination of the 7.5Al sample revealed the formation of corrosion nodules on its surface, Fig 3.142. These nodules were of uniform size (approximately 40 um) with some occurrence of coalescence, Fig 3.142b. The nodule free region was similar to the other surface scales previously seen on the 7.5Al sample at 500°C, Fig 3.143. Cross-sectional analysis revealed the same tri-layered scale with internal precipitate zone, Fig 3.144. The microprobe data for the dark gray scale penetrating into the substrate (Fig 3.145a) and the internal precipitate layer (Fig 3.145b) can be seen in Table 3.18. Fractured cross-sections revealed the thin scale as being roughly 60-80 nm thick, Fig 3.143b.

The 10Al and 12.5Al sample had similar surface scales observed in the nodule free region of the 7.5Al sample, Fig 3.146 and 3.147 respectively. The cross-sections were also similar with EDS analysis indicating high counts of aluminum and oxygen.

Exposure at 700°C

Figure 3.148 shows the low magnification SEI images of the samples exposed at 700°C. With the exception of the 5Al specimen, the others were relatively free of corrosion product on their surfaces with a shiny blue tint, Fig 3.132c. The 5Al specimen was tanish in color with dark growths on its surface, particularly located at the corners and edges, Fig 3.132b.

Higher magnification of the surface revealed that the 5Al sample was covered with nodules of corrosion product, Fig 3.149. These nodules were relatively uniform in size (approximately 135 um) with some coalescence observed. In the nodule free region, the scale was somewhat granular in nature, Fig 3.150a, and fractured cross-sections revealed it as a thin blanket of oxide, Fig 3.150b. The scale was uniform in thickness (roughly 100 nm) and had high counts of aluminum and oxygen. Polished cross-sections of the nodules revealed a bilayered structure with internal oxidation, Fig 3.151. The lighter, outer layer was found to be Fe_2O_3 while the blocky phase at the inner scale-outer

scale interface was Fe_3O_4. The scale found protruding into the substrate appeared homogeneous, however, its composition resided in a mixed scale region on the ternary phase diagram, Table 3.18. Separation between the nodule and substrate can be seen, as evidence of the charging epoxy in Fig 3.151b. Higher magnification of the internal oxidation layer can be seen in Fig 3.151c. While the precipitates were too fine to analyze using microprobe techniques, a scan of the area revealed that the composition resided in the two phase region of alpha iron plus alumina, Table 3.18.

The surface of the 7.5Al sample was found to have some corrosion nodule formations on its corners and edges, Fig 3.148b. These nodules, Fig 3.152, were of uniform size. While cross-sectional analysis could not be obtained of these features, EDS indicated the presence of iron and oxygen. The remaining areas of the surface was found to be covered by a similar scale observed in the nodular free region of the 5Al sample, Fig 3.153. Both the 10Al and 12.5Al samples had this coverage also, Fig 3.154 and 3.155. Fractured cross-sections revealed a similar thin scale (approximately 100 nm) that was uniform in thickness, regardless of the aluminum content of the alloy.

3.2.3.2 Corrosion Kinetics

Selected samples were also exposed in a thermogravimetric balance to obtain continuous weight gain data, Fig 3.156. Calculated n-values can be found in Table 3.19. These samples were chosen based upon the type of morphology that developed in the box furnace experiments. Surface characterization of these samples revealed similar microstructures to those observed above and will not be discussed again.

3.2.4 Discussion

3.2.4.1 Oxidation behavior of Fe-Al alloys

The results obtained in this study were similar to those found in the literature [Boggs; DeVan 1992, 1993a, 1993b; Hagel; Prescott 1992a, 1992b; Saegusa; Sakiyama; Smith 1987c; Tomaszewski 1978, 1983; Tortorelli 1992, 1993, 1994a; Wallwork]. In general, the relative amount of scale development was found to decrease with increasing aluminum content and temperature. Increasing the aluminum content of the alloy may have decreased the distance between adjacent alumina nuclei

on the surface, thus increasing the probability of forming a continuous, protective scale at early times. The increase in temperature provided more energy for diffusion of aluminum to the surface to aid in this coverage.

The morphology of these scales was also similar to that observed in literature. While the thin surface scale was not positively identified, enough data exists to assume it as gamma alumina. These facts range from the low weight gain observed to the color of the scales (Hagel (1965) also reports tan, blue, and purple colored scales for gamma formation). Many other researchers working in this temperature regime on similar alloys have also found protection due to the gamma scales [Hagel; Boggs; Prescott 1992a, 1992b; Sakiyama; Tomaszewski 1978; Tortorelli 1992]. The protectiveness of the scale also conforms with the values reported for the aluminum content and temperature dependence for eliminating nodular growth in oxidizing environments. It appears that at 700°C, the aluminum content necessary for full protection is above 7.5 wt%.

In terms of the iron oxide that was found to grow on the scale, whether in nodule or continuous scale form, the results are again similar to that observed in the literature [Boggs; Hagel; Prescott 1992b; Saegusa; Sakiyama; Smith 1987c; Tomaszewski 1981, 1983]. Growth of the oxides was predominantly by the outward diffusion of Fe cations to form an external layer of Fe_2O_3 and Fe_3O_4. Oxygen was also found to diffuse inward by short circuiting the protective scale. This was most clearly observed in the cross-sections of the 7.5Al sample exposed at 600°C (Fig 3.144a). The internal oxidation layer can only be found associated with the nodule, whereas the protective alumina scale did not allow for diffusion into the alloy beneath it as shown through microprobe analysis. Reports have typically found that these nodular growths tend to form at highly stressed areas such as corners and edges or at regions of crystal misfit such as grain boundaries or triple points [Tomaszewski 1983]. While much of the growth can be found located at the corners and edges, the nodules across the face of the sample were either found randomly distributed or well aligned with preparation marks on the surface. This was due to the rougher surface finish of these samples, compared to a polished surface conducted by other researchers, thus eliminating any effect of the grain boundaries.

The kinetic data suggests that the iron oxide grew from the onset of exposure due to the initial high weight gains. As time increased, the rate of weight change was observed to decrease,

suggesting that growth of the ensuing scale may be diffusion controlled. The 5Al alloys were found to have near identical weight gains at different temperatures. While this was unexpected, the explanation can be found by observing the cross-sectional microstructures. While the 700°C has less surface coverage by the iron oxides, due to the higher temperature, the scale was nearly twice as thick as at 600°C (Fig .141a versus Fig 3.151a). These two samples also show that as the temperature increased, the propensity to form a protective alumina scale increased for a given alloy content. This was also observed with the 7.5Al samples.

3.2.4.2 Mechanism for nodular formation

As previously discussed, there appears to be a lack in understanding the formation of nodular corrosion products during high temperature oxidation reactions. Two mechanisms proposed are based primarily upon the mechanical failure of an initially formed passive layer [Boggs; Quan; Patnaik 1985a] and the co-development of two different cation oxides [Boggs; Sakiyama; Tomaszewski 1983; Smith 1987c]. The first theory is typically associated with reactions in sulfidation or oxidation/sulfidation environments, while the latter is associated with exposures in oxidation atmospheres. This section will briefly review these two theories and discuss as they relate to the work conducted in this study.

As seen from the literature [Saegusa; Tomaszewski 1983; Smith 1987c; Sakiyama], as well as this work, formation of nodules on the surface of iron-aluminum alloys typically have kinetic data curves similar to that schematically shown in Fig 3.157 for co-development. This shows an initially high weight gain followed by a slower growing period. It is the shape of this curve that leads to the belief of nodular formation through co-development of different cation oxides. For the mechanisms based upon scale rupture (mechanical failure), a passive scale must form on the surface resulting in initially low weight gains. Upon mechanical failure, the weight gains would be expected to increase dramatically as shown in Fig 3.157. However, the results obtained here, as well as published in the literature, on the oxidation of Fe-Al alloys typically show high weight gains from the onset of exposure. Therefore, no protective scale initially exists that breaks down. Instead, it is believed that the iron and aluminum oxides form concurrently.

Tomaszewski and Wallwork (1983) have proposed a mechanistic model for the formation of nodules on Fe-Al alloys in an oxidizing environment which described the co-development of oxides. At early times, FeO and Al_2O_3 are expected to form on the surface due to thermodynamic considerations. Providing that the aluminum content of the alloy is high enough, alumina develops a somewhat continuous layer, isolating the few particles of FeO remaining. (For lower aluminum content alloys, the density of the iron oxide nuclei may be greater and outgrow the alumina nuclei to form a thick scale of iron oxide.) Reactions at the FeO-Al_2O_3 phase boundary lead to the formation of $FeAl_2O_4$ within the alloy, while the outer surface further reacts to form higher oxides of iron. Through physical flaws or discontinuities in the alumina scale, the iron oxide nodules continue to grow through iron diffusion in these defects. During its growth, the nodule typically consists of an outer shell of Fe_2O_3 with a porous interior containing other iron and aluminum oxides. If the aluminum content is low, the nodules may continue to develop and coalesce to form a bulky, stratified scale. However, if the aluminum content is high enough, development of an aluminum oxide healing layer may occur at the base of the nodule. This can limit the flow of iron outward resulting in the entire nodule oxidizing completely to Fe_2O_3 at long times. Published kinetic data for the oxidation of Fe-Al alloys supports this theory as rapid weight gains occur from the onset of reaction.

As seen from the kinetic results of this study (Fig 3.156), it appears that the nodules have grown concurrently with the alumina scale, thus supporting the validity of the co-development mechanism. For the 5Al samples at temperatures below 700°C, the widespread nucleation of nodules on the surface has occurred leading to full coverage at longer times. This may be attributed to decreased formation of alumina at lower temperatures and aluminum contents. In addition, the lower aluminum content of the alloy did not allow for the formation of a healing layer of alumina between the nodule and alloy to inhibit further development. Thus, a continuous scale formed of iron oxide was found. However, as the temperature and/or aluminum content increased, the number of nodules able to grow decreased as alumina formation was now promoted. For samples with higher aluminum contents (above 10 wt%), no nodules were found on surfaces. It appears that for these specimens, enough aluminum was present for widespread coverage of alumina, thus effectively isolating the initial iron oxide nuclei. Further, the aluminum content was great enough to maintain the protection through a continual supply of aluminum to the surface from the bulk of the alloy.

Whereas the kinetic data from the oxidation experiments typically showed initial high weight gains followed by slower rates at longer times, the kinetic data in reducing environments for nodular growth had a different shape, shown schematically in Fig 3.157 and experimentally in Fig 3.6 and 3.11 through 3.13. These curves were typically found to start out with negligible or relatively low weight gains followed by typical "breakdown" kinetics. These results were observed in this research, as well as by other authors [Patnaik 1985a; Quan] studying the sulfidation resistance of Fe-based alloys. In all cases, this type of behavior was attributed to the formation of a transient, passive scale which eventually failed due to mechanical means. Regardless of the reaction products that formed (for both passive scale and corrosion nodules), the effect was similar.

Quan and Young (1986) studied the sulfidation behavior of an Fe-4.5 wt% Mn- 8.8 wt% Al alloy in a sulfidizing gas ($10^{-8} < p(S_2) < 10^{-4}$ atm) at 700-900°C. Protection from extreme corrosion was afforded by a thin external scale of MnS that initially formed upon exposure under moderate conditions. However, when reaction conditions were severe (higher $p(S_2)$ and temperatures), protection was not found to last as mechanical failure of the MnS scale led to direct contact of the gas with the underlying alloy. Due to a Mn-depleted layer beneath the scale, re-establishment of the MnS could not occur and growth of iron sulfide nodules took place. These nodules typically consisted of an outer, irregularly-shaped scale of Fe(Mn)S that contained only trace amounts of aluminum. The lower half of the nodule that extended into the substrate was found to contain a fibrous microstructure in which the grains were oriented normal to the surface. EPMA analysis lead to their identification as $(Fe,Mn)Al_2S_4$ plus $(Fe,Mn)_{1-x}S$. Further examination of the nodule cross-section revealed the remains of the original protective scale between the outer sulfide scale and the inner mixed layer. Therefore, due to the kinetic data for these formations (displaying an initial period of slow sulfidation followed by rapid reaction) and the remnants of the initial surface scale in the nodule, they concluded that the nodules grew due to a mechanical breakdown in the MnS scale and short circuit diffusion by both cations and anions.

Patnaik and Smeltzer (1985a) gave rise to a similar type of morphology, but by a slightly different mechanism. In sulfidizing Fe-Al binary alloys at 900°C, they proposed that the nodular growths of FeS developed through a defective film of Al_2S_3 on the surface that appeared to provide initial protection. While the kinetic data obtained by Patnaik and Smeltzer supports the mechanism

proposed by Quan and Young (1986), detailed microscopy of the nodule cross-section was not given in order to confirm or disavow growth through the mechanical failure mechanism.

Results from this research also indicated that the mechanism for nodular development in the oxidizing/sulfidizing environment was through breakdown of an initially formed passive layer. It was interesting to note that whether the initial passive scale was MnS, Al2S3, or Al2O3, the breakdown in protection led to similar corrosion morphologies. The breakdown in the alumina scale was explicitly demonstrated through the kinetic data obtained for the 10Al samples tested at 700°C, Fig 3.12. With very low initial weight gains, the sample exposed for 2 hours did not develop the formation of corrosion nodules. However, as time progressed and the alumina scale increased in thickness, mechanical failure at the corners and edges lead to the "breakdown" kinetics observed on the 50 hour sample. In addition, the 7.5Al samples also demonstrated this mechanism through both the kinetic data (Fig 3.11) and the morphological features. The observance of the initial surface scale in between the two interfacial layers on the 7.5Al samples also readily suggests their growth by this manner (Fig 3.100b, 3.107b, and 3.108b).

The difference between these two growth mechanisms may lie in the growth rates of the iron-based reaction products that form in the given environment. It is well established that the sulfidation rate of iron is nearly two orders of magnitude higher than that of oxidation [Mrowec; Strafford 1989; Wang]. These faster kinetics are due to the sulfide having a very large defect concentration and resulting higher iron diffusion coefficient [Meier]. Therefore, upon initial exposure to the environment, if alumina cannot attain full coverage of the surface, its nuclei is quickly overgrown and the formation of a continuous surface scale of sulfides can occur. This was typically found for all alloys with less than 7.5 wt% Al. As the aluminum content increases, alumina can obtain full coverage of the surface and provide initial protection. The length of this protection was found to be dependent upon the aluminum content of the alloy, as well as the temperature. The 7.5 wt% alloys were found to have extremely short times, and the question may be raised as to whether they formed the initial alumina scale to start. The results, in terms of the shape of the kinetic curve and the remains of the initial scale between the outer and inner layer, was proof that it did. The reason for its breakdown was most likely related to the lack of aluminum available to re-establish the scale after mechanical failure at short times. This lead to short circuit diffusion of sulfur to the alloy interior

and eventual nodule formation. As the aluminum content increases further (above 12.5 wt%), the ability of the alumina layer to heal itself was shown in the longer periods of protection. When failure did occur, the nodules were located primarily on the corners and edges which may suggest a limitation of the testing procedure, for both oxidation and sulfidation studies, and may not be indicative of the protective nature of the scales. For the case of oxidation, a different scenario can be found. Since the iron oxides grow at a much slower rate, rampant overgrowth of the alumina nuclei may not occur. Depending upon the aluminum content of the alloy, the iron oxide nuclei can either co-develop with the alumina scale into nodules (lower temperatures and aluminum contents), or be completely isolated, effectively ending its growth (higher temperatures and aluminum contents). Once again, the model proposed by Tomaszewski and Wallwork (1983) can be referred to for this type of development.

The development of nodular growth is not only limited to high temperature exposure to oxidants. The breakdown of passive scales in other "corrosion" environments has also been encountered. Studying the interfacial morphological developments of phases formed during a hot-dip galvanizing process, Jordan and Marder (1997b) observed the formation of Fe-Zn outbursts into the zinc coating. This was observed when the zinc bath contained 0.20 wt% Al. For pure zinc baths (0.0 wt% Al), uniform attack of the substrate was found [Jordan 1997a]. The reason for this change in morphology was the formation of an initial iron aluminide inhibition layer at the iron substrate/coating interface that acted as a physical barrier to zinc diffusion. However, this protection did not last as liquid zinc eventually penetrated the scale to form localized growths of Fe-Zn phases. These growths developed into Fe-Zn outbursts due to the short circuit diffusion of iron through the protective layer.

3.2.5 Oxidation Study Summary

The formation of nodular corrosion products has been observed in a number of different systems. Review of the literature found two mechanism by which these outbursts have been proposed to form based upon experimental results. The first mechanism relies upon the co-development of different cation oxides from initial exposures. This type of behavior was primarily found for Fe-based alloys in an oxidizing environment. The basis for the theory can be developed

from the kinetic data observations in which initial high weight gains are found indicating non-protective product formation from early exposures. The second mechanism proposed is related to the initial formation of a passive scale due to preferential "oxidation" of the alloy surface. This scale is typically thin, yet able to inhibit rapid degradation of the underlying substrate. At later times, mechanical failure of the scale leads to high weight gains from non-protective corrosion product formation due to short circuit diffusion of the protective layer. These results were observed when sulfur was present in the atmosphere. From oxidation and oxidation/sulfidation experiments conducted in this study, it appears that the validity of both growth mechanisms can be substantiated by this research through kinetic data analysis and morphological developments in the respective environments.

3.3 Corrosion Studies Tables

Table 3.1: Alloy compositions as determined by wet chemical analysis

Alloy	Designation	wt% Fe	wt% Al	wt% S	wt% C
Fe-5wt% Al	5Al	95.24	5.08	0.003	0.005
Fe-7.5wt% Al	7.5Al	92.90	7.70	0.002	0.003
Fe-10wt% Al	10Al	89.95	9.93	0.003	0.003
Fe-12.5wt% Al	12.5Al	87.51	12.51	0.002	0.004
Fe-15wt% Al	15Al	85.23	14.29	0.002	0.002
Fe-20wt% Al	20Al	80.24	19.79	0.002	0.005
low carbon steel	LCS	99.52	NA	0.019	0.049

Table 3.2: Grain size measurements for as-received and heat-treated substrates.

	As-received			Heat treated at 700°C for 100 hrs		
Alloys	Width (mm)	Length (mm)	Aspect Ratio	Width (mm)	Length (mm)	Aspect Ratio
5	1.2 ± 0.4	2.0 ± 0.6	1.65	1.2 ± 0.3	1.9 ± 0.5	1.66
7.5	1.1 ± 0.4	1.9 ± 0.8	1.66	1.0 ± 0.4	1.7 ± 0.7	1.61
10	0.7 ± 0.2	1.9 ± 0.9	2.89	0.7 ± 0.2	2.0 ± 0.9	2.80
12.5	0.5 ± 0.2	2.3 ± 0.6	4.63	0.4 ± 0.2	2.2 ± 0.6	5.05
15	0.4 ± 0.1	3.4 ± 1.1	9.30	0.4 ± 0.2	3.5 ± 1.0	8.21
20	0.2 ± 0.1	2.2 ± 0.6	9.08	0.2 ± 0.1	2.5 ± 0.5	10.33

Table 3.3: Typical temperature program for 50 hr exposure at 700°C

Temperature Segment	Rate (K/min)	Temperature (°C)	Time
Initial		20	
Dynamic (heating)	50	685	13 min
Dynamic (heating)	5	700	3 min
Isothermal		700	50 hrs
Dynamic (cooling)	20	20	34 min
Isothermal		20	1 hr
Emergency		750	

Table 3.4: Corrosion gas compositions and corresponding partial pressures of oxygen (measured) and sulfur (calculated) at temperature.

Gas Composition (by volume)	Temp (°C)	$p(O_2)$ (atm)	$p(S_2)$ (atm)
1.1%H_2S-0.0%H_2-98.9%Ar (500 ppm O_2)	500	9.2×10^{-26}	7.5×10^{-4}
0.9%H_2S-0.0%H_2-99.1%Ar (50 ppm O_2)	600	7.4×10^{-25}	4.0×10^{-4}
1.0%H_2S-0.1%H_2-98.9%Ar (5 ppm O_2)	700	3.4×10^{-25}	5.4×10^{-4}

Table 3.5: Calculation of n-values for samples tested at 500°C.

Sample	Time Interval (in hrs)	Calculated n-value
T052	Full	1.00
T552	Full	0.73
T7.552	Full	0.42

Table 3.6: Calculation of n-values for samples tested at 600°C.

Sample	Time Interval (in hrs)	Calculated n-value
T062	Full	1.00
T562	Full	0.62
T7.562	Full	1.52

Table 3.7: Calculation of n-values for samples tested at 700°C.

Sample	Time Interval (in hrs)	Calculated n-value
T072hr1	Full	0.55
T072	Full	0.86
T072	0.8-1.2	0.50
T072	1.3-end	0.94
T572	Full	1.09
T7.572	Full	1.36
T1072	1.7-3.0	0.16
T1072	4.6-12.3	2.41
T1072	30-end	1.22
T12.572	1.5-5.3	0.06
T12.572	5.4-end	0.85

Table 3.8: EPMA data for sample T052 (composition is in wt% of element)

Location	Fe	Al	S	O
Alloy	99.5 ± 0.4	0.0	0.0	0.6 ± 0.2
Outer scale	60.8 ± 0.0	0.0	38.0 ± 0.3	0.3 ± 0.2
Substrate near corrosion front	99.3 ± 0.4	0.0	0.0	0.6 ± 0.4

Table 3.9: EPMA data for sample T552 (composition in wt% of element)

Location	Fe	Al	S	O
Alloy	95.8 ± 0.3	4.9 ± 0.6	0.0	0.4 ± 0.3
Outer scale	59.9 ± 0.2	0.0	38.0 ± 0.1	0.5 ± 0.0
Base of outer scale FeS plates	60.1 ± 0.3	0.4 ± 0.3	38.2 ± 0.5	0.6 ± 0.4
Scan of inner layer	46.5 ± 0.5	7.4 ± 0.3	43.9 ± 0.4	1.1 ± 0.2
Inner FeS layer	60.9 ± 0.3	0.4 ± 0.2	37.9 ± 0.4	0.3 ± 0.2
Substrate near protrusions	95.4 ± 0.5	4.9 ± 0.3	0.0	0.5 ± 0.2

Table 3.10: EPMA data for sample T7.552 (composition in wt% of element)

Location	Fe	Al	S	O
Alloy	92.4 ± 0.5	7.7 ± 0.3	0.0	0.6 ± 0.2
Outer scale	59.1 ± 0.4	0.0	39.7 ± 0.2	0.4 ± 0.2
Base of outer scale FeS plates	59.8 ± 0.3	0.4 ± 0.3	38.6 ± 0.3	0.5 ± 0.2
Scan of inner layer	34.7 ± 0.5	14.3 ± 06	48.2 ± 0.4	1.1 ± 03
Substrate near protrusions	92.4 ± 0.4	7.6 ± 0.4	0.0	0.5 ± 0.3

Table 3.11: EPMA data for sample T062 (composition is in wt% of element)

Location	Fe	Al	S	O
Alloy	99.7 ± 0.7	0.0	0.0	0.5 ± 0.2
Outer scale	61.8 ± 0.3	0.0	37.2 ± 0.3	0.5 ± 0.2
Substrate near corrosion front	99.6 ± 0.4	0.0	0.0	0.5 ± 0.4

Table 3.12: EPMA data for sample T562 (composition in wt% of element)

Location	Fe	Al	S	O
Alloy	95.2 ± 0.4	4.7 ± 0.6	0.0	0.5 ± 0.3
Outer scale	61.7 ± 0.2	0.0	37.4 ± 0.3	0.6 ± 0.1
Base of outer scale FeS plates	61.2 ± 0.3	0.3 ± 0.1	37.3 ± 0.5	0.6 ± 0.3
Grainy particles	61.4 ± 0.5	0.6 ± 0.2	37.3 ± 0.3	0.6 ± 0.1
Scan of inner layer	45.2 ± 0.4	8.9 ± 0.2	43.0 ± 0.5	1.4 ± 0.4
Substrate near protrusions	95.4 ± 0.5	4.9 ± 0.3	0.0	0.5 ± 0.2

Table 3.13: EPMA data for sample T7.562 (composition in wt% of element)

Location	Fe	Al	S	O
Alloy	92.7 ± 0.4	7.5 ± 0.3	0.0	0.7 ± 0.2
Outer scale	62.0 ± 0.3	0.0	37.1 ± 0.4	0.5 ± 0.1
Base of outer scale FeS plates	60.3 ± 0.3	0.3 ± 0.2	37.5 ± 0.1	0.6 ± 0.2
Scan of inner layer	37.3 ± 0.4	12.5 ± 0.4	47.1 ± 0.2	1.3 ± 0.2
Substrate under bare area	92.9 ± 0.3	7.3 ± 0.3	0.0	0.6 ± 0.3
Substrate near protrusions	92.6 ± 0.3	7.4 ± 0.2	0.0	0.5 ± 0.0

Table 3.14: EPMA data for sample T072 (composition is in wt% of element)

Location	Fe	Al	S	O
Alloy	99.9 ± 0.6	0.0	0.0	0.5 ± 0.1
Outer scale	61.9 ± 0.3	0.0	37.3 ± 0.3	0.3 ± 0.2
Substrate near corrosion front	99.8 ± 0.5	0.0	0.0	0.4 ± 0.2
Corner plate	62.2 ± 0.3	0.0	38.0 ± 0.3	0.3 ± 0.2

Table 3.15: EPMA data for sample T572 (composition in wt% of element)

Location	Fe	Al	S	O
Alloy	95.7 ± 0.3	4.9 ± 0.5	0.0	0.5 ± 0.2
Outer scale	61.7 ± 0.5	0.0	37.7 ± 0.3	0.6 ± 0.1
Small platelets	61.2 ± 0.6	0.4 ± 0.3	37.0 ± 0.3	0.7 ± 0.1
Corner plates	62.1 ± 0.3	0.0	37.9 ± 0.3	0.6 ± 0.1
Inner plates	24.0 ± 0.8	20.7 ± 0.3	52.8 ± 1.0	1.3 ± 0.1
Transformed plates	61.2 ± 0.8	0.7 ± 0.5	37.3 ± 0.4	0.8 ± 0.2
Scan of inner layer	45.1 ± 0.3	8.3 ± 0.5	43.3 ± 0.7	1.6 ± 0.4
Substrate near protrusions	95.4 ± 0.3	4.9 ± 0.1	0.0	0.4 ± 0.0

Table 3.16: EPMA data for sample T7.572 (composition in wt% of element)

Location	Fe	Al	S	O
Alloy	93.5 ± 0.3	7.4 ± 0.4	0.0	0.8 ± 0.2
Outer scale	62.0 ± 0.2	0.0	37.6 ± 0.2	0.6 ± 0.1
Small platelets	61.4 ± 0.3	0.6 ± 0.2	37.5 ± 0.3	0.8 ± 0.2
Corner plates	62.1 ± 0.1	0.0	37.9 ± 0.3	0.6 ± 0.0
Inner plates	24.5 ± 0.5	21.0 ± 0.4	51.9 ± 1.1	1.4 ± 0.2
Scan of inner layer	34.9 ± 0.5	14.9 ± 0.5	47.4 ± 0.5	1.5 ± 0.3
Transformed plates	61.7 ± 0.5	0.9 ± 0.2	37.6 ± 0.4	0.9 ± 0.4
Substrate under bare area	93.2 ± 0.3	7.4 ± 0.2	0.0	0.7 ± 0.4
Substrate near protrusions	93.3 ± 0.4	7.4 ± 0.0	0.0	0.5 ± 0.1

Table 3.17: EPMA data for sample T1072 (composition in wt% of element)

Location	Fe	Al	S	O
Alloy	89.9 ± 0.5	9.8 ± 0.1	0.0	0.4 ± 0.0
Outer scale	61.6 ± 0.2	0.0	37.5 ± 0.7	0.4 ± 0.1
Small platelets	61.7 ± 0.2	0.8 ± 0.2	37.2 ± 0.3	0.7 ± 0.2
Inner plates	24.3 ± 0.5	20.9 ± 0.6	52.9 ± 0.9	1.6 ± 0.2
Scan of inner layer	29.7 ± 2.7	17.4 ± 2.1	47.2 ± 2.1	4.5 ± 1.6
Substrate under bare area	89.7 ± 0.3	9.8 ± 0.2	0.0	0.5 ± 0.4
Substrate near protrusions	89.7 ± 0.5	9.7 ± 0.3	0.0	0.6 ± 0.1

Table 3.18: EPMA data for various scale constituents.

Sample	Area	Fe (wt%)	Al (wt%)	O (wt%)
T553	Inner scale	61.4 ± 0.3	7.7 ± 0.3	30.3 ± 0.2
T7.553	Inner scale	57.2 ± 0.3	10.6 ± 0.1	30.3 ± 0.3
T563	Inner scale	62.0 ± 0.3	7.4 ± 0.2	29.0 ± 0.3
"	Inner ppt region	91.3 ± 0.3	5.4 ± 0.3	4.5 ± 0.5
T7.563	Inner scale	57.6 ± 0.1	11.5 ± 0.1	30.3 ± 0.2
"	Inner ppt region	86.4 ± 0.5	7.8 ± 0.0	6.2 ± 0.1
T573	Inner scale	66.4 ± 0.2	4.0 ± 0.1	29.2 ± 0.5
"	Inner ppt region	91.2 ± 0.7	5.5 ± 0.2	5.0 ± 0.2

Table 3.19: Calculated n-values for oxidation kinetics

Sample	Exposure Temperature (°C)	n-value
T563	600	0.62
T7.563	600	0.94
T1063	600	0.36
T573	700	0.67
T7.573	700	0.44

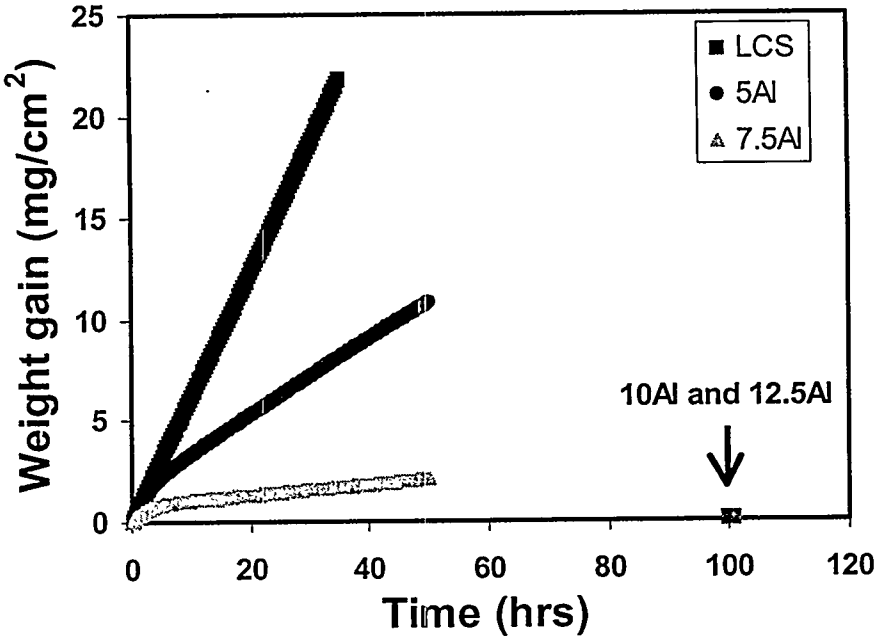

Figure 3.1: Plot of weight gain versus time for alloys tested at 500°C.

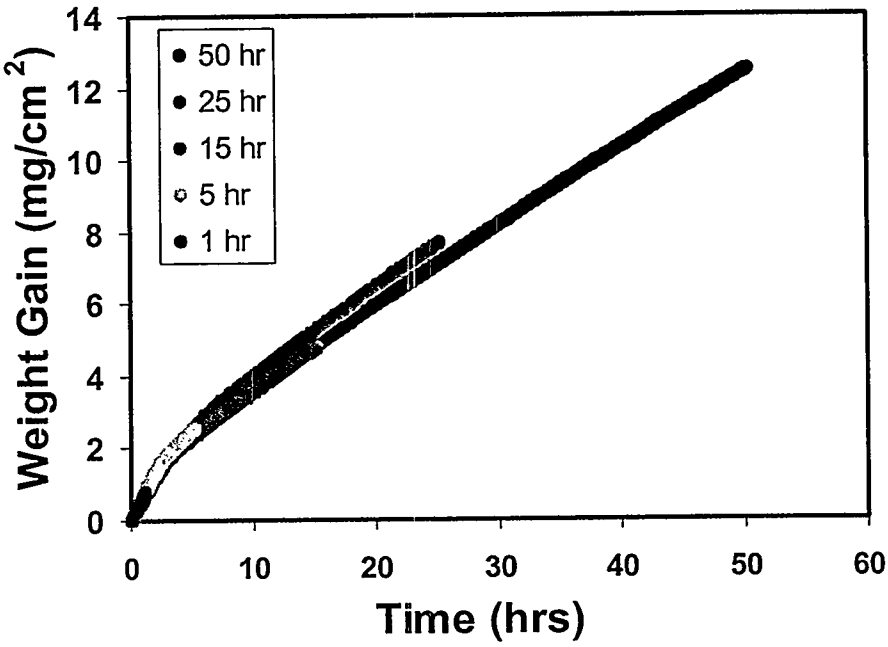

Figure 3.2: Plot of weight gain versus time for Fe-5Al alloys tested at 500°C.

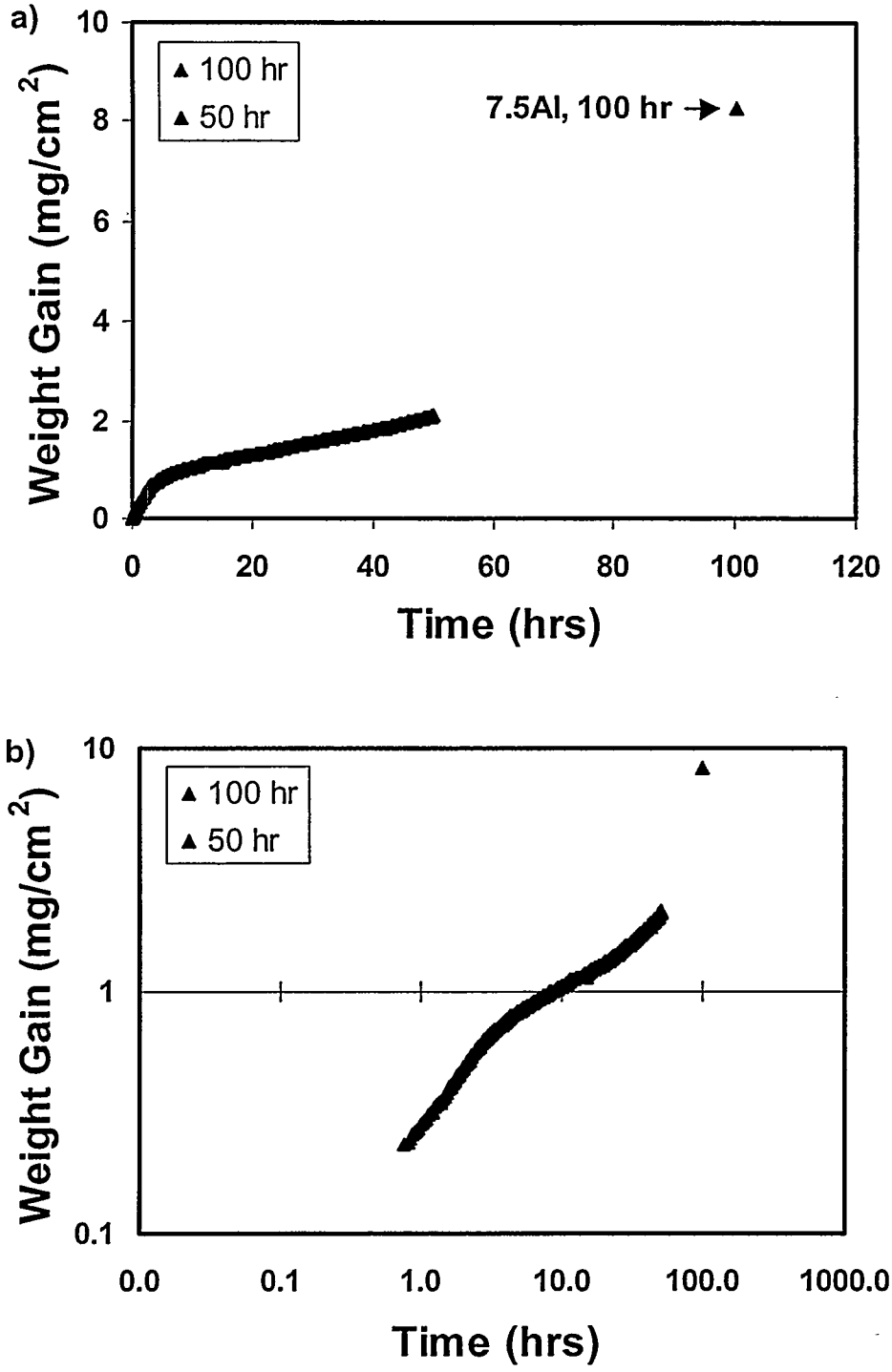

Figure 3.3: Plot of weight gain versus time for Fe-7.Al alloys tested at 500°C. a) regular axises, b) logarithmic axises

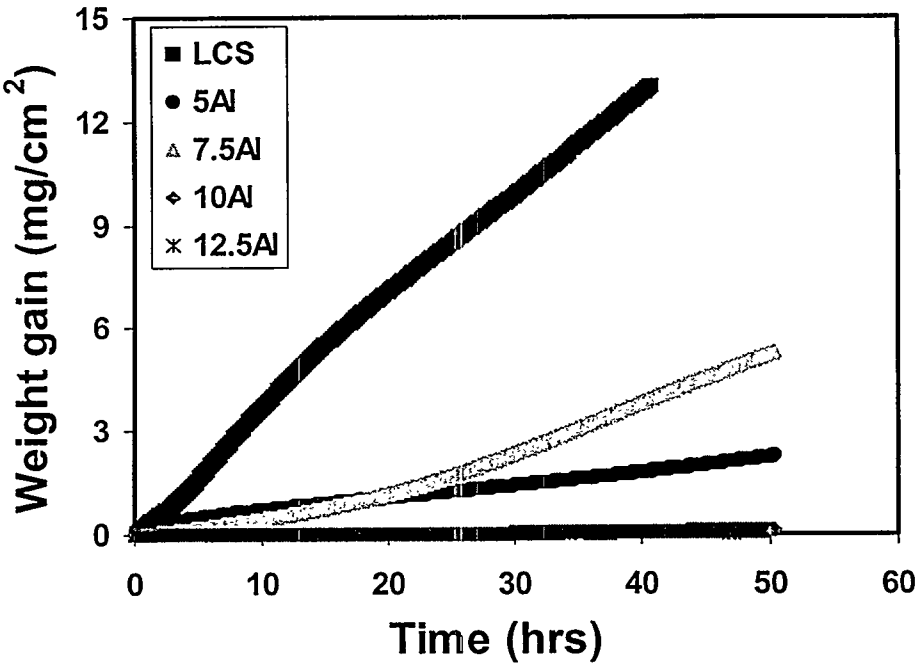

Figure 3.4: Plot of weight gain versus time for alloys tested at 600°C.

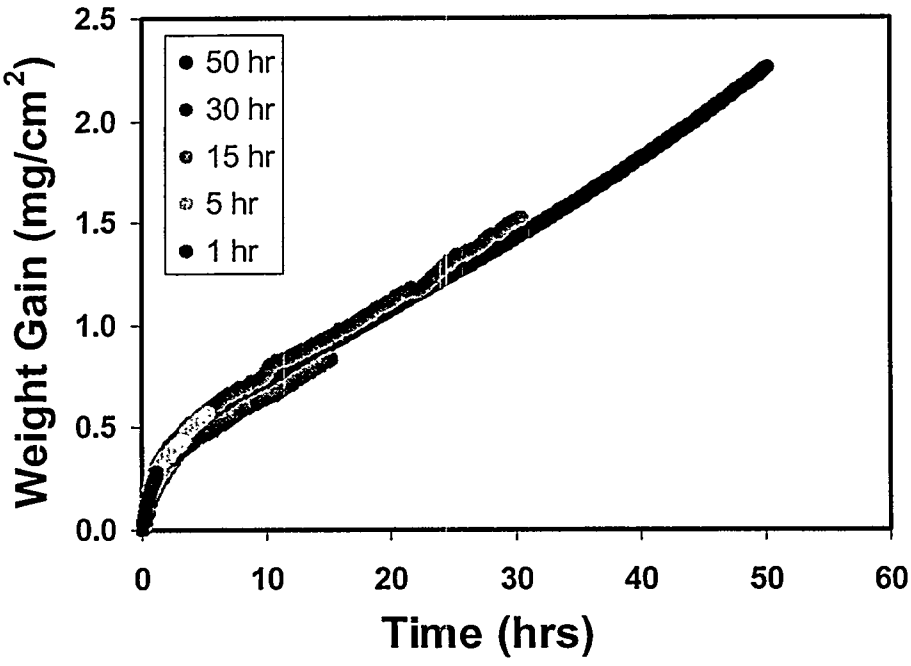

Figure 3.5: Plot of weight gain versus time for Fe-5Al alloys tested at 600°C.

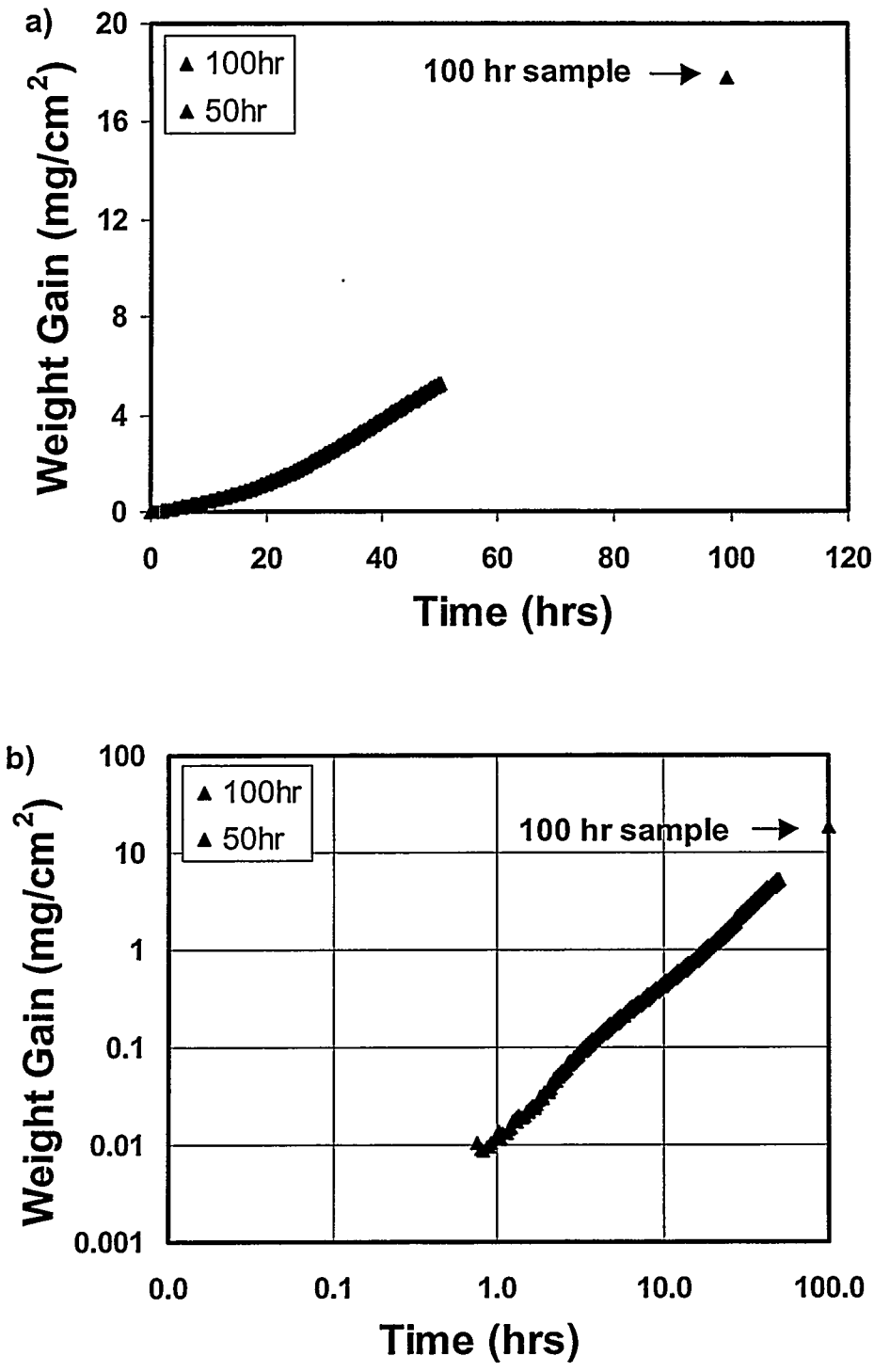

Figure 3.6: Plot of weight gain versus time for Fe-7.5Al alloys tested at 600°C. a) regular axises, b) logarithmic axises

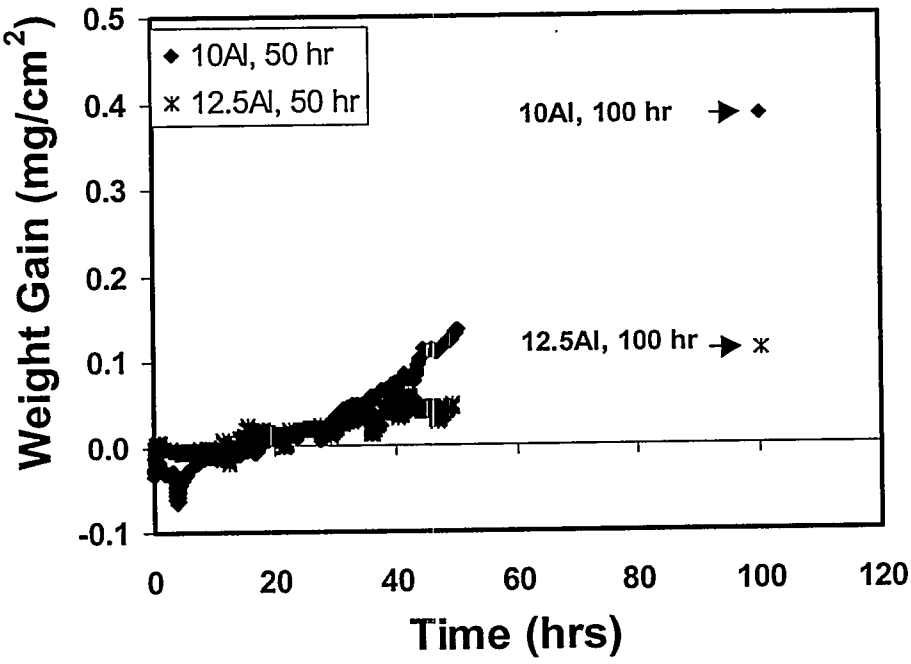

Figure 3.7: Plot of weight gain versus time for Fe-10Al and Fe-12.Al alloys tested at 600°C.

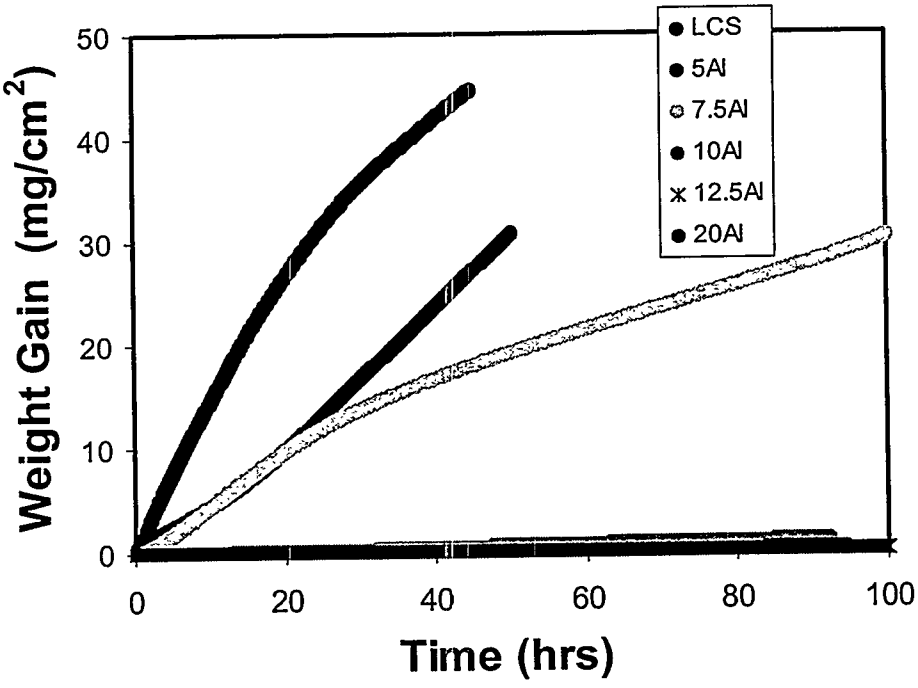

Figure 3.8: Plot of weight gain versus time for alloys tested at 700°C.

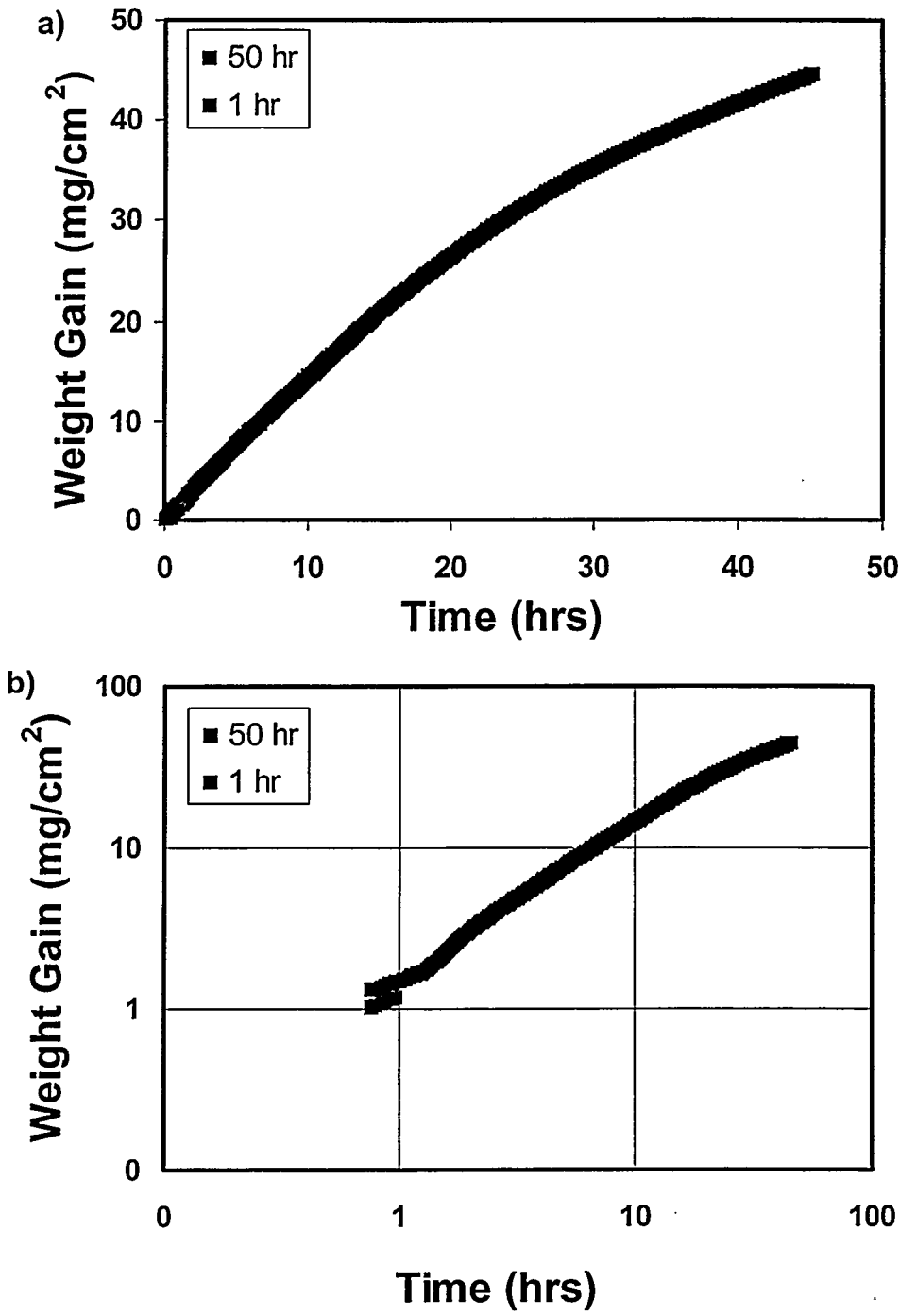

Figure 3.9: Plot of weight gain versus time for low carbon steel alloys tested at 700°C.

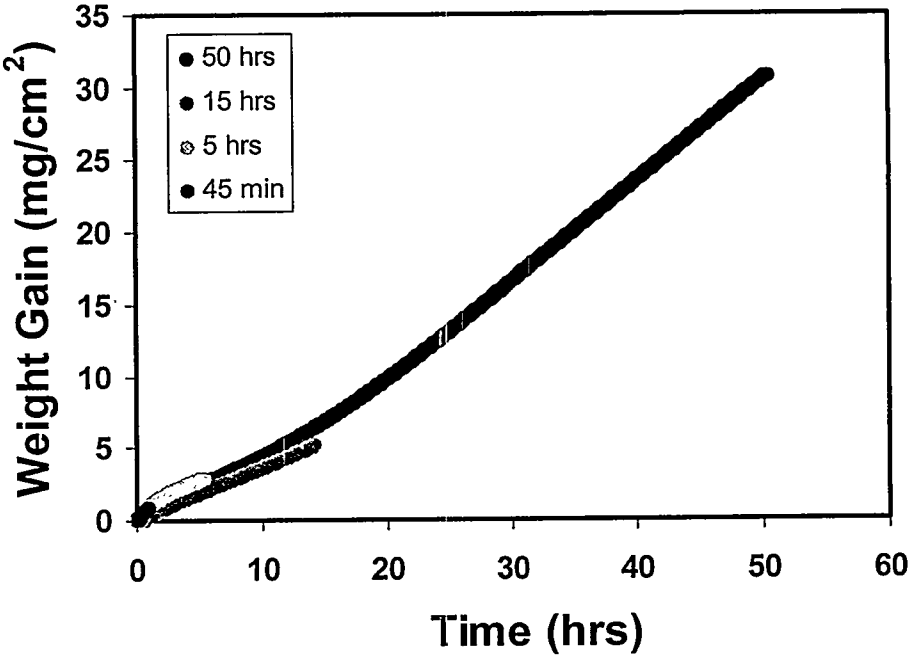

Figure 3.10: Plot of weight gain versus time for Fe-5Al alloys tested at 700°C.

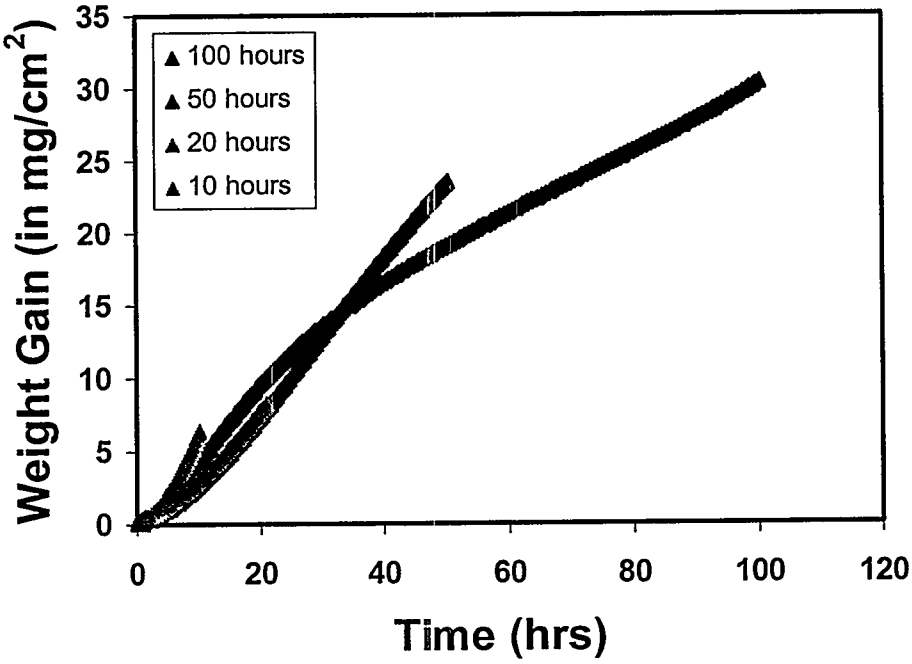

Figure 3.11: Plot of weight gain versus time for Fe-7.5Al alloys tested at 700°C.

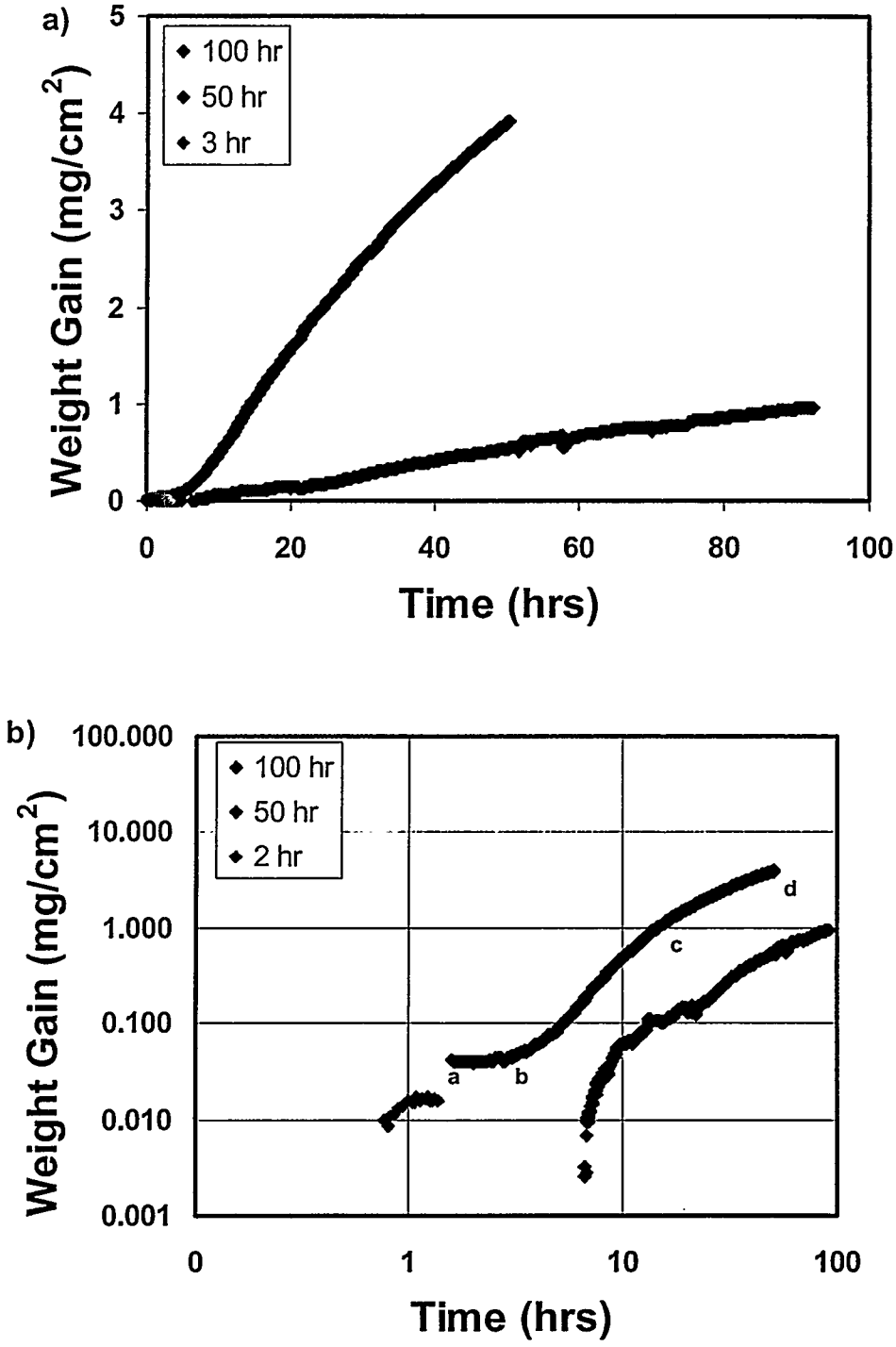

Figure 3.12: Plot of weight gain versus time for Fe-10Al alloys tested at 700°C.

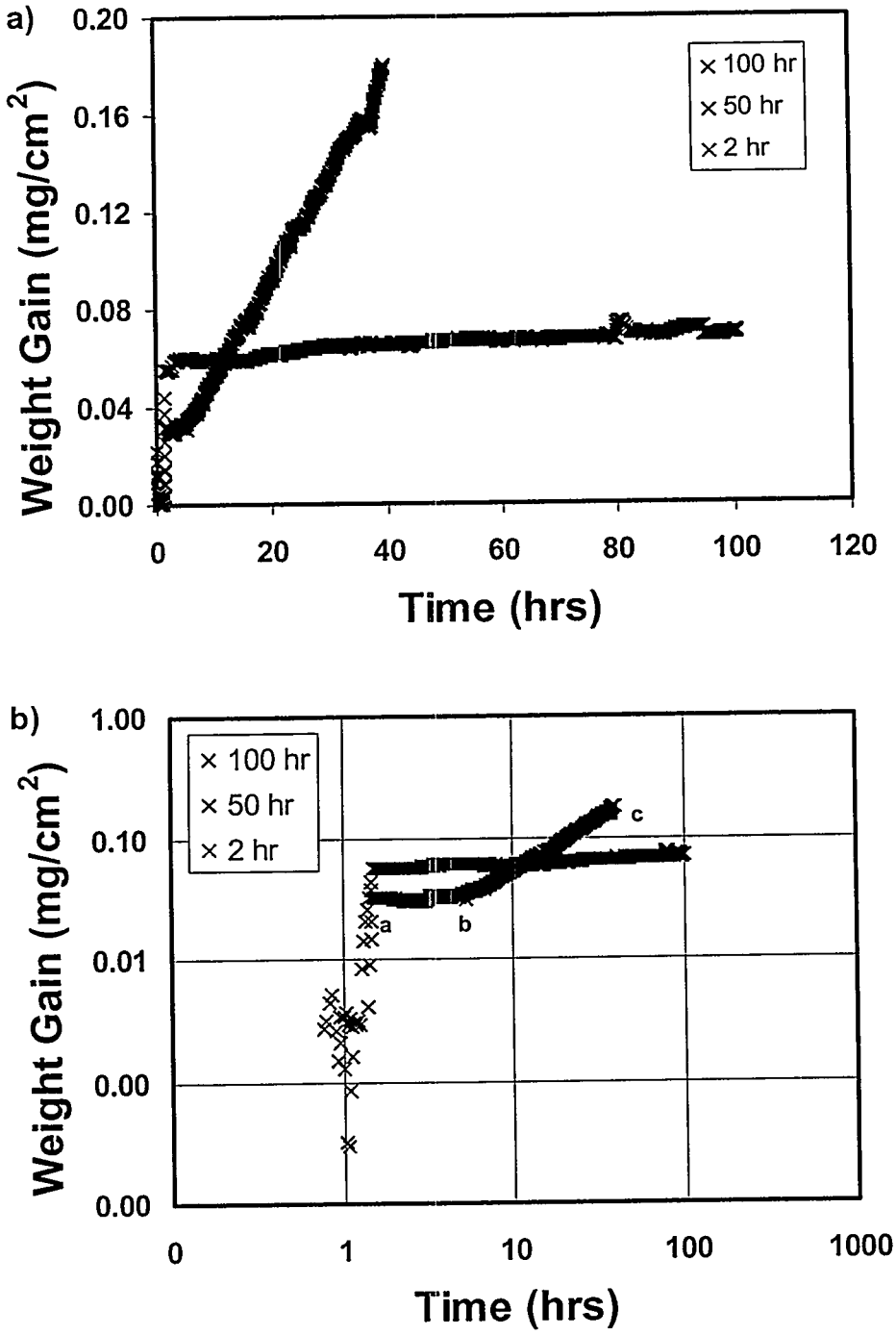

Figure 3.13: Plot of weight gain versus time for Fe-12.5Al alloys tested at 700°C.

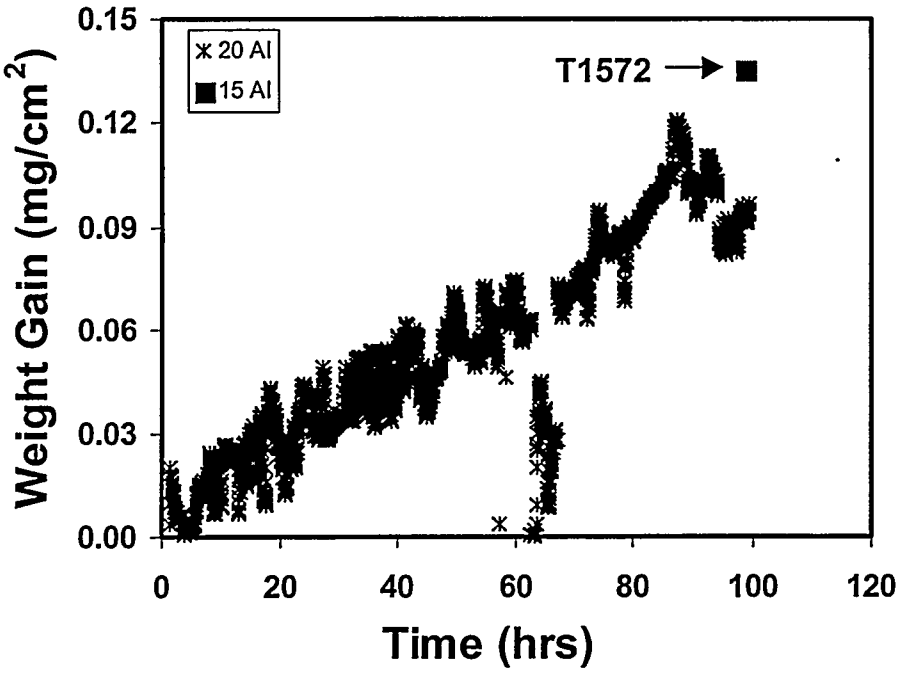

Figure 3.14: Plot of weight gain versus time for Fe-15Al and Fe-20Al alloys tested at 700°C.

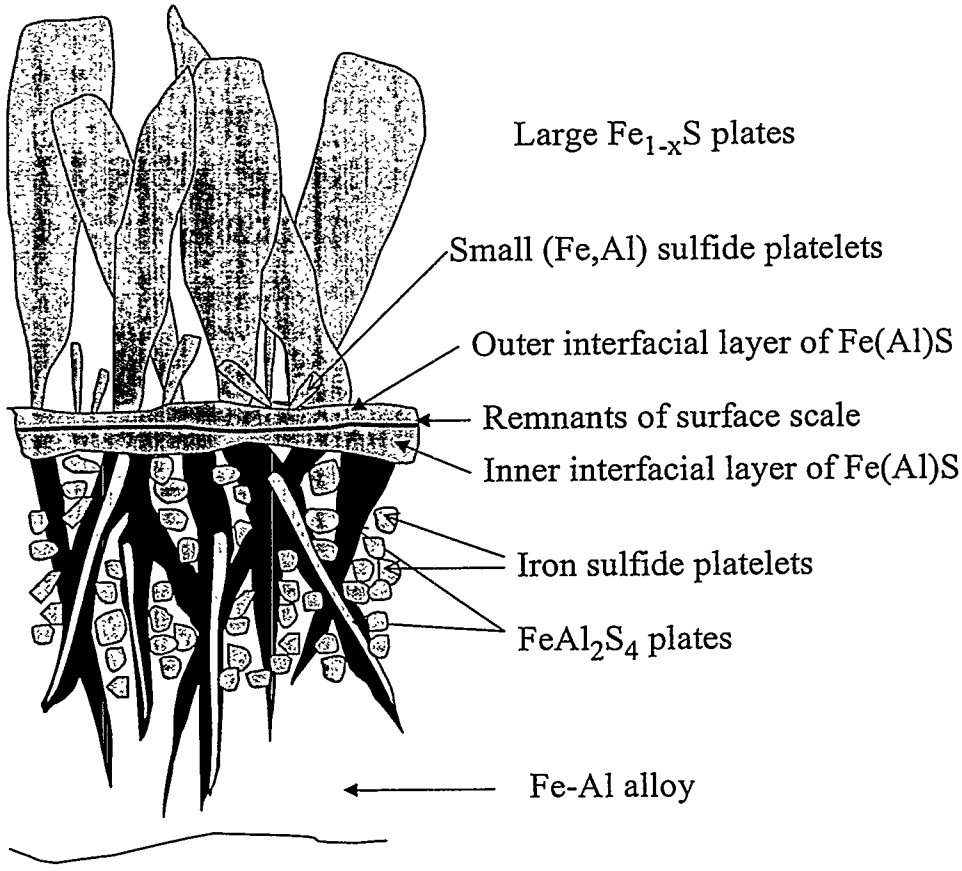

Figure 3.15: Schematic displaying Type I scale development.

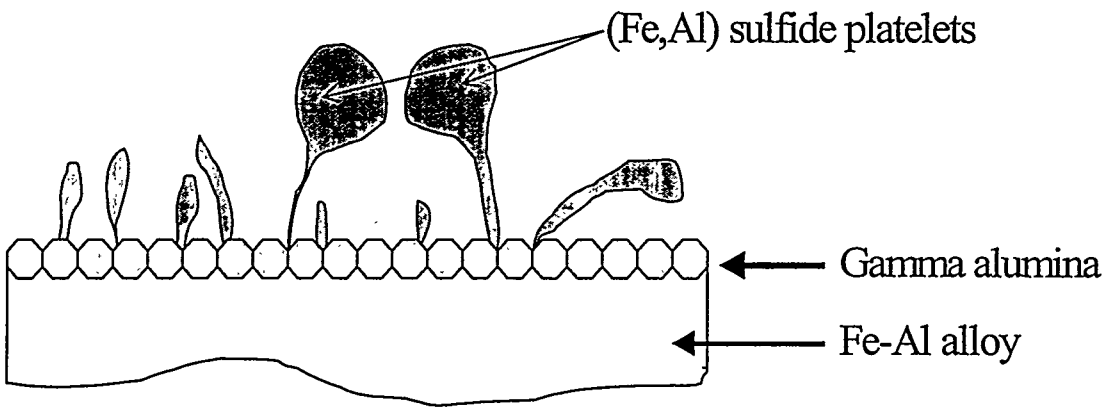

Figure 3.16: Schematic displaying Type II scale development.

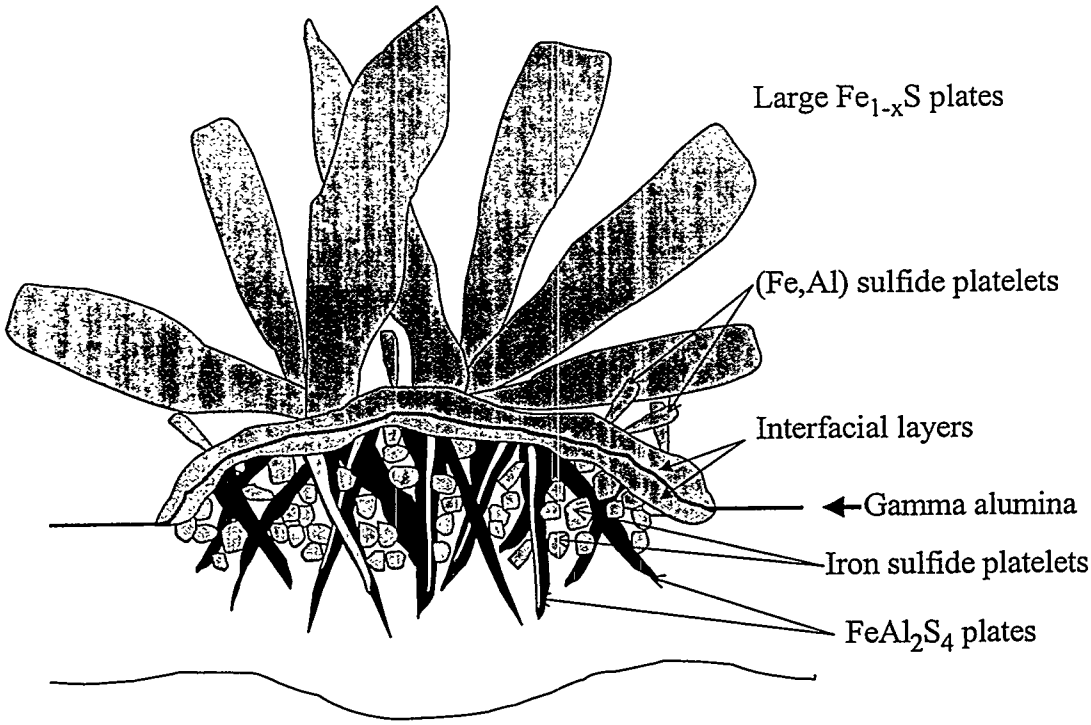

Figure 3.17: Schematic displaying Type III scale development.

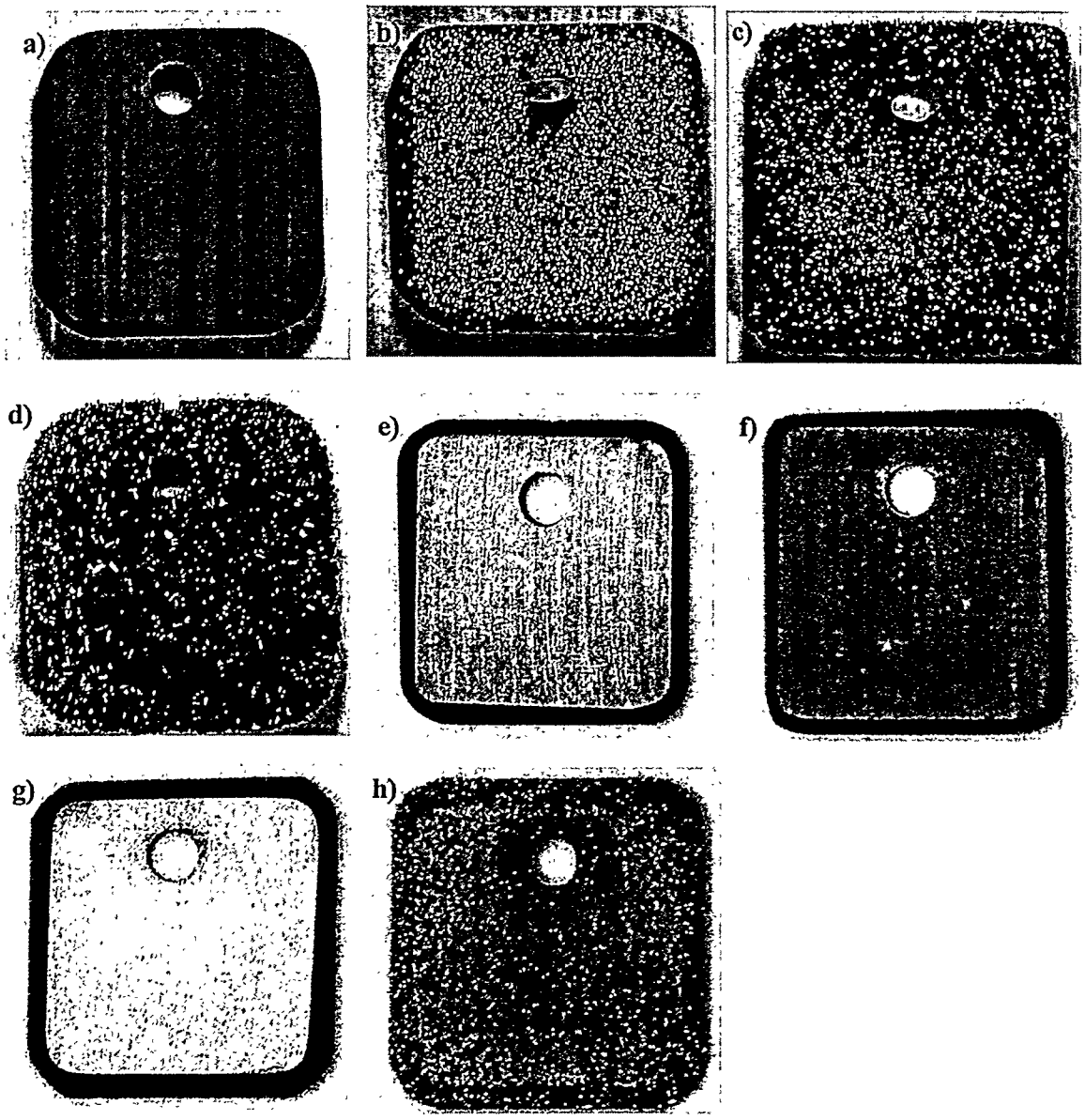

Figure 3.18: Light optical macrographs displaying characteristic surfaces of corroded samples.

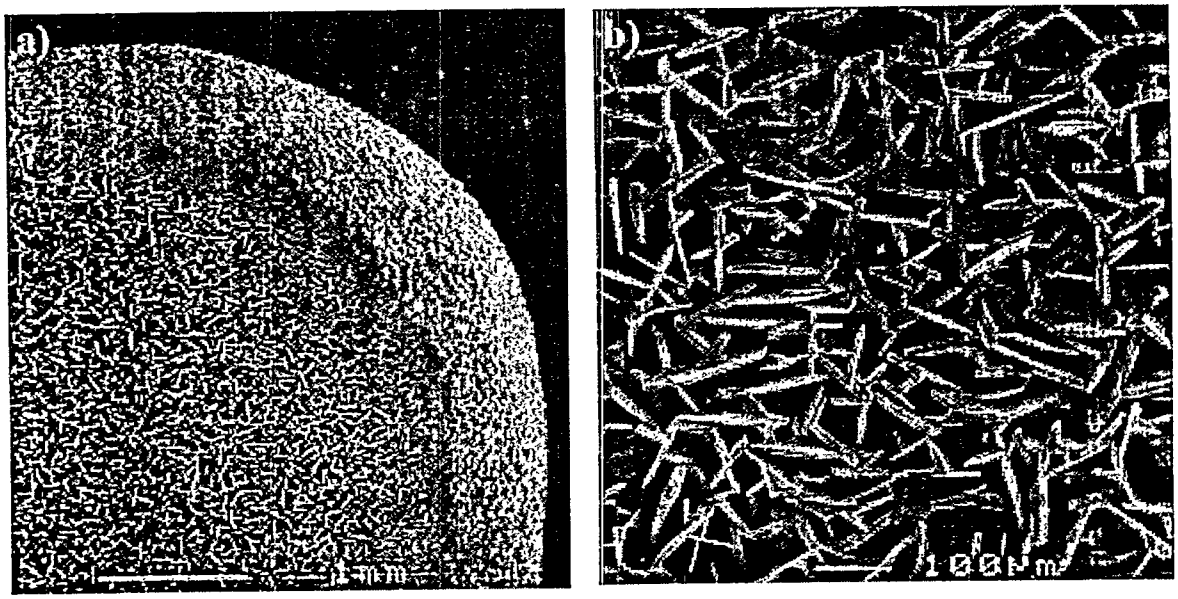

Figure 3.19: SEI micrographs of T052 surface scale. a) 20x, b) 100x

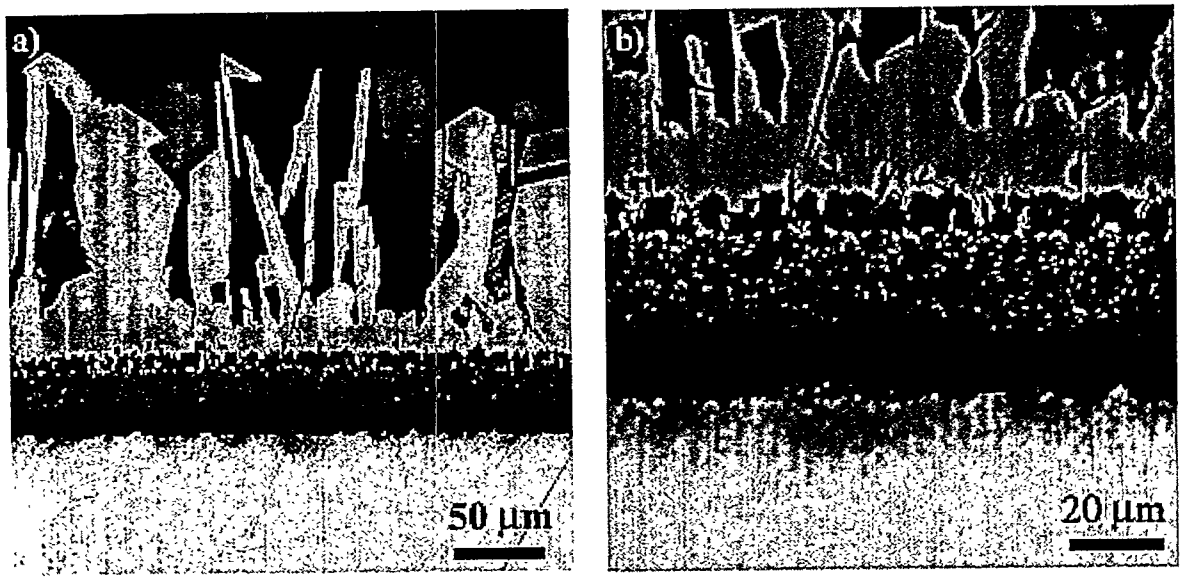

Figure 3.20: Light optical micrographs showing the cross-section of T052.
a) 200x, b) 500x

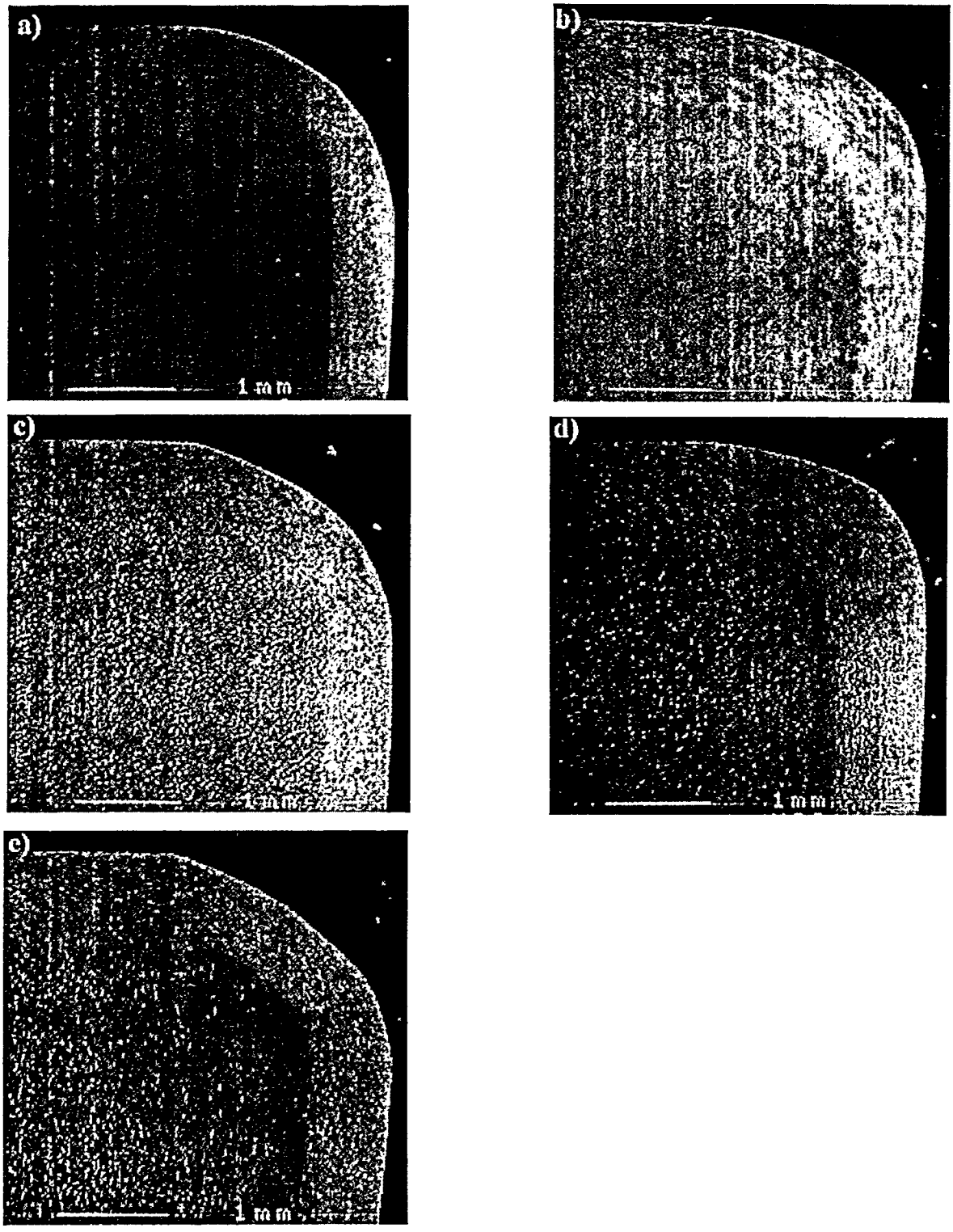

Fiigure 3.21: Low magnification (20x) SEI micrographs of T552 at various times. a) 1 hr, b) 5 hr, c) 15 hr, d) 25 hr, and e) 50 hr.

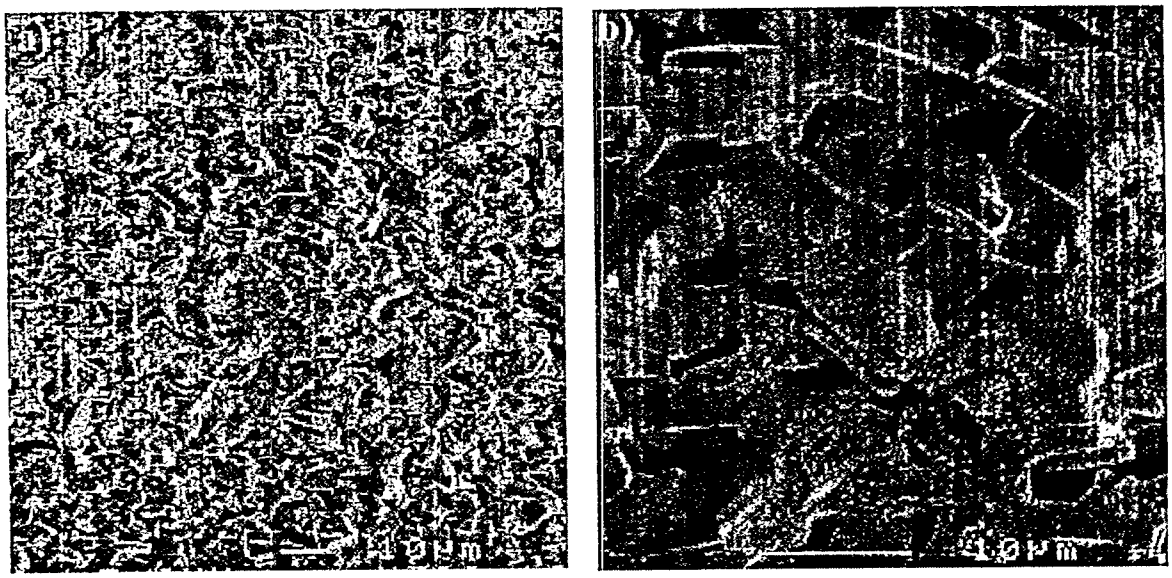

Figure 3.22: SEI micrographs of T552 after 1 hour exposure showing surface scale.
a) 500x, b) 2,000x

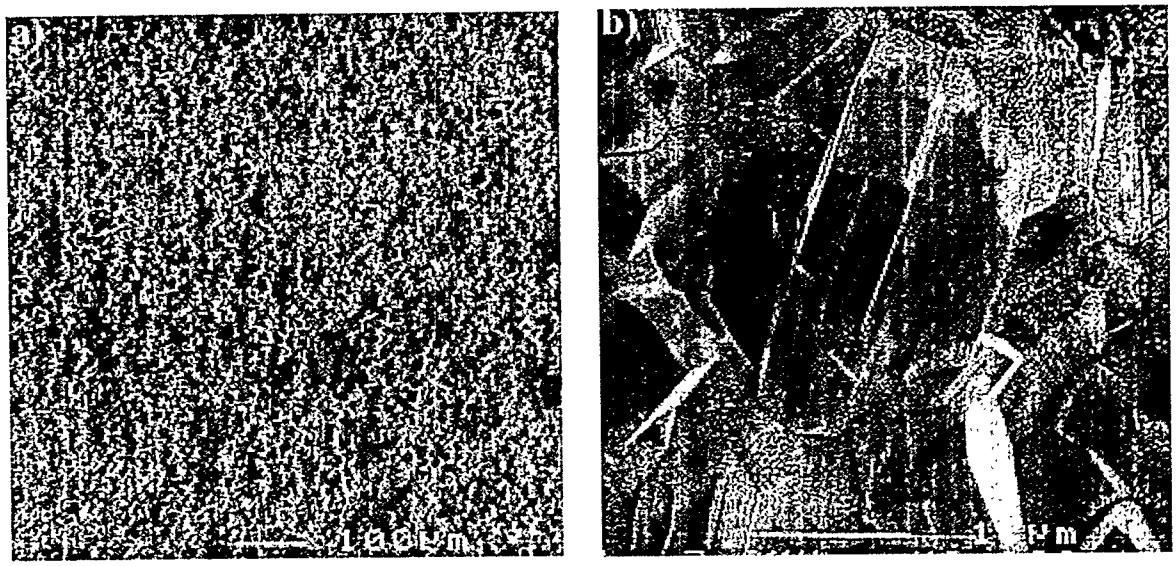

Figure 3.23: SEI micrographs of T552 after 5 hour exposure showing surface scale.
a) 500x, b) 2,000x

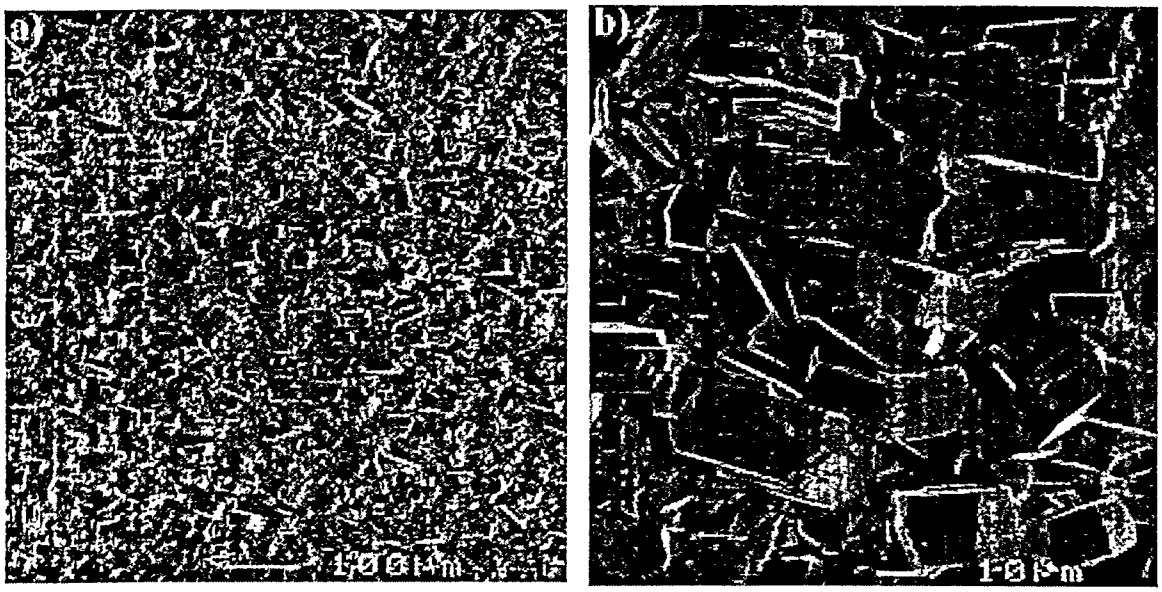

Figure 3.24: SEI micrographs of T552 after 15 hour exposure showing surface scale.
a) 100x, b) 500x

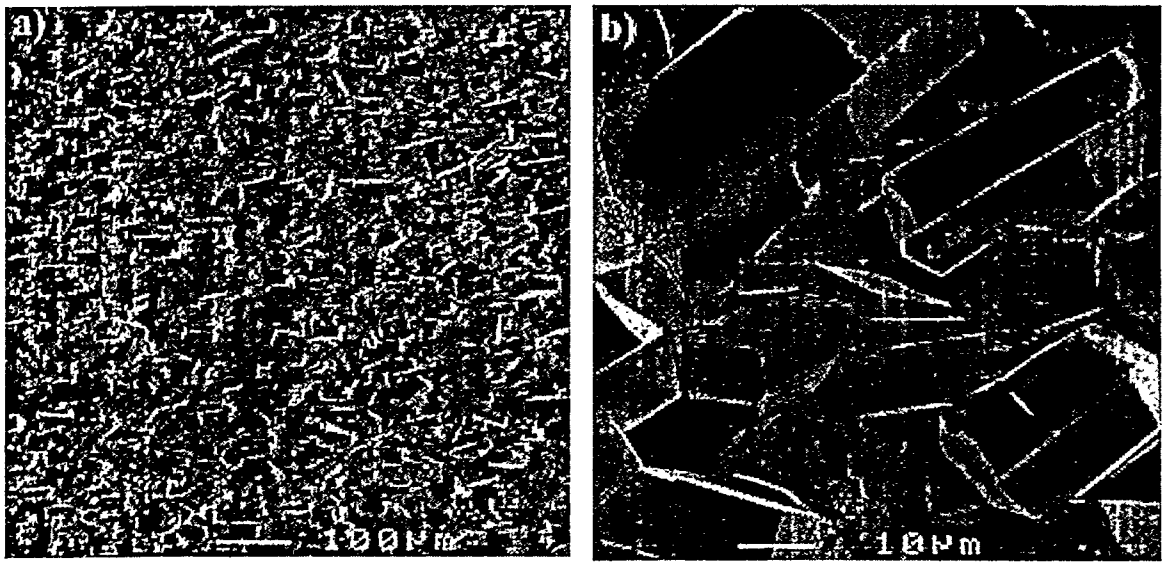

Figure 3.25: SEI micrographs of T552 after 25 hour exposure showing surface scale.
a)100x, b) 1,000x

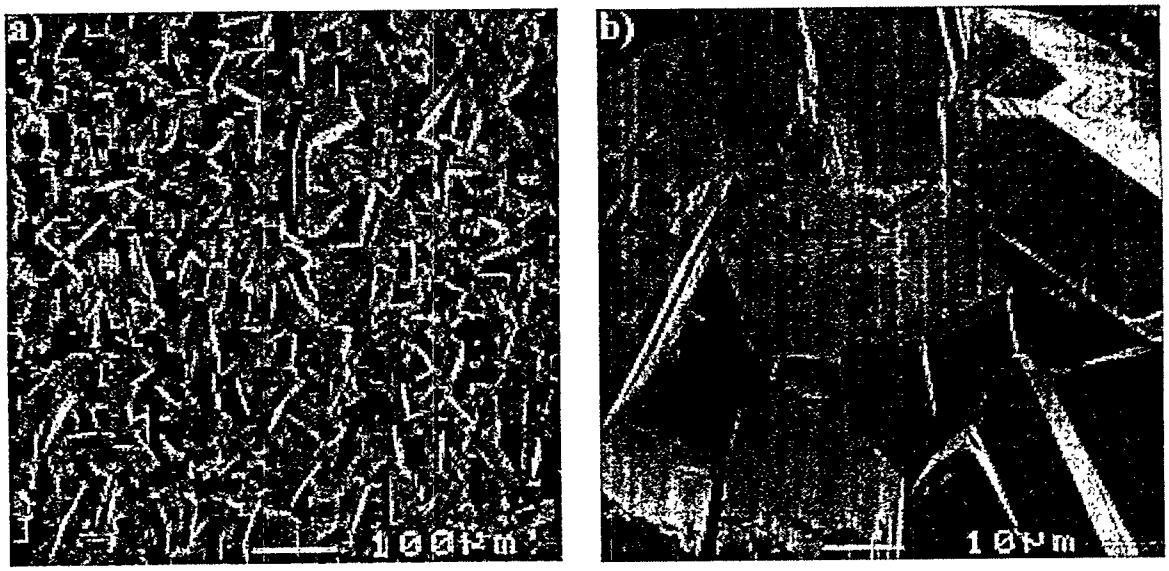

Figure 3.26: SEI micrographs of T552 after 50 hour exposure showing surface scale. a) 100x, b) 1,000x

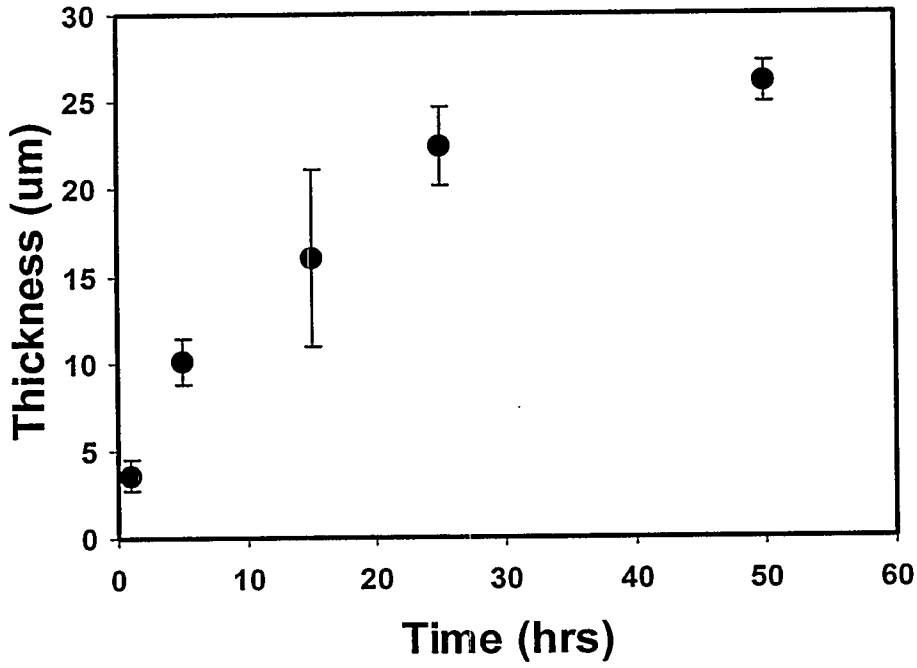

Figure 3.27: Plot of outer FeS plates thickness versus time.

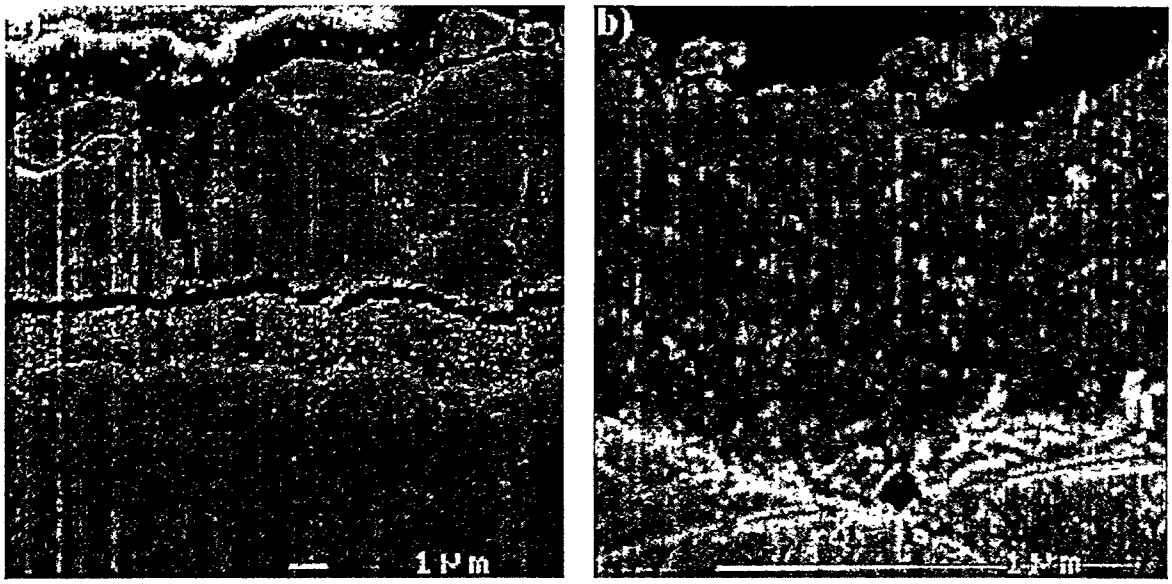

Figure 3.28: SEI micrographs of polished cross-section: T552 after 1 hour exposure.
a) bilayered scale at 5,000x, b) inner scale at 27,000x.

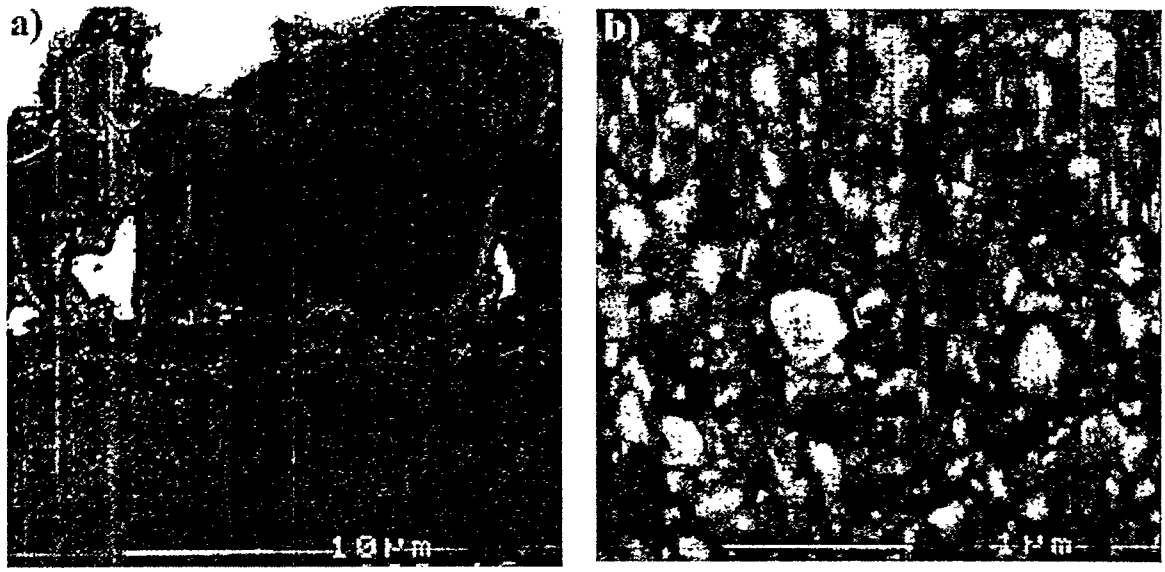

Figure 3.29: SEI micrographs of polished cross-section: T552 after 5 hour exposure.
a) bilayered scale at 2,000x, b) inner scale at 25,000x.

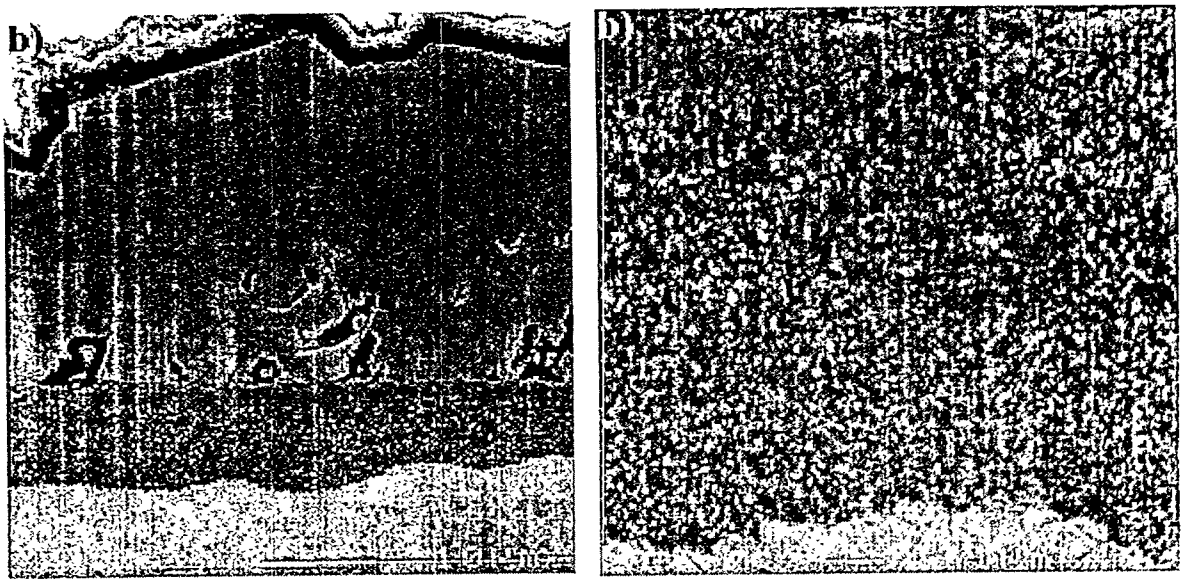

Figure 3.30: SEI micrographs of polished cross-section: T552 after 15 hour exposure. a) bilayered scale at 1,500x, b) inner scale at 7,500x.

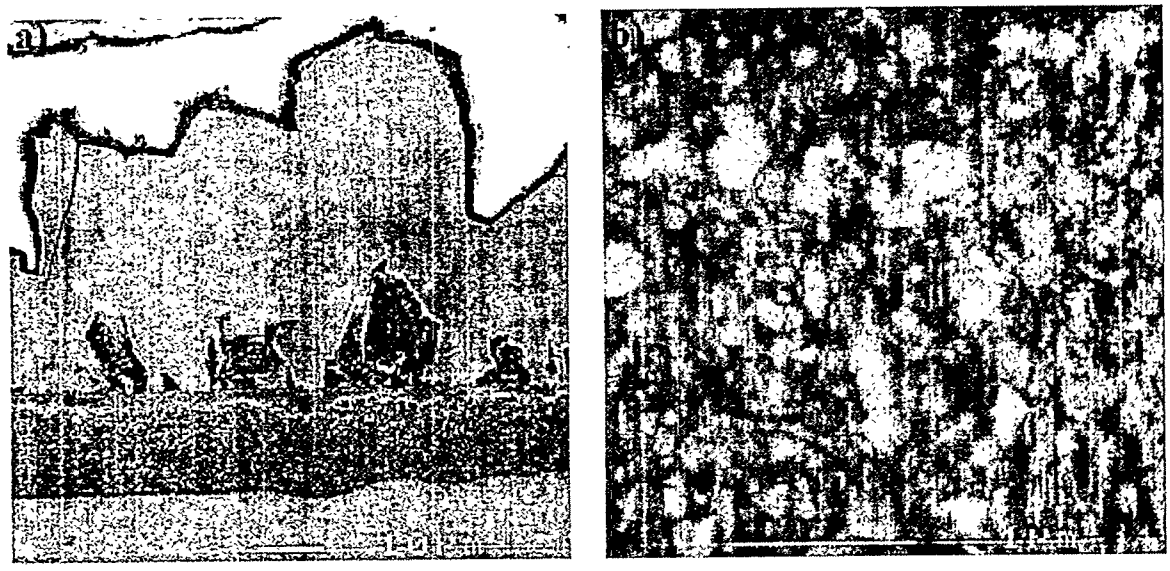

Figure 3.31: SEI micrographs of polished cross-section: T552 after 25 hour exposure. a) bilayered scale at 1,000x, b) inner scale at 25,000x.

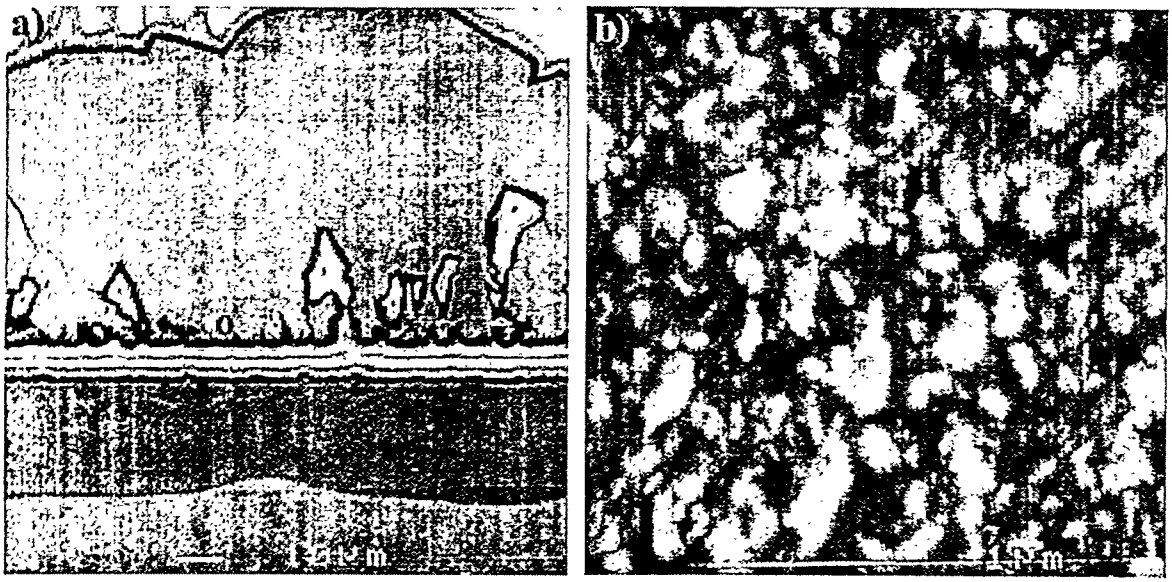

Figure 3.32: SEI micrographs of polished cross-section: T552 after 50 hour exposure. a) bilayered scale at 600x, b) inner scale at 25,000x.

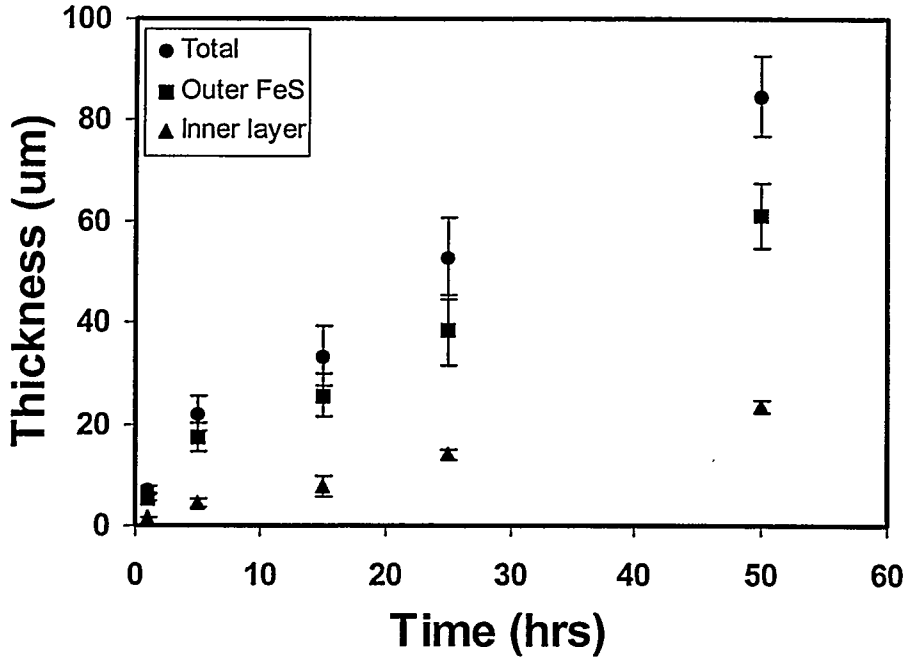

Figure 3.33: Plot of scale cross-sectional thickness versus time for T552 samples.

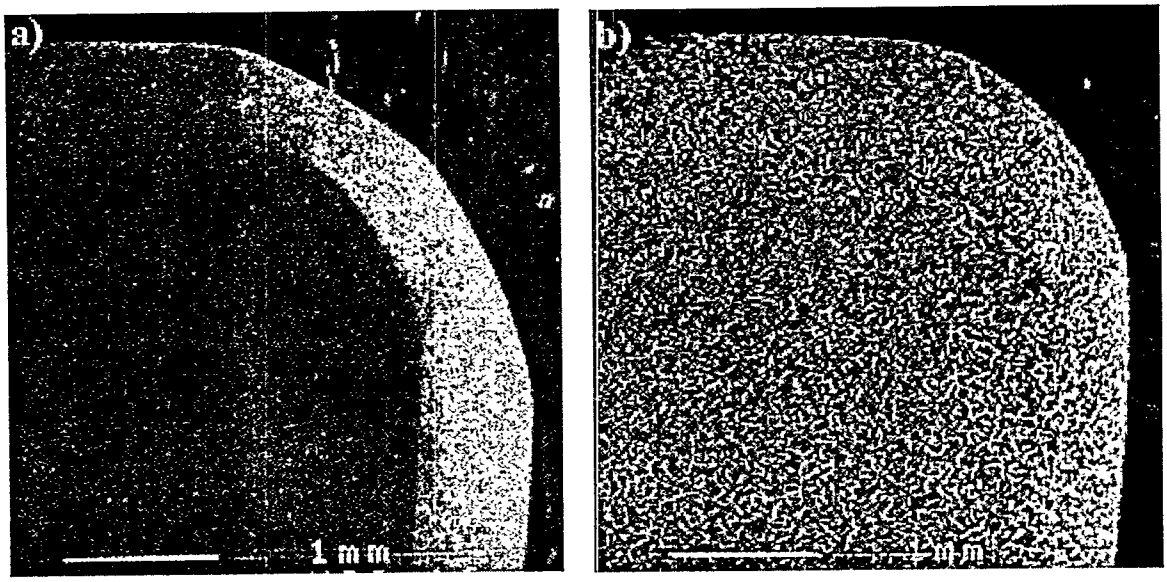

Figure 3.34: Low magnifications (20x) SEI micrograph of T7.552 at various times
a) 50 hrs, b) 100hrs

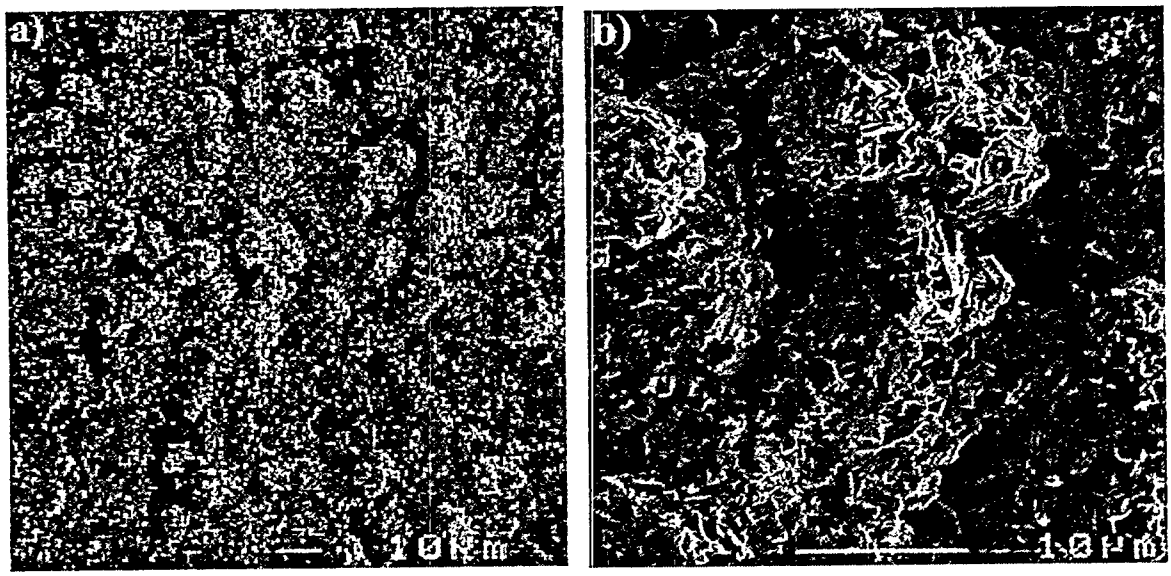

Figure 3.35: SEI micrographs of T7.552 after 50 hour exposure showing surface scale.
a)500x, b) 2,000x

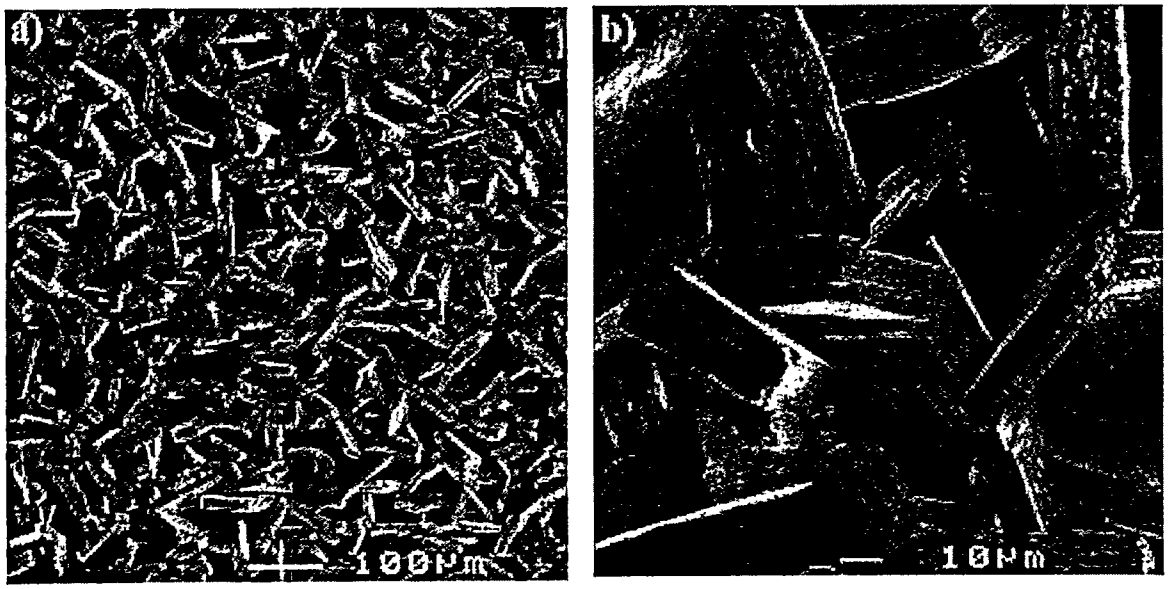

Figure 3.36: SEI micrographs of T7.552 after 100 hour exposure showing surface scale.
a) 100x, b) 500x

Figure 3.37: SEI micrographs of polished cross-section: T7.552 after 50 hour exposure.
a) bilayered scale at 3,000x, b) inner scale at 10,000x

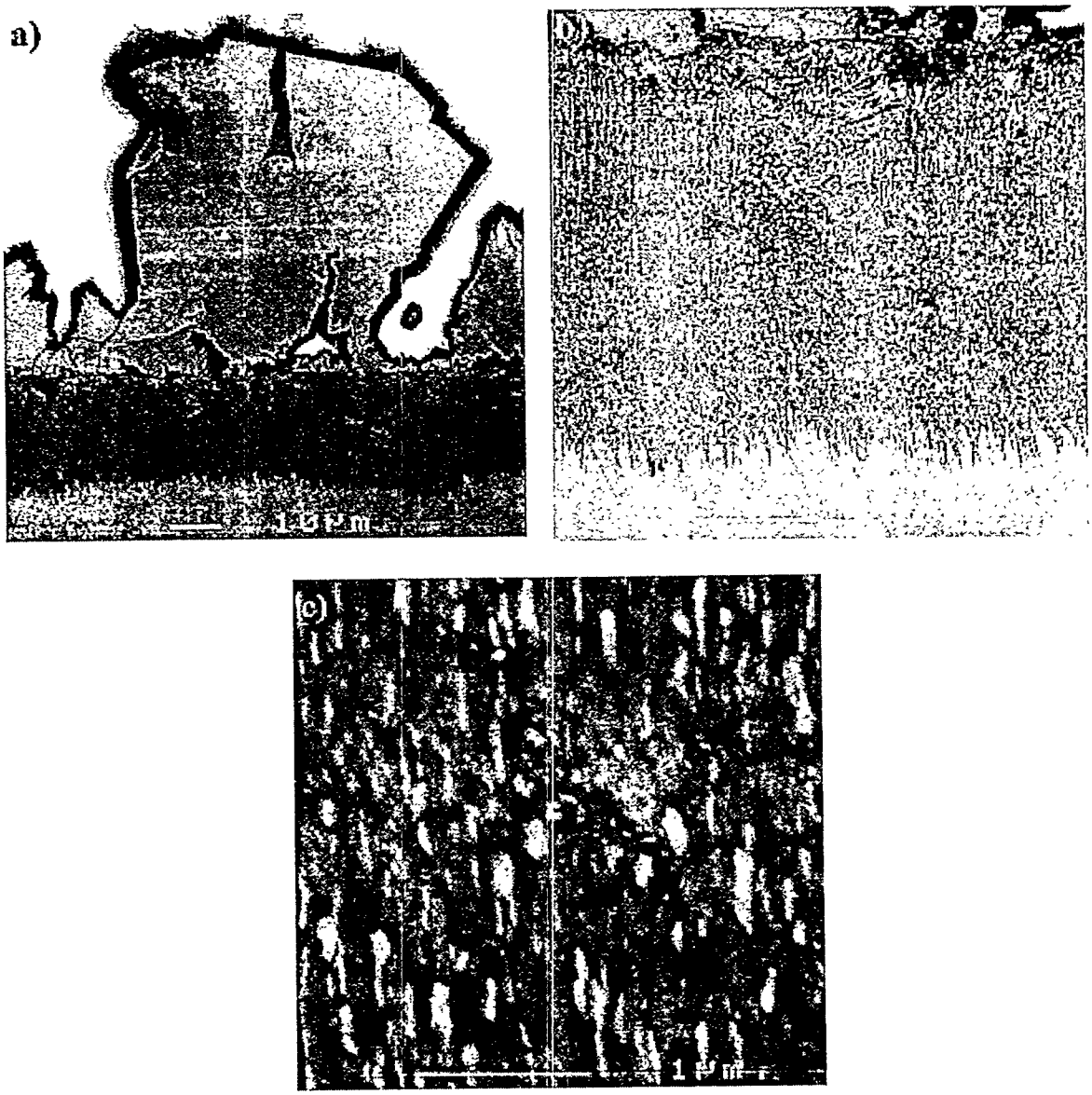

Figure 3.38: SEI micrograph of polished cross-section: T7.552 after 100 hour exposure. a) bilayered scale at 700x and inner scale at b) 2,700x, c) 25,000x

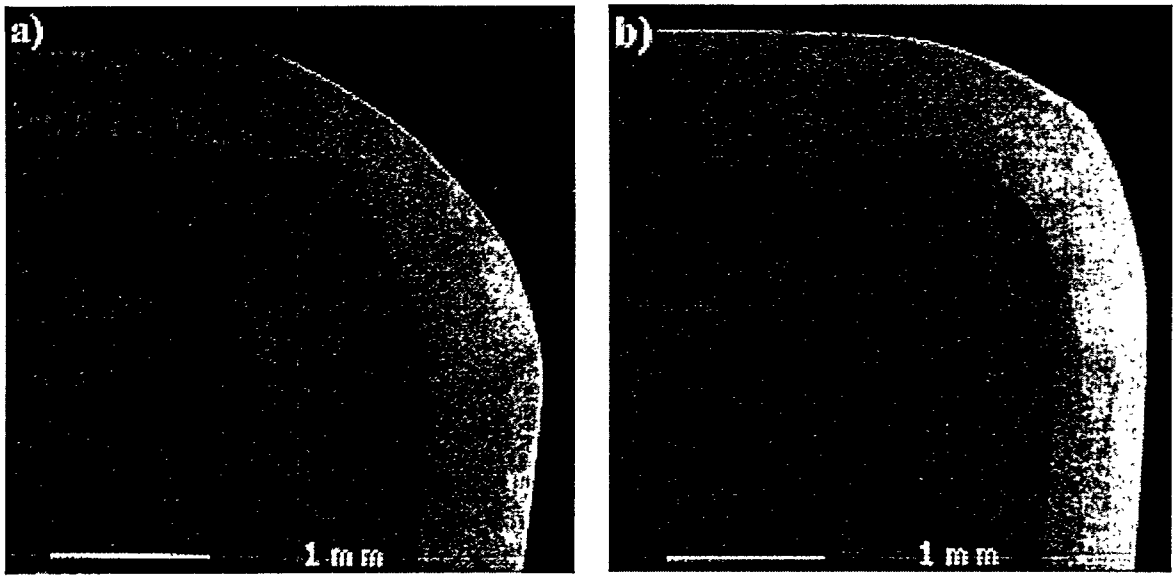

Figure 3.39: Low magnification (20x) SEI micrographs of a) T1052 and b) T12.552.

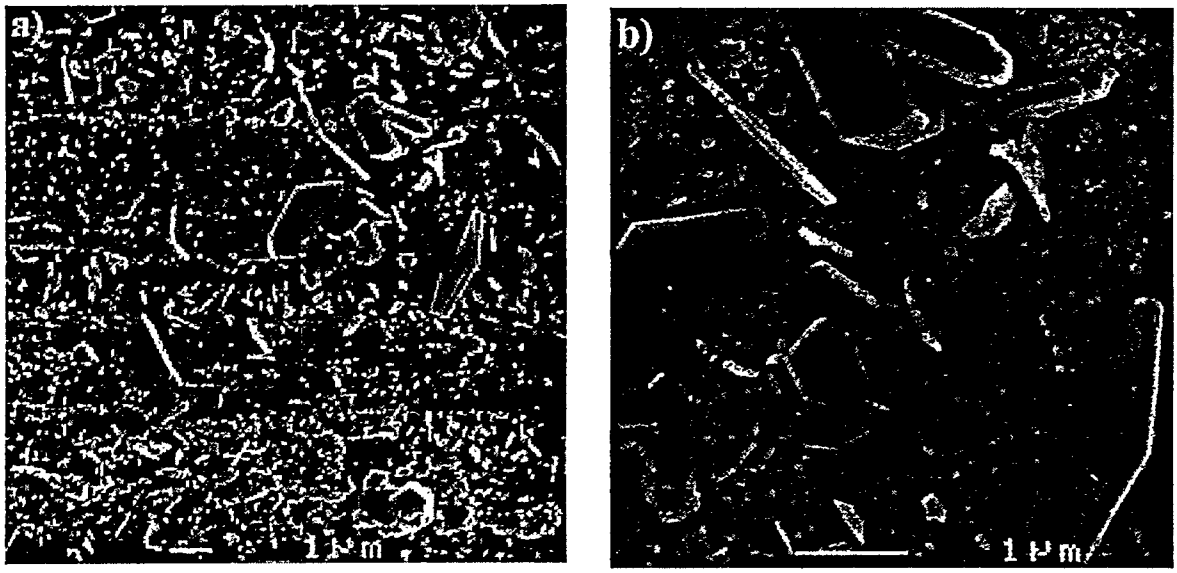

Figure 3.40: SEI micrographs of T1052 showing surface scale. a) 5,000x, b) 14,000x

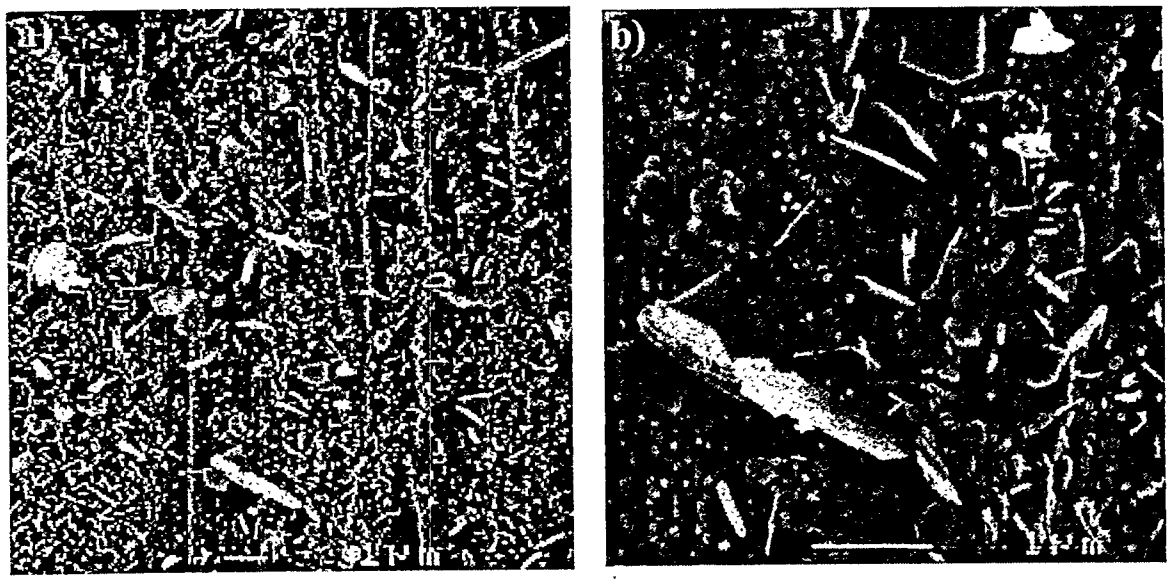

Figure 3.41: SEI micrographs of T12.552 showing surface scale. a) 5,000x, b) 15,000x

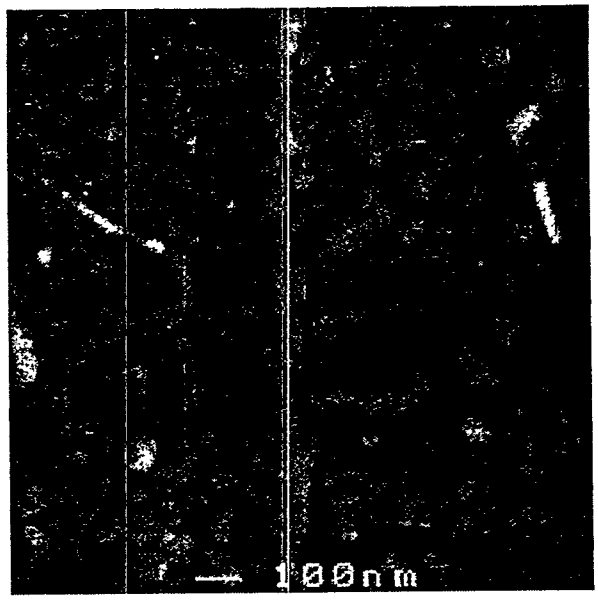

Figure 3.42: SEI micrograph of granular scale that was found on T1052 and T12.552 (50,000x)

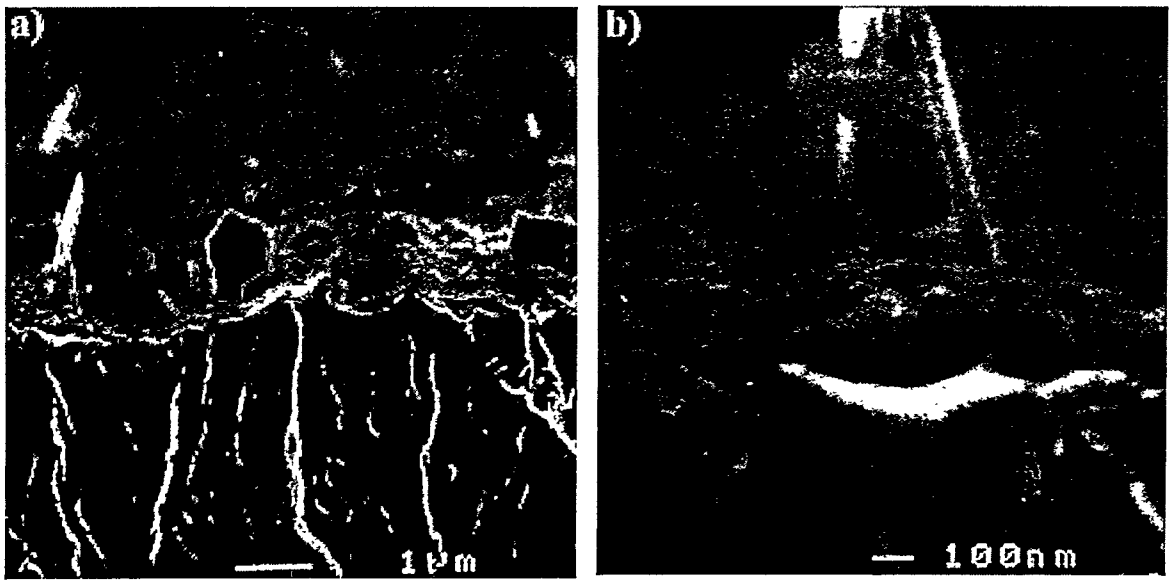

Figure 3.43: SEI micrograph showing fractured cross-section typical of T1052 and T12.552.

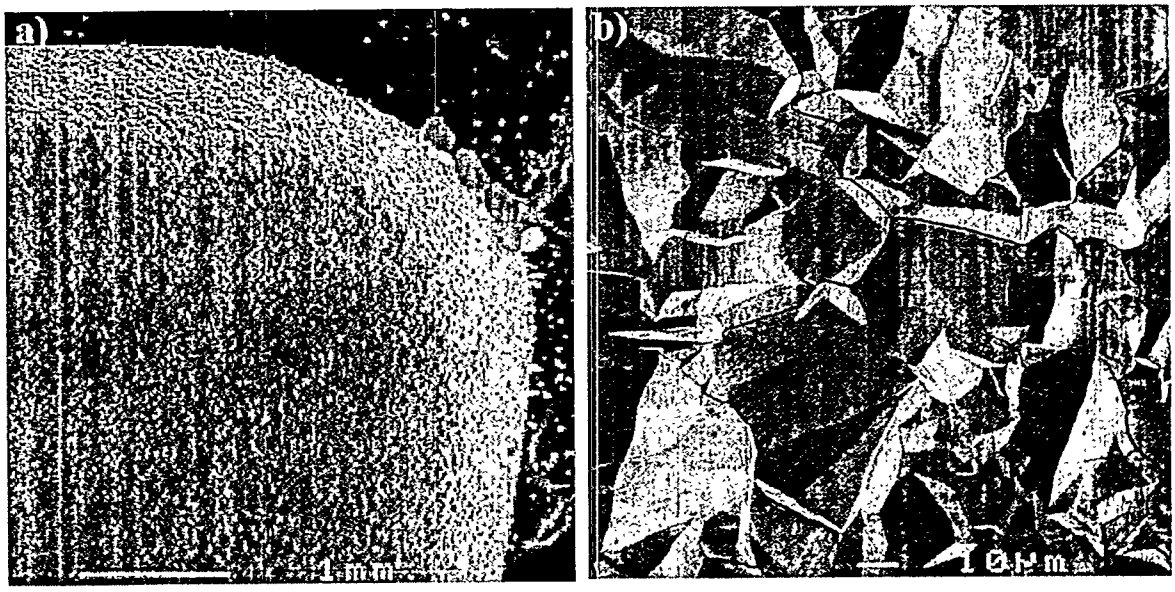

Figure 3.44: SEI micrographs of T062 surface scale. a) 20x, b) 500x

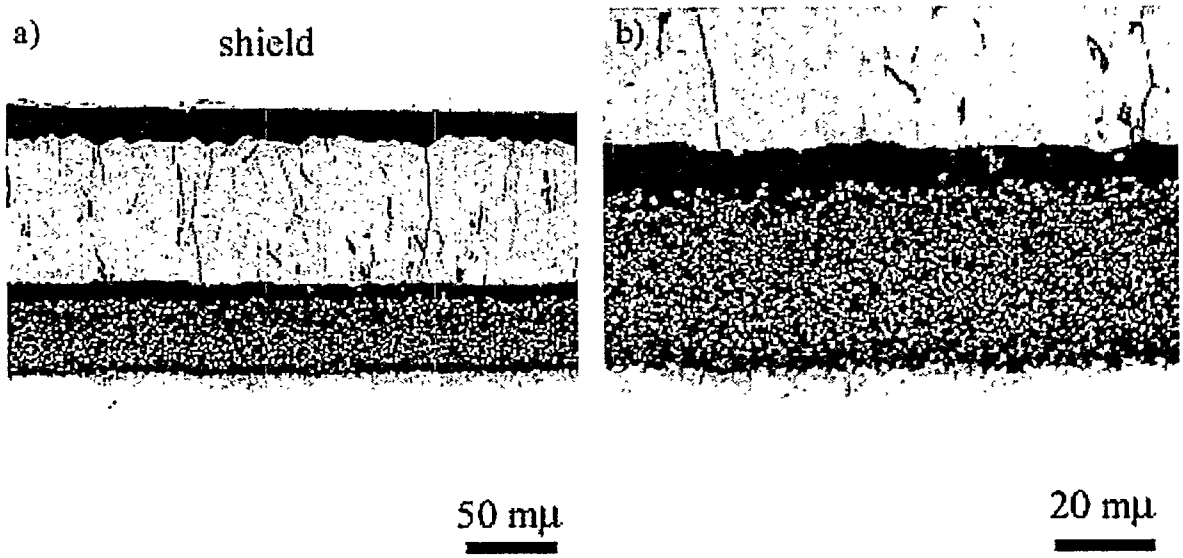

Figure 3.45: Light optical micrographs showing the cross-section of T062.
a) 200x, b) 500x

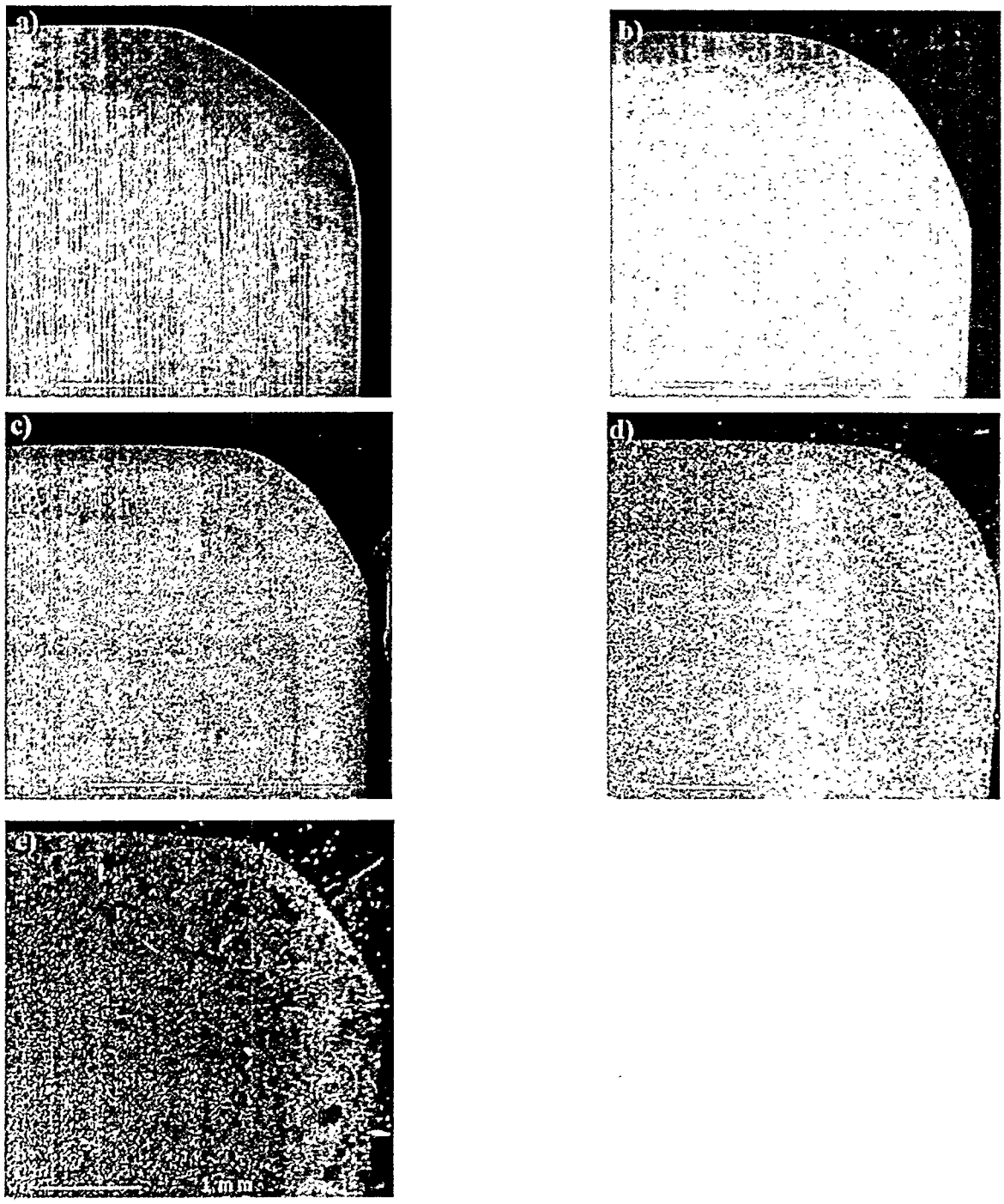

Figure 3.46: Low magnification (20x) SEI micrographs of T562 at various times. a) 1hr, b) 5 hr, c) 15 hr, d) 30 hr, and e) 50hr

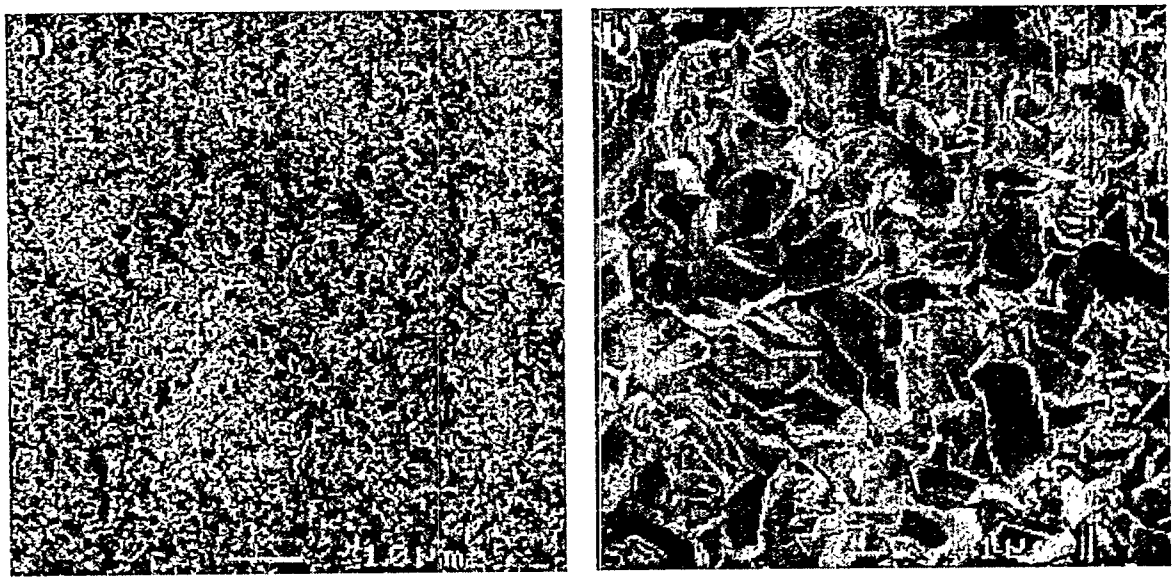

Figure 3.47: SEI micrographs of T562 after 1 hour exposure showing surface scale.
a) 1,000x, b) 5,000x

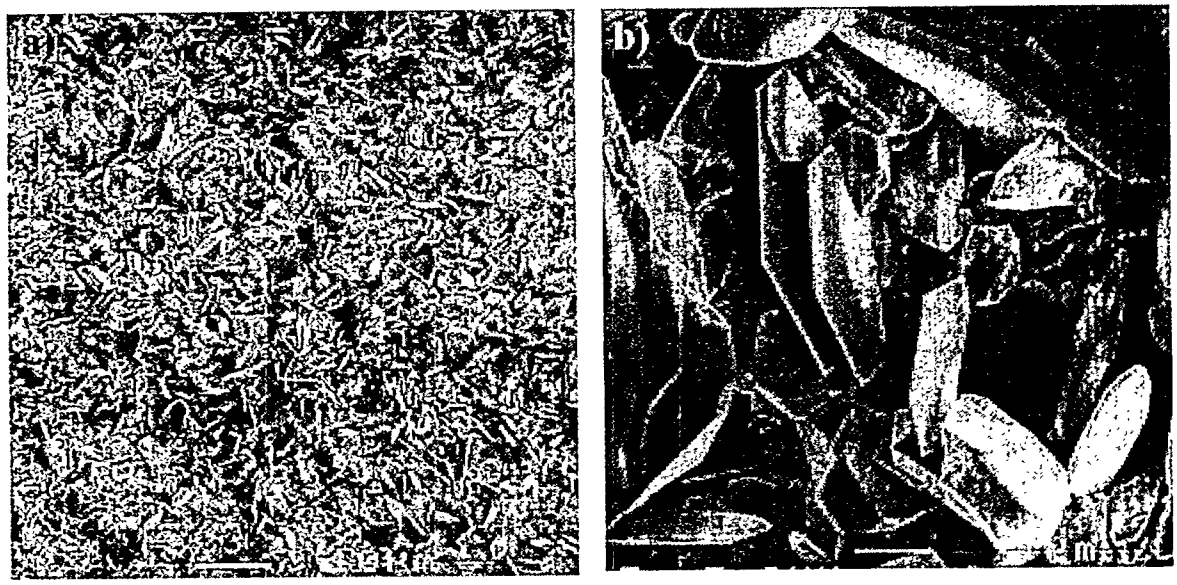

Figure 3.48: SEI micrographs of T562 after 5 hour exposure showing surface scale.
a) 1,000x, b) 10,000x

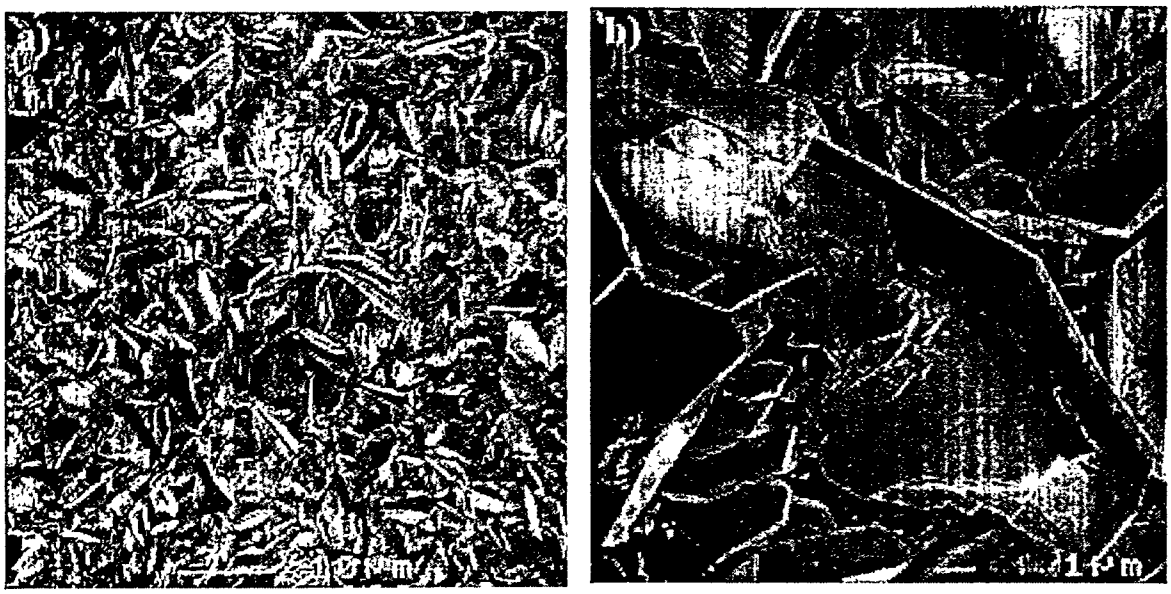

Figure 3.49: SEI micrographs of T562 after 15 hour exposure showing surface scale.
a) 1,000x, b) 5,000x

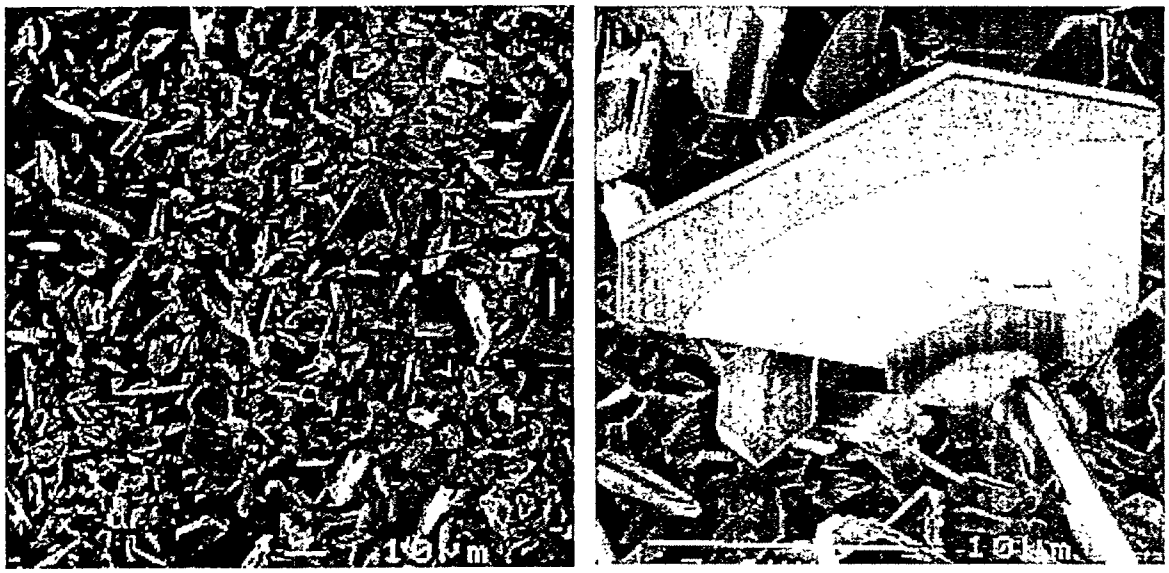

Figure 3.50: SEI micrographs of T562 after 30 hour exposure showing surface scale.
a) 500x, b) 3,500x

Figure 3.51: SEI micrographs of T562 after 50 hour exposure showing surface scale.
a) 500x, b) 1,000x

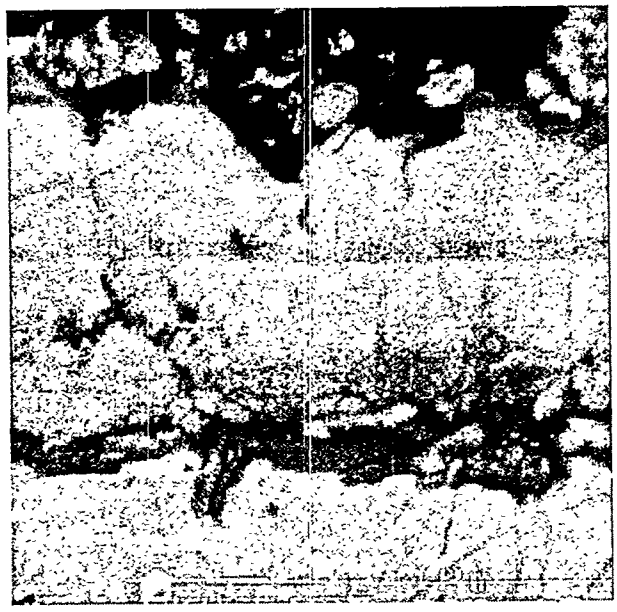

Figure 3.52: SEI micrograph of polished cross-section: T562 after 1 hour exposure. 25,000x

Figure 3.53: SEI micrograph of polished cross-section: T562 after 5 hour exposure. 10,000x

Figure 3.54: SEI micrographs of polished cross-section: T562 after 15 hour exposure.
a) bilayered scale at 5,000x, b) inner scale at 25,000x.

Figure 3.55: SEI micrographs of polished cross-section: T562 after 30 hour exposure.
a) bilayered scale at 19,000x, b) inner scale at 15,000x.

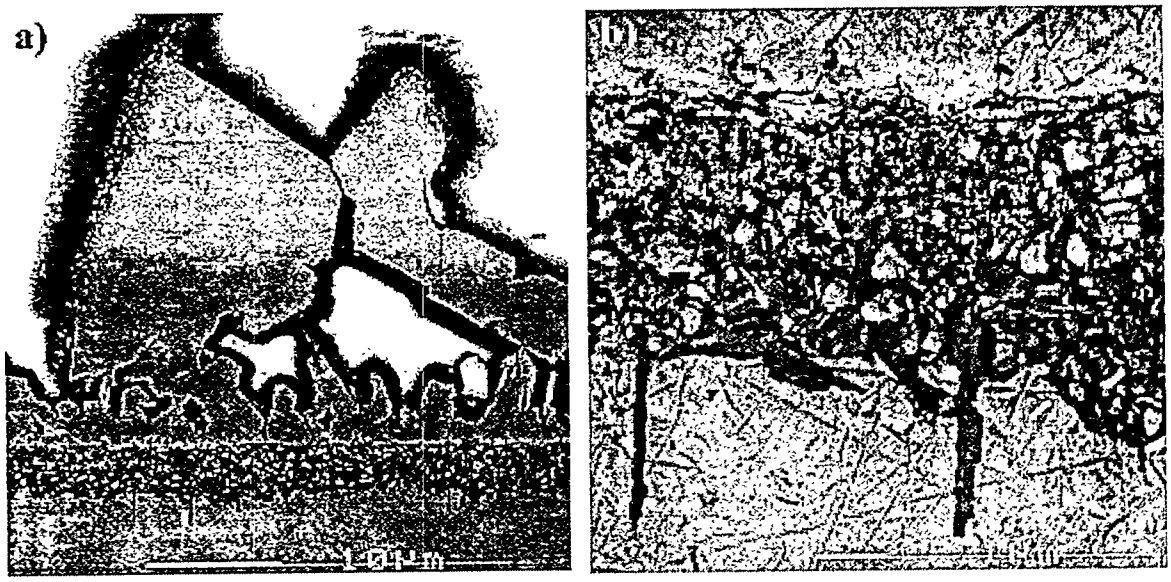

Figure 3.56: SEI micrographs of polished cross-section: T562 after 50 hour exposure.
a) bilayered scale at 1,800x, b) inner scale at 10,000x.

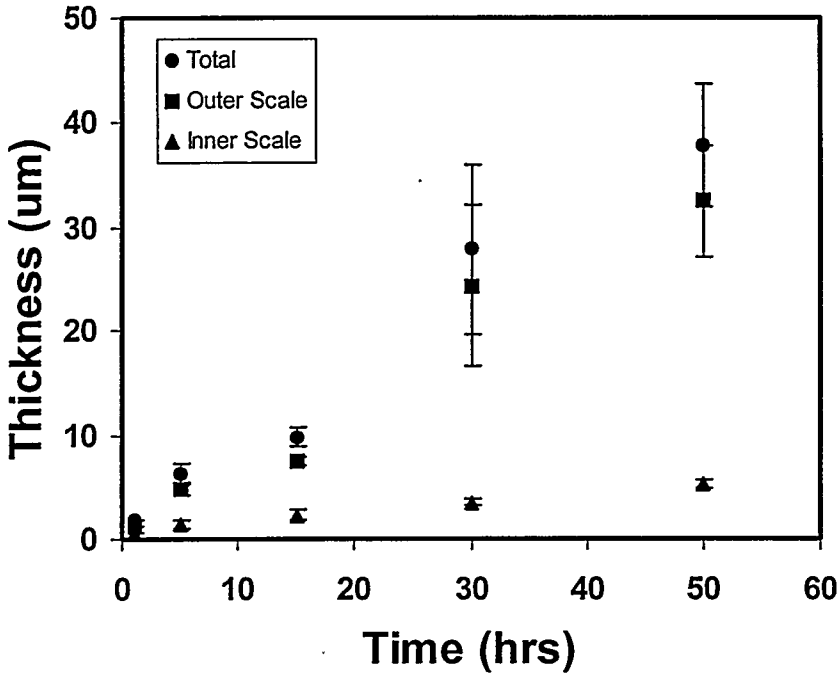

Figure 3.57: Plot of scale cross-sectional thickness versus time for T562 samples.

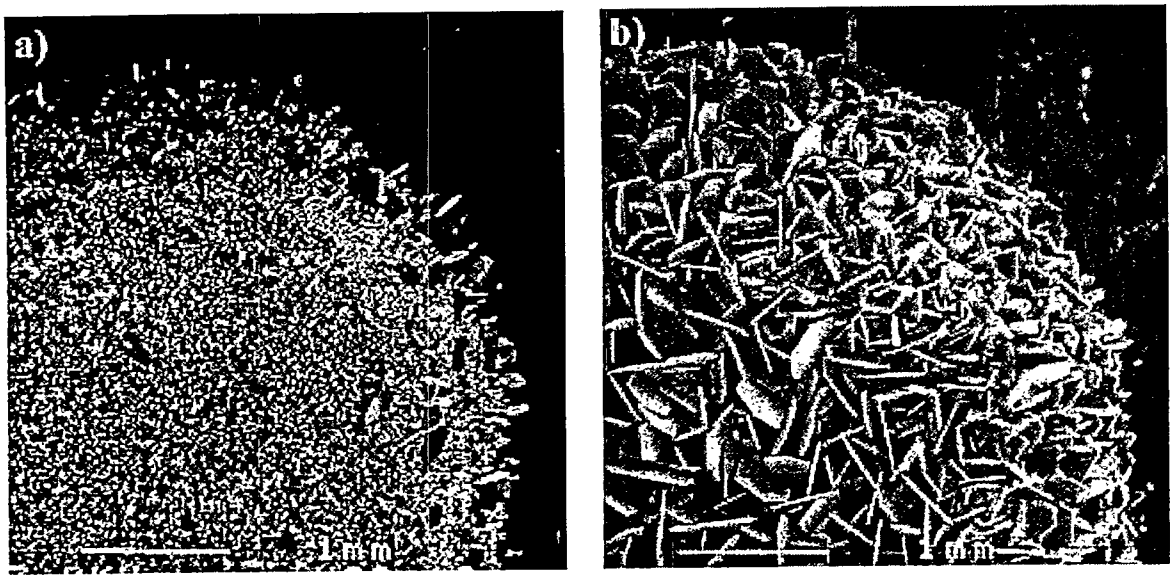

Figure 3.58: Low magnification (20x) SEI micrographs of T7.562 at various times.
a) 50 hrs, b) 100hrs

Figure 3.59: SEI micrographs of T7.562 after 50 hour exposure showing surface scale.
a) 100x, b) 500x

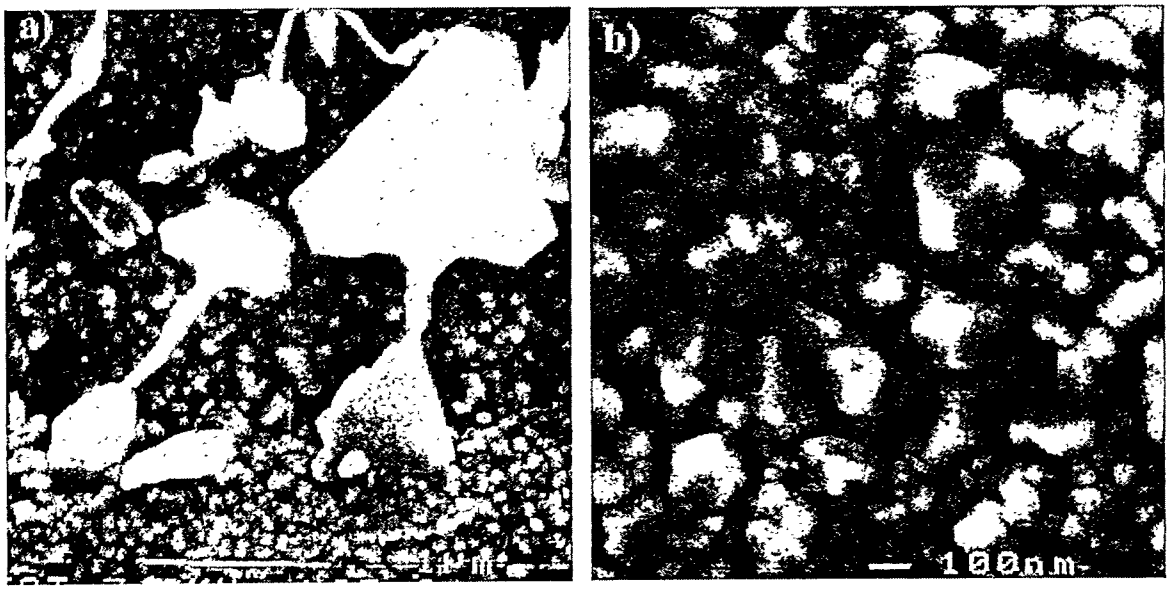

Figure 3.60: SEI micrographs of T7.562 after 50 hour exposure showing granular surface scale. a) 25,000x, b) 50,000x

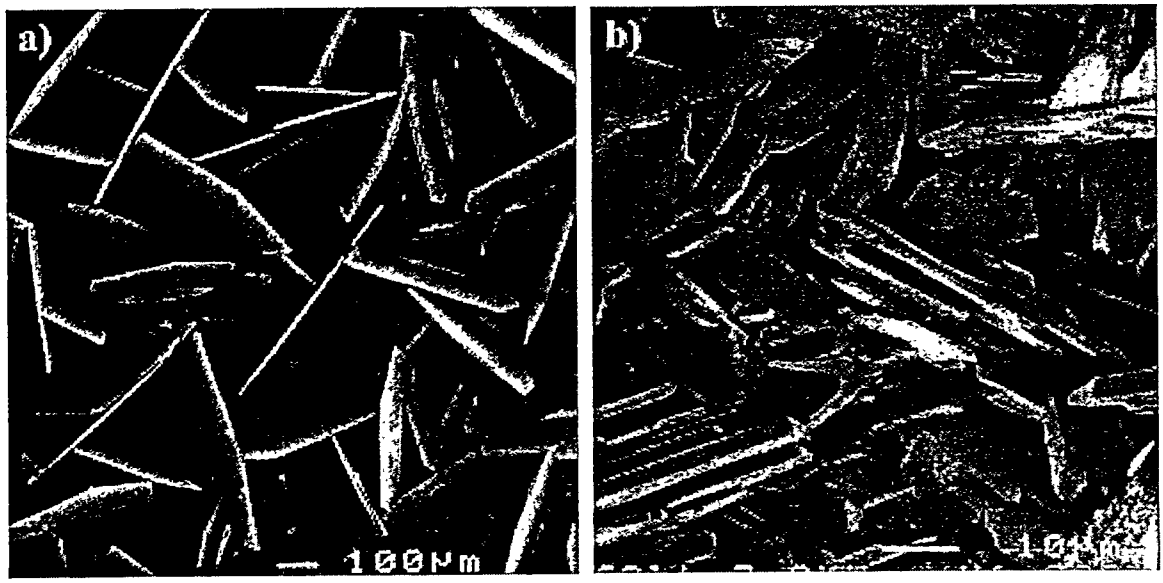

Figure 3.61: SEI micrographs of T7.562 after 100 hour exposure showing surface scale. a) 50x, b) 1,000x

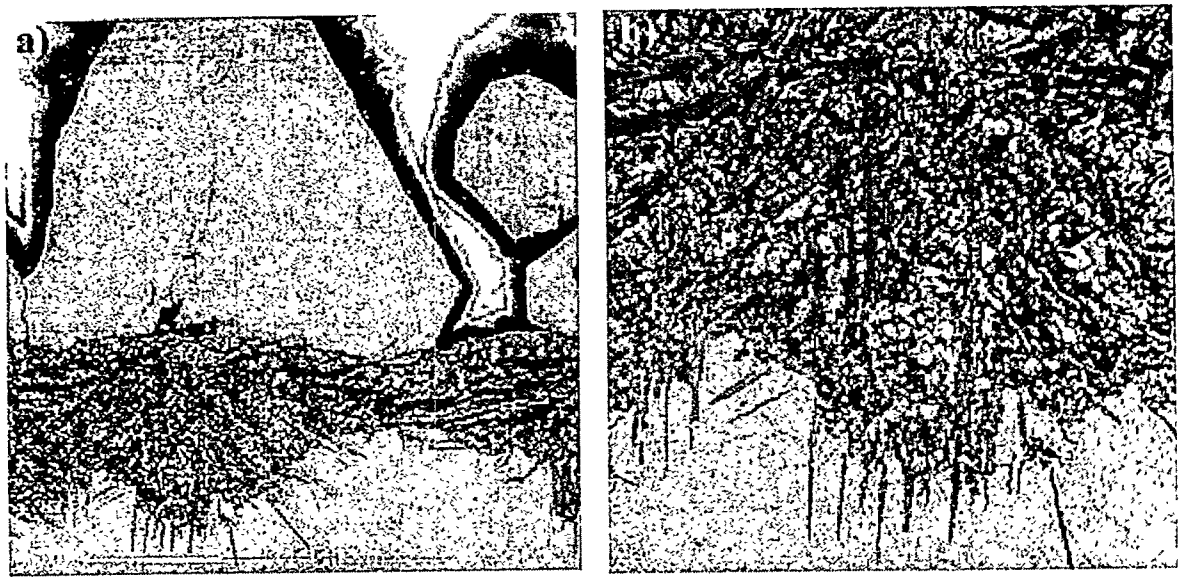

Figure 3.62: SEI micrographs of polished cross-section: T7.562 after 50 hour exposure.
a) bilayered scale at 1,800x, b) inner scale at 4,500x.

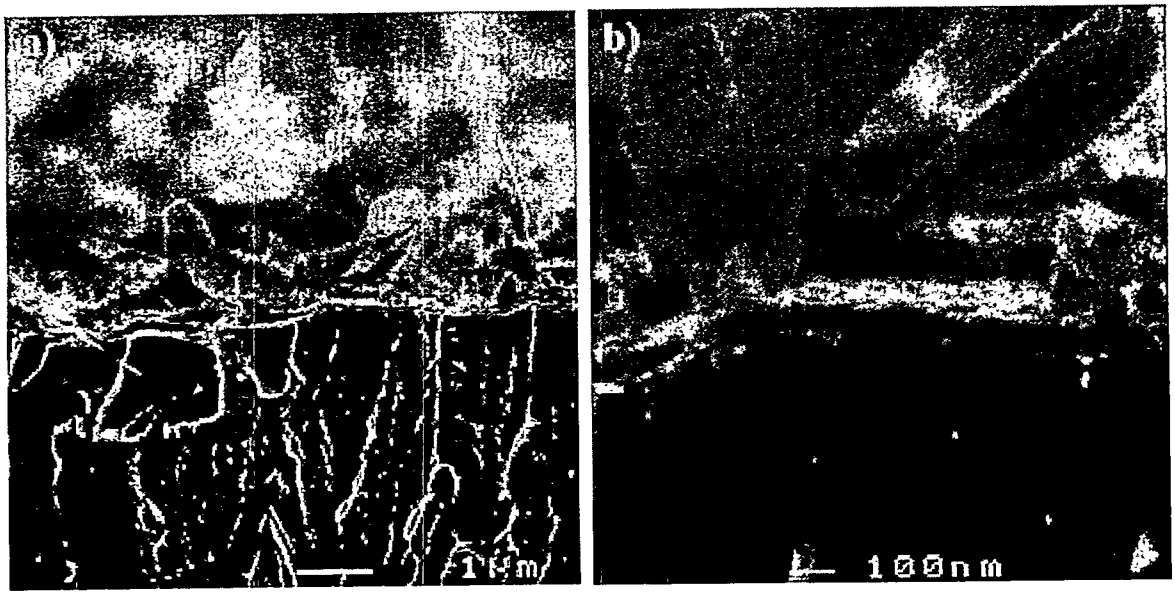

Figure 3.63: SEI micrographs showing fractured cross-section of T7.562.
a) 10,000x, b) 55,000x

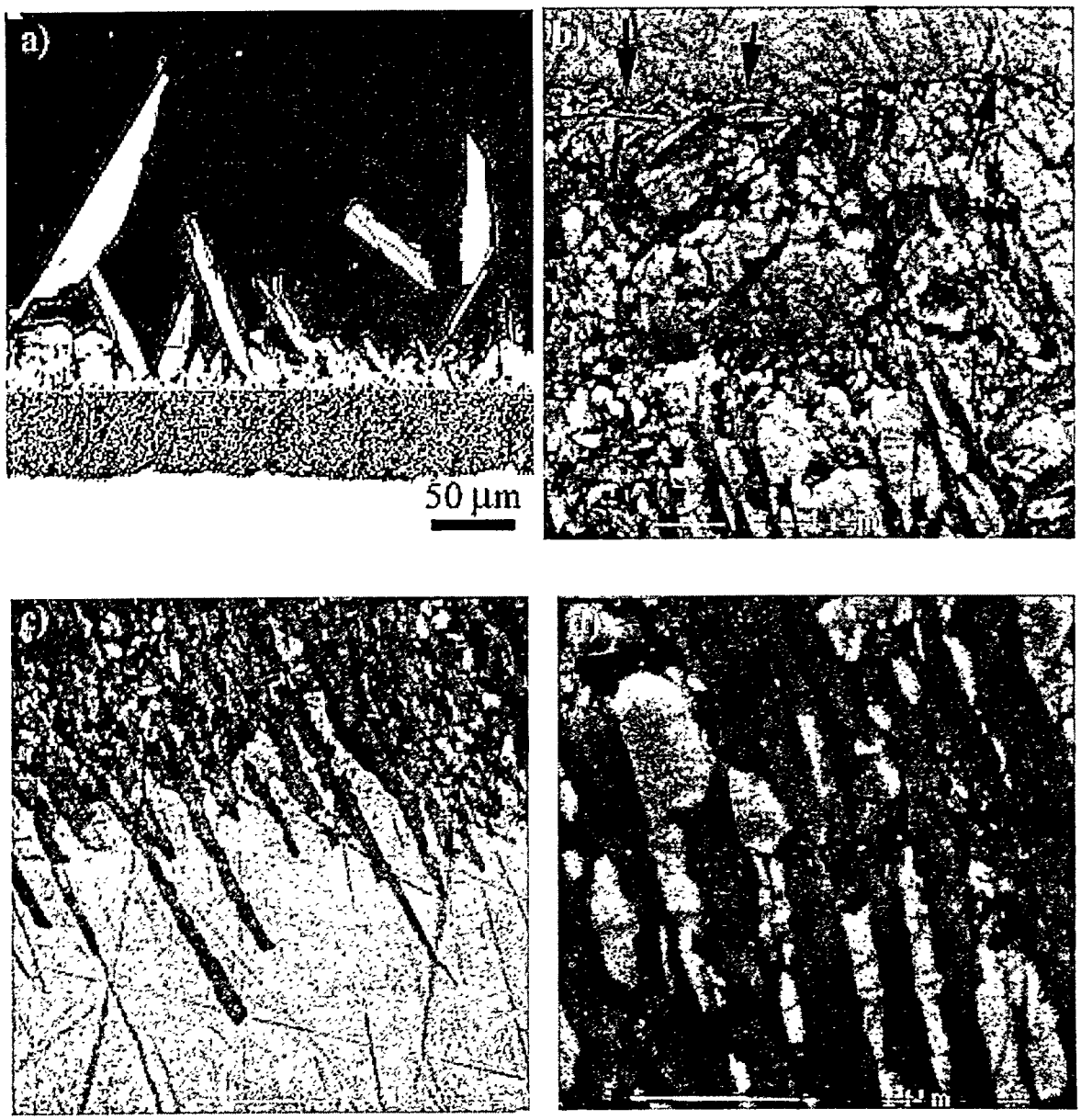

Figure 3.64: Micrographs of polished cross-section: T7.562 after 100 hour exposure. a) LOM bilayered scale at 200x, b) SEI inner scale at 10,000x, c) SEI inner scale-alloy interface at 10,000x, d) SEI inner scale at 25,000x.

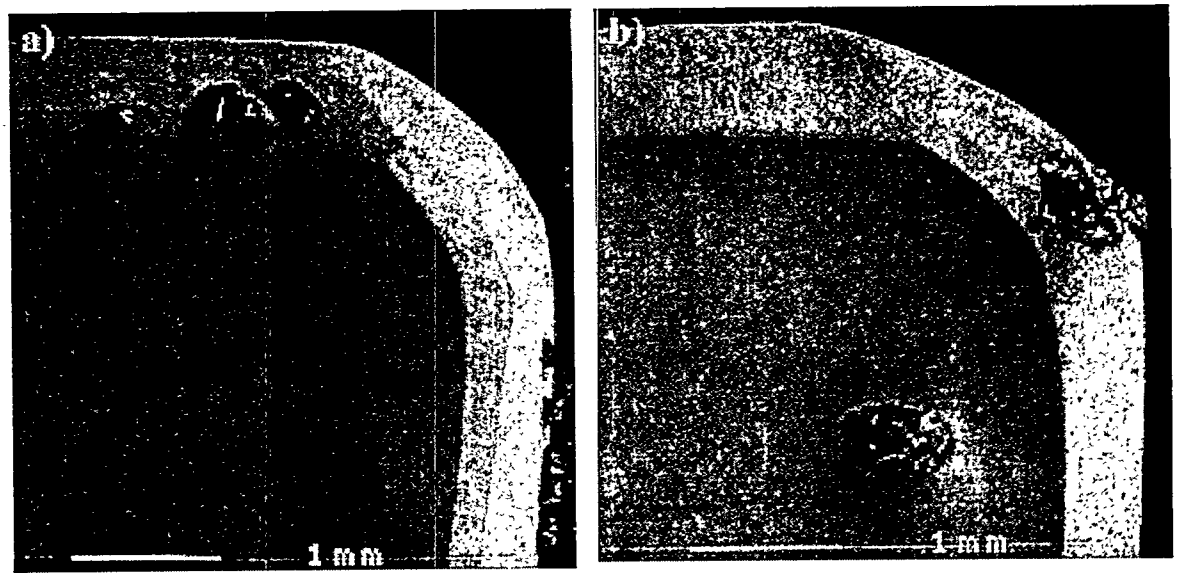

Figure 3.65: Low magnification SEI micrographs of T1062 at various times.
a) 50 hr, b) 100hr

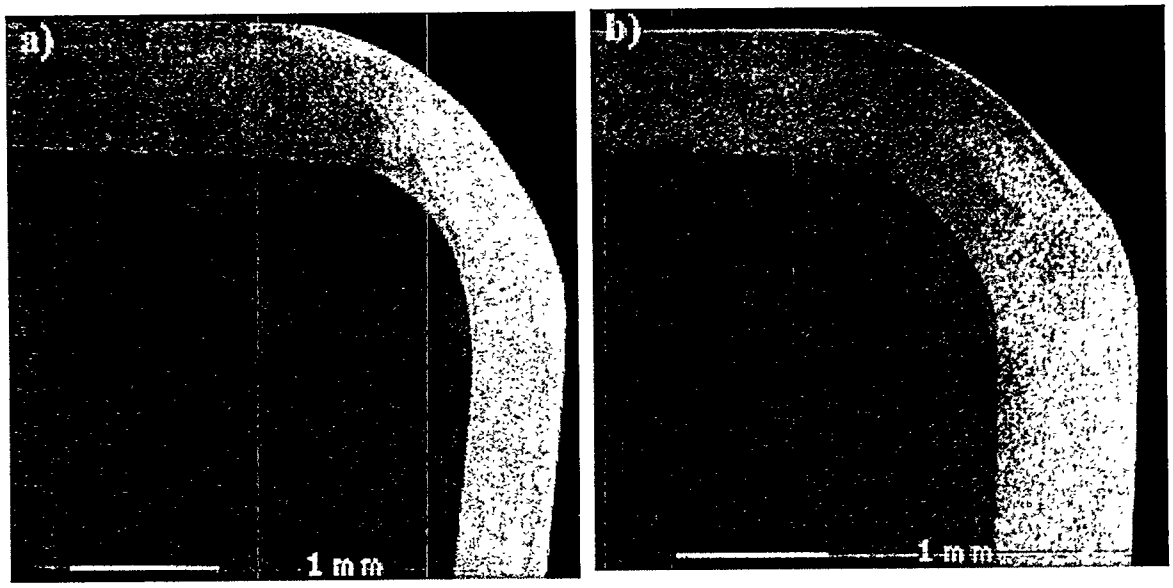

Figure 3.66: Low magnification SEI micrographs of T12.562 at various times.
a) 50 hr, b) 100 hr

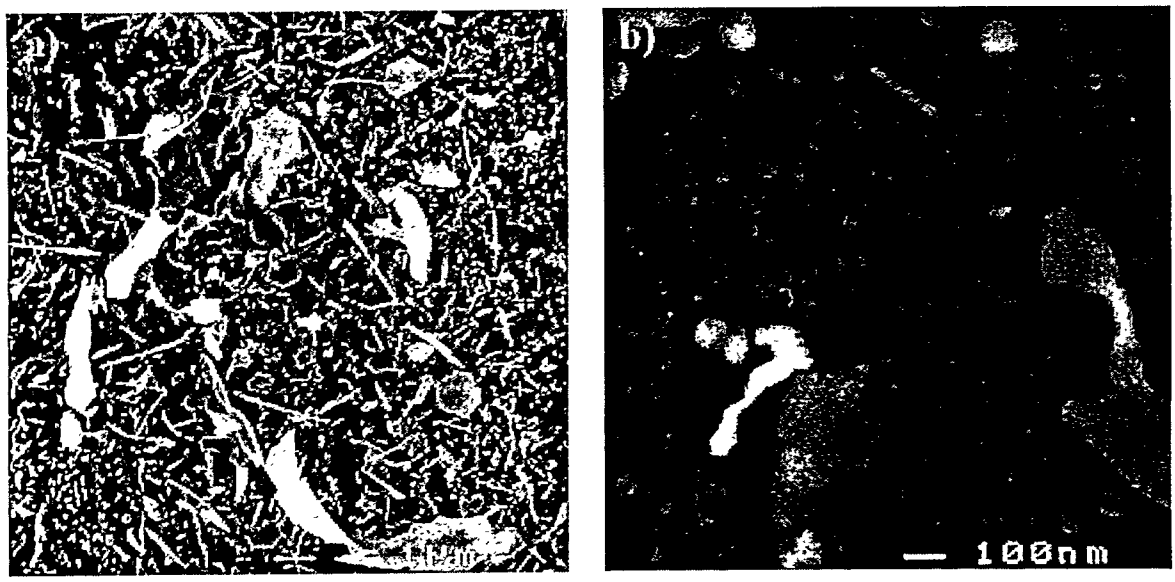

Figure 3.67: Characteristic SEI micrographs showing surface scales after 50 hrs exposure. a) 5,000x, b) 50,000x

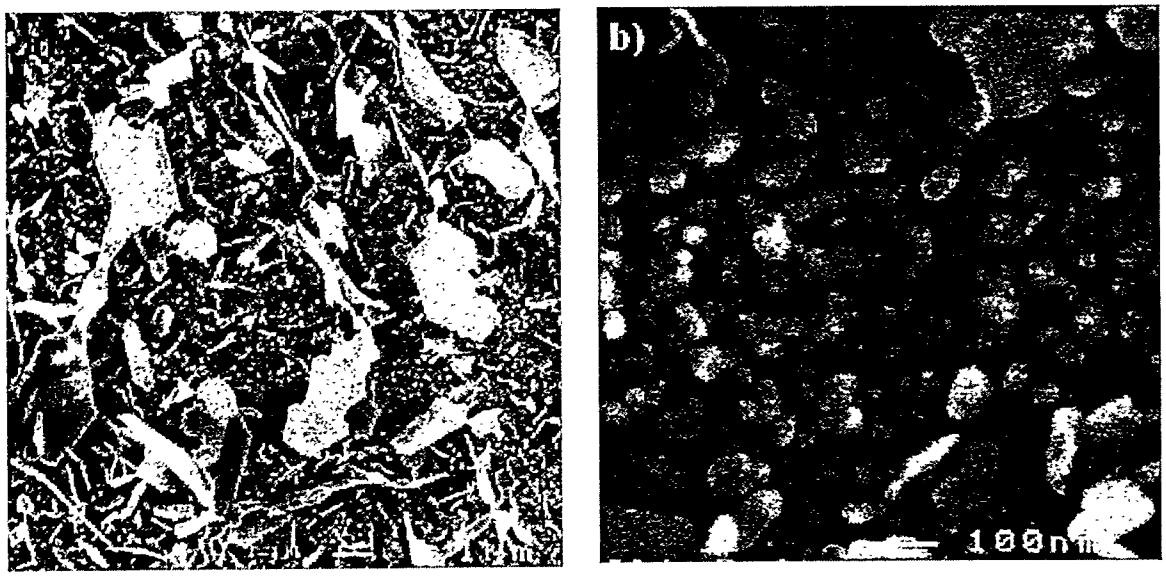

Figure 3.68: Characteristic SEI micrographs showing surface scale after 100 hr exposure. a) 5,000x, b) 50,000x

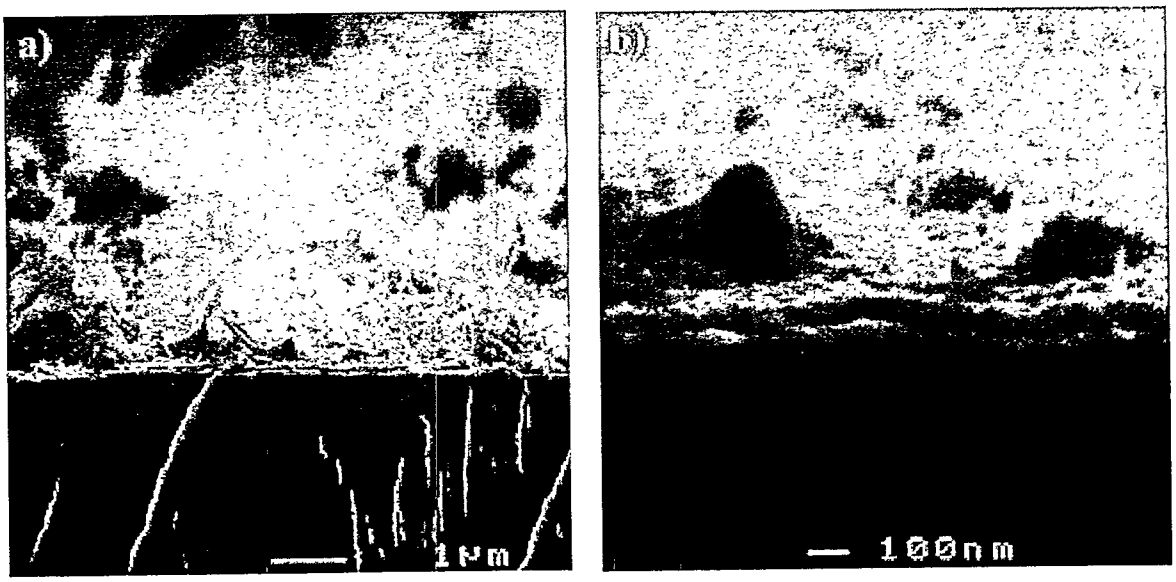

Figure 3.69: Characteristic SEI micrographs showing fractured cross-sections after 50 hr exposure. a) 10,000x, b) 50,000x

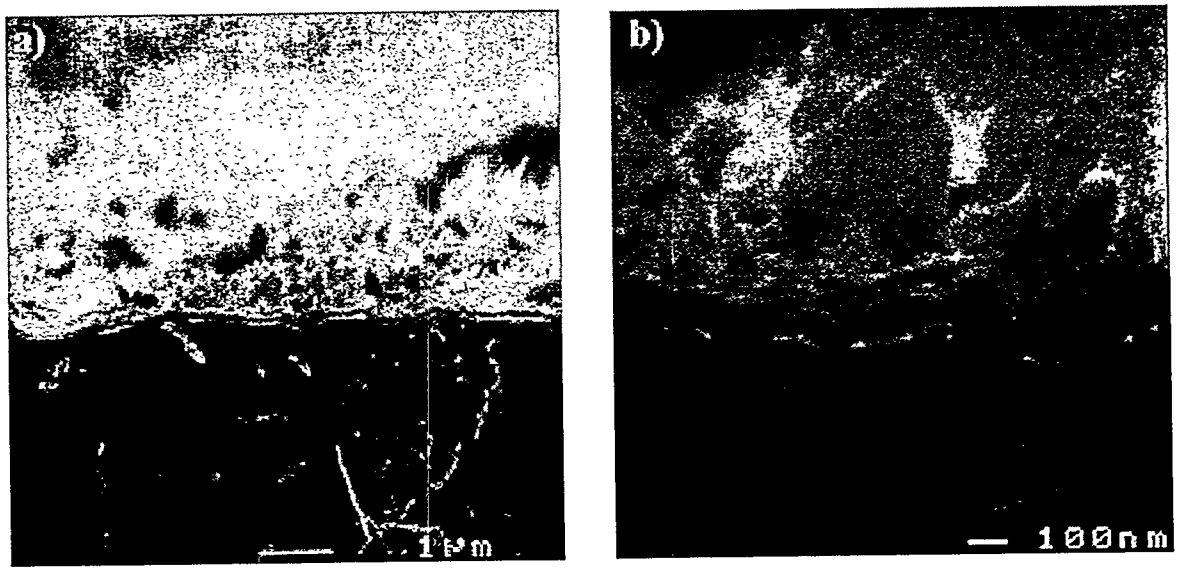

Figure 3.70: Characteristic SEI micrographs showing fractured cross-sections after 100 hr exposure. a) 10,000x, b) 50,000x

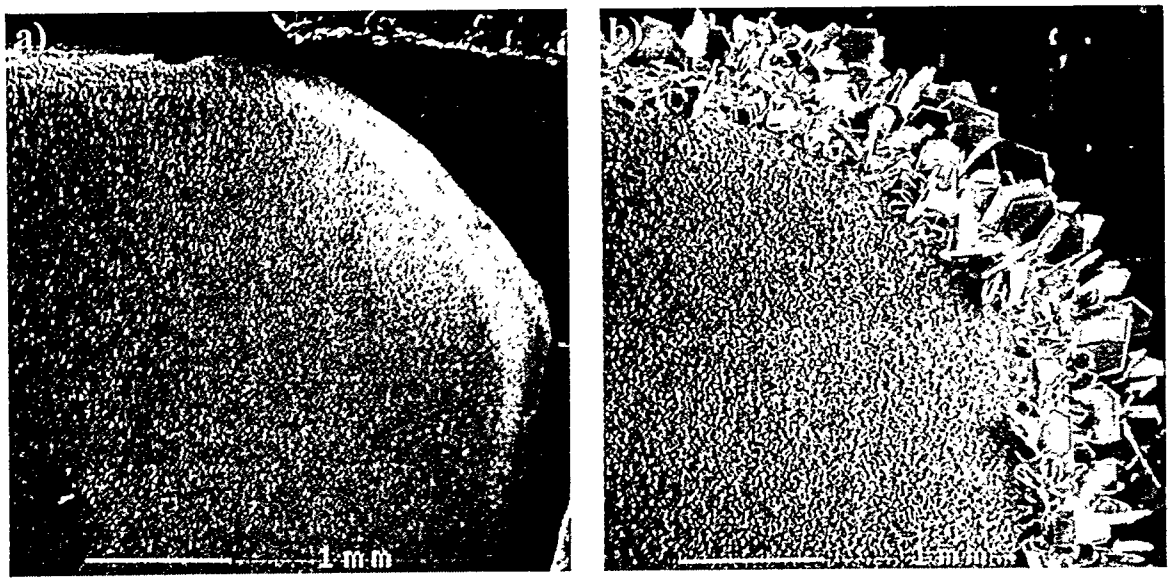

Figure 3.71: Low magnification (20x) SEI micrographs of T072 at various times.
a) 1 hr, b) 50 hr

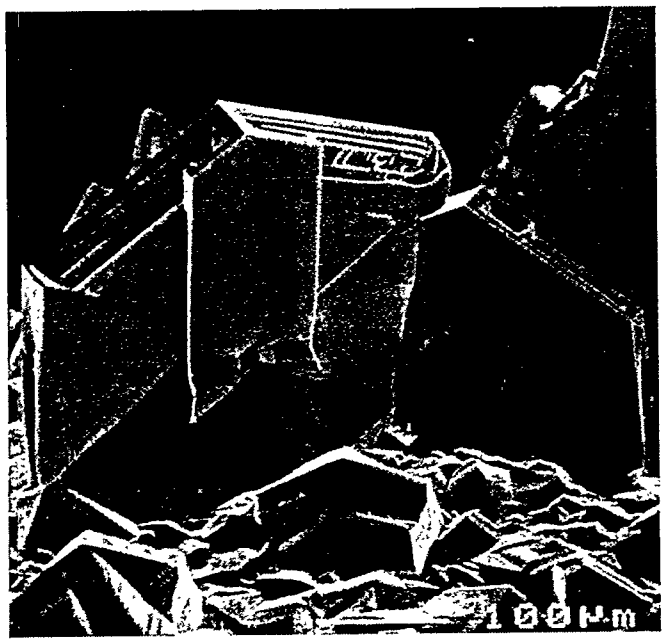

Figure 3.72: Characteristic SEI micrograph of a corner or edge plate on T072.

Figure 3.73: SEI micrographs of the surface scale for T072 after exposure for a) 1 hr (2,500x) and b) 50 (1,000x)

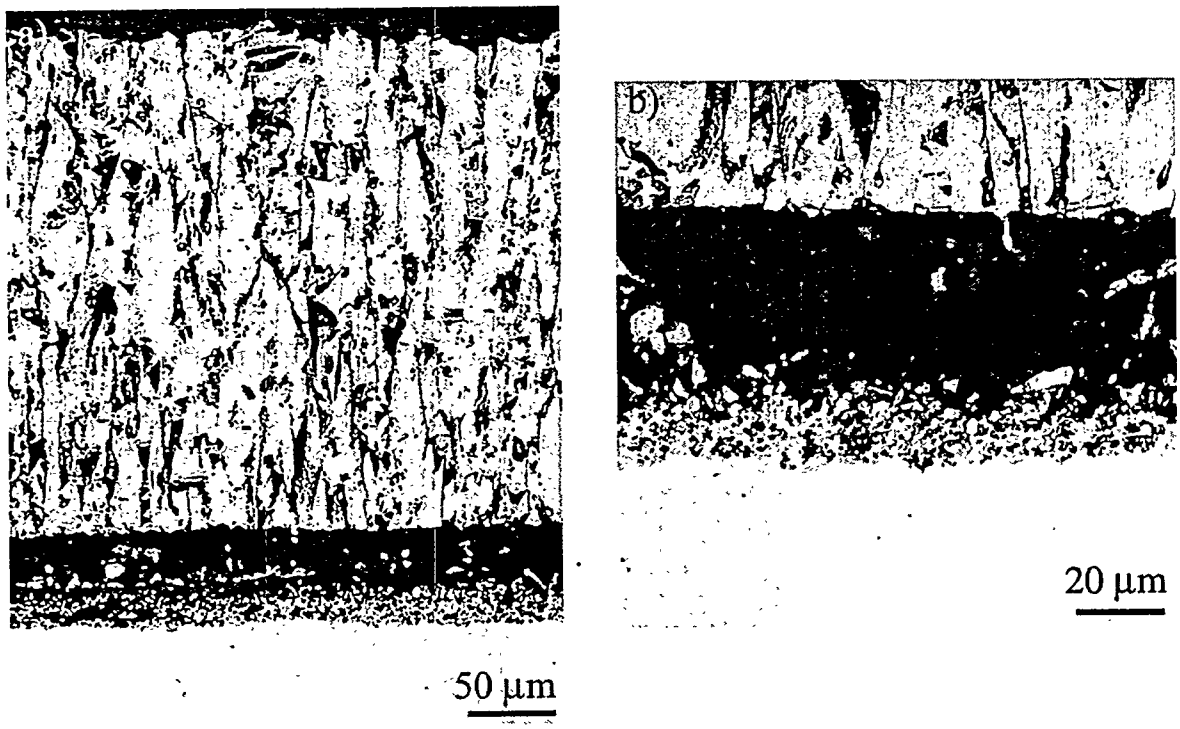

Figure 3.74: Light optical micrographs showing the cross-section of T072 after 50 hour exposure. a) 200x, b) 500x

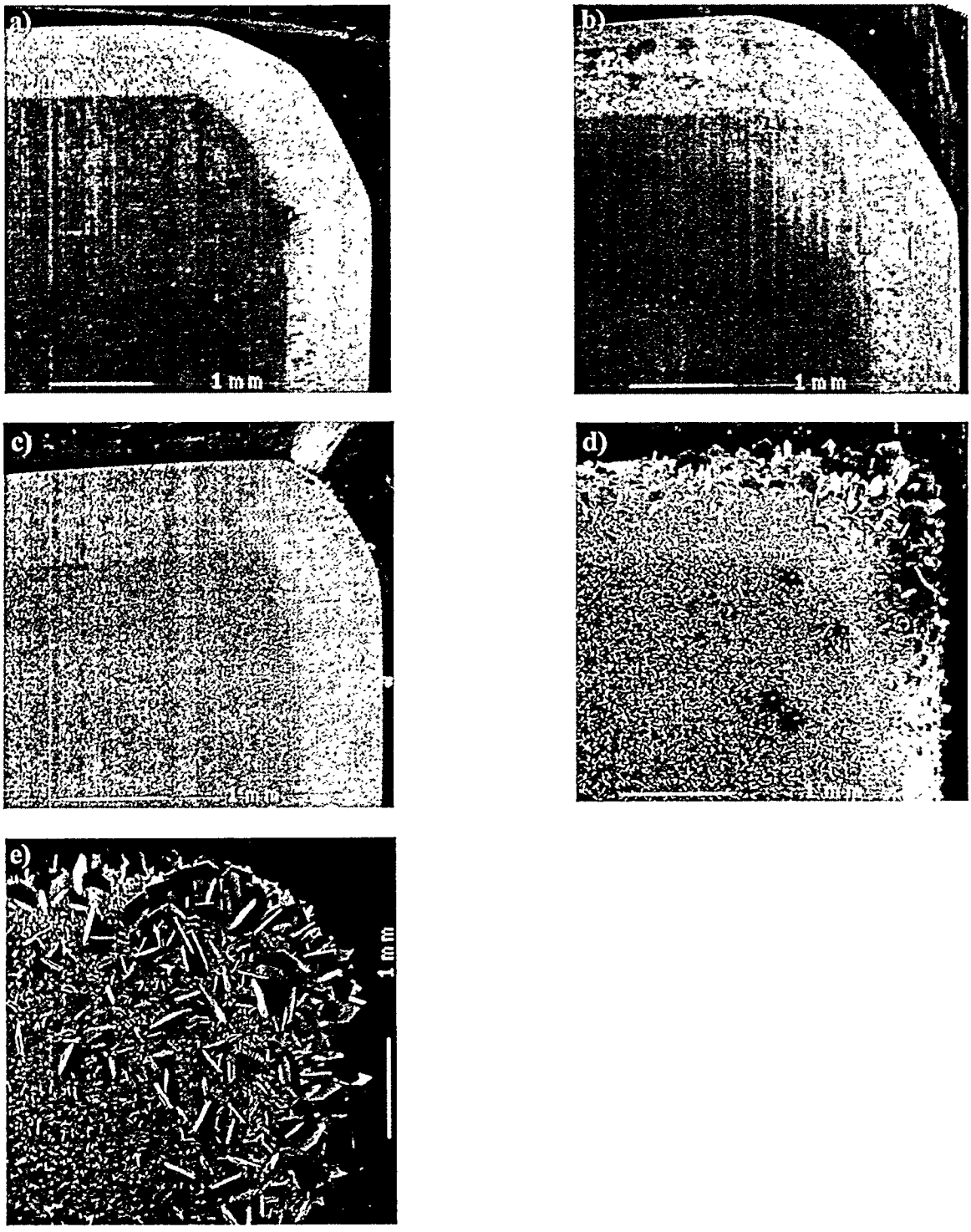

Figure 3.75: Low magnification (20x) SEI micrographs of T572 at various times. a) 7 min, b) 45 min, c) 5 hrs, d) 15 hrs, and e) 50 hrs

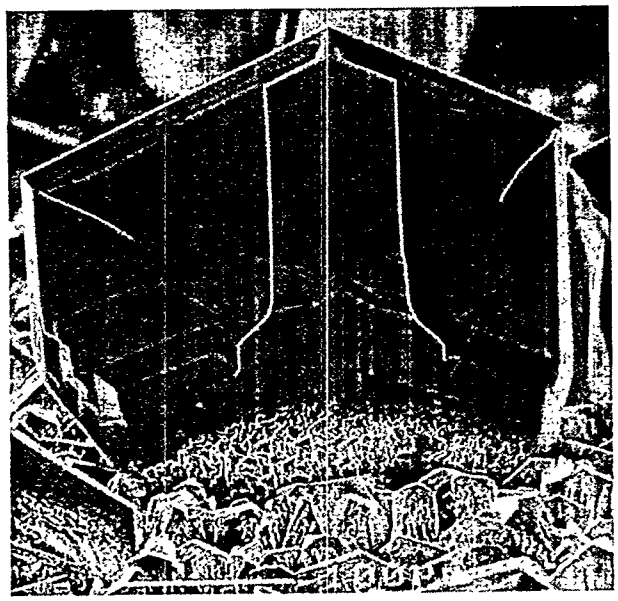

Figure 3.76: Characteristic SEI micrograph of a corner or edge plate on T572. (230x)

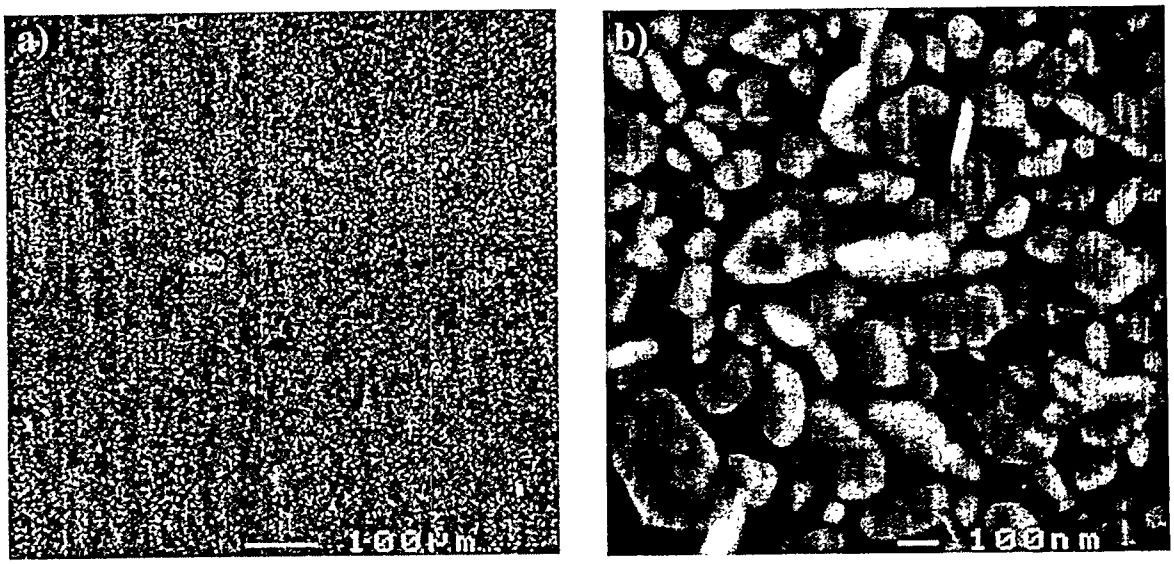

Figure 3.77: SEI micrographs of T572 after 7 minutes of exposure showing surface scale. a)100x, b) 50,000x

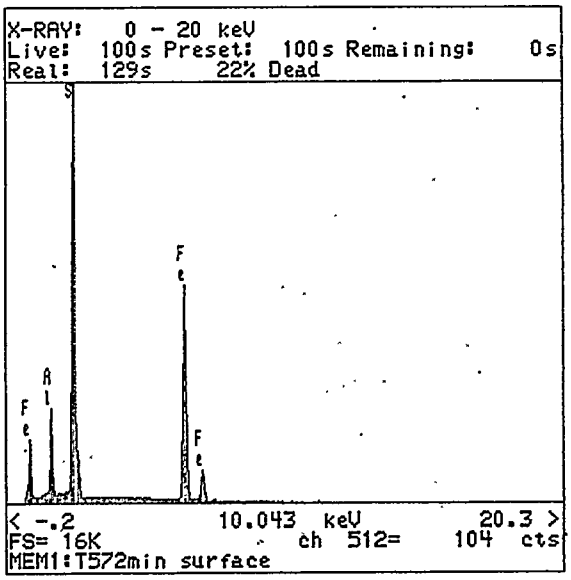

Figure 3.78: EDS spectra for the surface scale on T572 after 7 minutes.

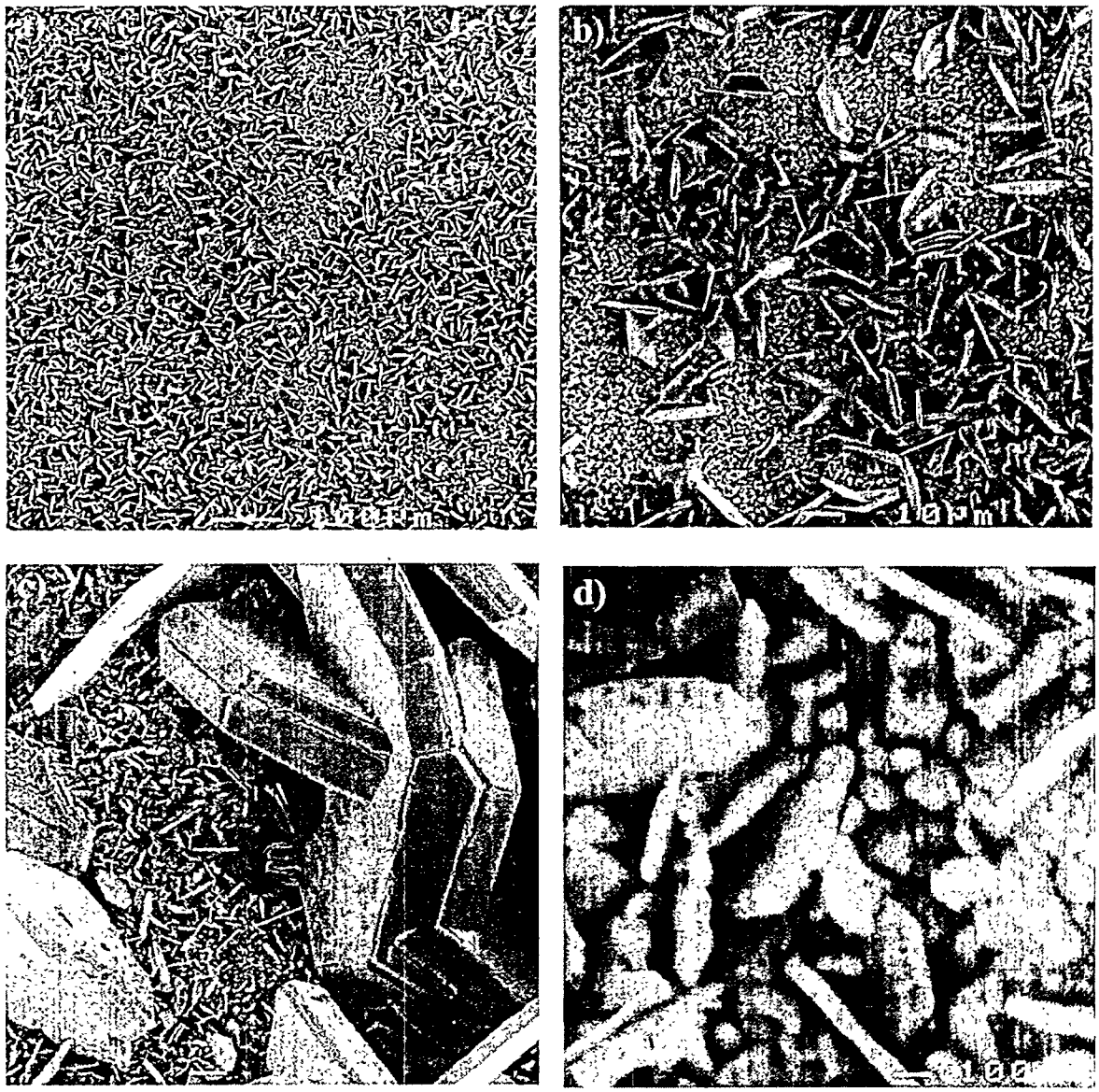

Figure 3.79: SEI micrographs of T572 after 45 minutes of exposure showing surface scale. a) 100x, b) 500x, c) 5,000x, and d) 50,000x

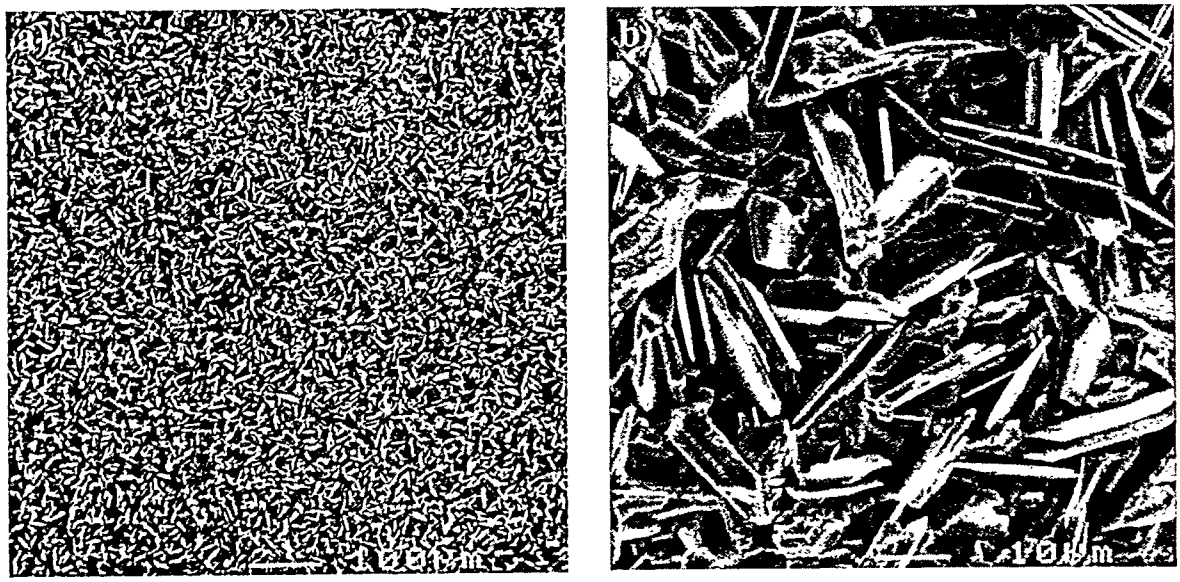

Figure 3.80: SEI micrographs of T572 after 5 hour exposure showing surface scale.
a) 100x, b) 1,000x

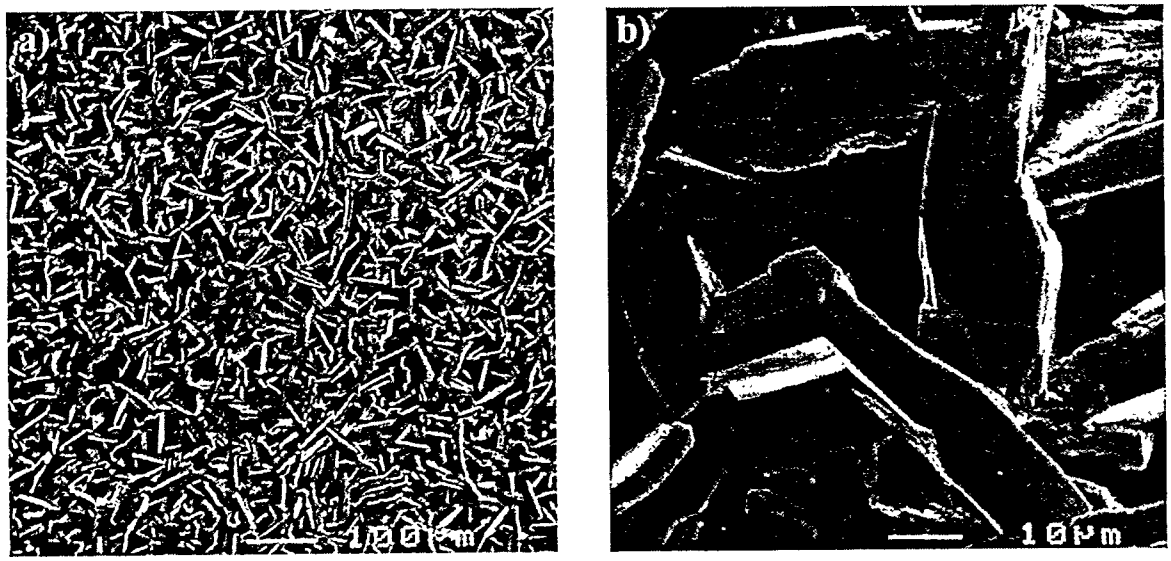

Figure 3.81: SEI micrographs of T572 after 15 hour exposure showing surface scale.
a) 100x, b) 1,000x

Figure 3.82: SEI micrographs of T572 after 50 hour exposure showing surface scale.
a) 250x, b) 1,000x

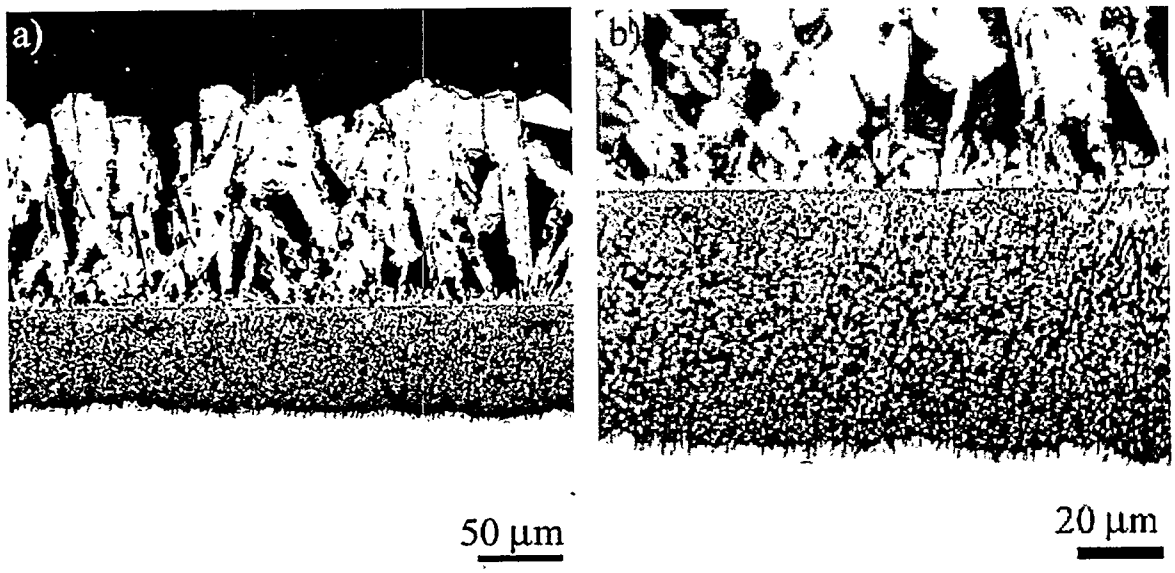

Figure 3.83: Light optical micrographs of polished cross-section: T572 after 50 hour exposure. a) 200x, b) 500x

Figure 3.84: SEI micrographs of polished cross-section: T572 after 50 hour exposure.
a) 1,500x, b) 10,000x

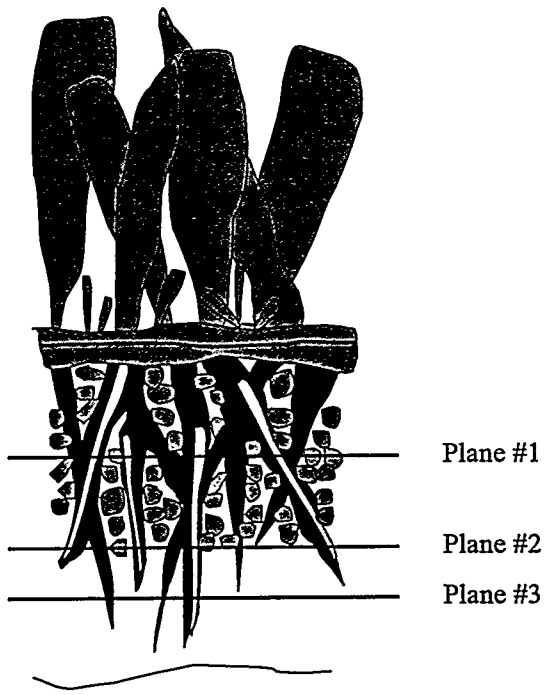

Figure 3.85: Schematic illustrating the different locations of polishing depths in the scale.

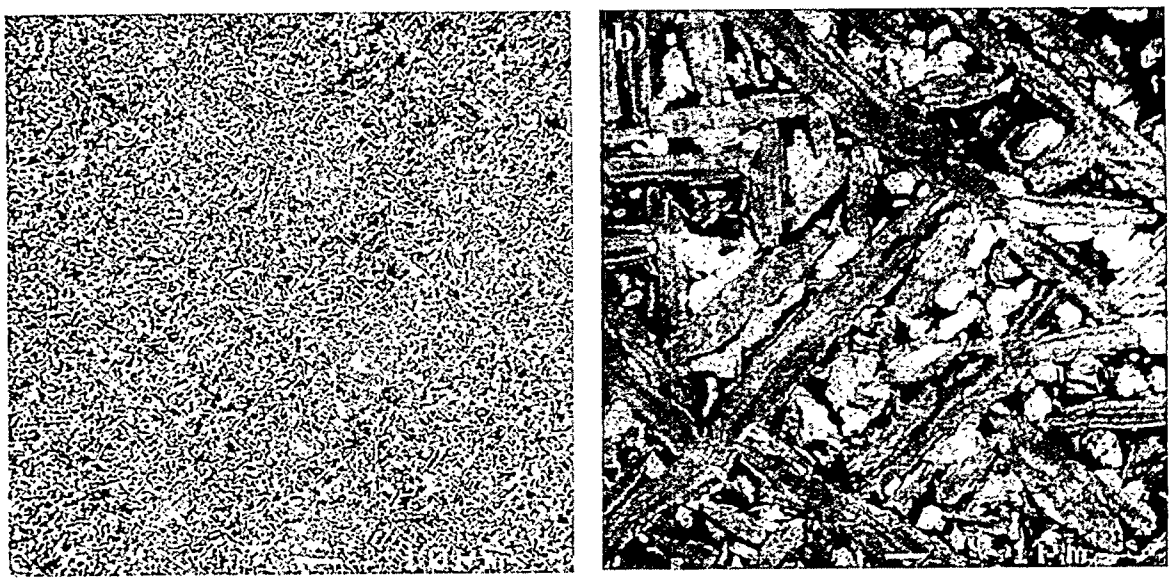

Figure 3.86: SEI micrographs of polished face on T572 after 50 hour exposure, plane #1. a) 500x, b) 5,000x

Figure 3.87: SEI micrographs of polished face on T572 after 50 hour exposure, plane #2. a) 500x, b) 5,000x

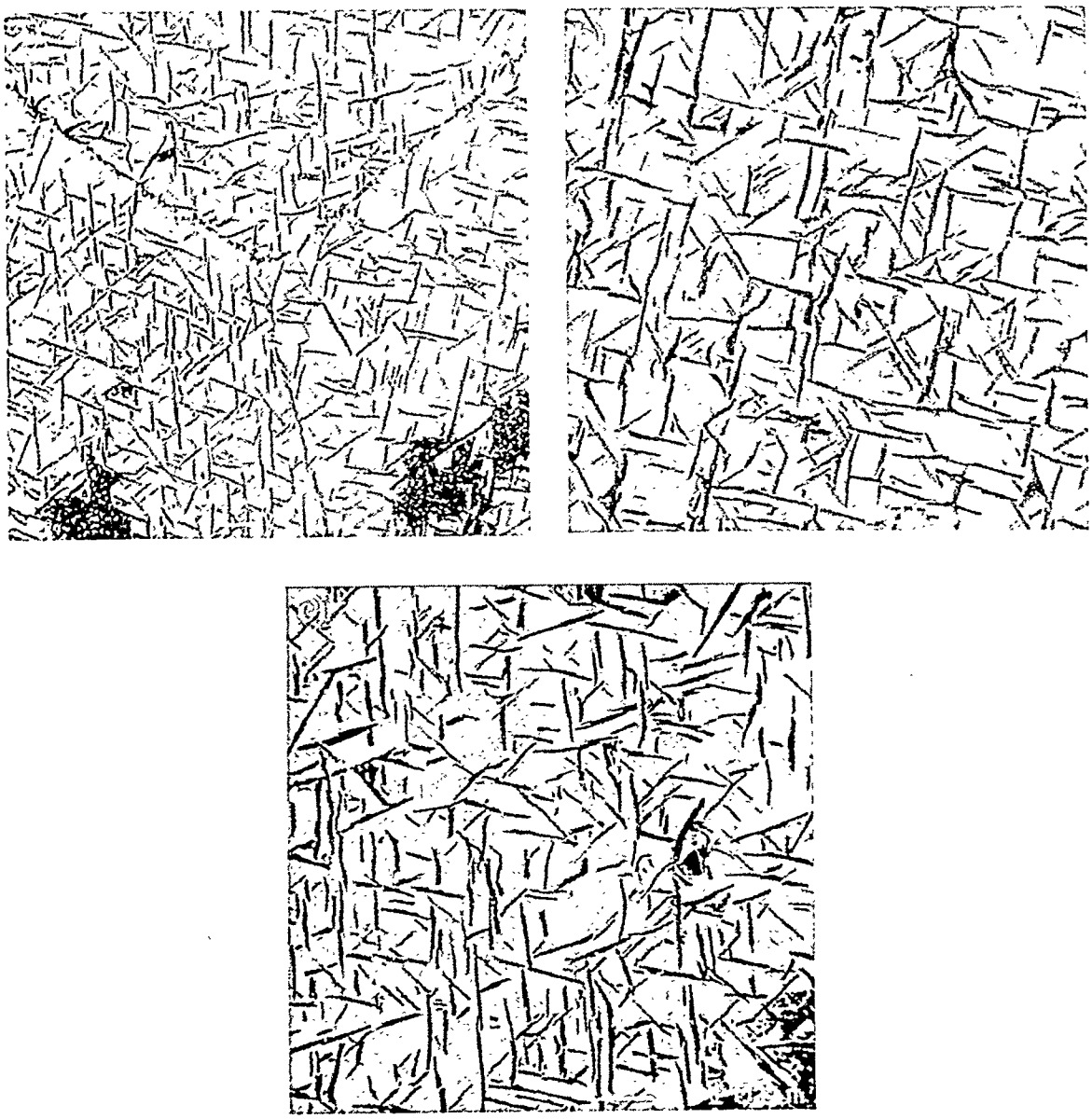

Figure 3.88: SEI micrographs of polished face on T572 after 50 hour exposure, plane #3. a) showing attack in grains and grain boundary at 500x, b) 4 growth directions, and c) 6 growth directions.

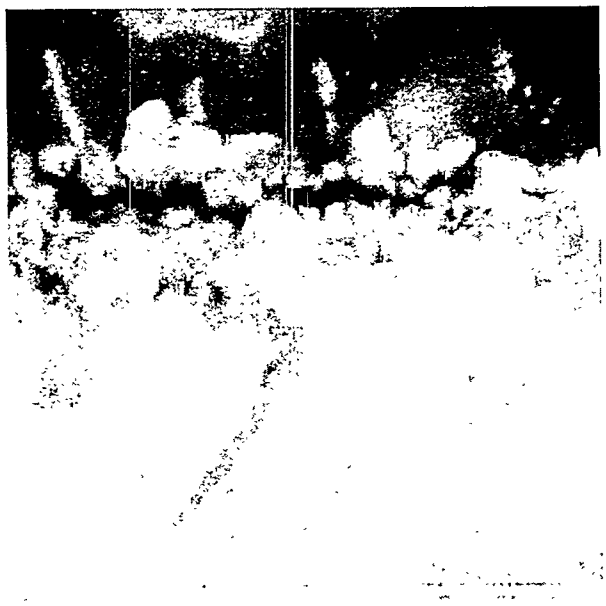

Figure 3.89: SEI micrograph of polished cross-section: T572 after 7 minutes of exposure. 25,000x

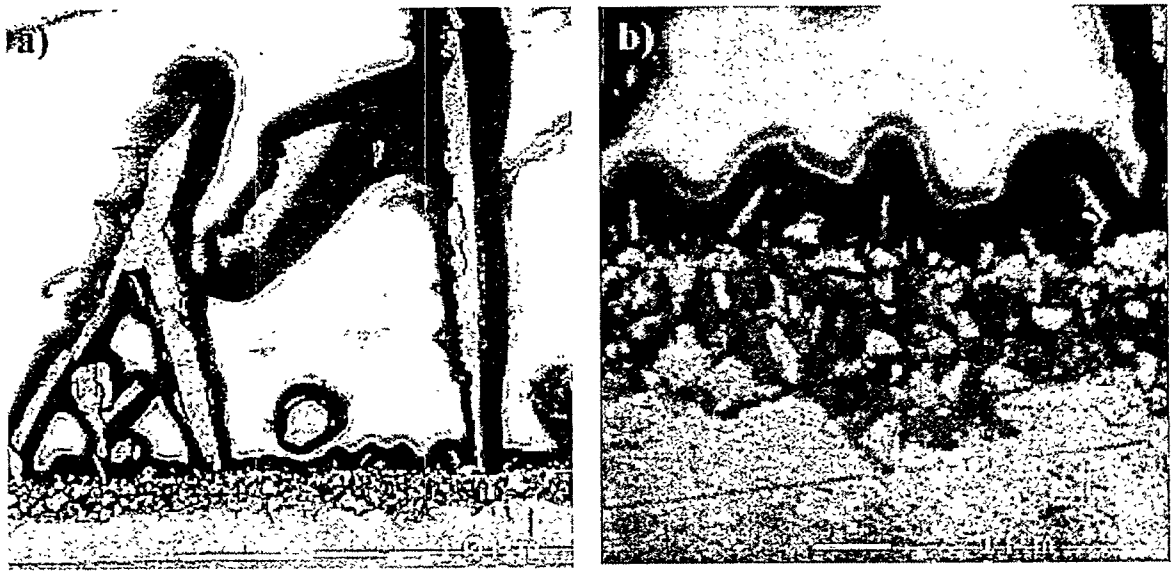

Figure 3.90: SEI micrographs of polished cross-section: T572 after 45 minutes of exposure. a) bilayered scale at 2,700x, b) inner scale at 10,000x.

Figure 3.91: SEI micrograph of polished cross-section: T572 after 5 hour exposure. 1,900x

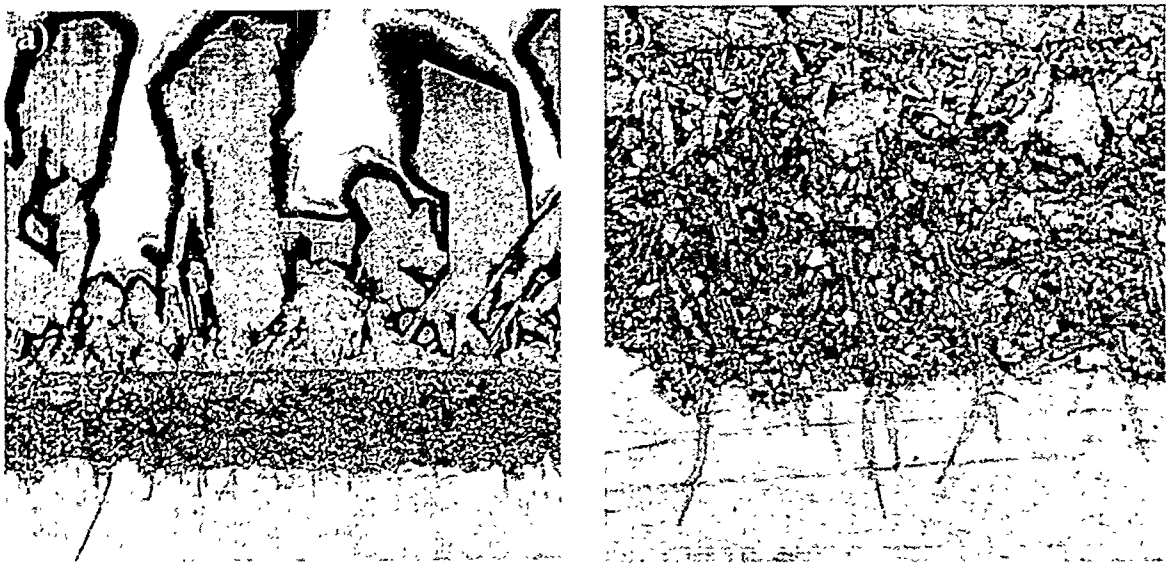

Figure 3.92: SEI micrographs of polished cross-section: T572 after 15 hour exposure.
a) bilayered scale at 700x, b) inner scale at 2,500x.

Figure 3.93: SEI micrograph of polished cross-section: T572 after 50 hour exposure. 350x

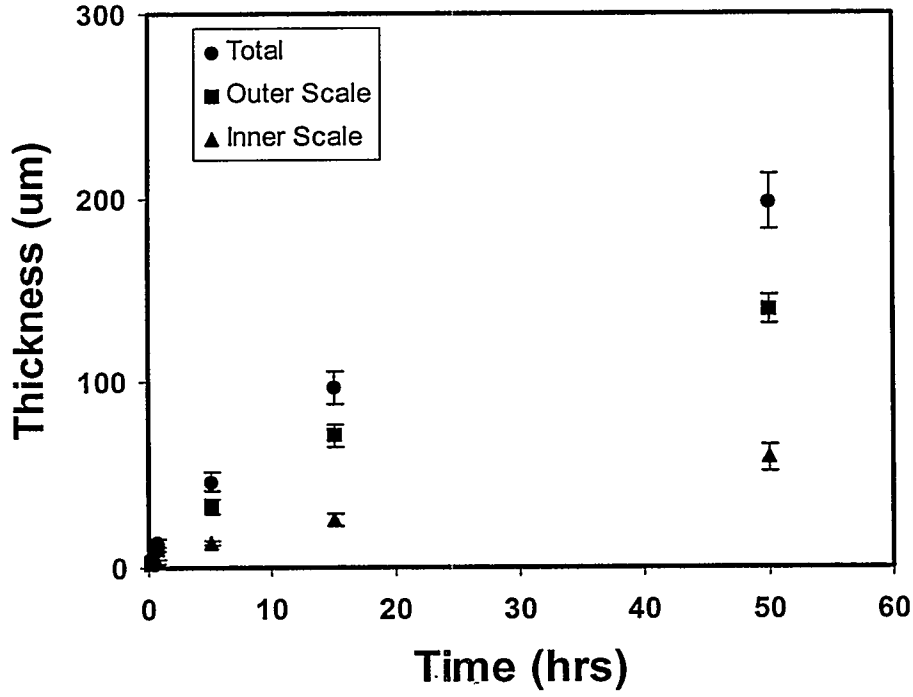

Figure 3.94: Plot of scalecross-sectional thickness versus time for T572 samples.

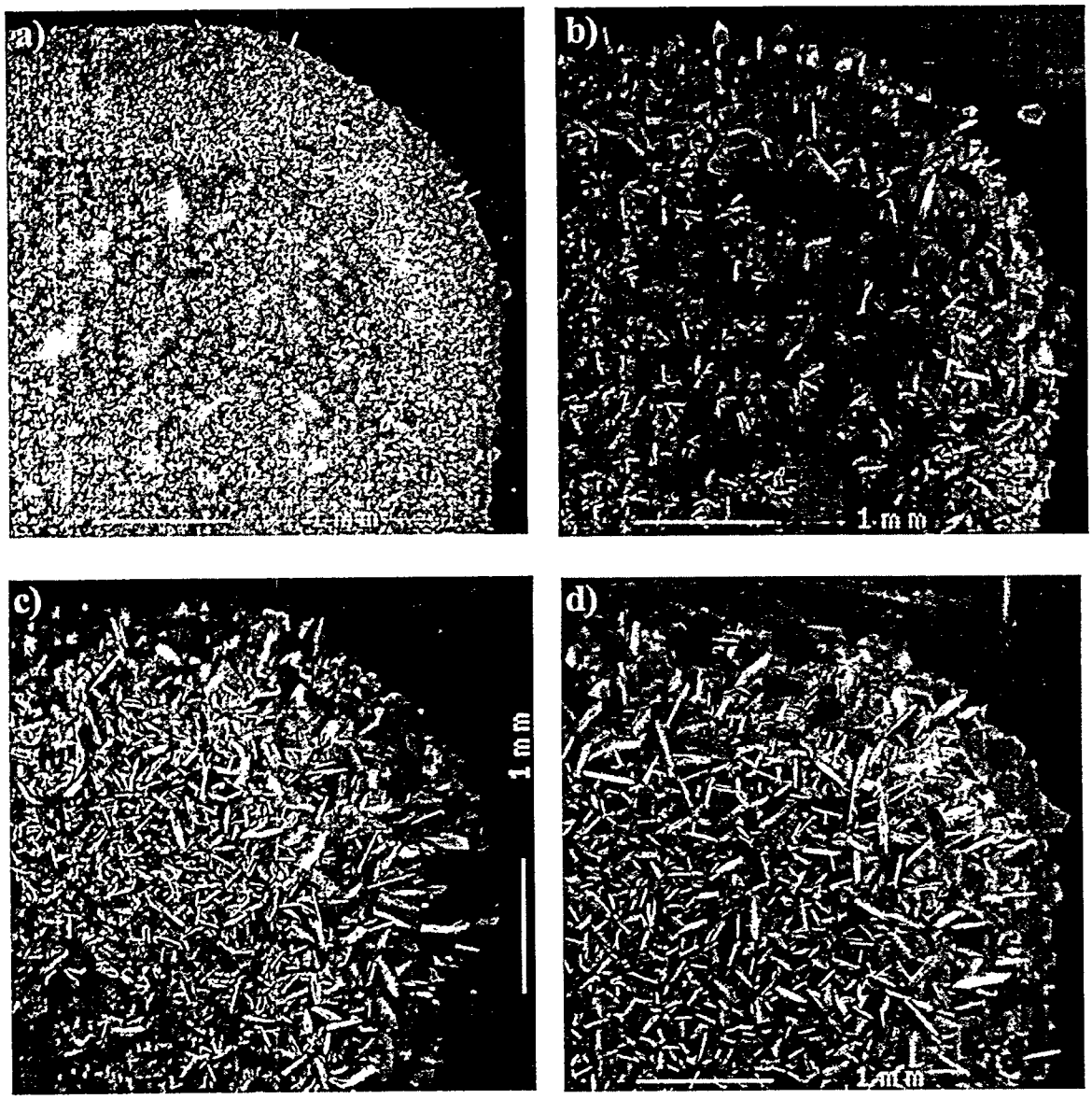

Figure 3.95: Low magnification (20x) SEI micrographs of T7.572 at various times. a) 10 hrs, b) 20 hrs, c) 50 hrs, and d) 100hrs

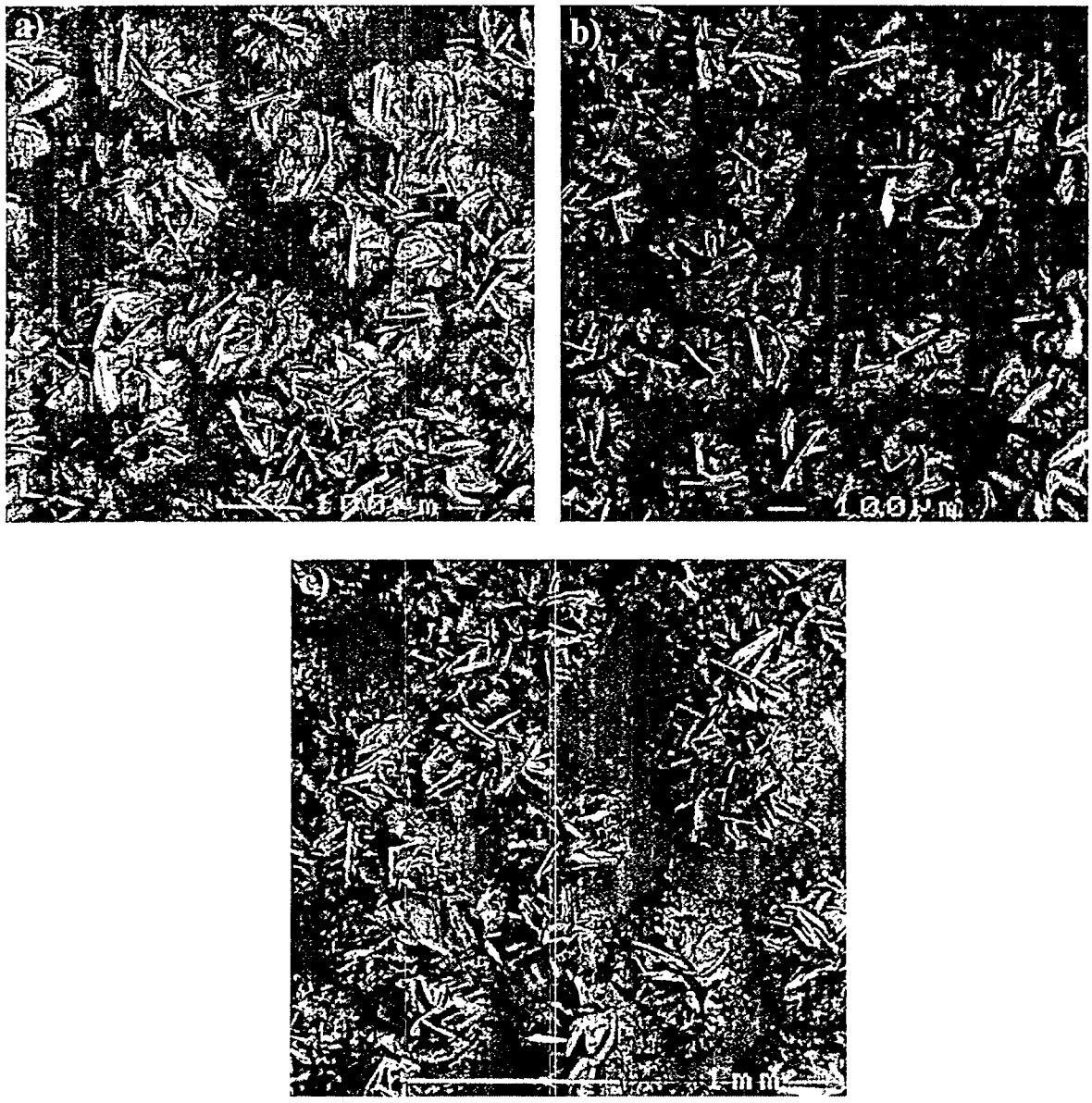

Figure 3.96: SEI micrographs of T7.572 showing nodules on surface. a) 10 hrs at 100x, b) 20 hrs at 50x , and c) 50 hrs at 30x

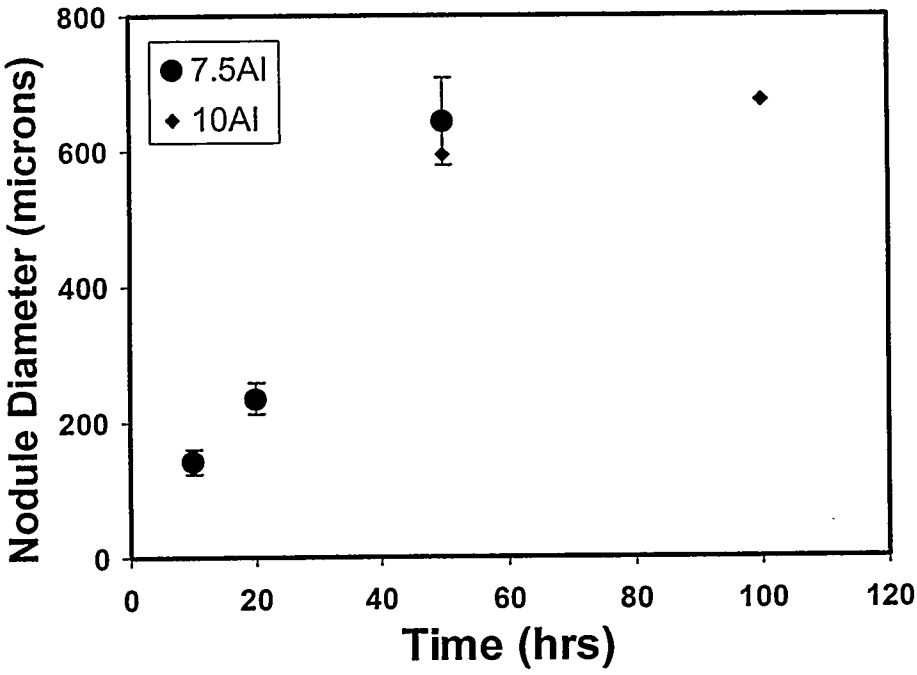

Figure 3.97: Plot of nodule diameter size versus time for various alloys at 700°C.

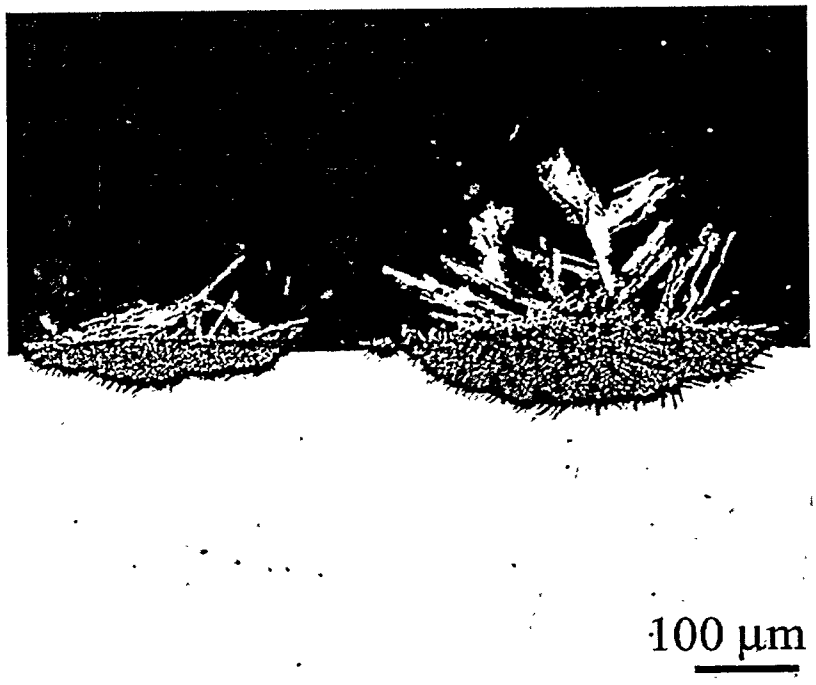

Figure 3.98: Light optical micrograph showing polished cross-section of T7.572 after 50 hour exposure. 100x

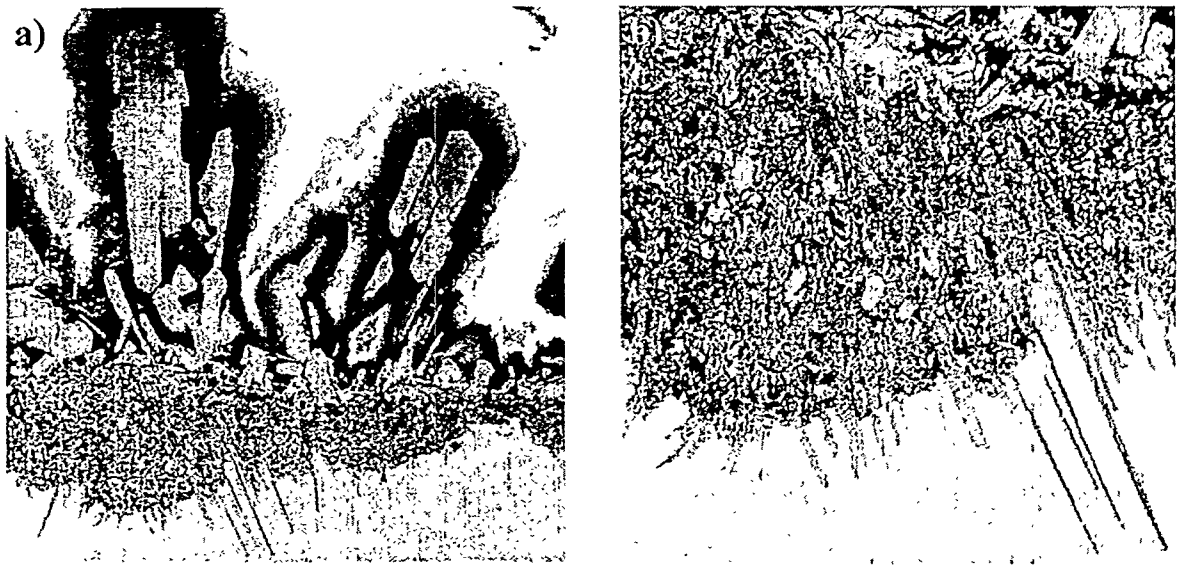

Figure 3.99: SEI micrographs of polished cross-section of T7.572 after 10 hr exposure. a) 750x, b) 2,200x

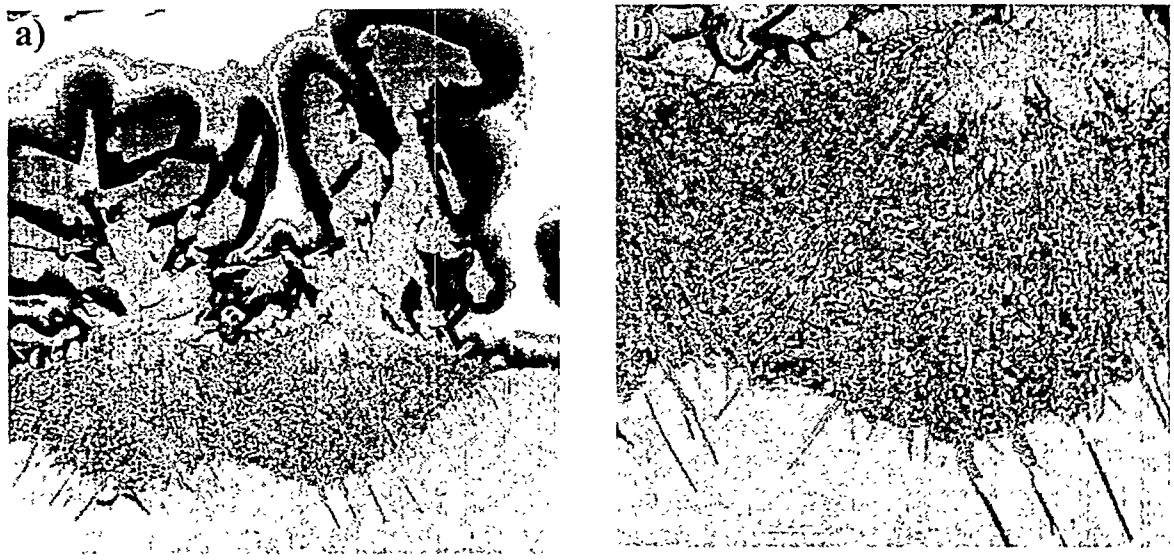

Figure 3.100: SEI micrographs of polished cross-section of T7.572 after 20 hr exposure. a) 450x, b) 1,200x

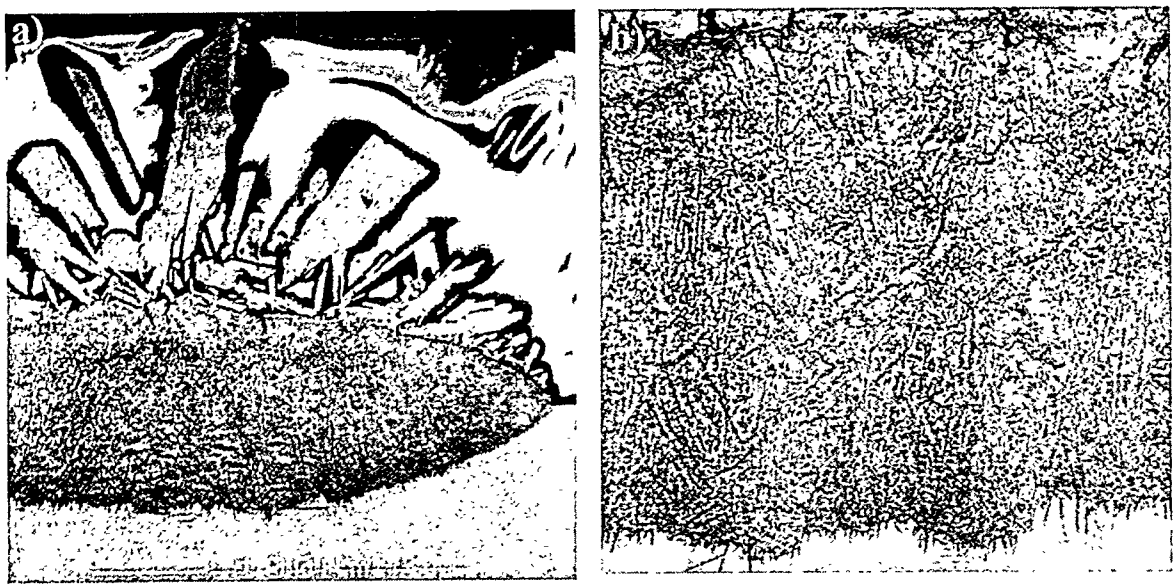

Figure 3.101: SEI micrographs of polished cross-section of T7.572 after 50 hour exposure. a) 150x, b) 400x

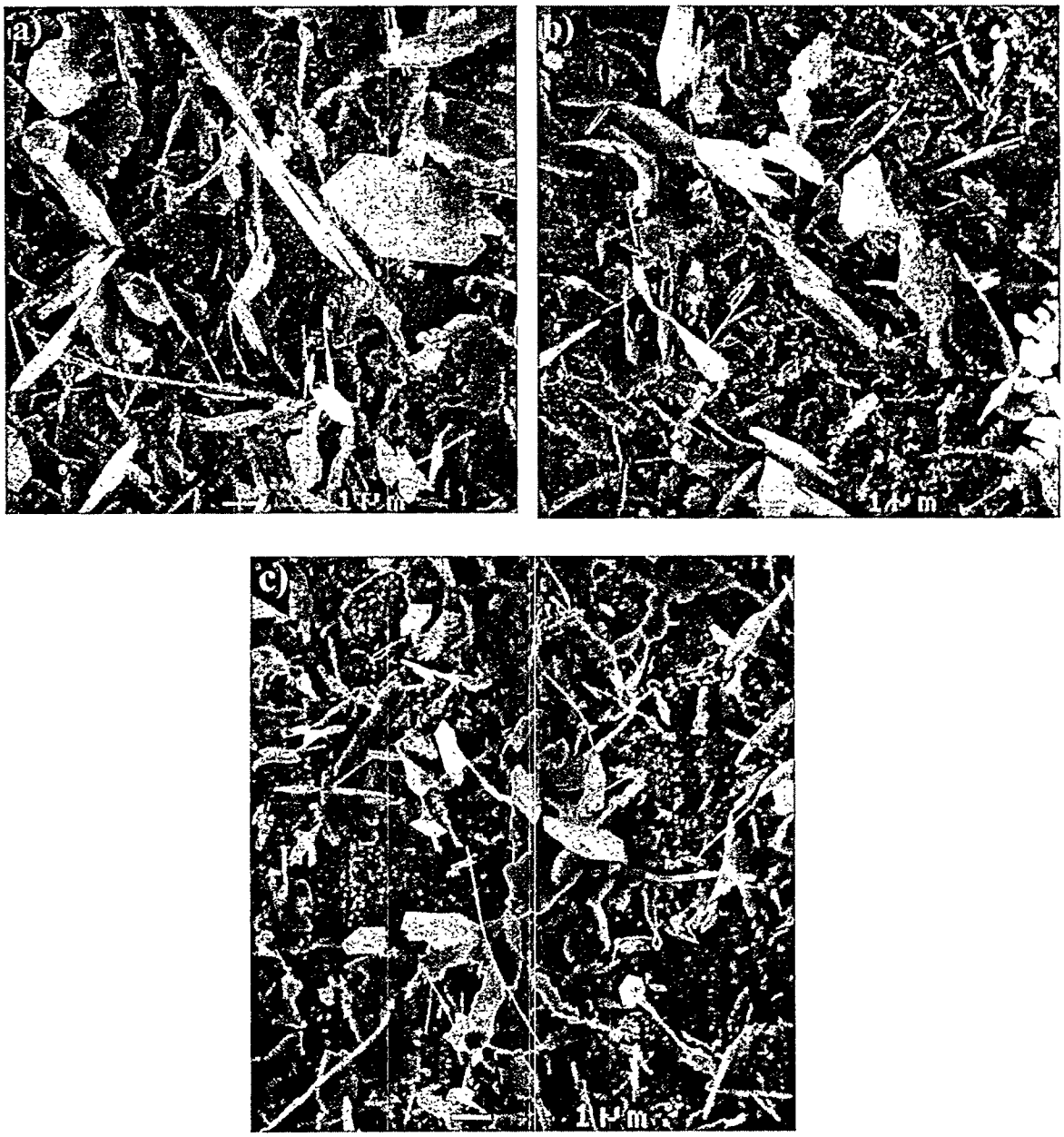

Figure 3.102: SEI micrographs of platelets on surface scale for T7.572 for various times. a) 10 hrs, b) 20 hrs, and c) 50 hrs (5,000x)

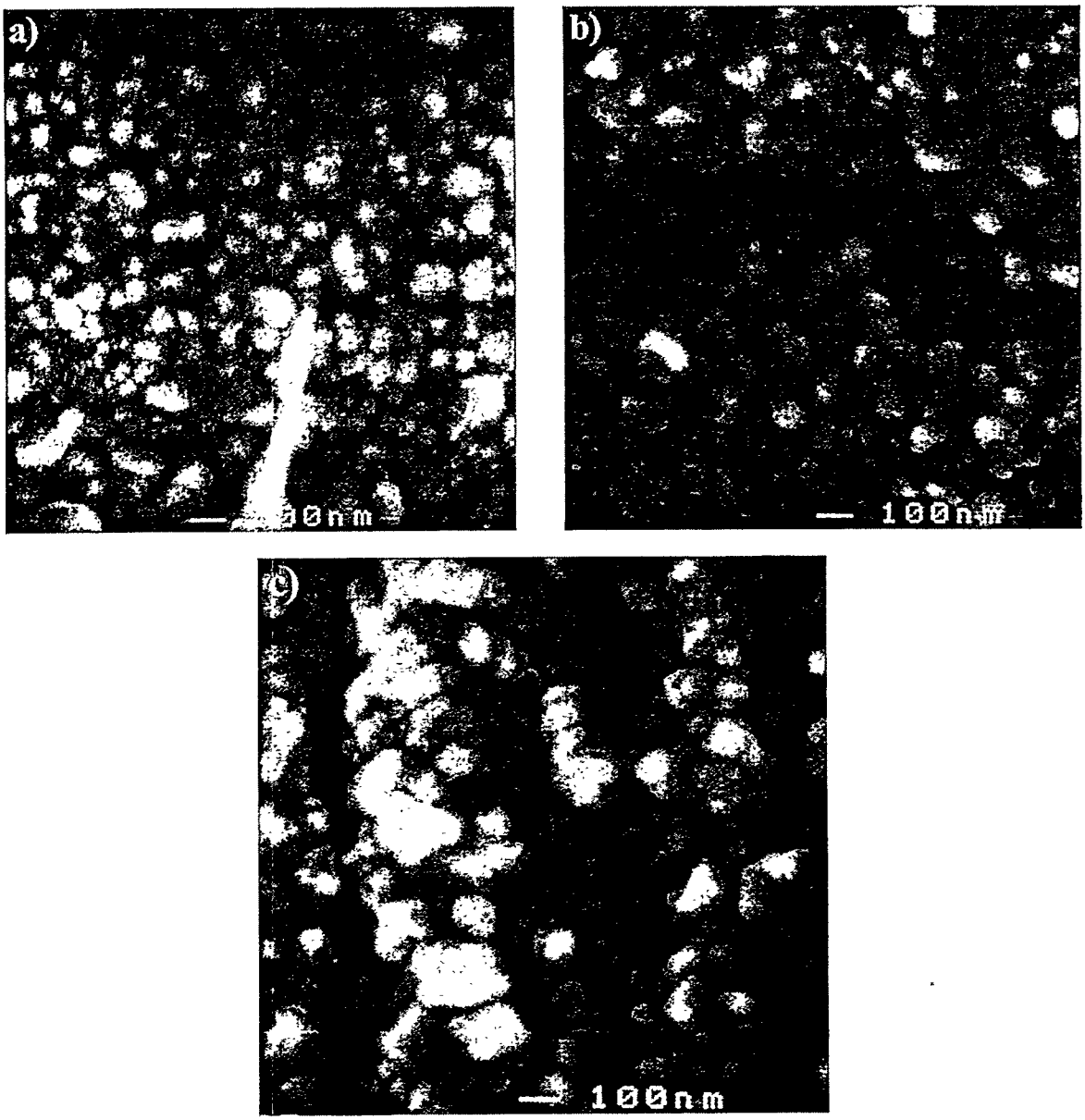

Figure 3.103: SEI micrographs of granular surface scale on T7.572 for various times.
a) 10 hrs, b) 20 hrs, and c) 50 hrs (50,000x)

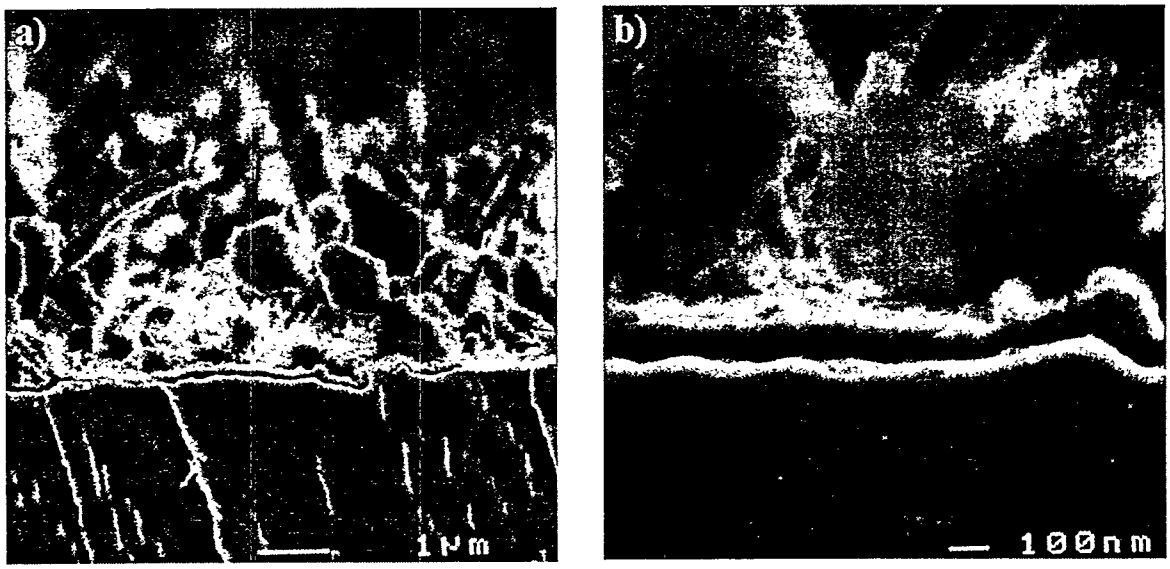

Figure 3.104: SEI micrographs showing fractured cross-section of T7.572 for 50 hrs.
a) 10,000x, b) 50,000x

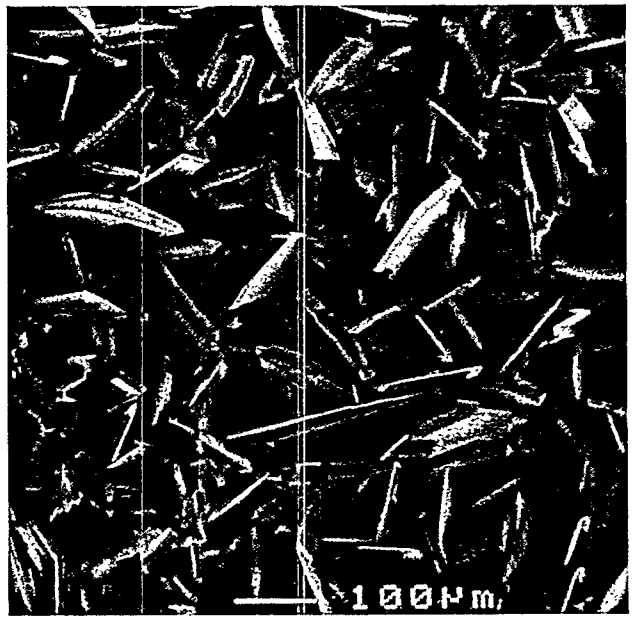

Figure 3.105: SEI micrograph of T7.572 after 100 hour exposure showing surface scale.
100x

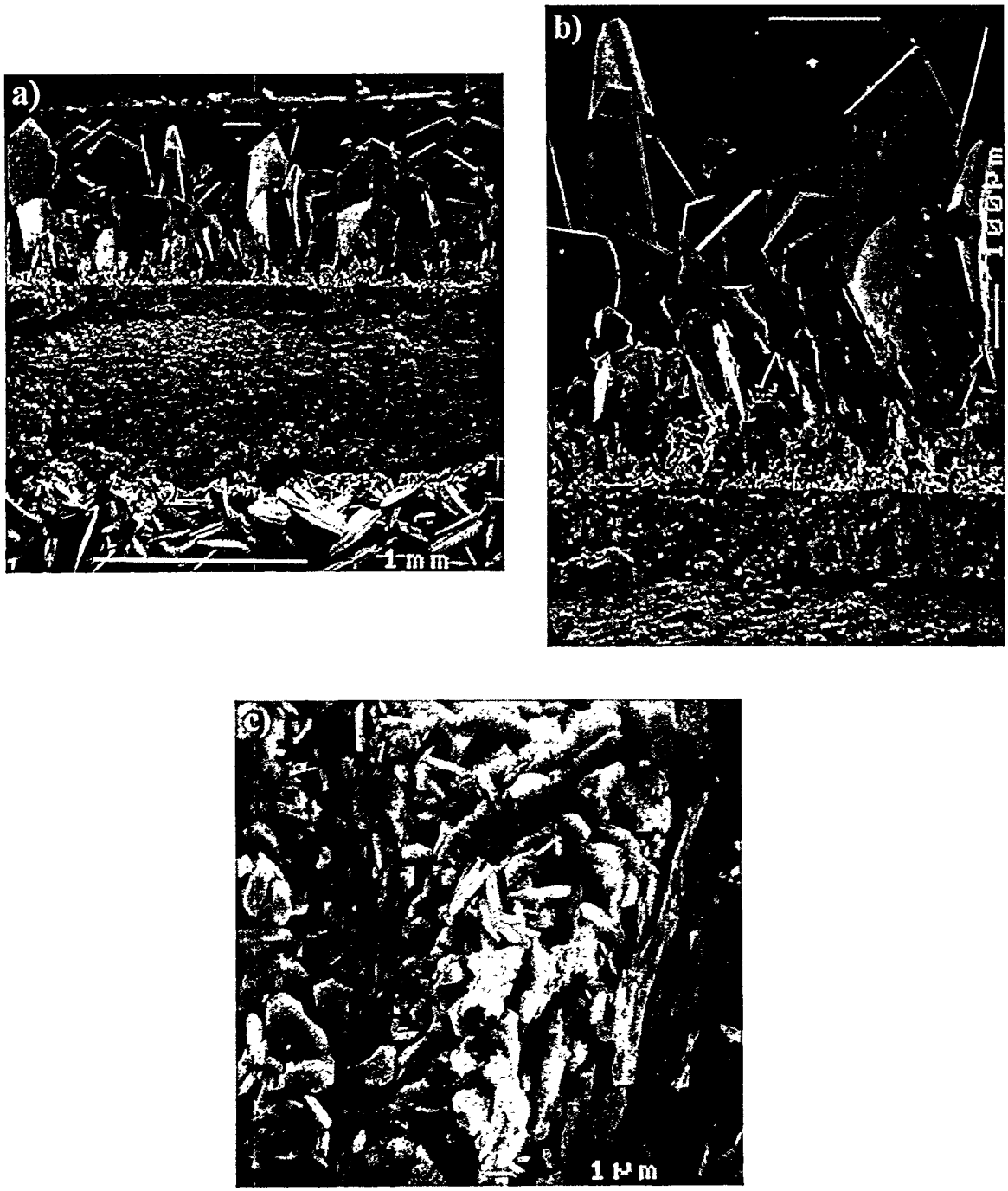

Figure 3.106: SEI micrographs showing fractured cross-section of T7.572 after 100 hrs of exposure. a) fractured section at 33x, b) fractured section at 100x, c) inner scale region at 4,000x

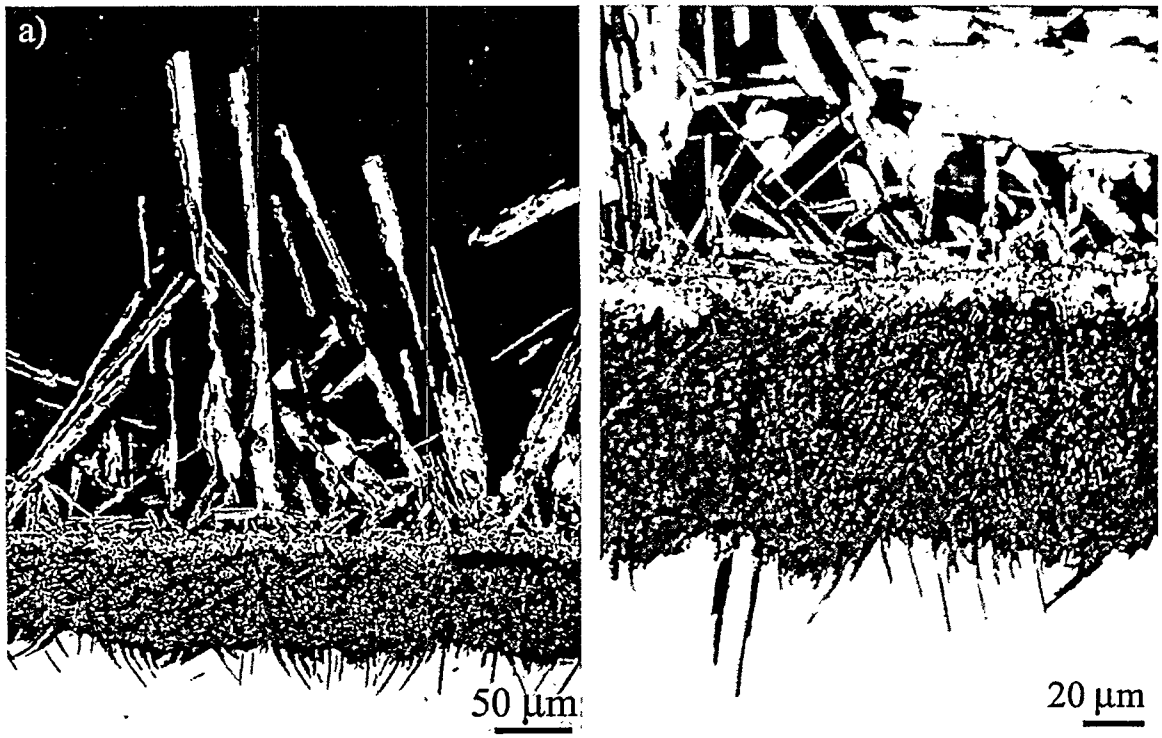

Figure 3.107: Light optical micrographs showing polished cross-section of T7.572 after 100 hrs of exposure. a) 200x, b) 500x

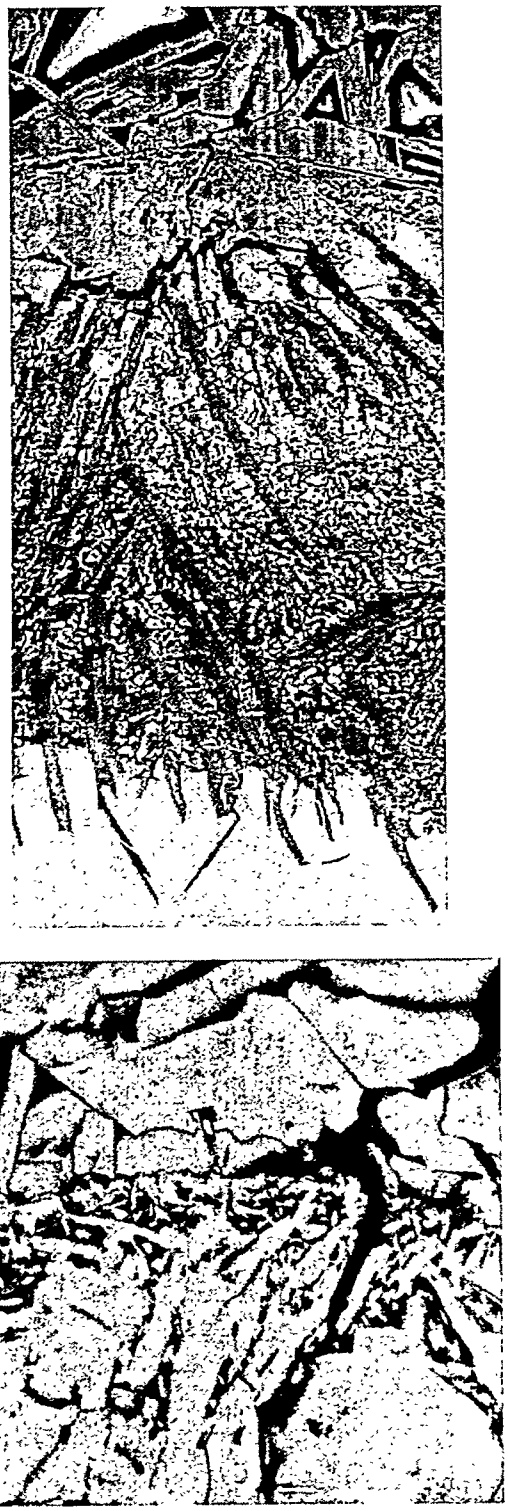

Figure 3.108: SEI micrographs of polished cross-section of T7.572 after 100 hrs of exposure at a) 1,500x, b) 5,000x

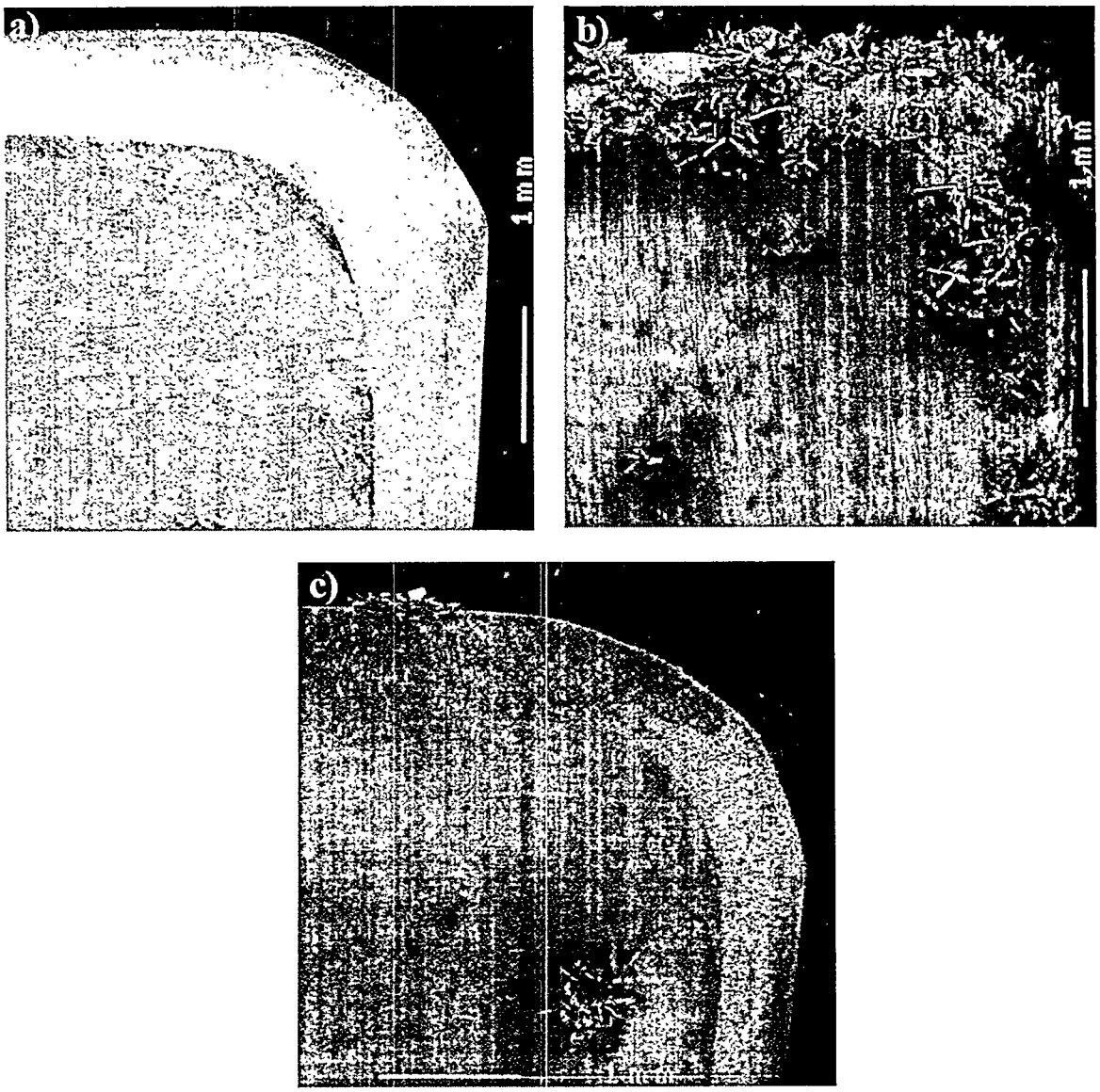

Figure 3.109: Low magnification (20x) SEI micrographs of T1072 at various times. a) 2 hrs, b) 50 hrs, c) 100 hrs

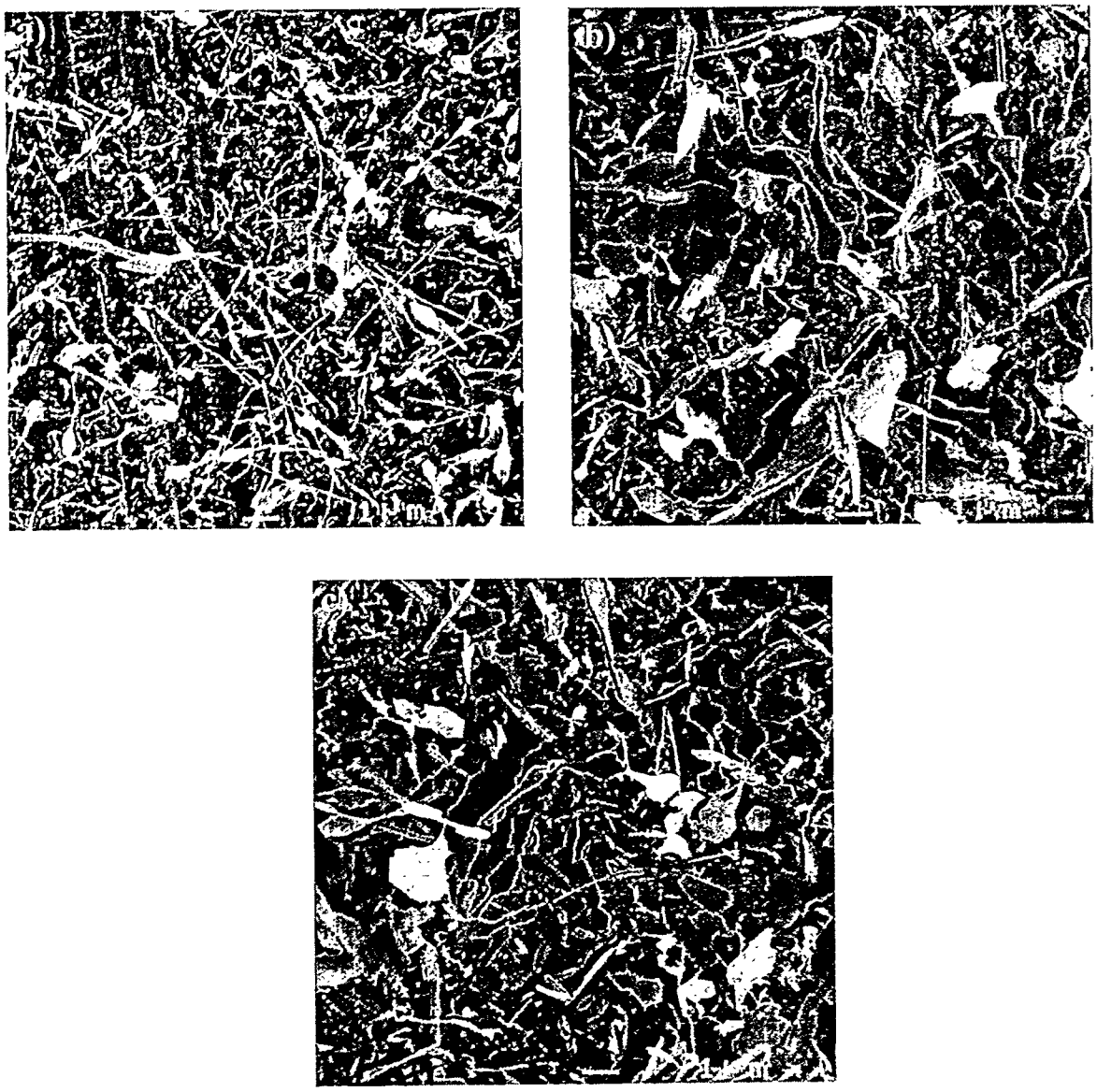

Figure 3.110: SEI micrographs of T1072 showing surface scale at various times a) 2 hrs, b) 50 hrs, c) 100 hrs (5,000x)

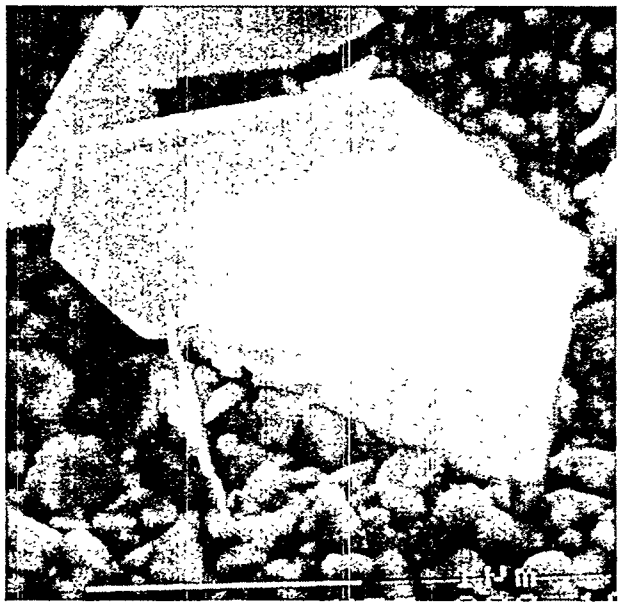

Figure 3.111: SEI micrograph showing platelet growing from granular scale, T1072. 35,000x

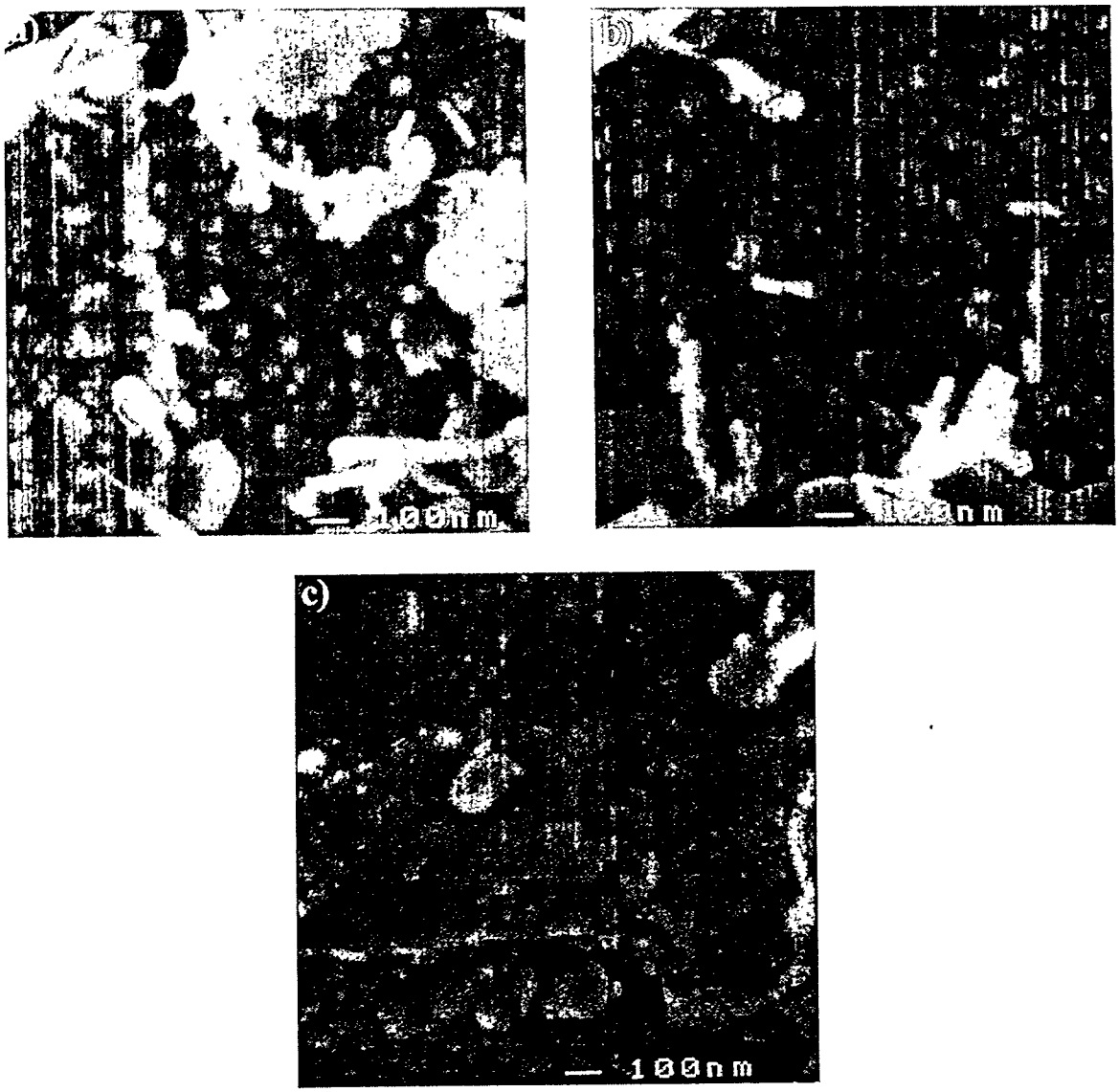

Figure 3.112: SEI micrographs showing the granular scale at various times for T1072. a) 2 hrs, b) 50 hrs, c) 100 hrs (50,000x)

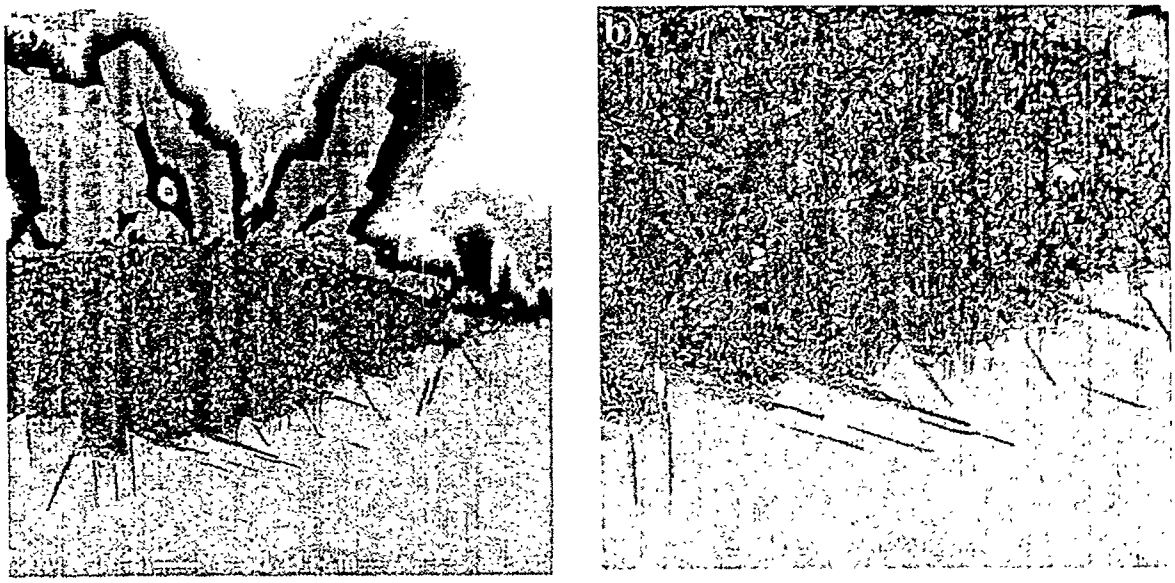

Figure 3.113: SEI micrographs of polished cross-section for T1072 after 50 hrs exposure. a) 600x, b) 1,200x

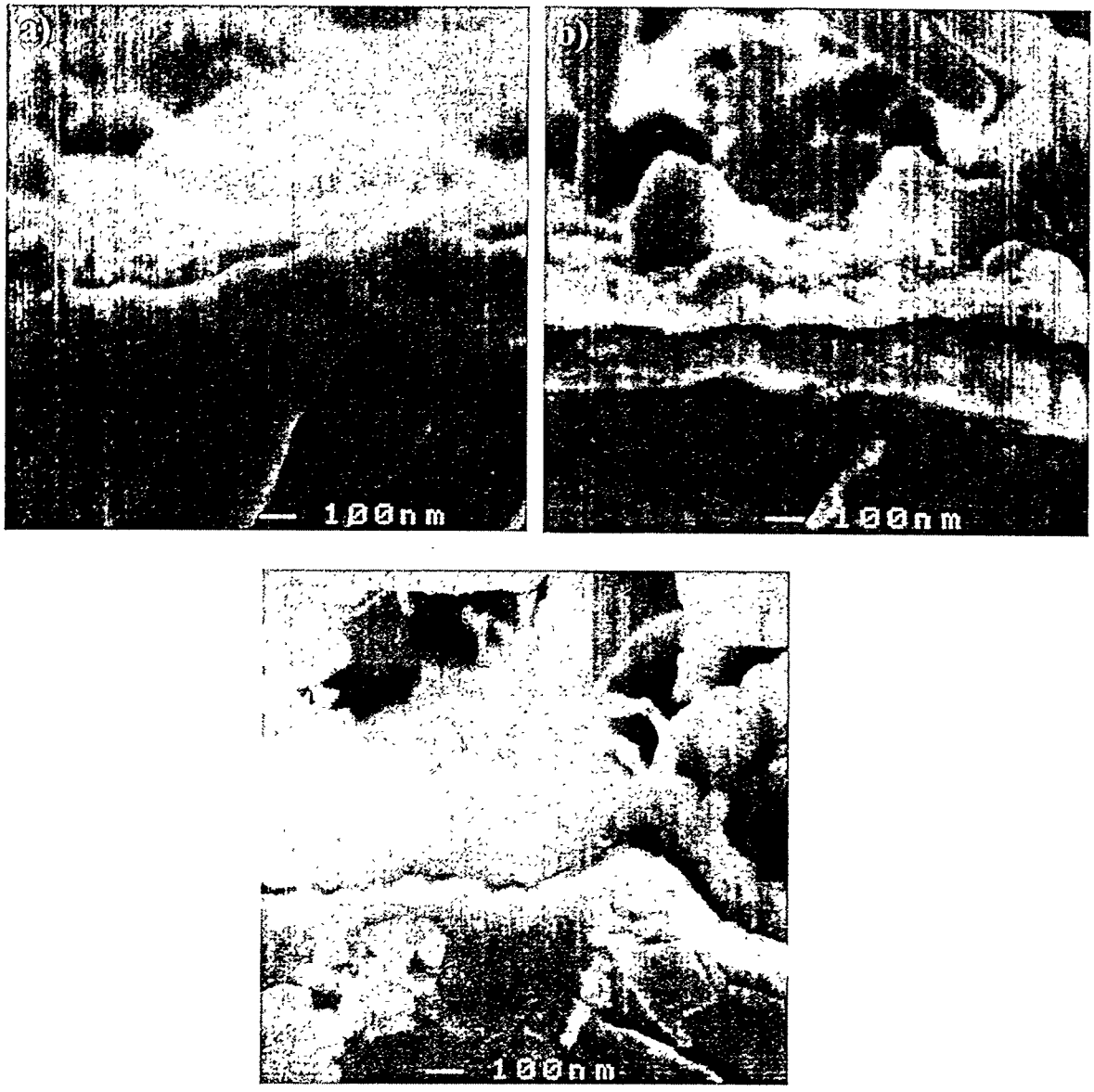

Figure 3.114: SEI micrographs of fractured cross-sections for various times for T1072. a) 2 hrs, b) 50 hrs, c) 100 hrs (50,000x)

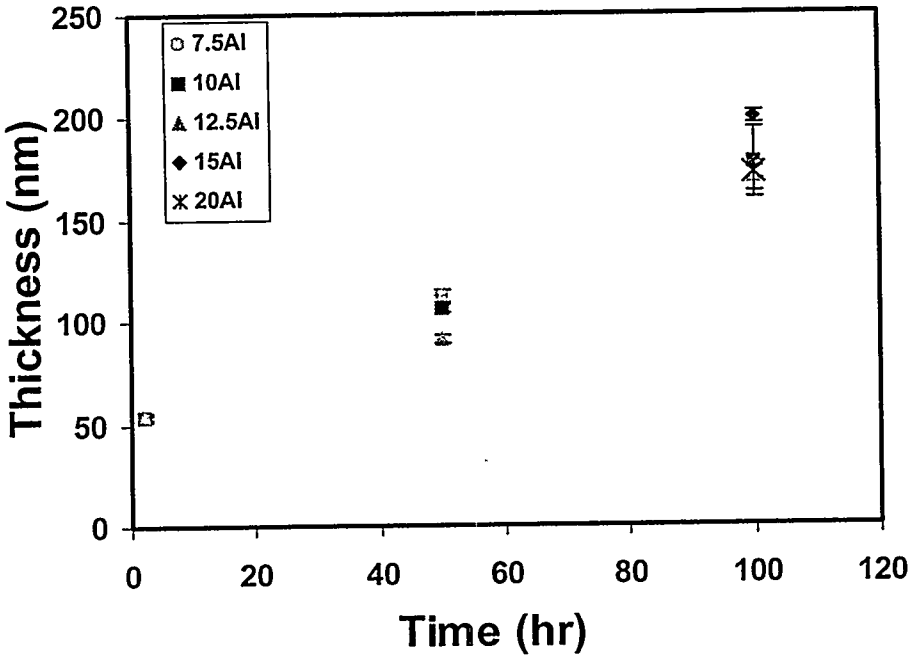

Figure 3.115: Plot of alumina cross-sectional scale thickness as a function of time for various alloys.

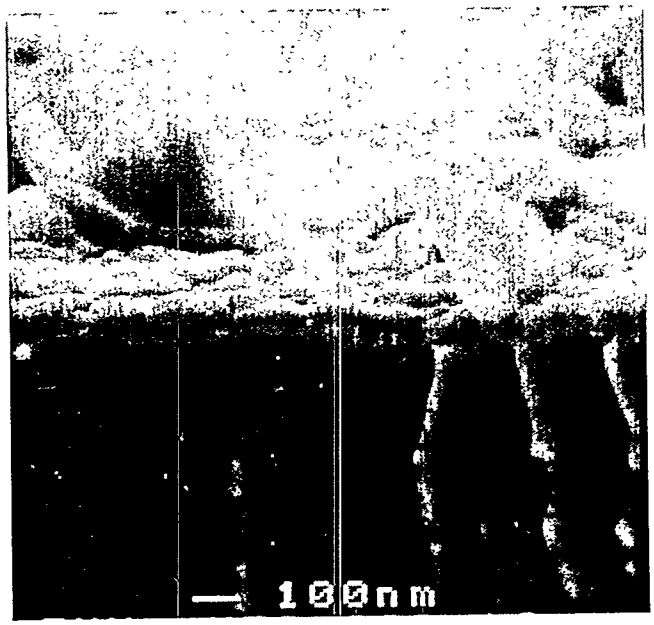

Figure 3.116: SEI micrograph of fractured cross-ssection showing growth of sulfide plate throgh alumina scale, T1072 for 50 hrs. 50,000x

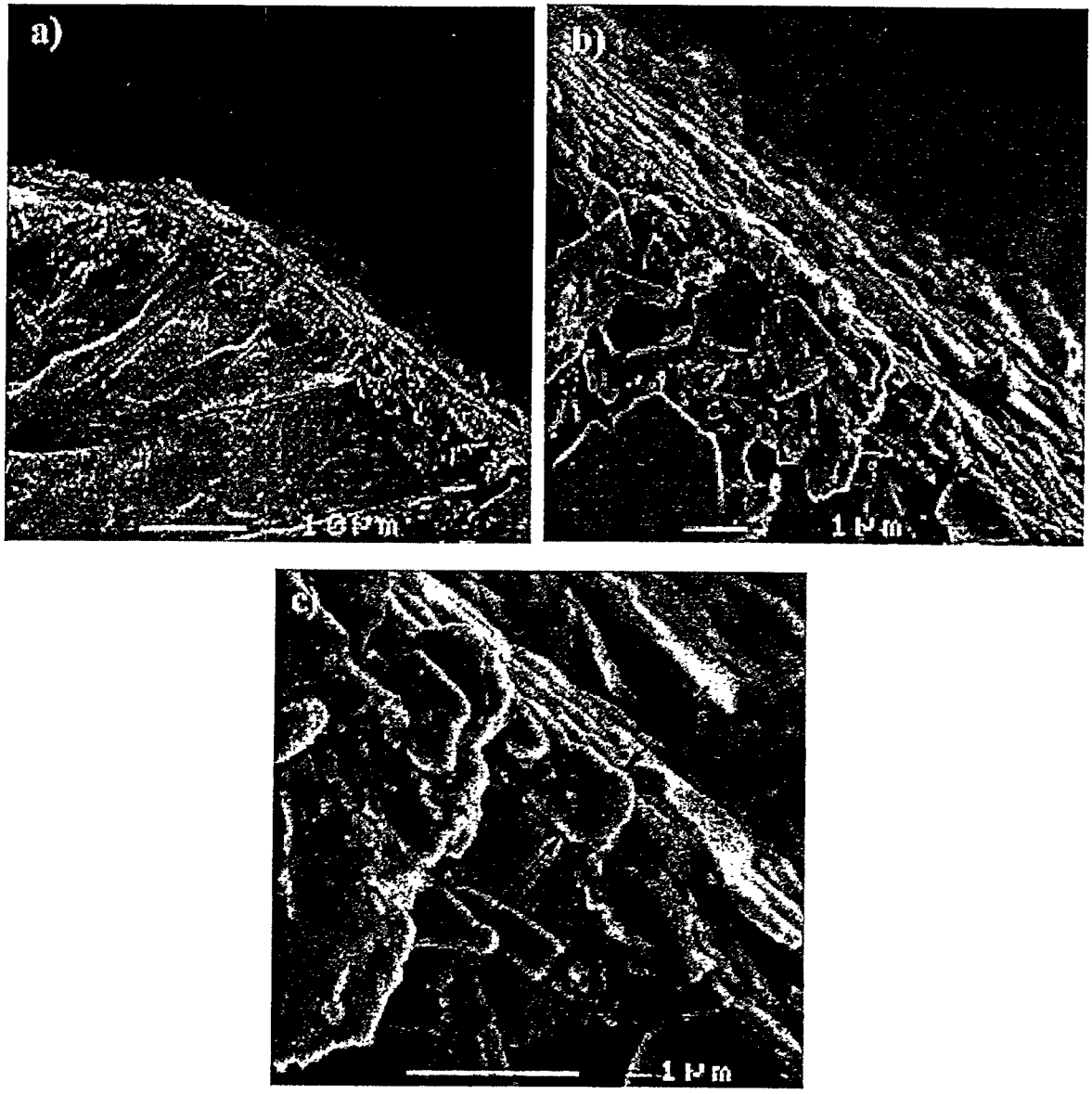

Figure 3.117: SEI micrographs of fractured cross-section on the corner of sample T1072 for 50 hrs exposure. Arrows indicate scale thickness. a) 1,500x, b) 9,000x, and c) 25,000x

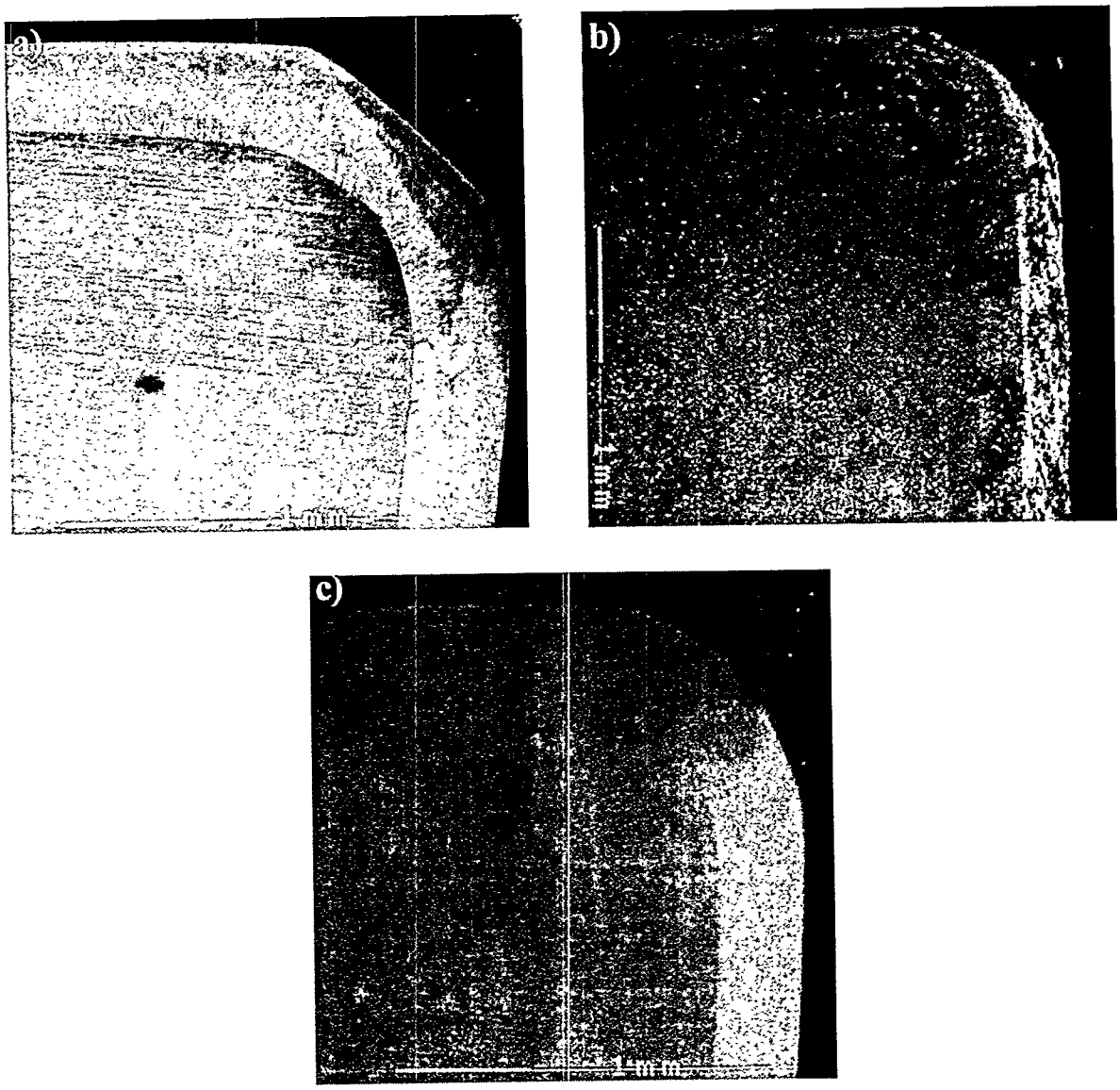

Figure 3.118: Low magnification (20x) SEI micrographs of T12.572 at various times. a) 2 hrs, b) 50 hrs, and c) 100 hrs

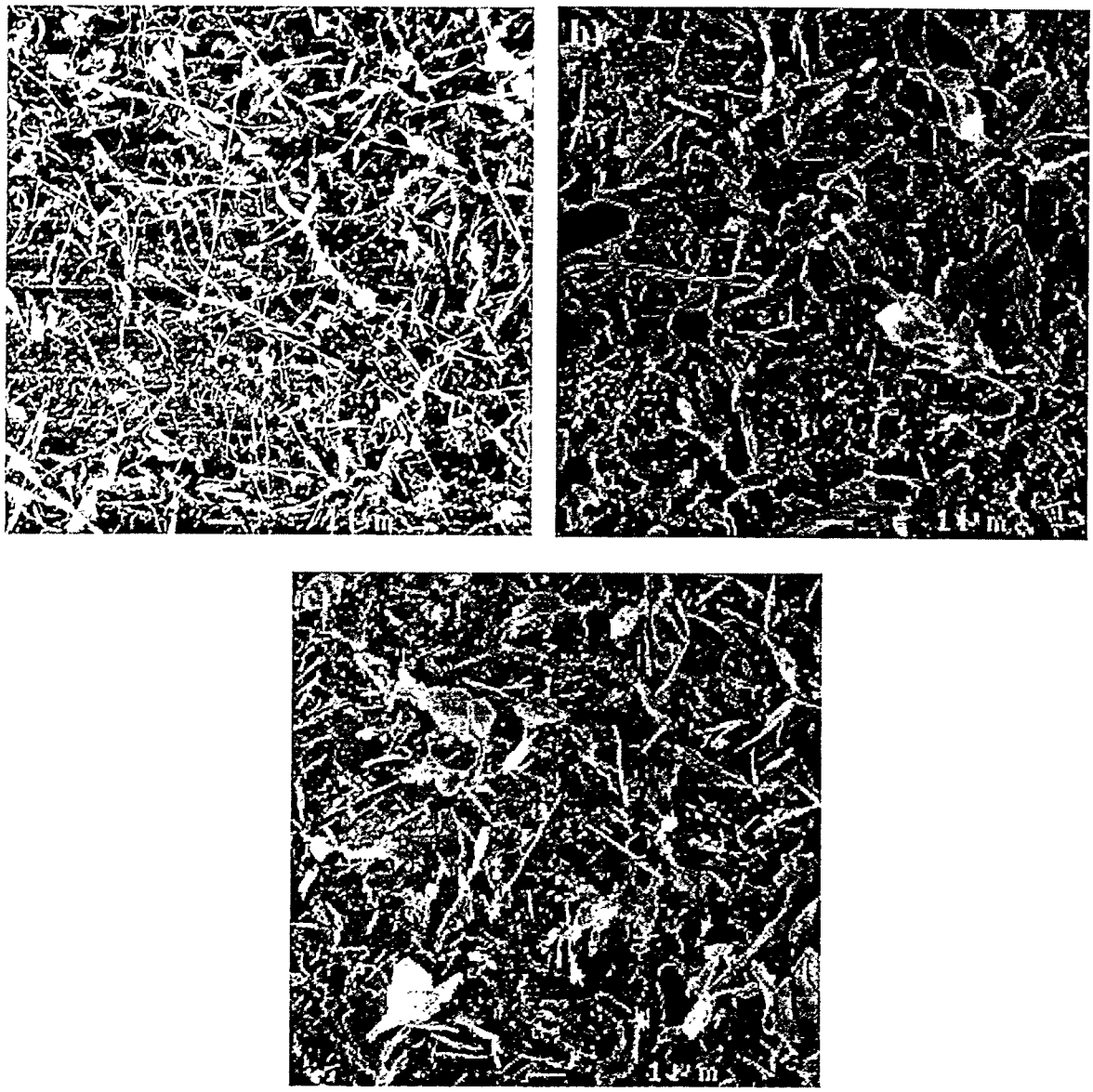

Figure 3.119: SEI micrographs of T12.572 showing surface scale at various times.
a) 2 hrs, b) 50 hrs, and c) 100 hrs

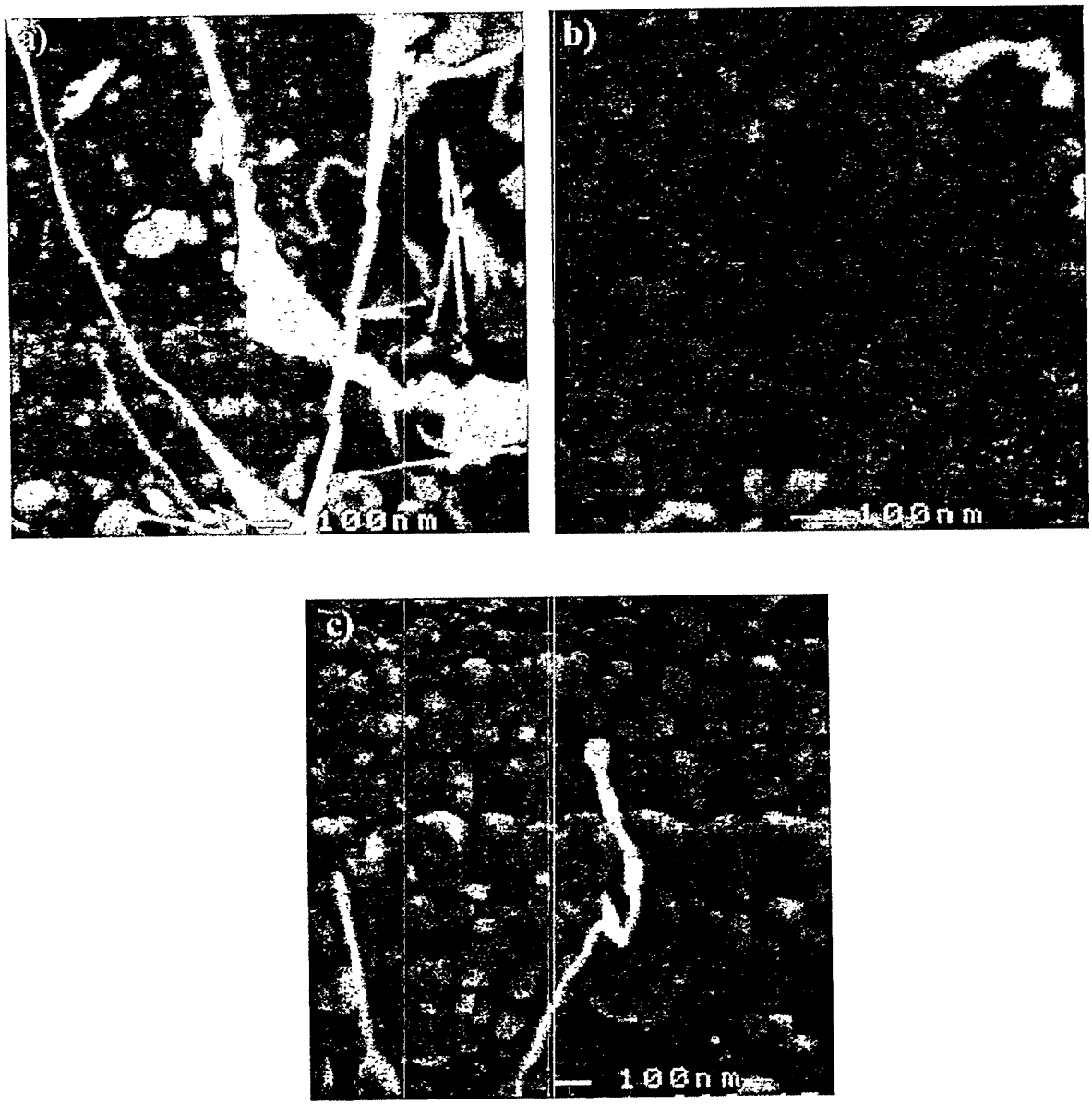

Figure 3.120: SEI micrographs of T12.572 showing the granular surface scale at various times. a) 2 hrs, b) 50 hrs, and c) 100 hrs

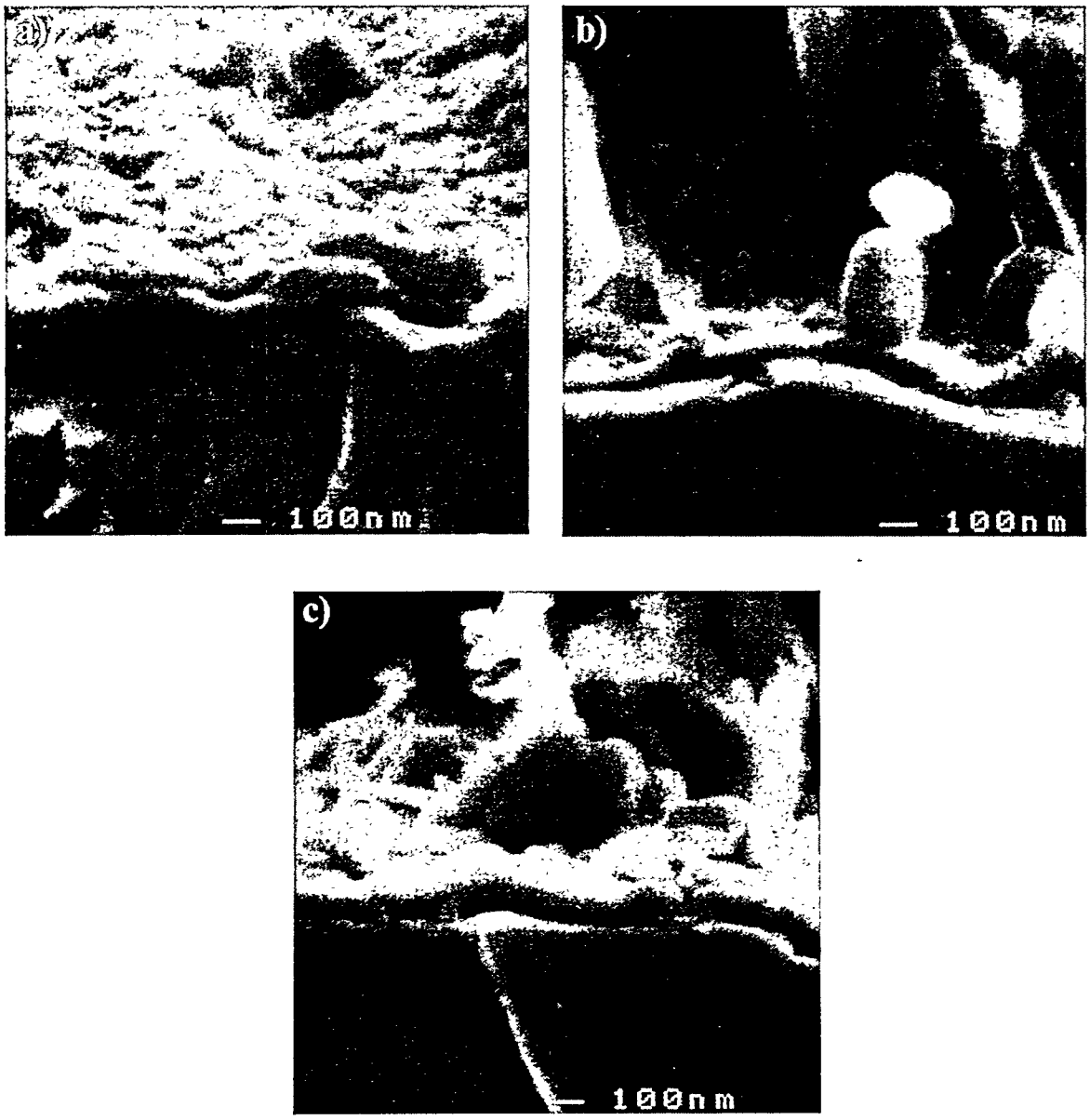

Figure 3.121: SEI micrographs showing fractured cross-section of T12.572 at various times. a) 2 hrs, b) 50 hrs, and c) 100 hrs

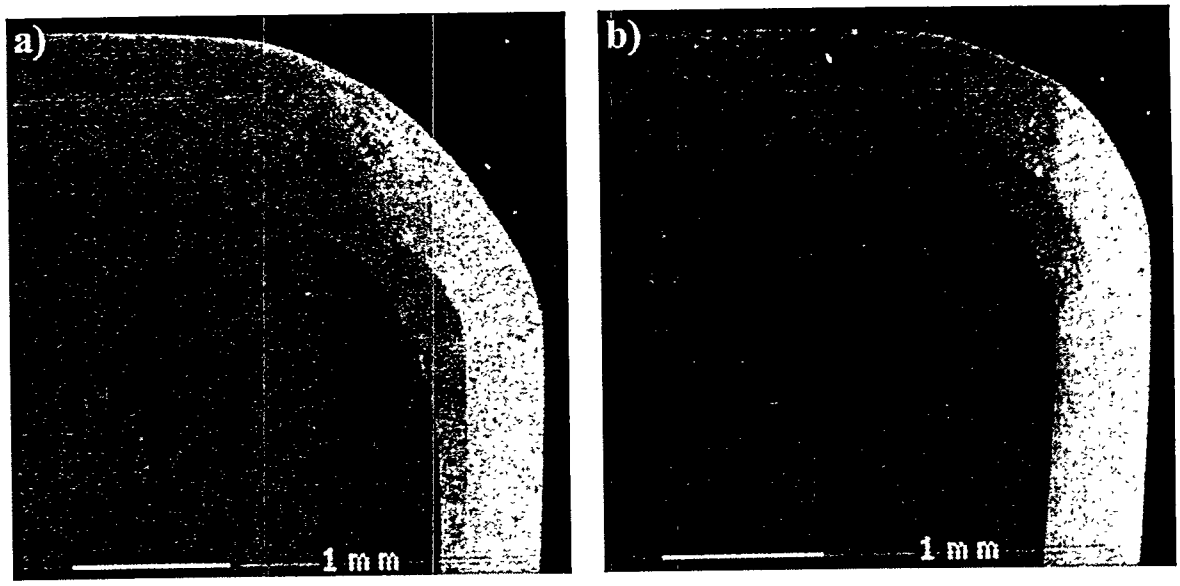

Figure 3.122: Low magnification (20x) SEI micrographs for a) T1572 and b) T2072.

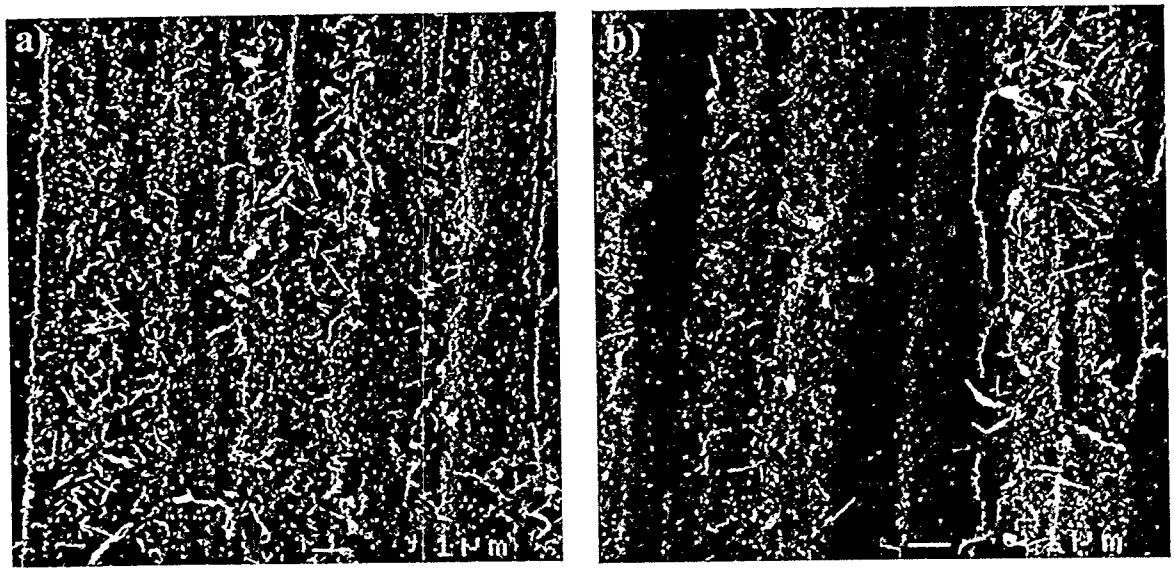

Figure 3.123: SEI micrograph showing the platelets for a) T1572 and b) T2072. (5000x)

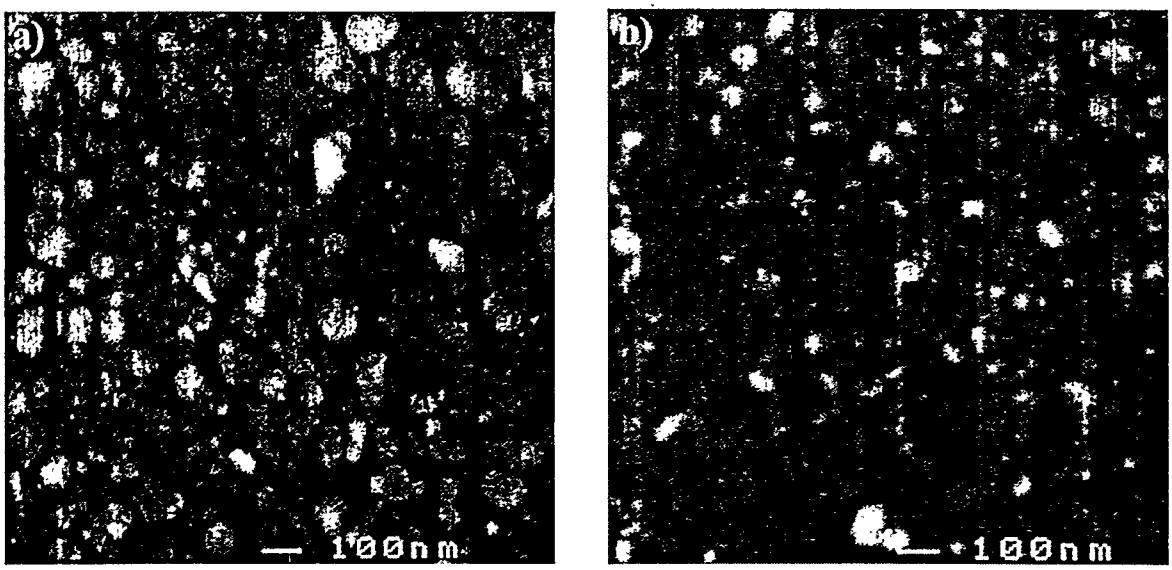

Figure 3.124: SEI micrographs showing the granular surface scales for a) T1572 and b) T2072. (50,000x)

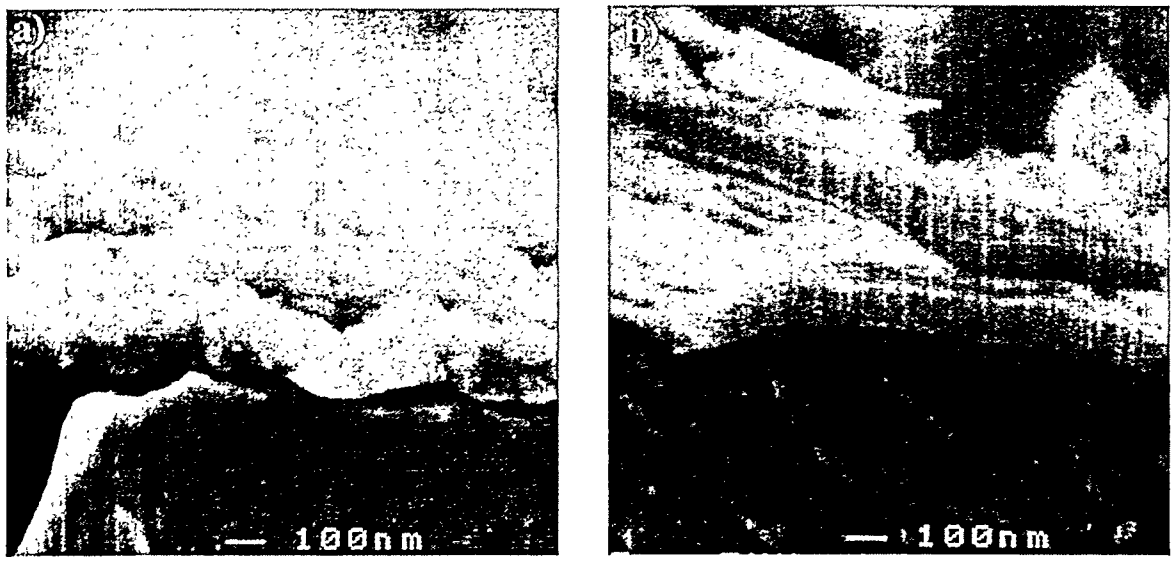

Figure 3.125: SEI micrographs showing fractured cross-sections for a) T1572 and b) T2072. 50,000x

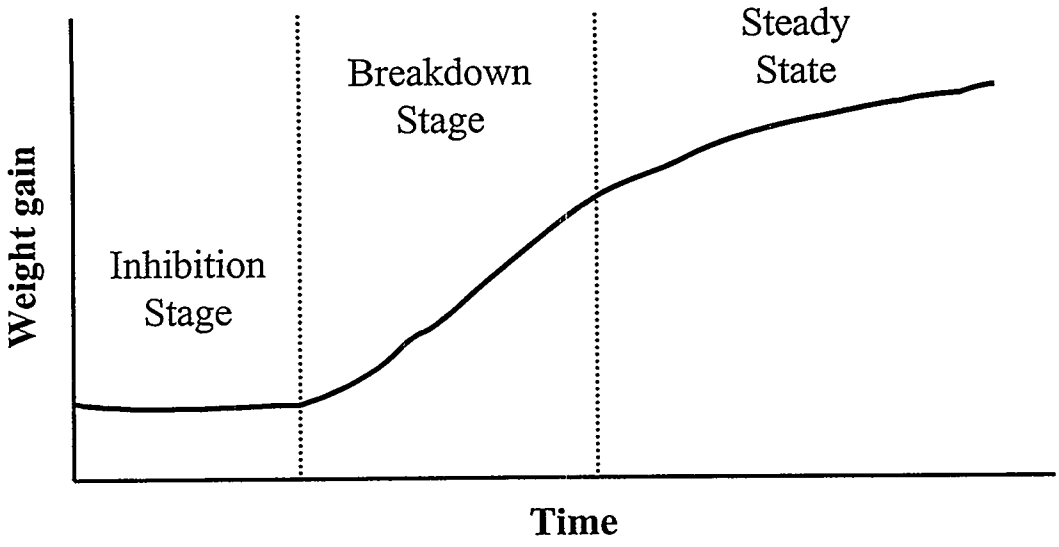

Figure 3.126: Schematic showing the three stages of corrosion behavior.

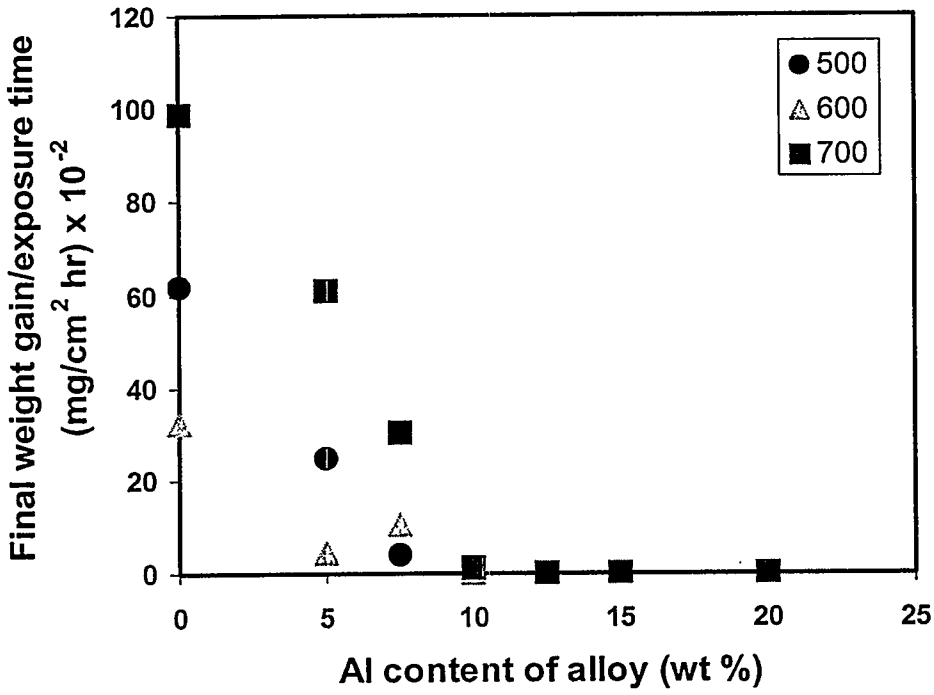

Figure 3.127: Plot of weight gain normalized for exposure time as a function of aluminum content of the alloy.

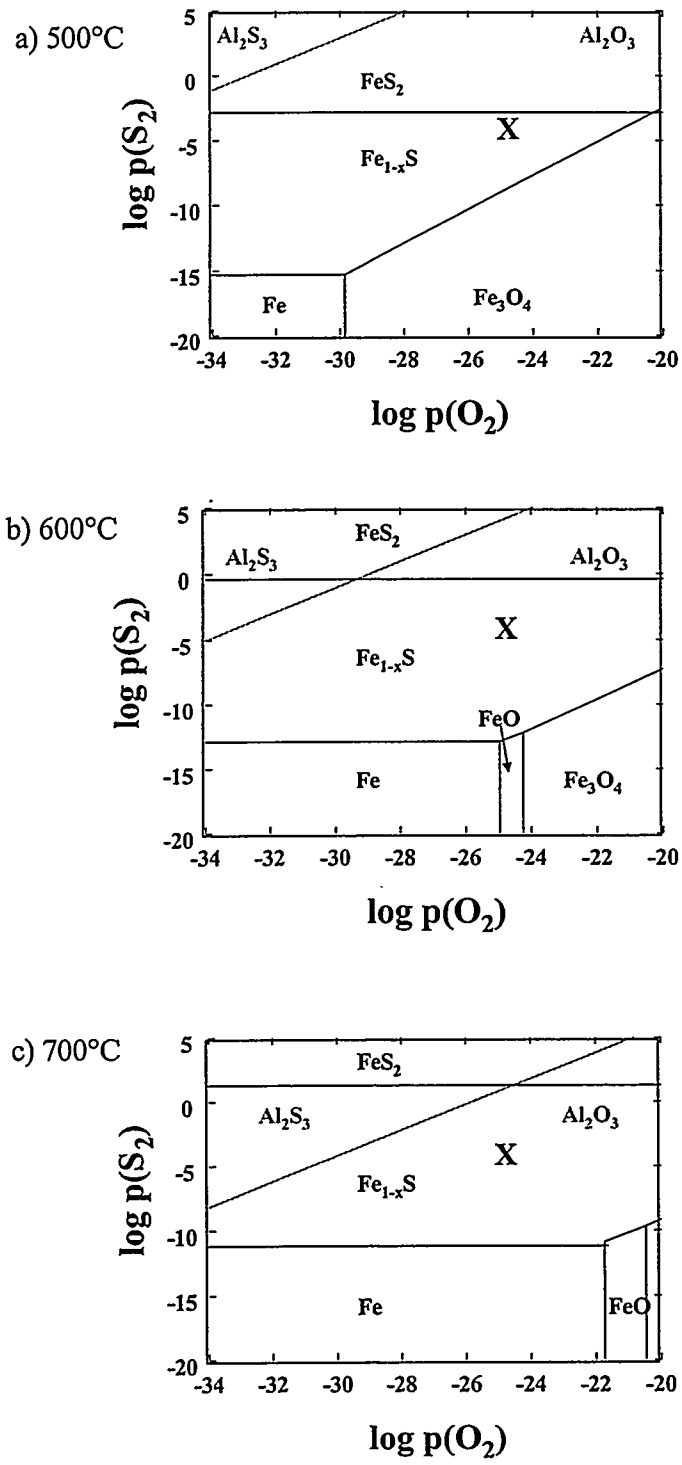

Figure 3.128: Superimposed thermostability diagrams for Al and Fe at a) 500°C, b) 600°C, and c) 700°C.

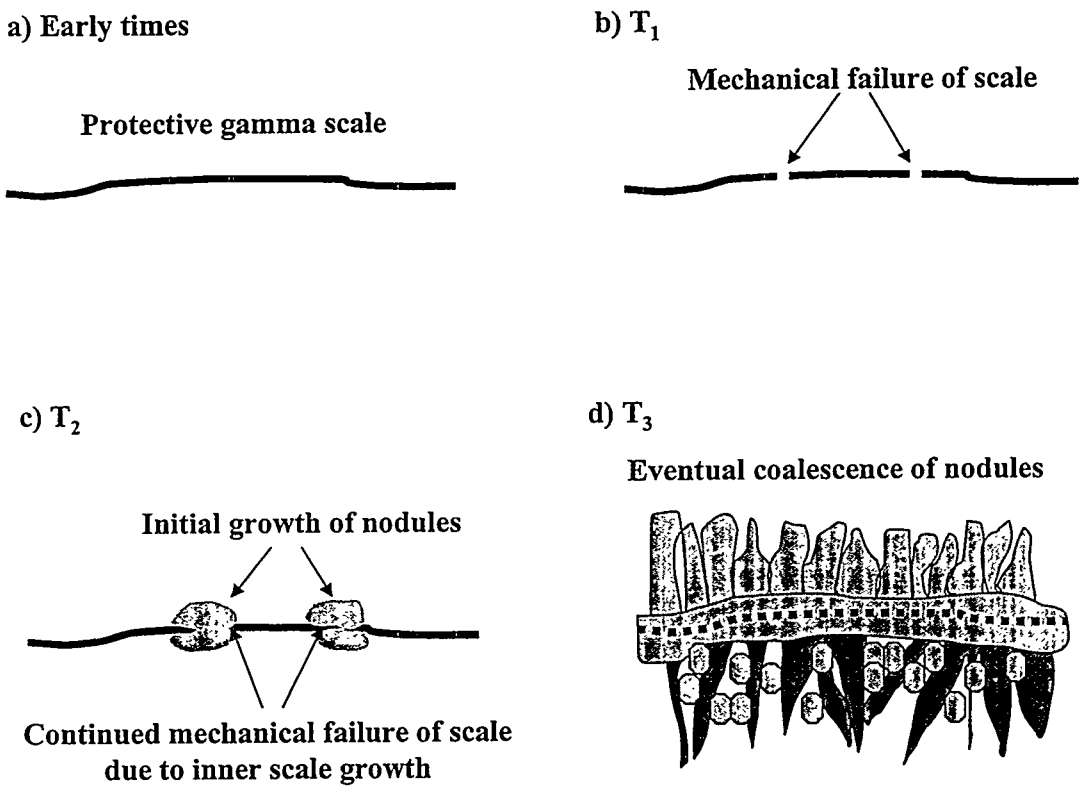

Figure 3.129: Schematic showing the growth of scales at various times for breakdown stage, where $T_3 > T_2 > T_1 >$ early times. a) initial protection by gamma scale, b) mechanical failure of scale with ingress of sulfur, c) formation and growth of nodules leads to further degradation of the initial passive scale, d) final growth stage of coalesced nodules, remnants of original passive scale can still be observed.

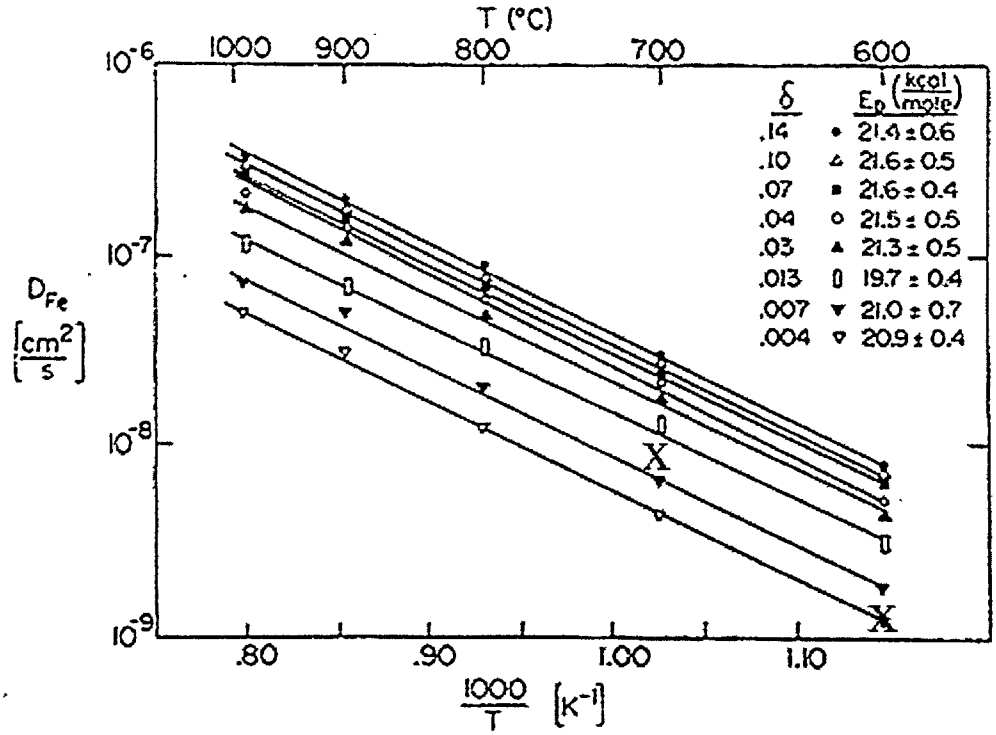

Figure 3.130: Temperature dependence of the iron self-diffusion coefficient at different levels of nonstoichiomery for iron sulfide. The blue "x" indicates the calculated diffusion coefficient for the T062 sample, while the red "x" is for T072. [Fryt 1979b]

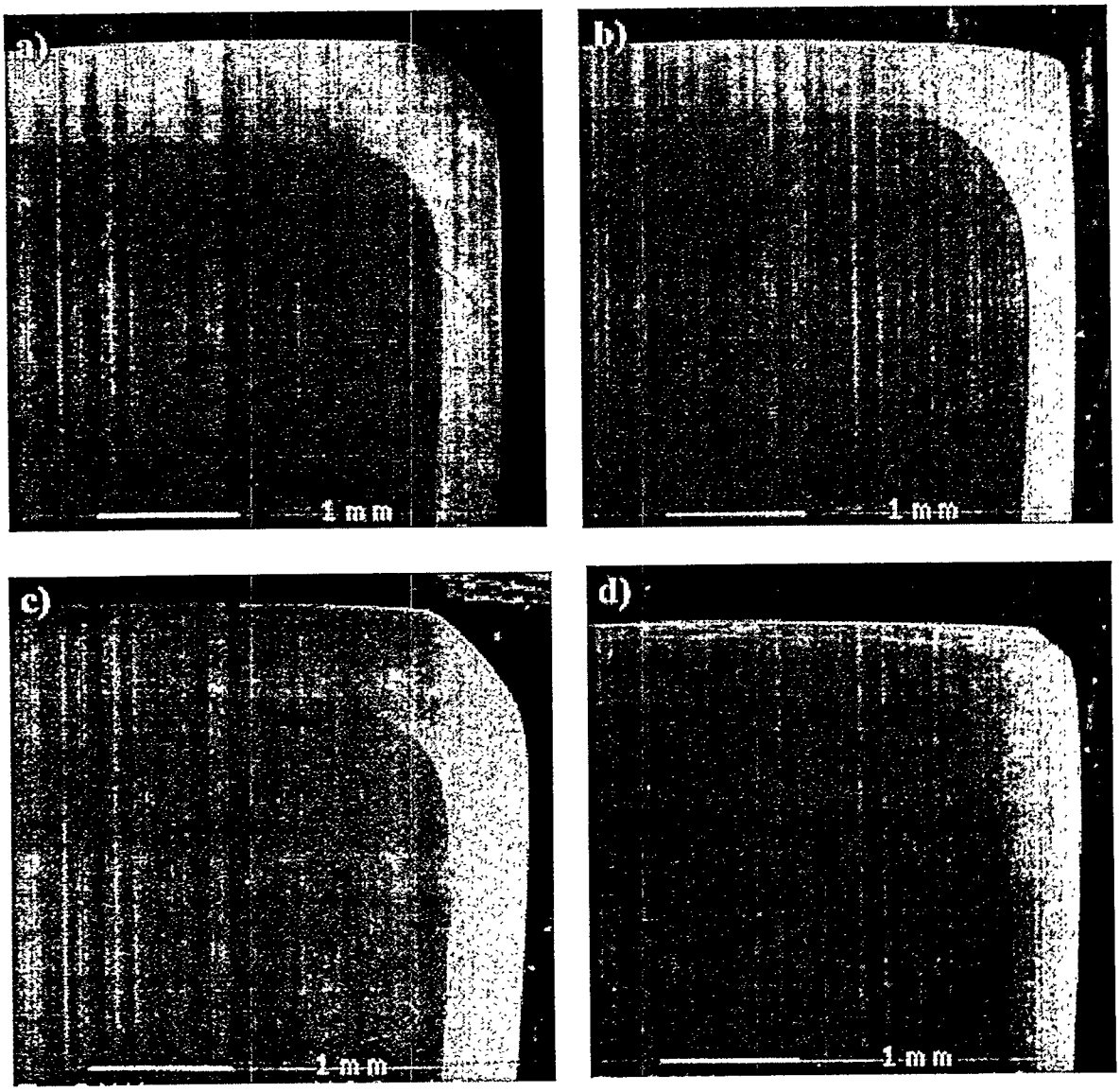

Figure 3.131: Low magnification (20x) SEI micrographs of Fe-Al alloys exposed at 500°C. a) 5 wt% Al, b) 7.5 wt% Al, c) 10 wt% Al, and d) 12.5 wt% Al

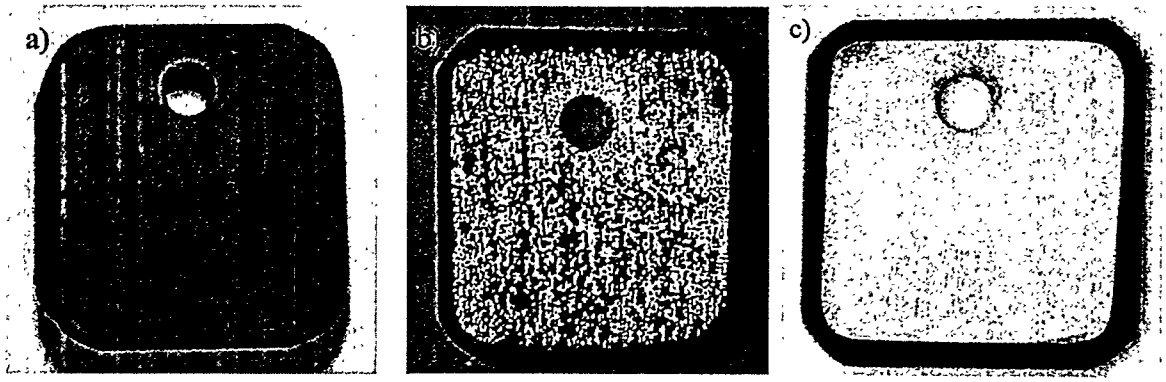

Figure 3.132: Light optical macrographs showing the various surface scale colorings and morphologies.

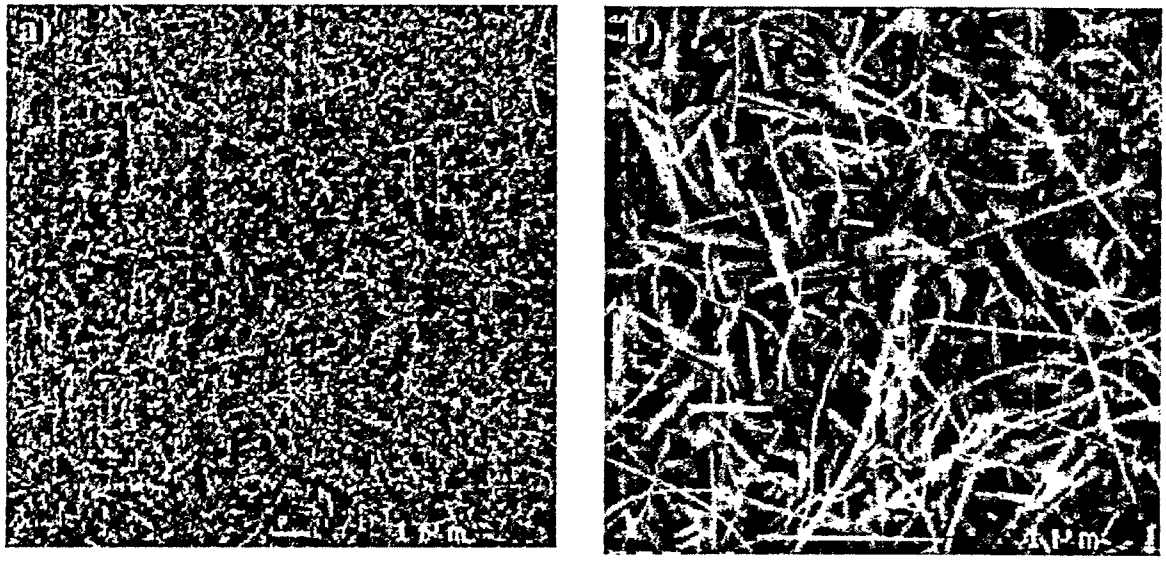

Figure 3.133: SEI micrographs of the 5Al surface scale exposed at 500°C.
a) 5,000x, b) 25,000x

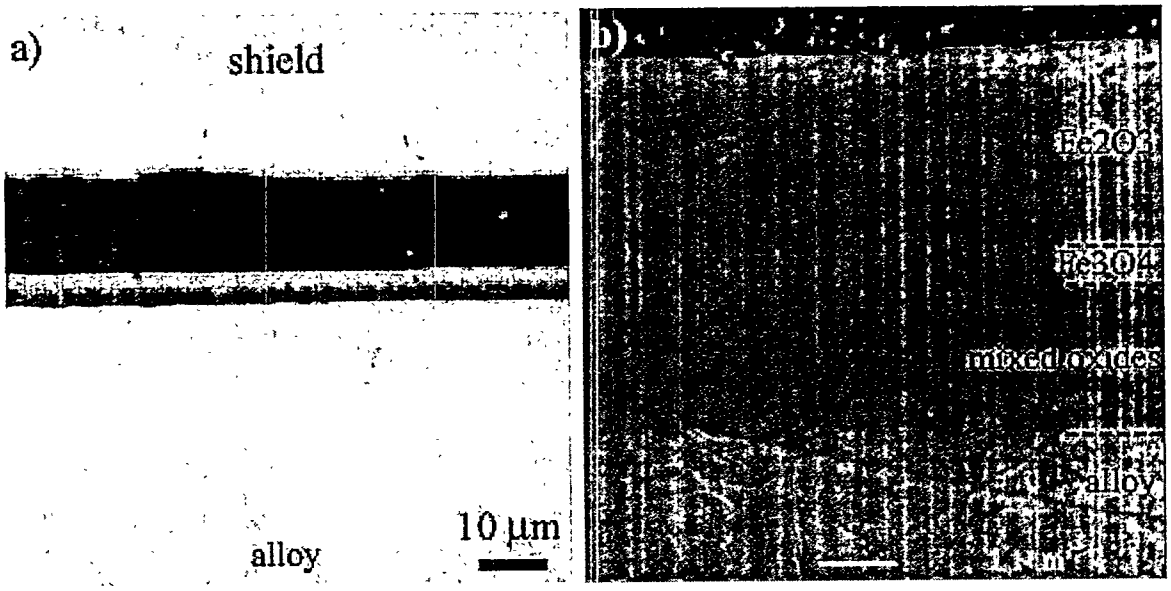

Figure 3.134: Polished cross-section of the 5Al sample exposed at 500°C. a) LOM at 1,000x, b) SEI at 10,000x

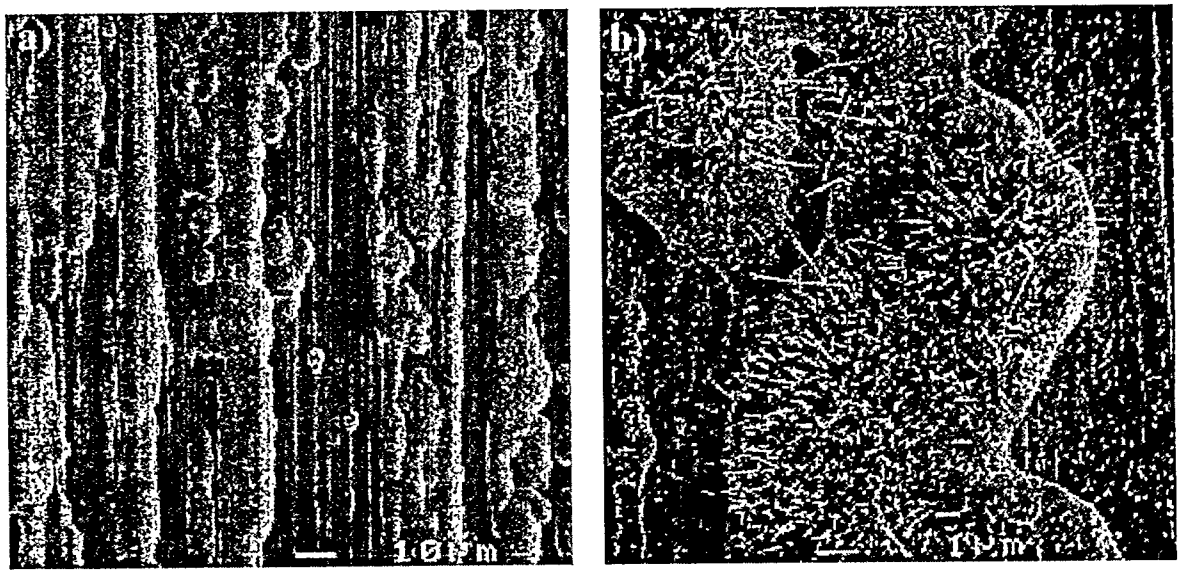

Figure 3.135: SEI micrographs of the 7.5Al surface scale exposed at 500°C (thick growth). a) 500x, b) 5,000x

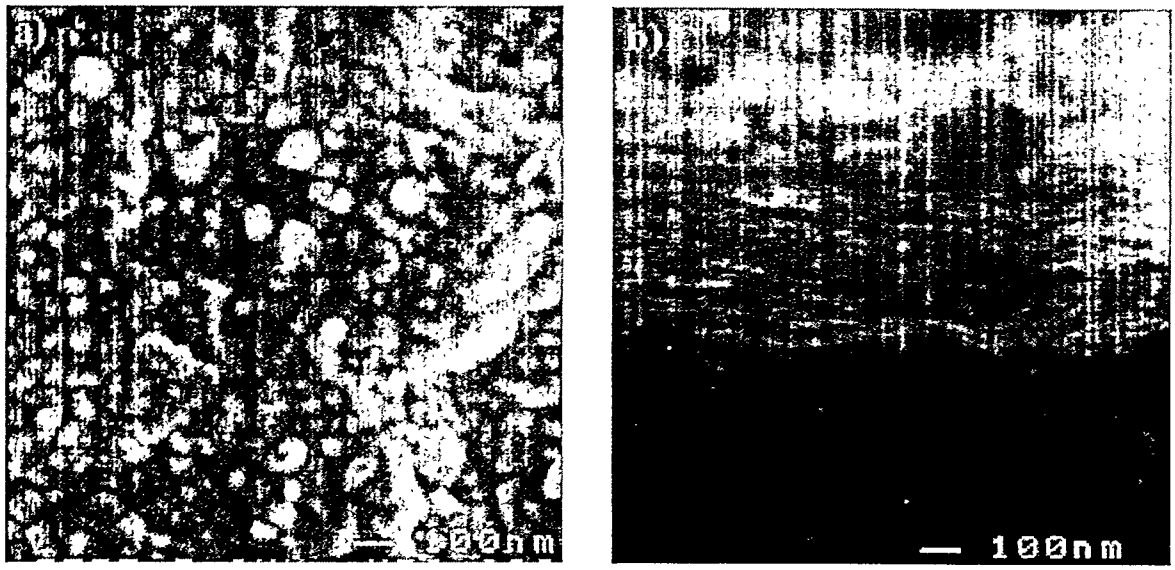

Figure 3.136: SEI micrographs of the 7.5Al surface scale exposed at 500°C. a) Granular scale at 50,000x, b) fractured cross-section at 50,000x

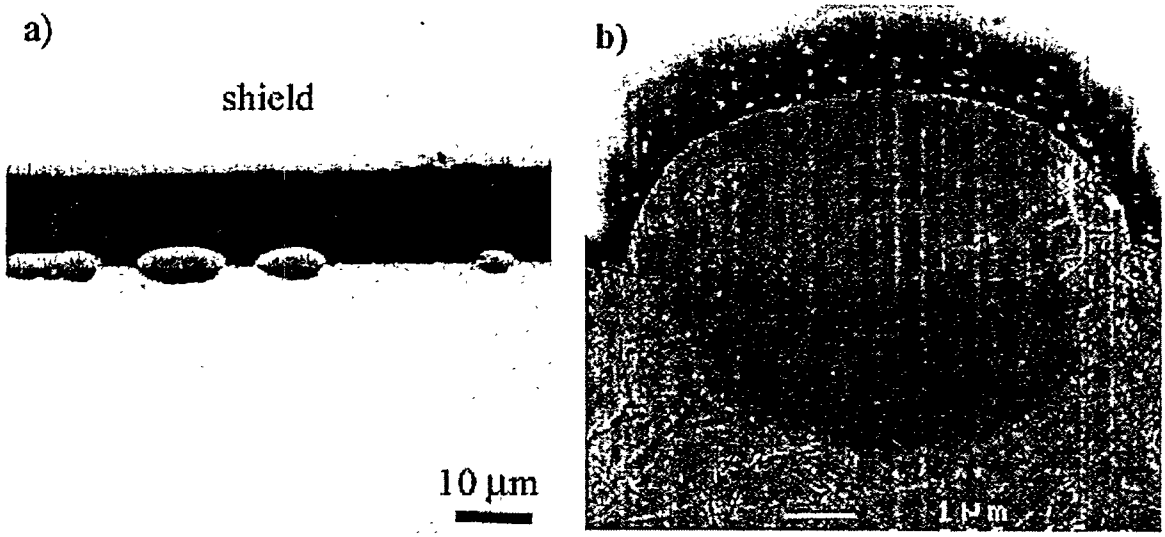

Figure 3.137: Polished cross-section of the 7.5Al sample exposed at 500°C. a) LOM at 1,000x, b) SEI at 10,000x

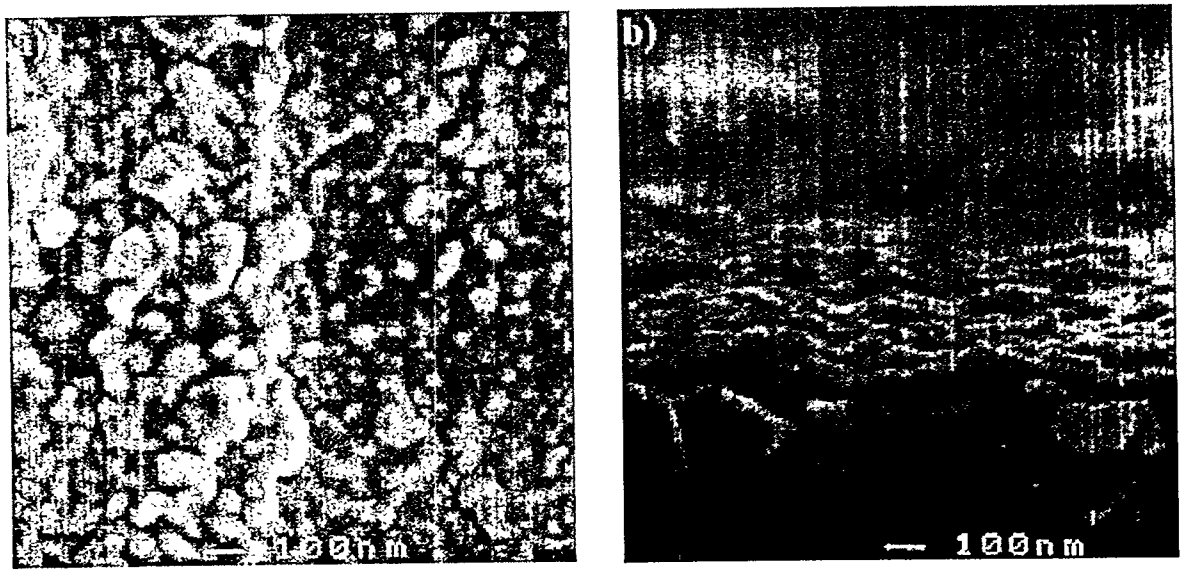

Figure 3.138: Characteristic SEI micrograph of the surface scale found on 10Al and 12.5Al exposed at 500°C. a) granular scale at 50,000x, b) fractured cross-section at 50,000x

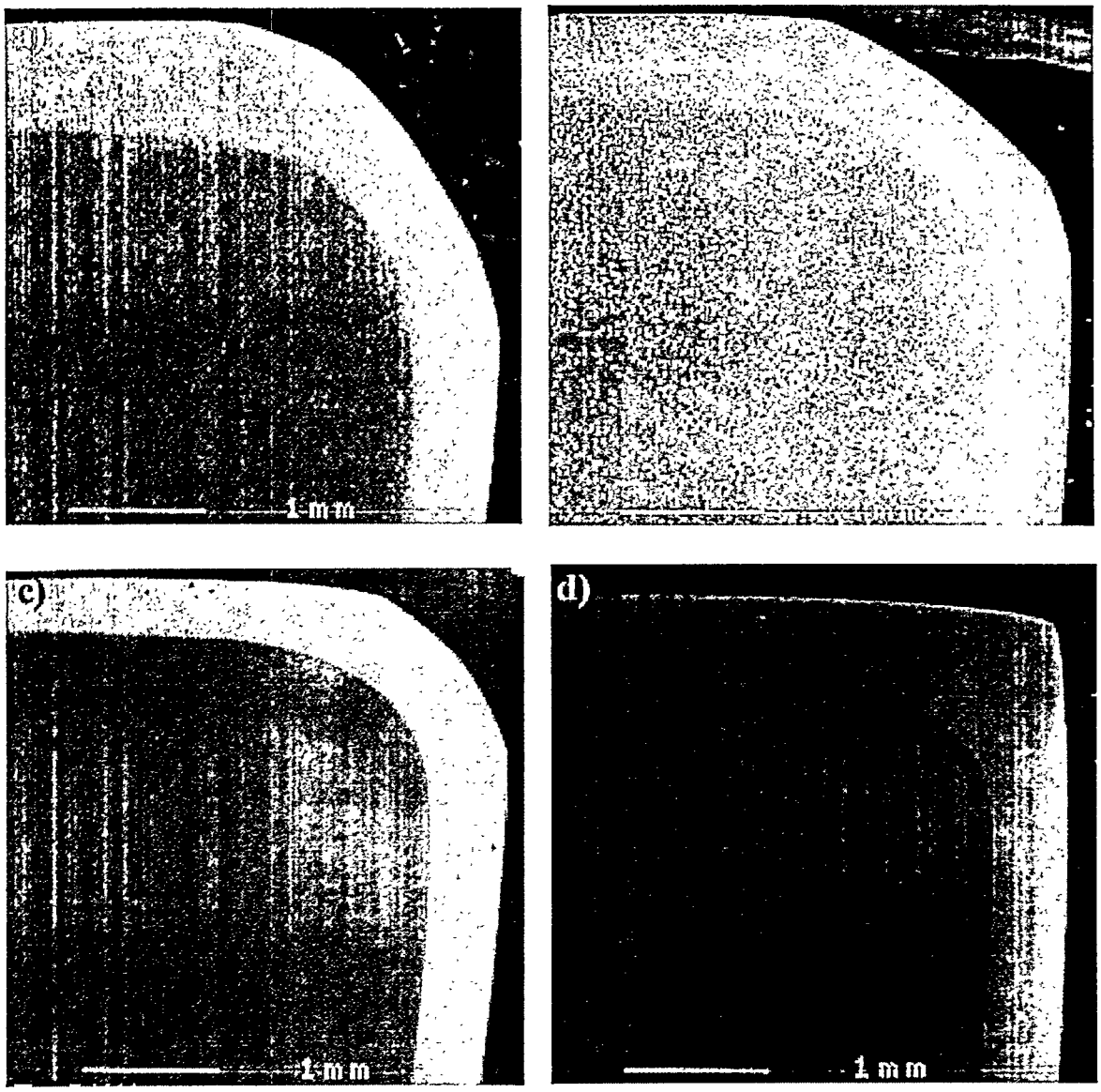

Figure 3.139: Low magnification SEI micrographs of Fe-Al alloys exposed at 600°C. a) 5 wt% Al, b) 7.5 wt% Al, c) 10 wt% Al, and d) 12.5 wt% Al

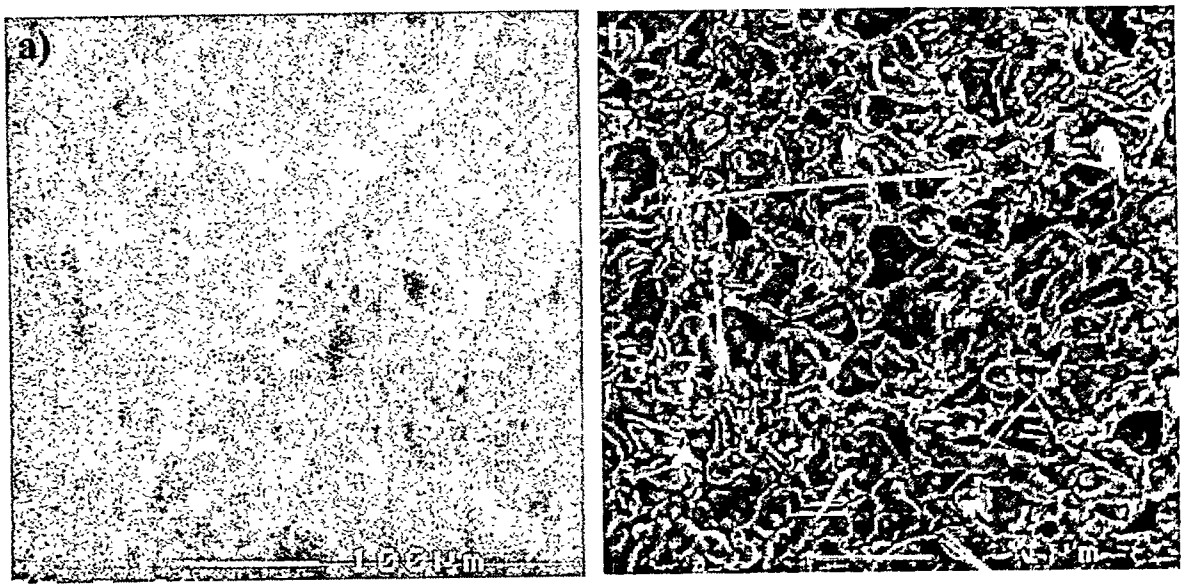

Figure 3.140: SEI micrographs of the 5Al surface scale exposed at 600°C. a) observation of grain boundary at 200x, b) porous surface scale at 15,000x

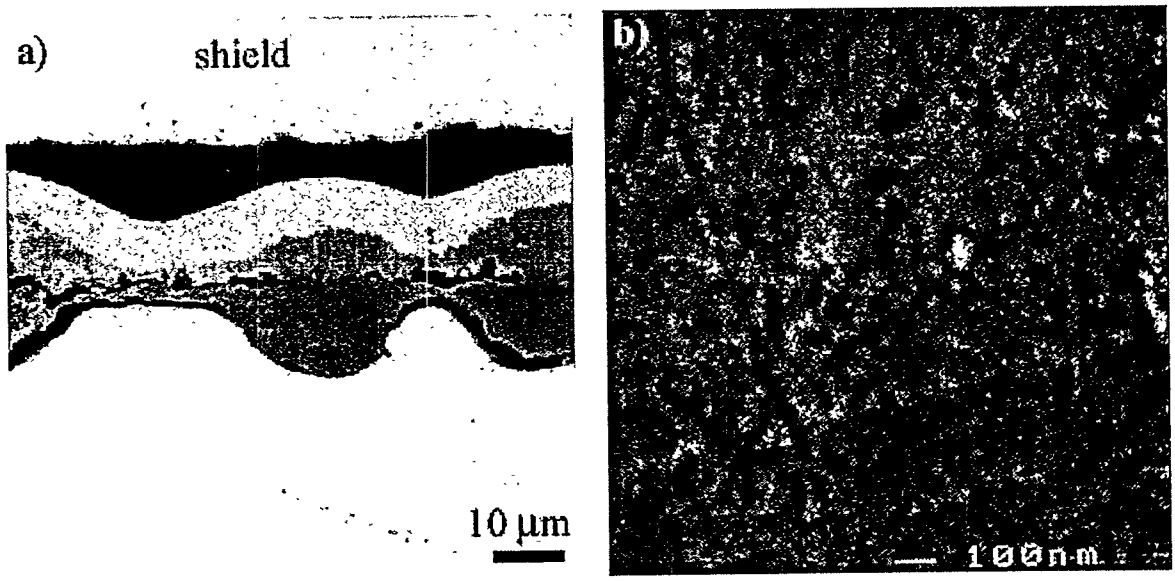

Figure 4.141: Polished cross-section of the 5Al sample exposed at 600°C. a) LOM at 1,000x, b) SEI of internal precipitate zone at 50,000x

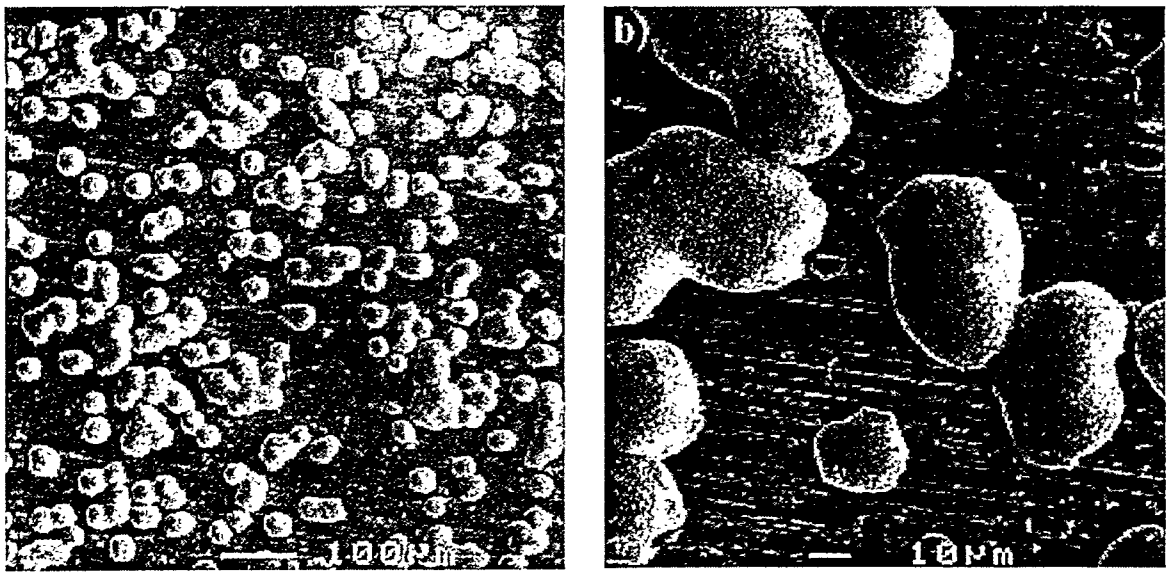

Figure 3.142: SEI micrographs of the 7.5Al surface scale exposed at 600°C. Nodules seen at a) 100x, b) 500x

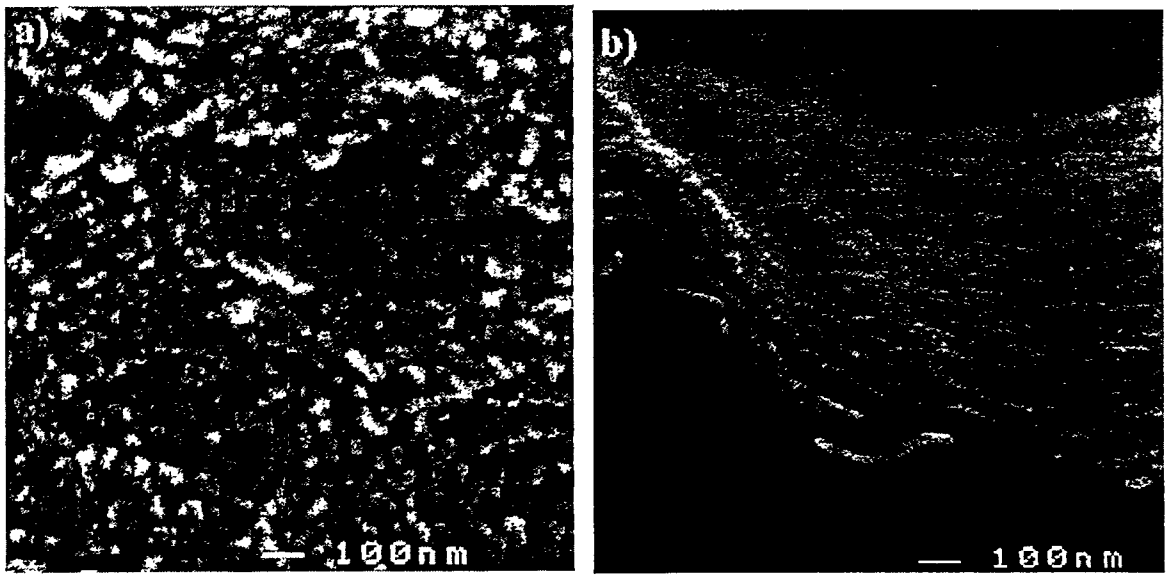

Figure 3.143: SEI micrographs of the 7.5Al surface scale exposed at 600°C (nodular free region). a) granular scale at 50,000x, b) fractured cross-section at 50,000x

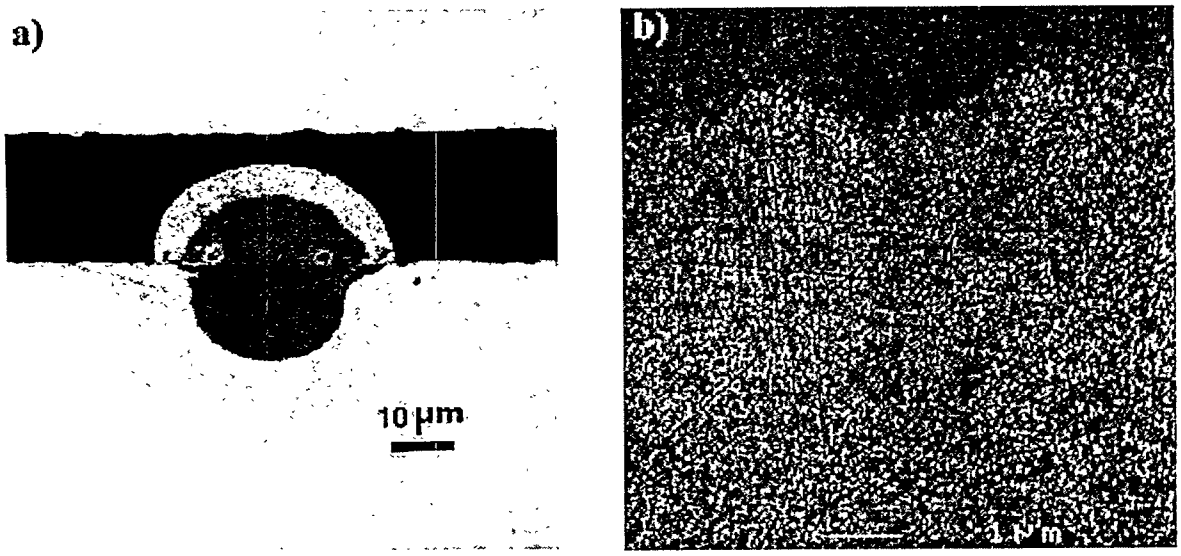

Figure 4.144: Polished cross-section of the 7.5Al sample exposed at 600°C.
a) LOM at 1,000x, b) internal precipitate zone at 10,000x

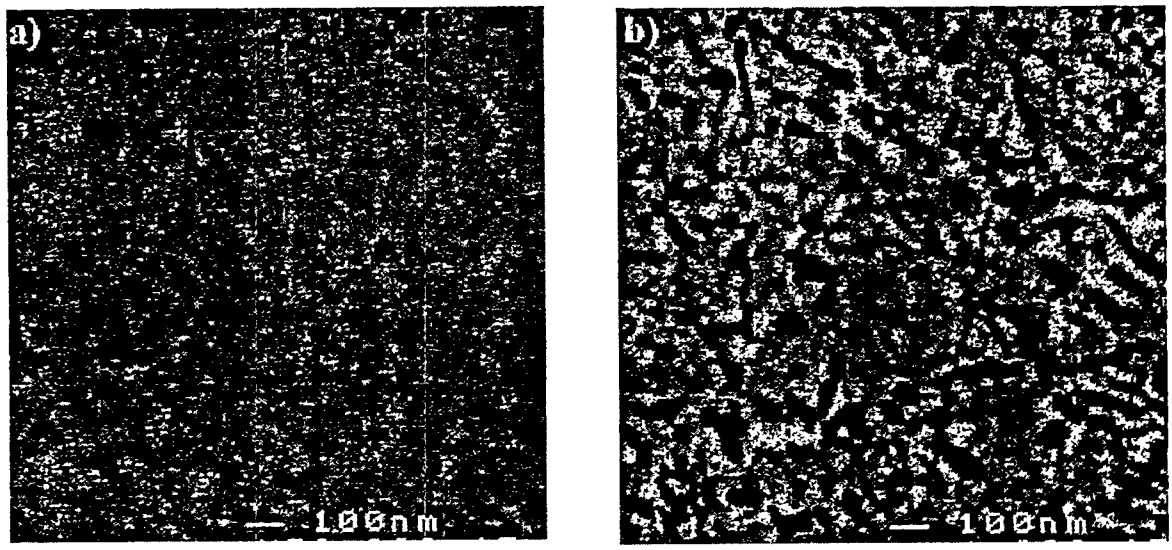

Figure 3.145: SEI micrograph showing the inner scales formed on the 7.5Al sample exposed at 600°C. a) multiphase zone at 50,000x, b) internal precipitate region at 50,000x

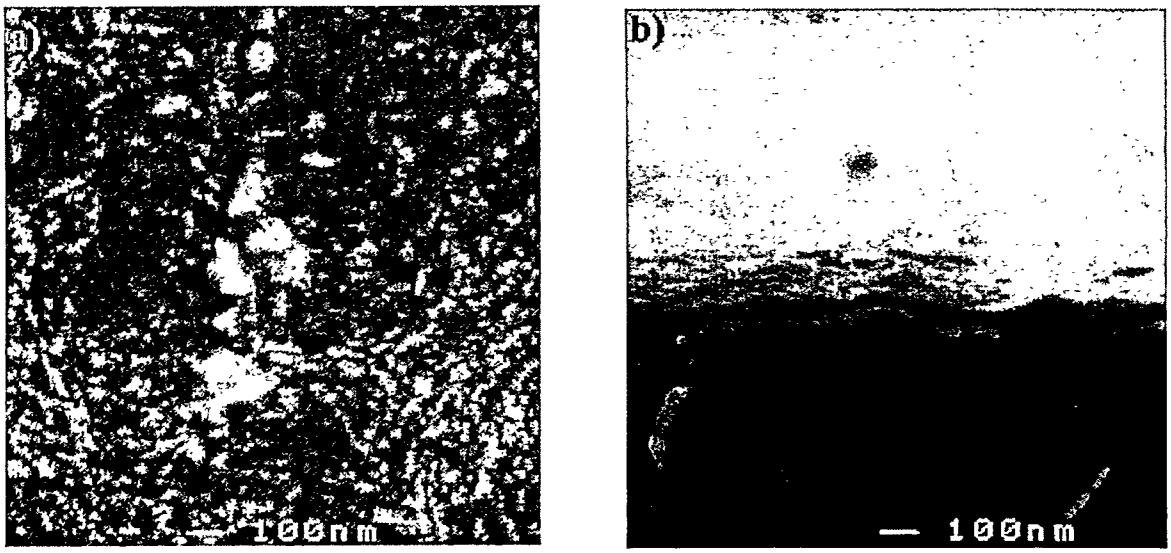

Figure 3.146: SEI micrographs of the surface scale found on 10Al exposed at 600°C.
a) granular scale at 50,000x, b) fractured cross-section at 50,000x

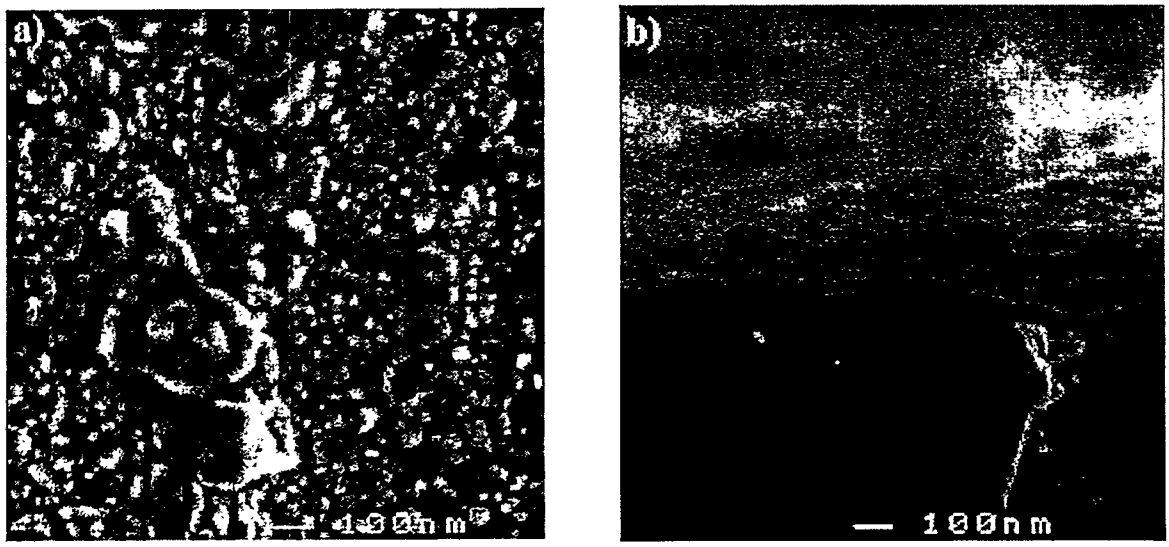

Figure 3.147: SEI micrographs of the surface scale found on 12.5Al exposed at 600°C.
a) granular scale at 50,000x, b) fractured cross-section at 50,000x

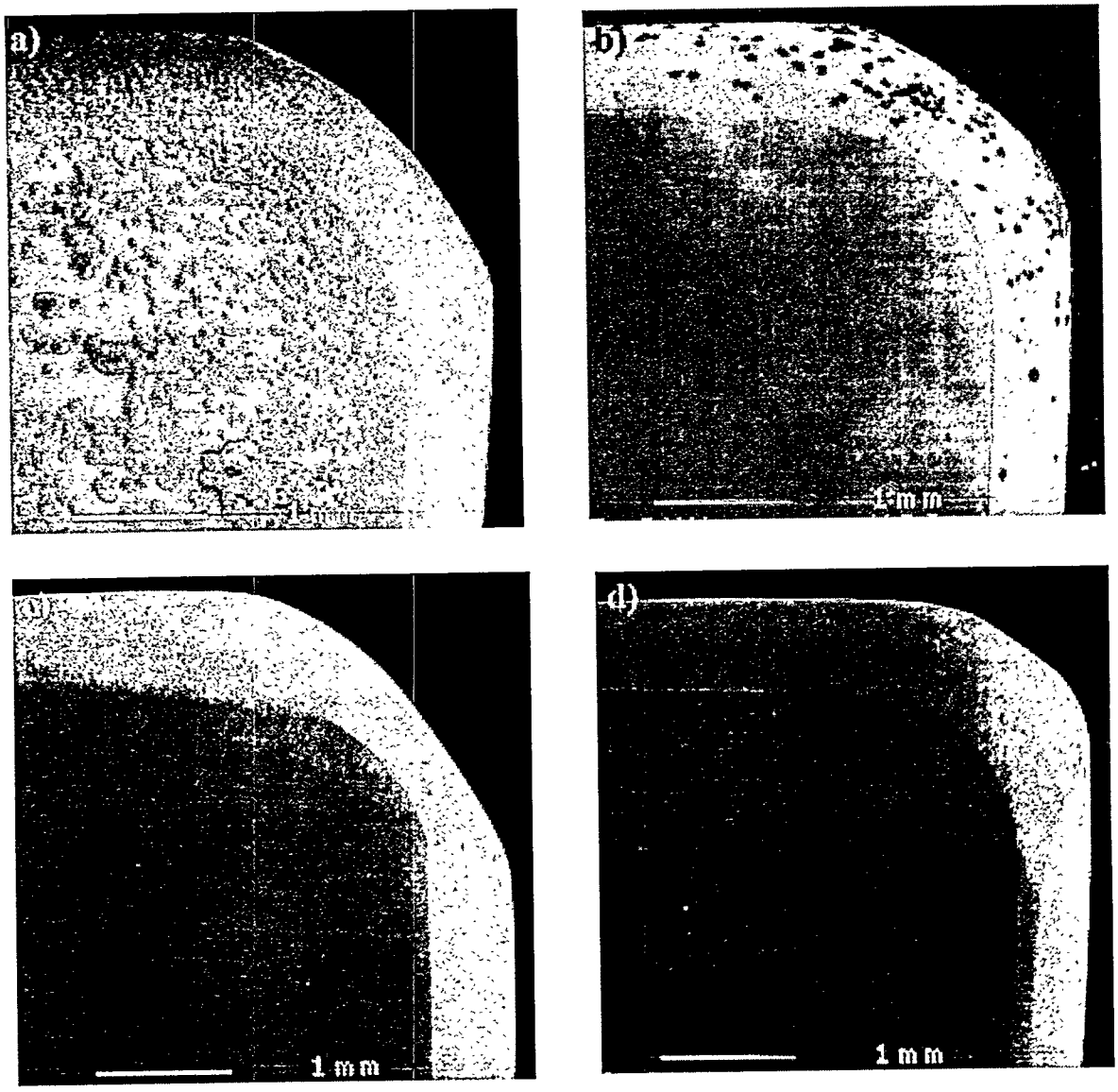

Figure 3.148: Low magnification (20x) SEI micrographs of Fe-Al alloys exposed at 700°C. a) 5 wt% Al, b) 7.5 wt% Al, c) 10 wt% Al, and d) 12.5 wt% Al

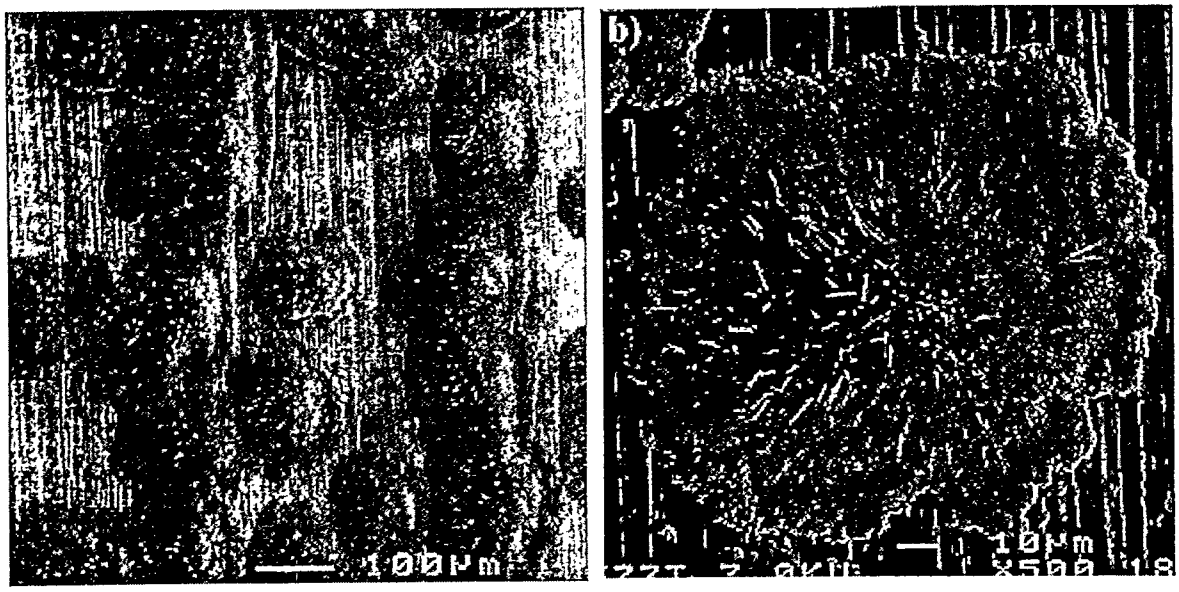

Figure 3.149: SEI micrographs of the 5Al surface scale exposed at 700°C. Nodules at a) 100x, b) 500x

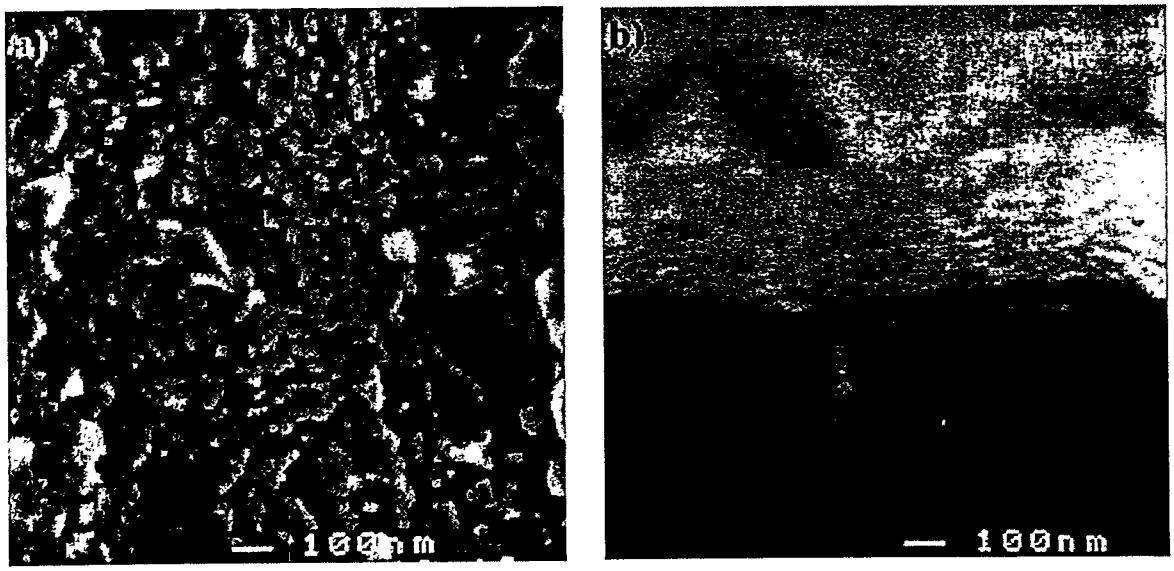

Figure 3.150: SEI micrographs of the 5Al surface scale exposed at 700°C. Nodular free region a) granular scale at 50,000x, b) fractured cross-section at 50,000x

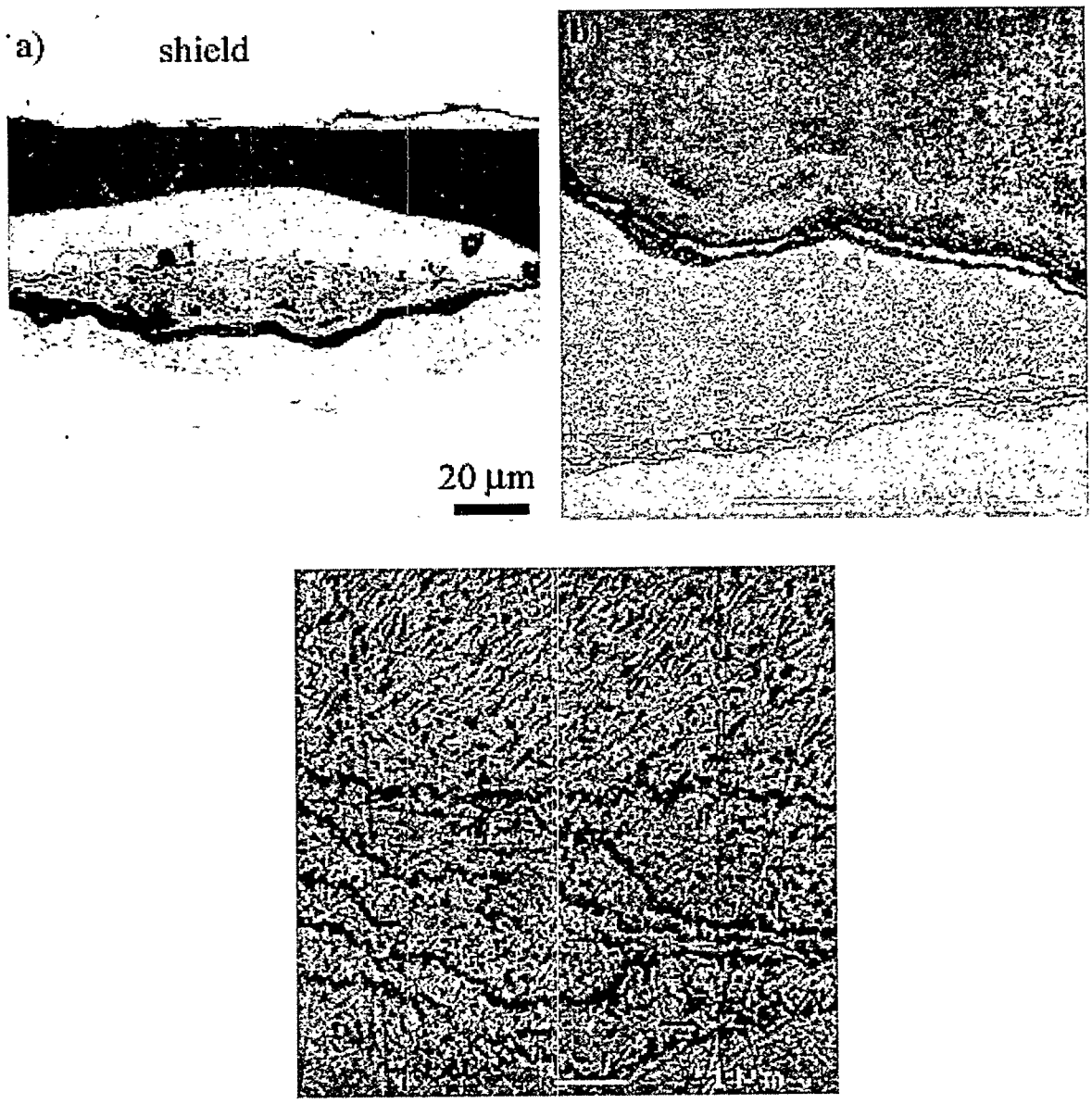

Figure 3.151: Polished cross-section of the 5Al sample exposed at 700°C. a) LOM at 500x, and internal precipitate zone at b) 1,500x, and c) 10,000x

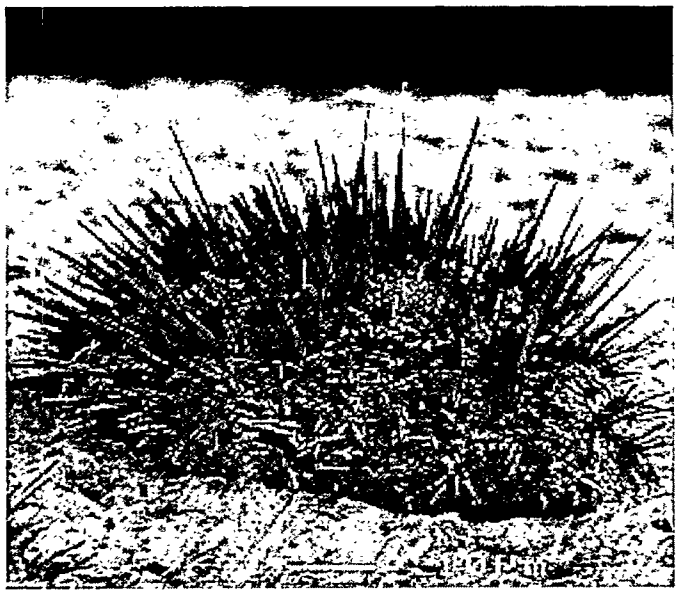

Figure 3.152: SEI micrograph of an edge nodule on the 7.5Al surface scale exposed at 700°C. 1,100x

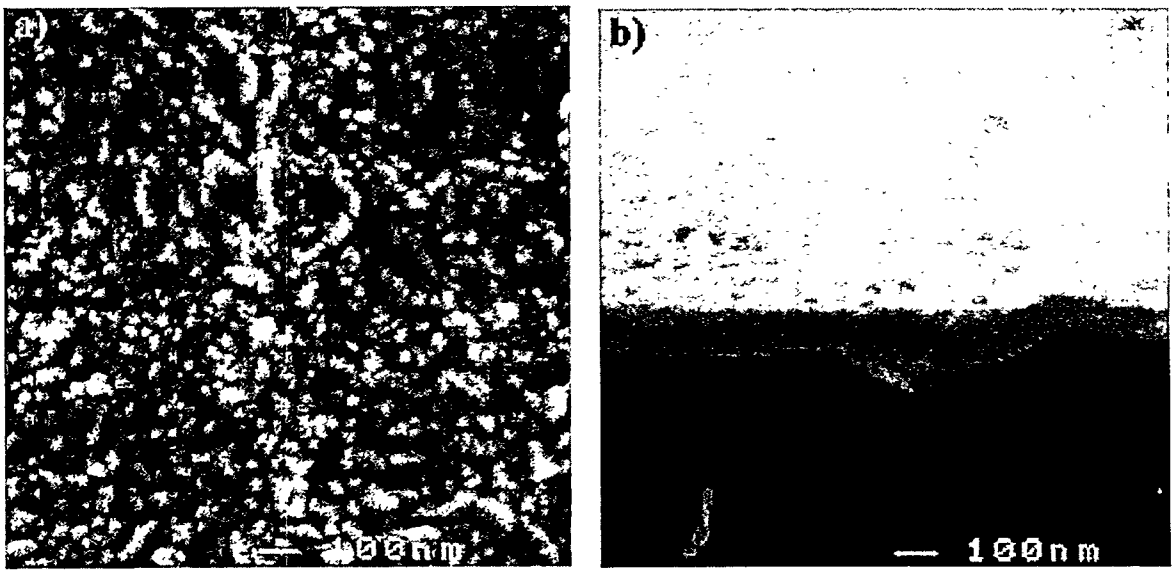

Figure 3.153: SEI micrograph of the 7.5Al surface scale exposed at 700°C. a) granular scale at 50,000x, b) fractured cross-section at 50,000x

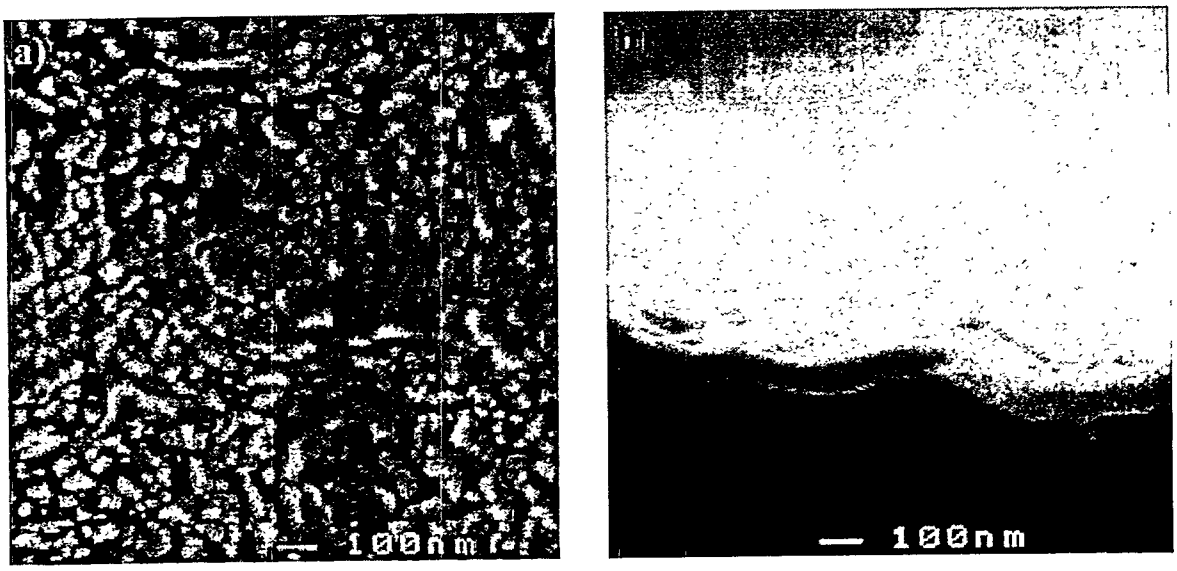

Figure 3.154: SEI micrographs of the surfaces found on 10Al exposed at 700°C. a) granular scale at 50,000x, b) fractured cross-section at 50,000x

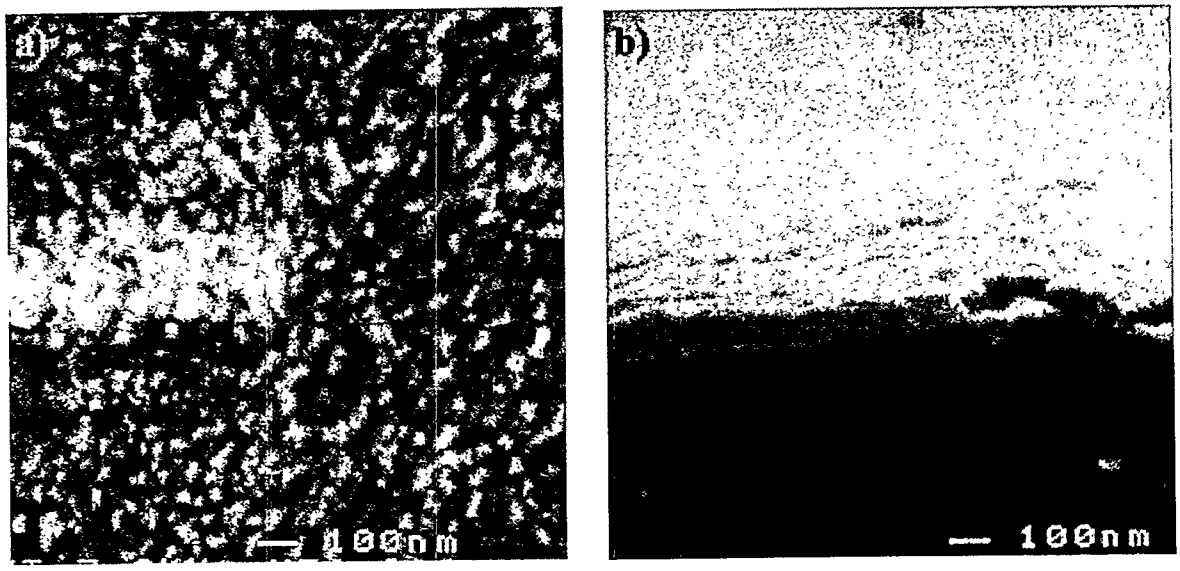

Figure 3.155: SEI micrographs of the surfaces found on 12.5Al exposed at 700°C. a) granular scale at 50,000x, b) fractured cross-section at 50,000x

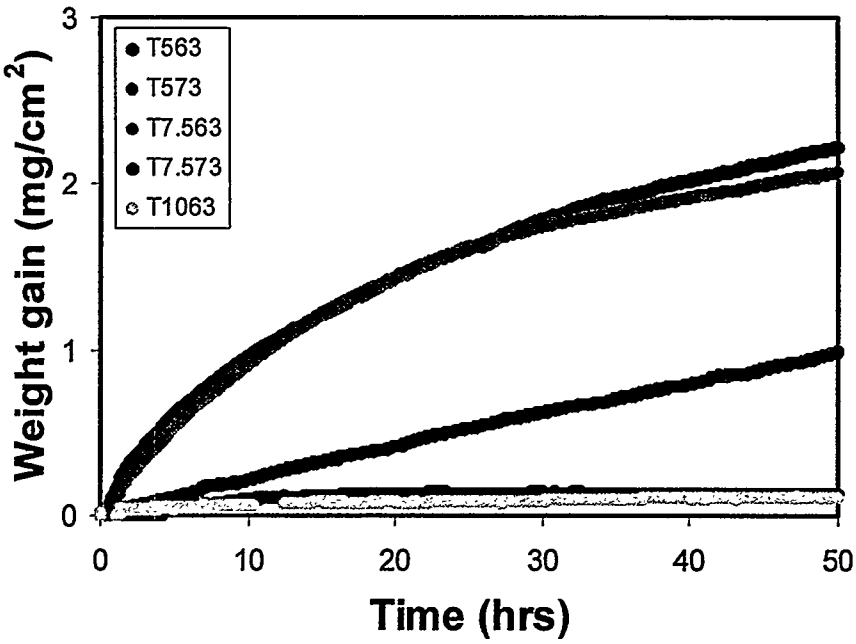

Figure 3.156: Continuous weight gain data obtained for various samples in an oxidizing atmosphere.

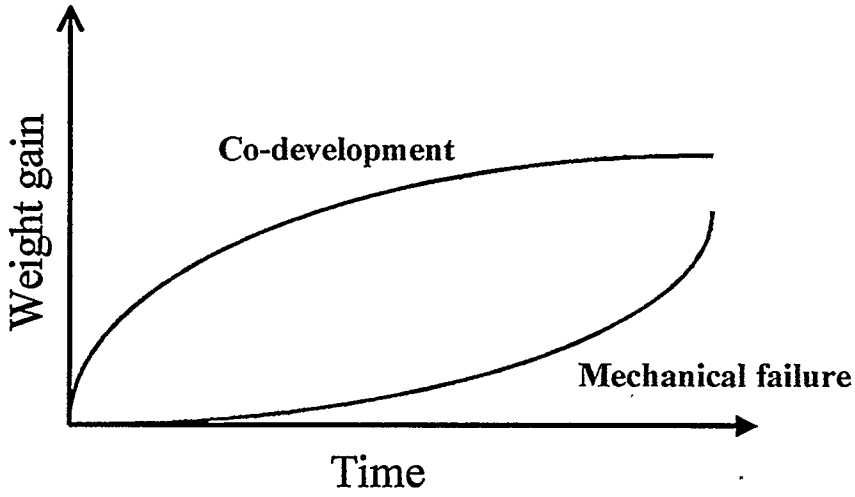

Figure 3.157: Schematic showing the various weight gain data for different nodule formation mechanisms.

4.0 EROSION STUDIES

4.1 Introduction

The erosion of materials by the impact of solid particles has received increasing attention during the past 20 years. Today, solid particle erosion damage remains one of the most significant performance problems among US utilities, affecting roughly 80% of fossil fuel systems. Wastage associated with erosion has caused an increase in power plant down time due to increased maintenance, therefore reducing plant efficiency. This problem has led to various methods to combat solid particle erosion. One method is to apply coatings to the components subjected to erosive environments. Protective weld overlay coatings are particularly advantageous in terms of coating quality. The weld overlay coatings are essentially immune to spallation due to a strong mechanical bond with the substrate material, and using powder mixtures, a wide range of alloys can be applied in order to achieve the best performance in an erosive environment. Therefore, research was initiated in order to determine the relative erosion resistance of Fe-Al alloys compared to commercial alloys presently in use.

4.2 Experimental Procedure

Numerous weld overlay coatings were selected for erosion testing, Table 4.1. These tests were conducted using an automated erosion tester. The system is driven by an air compressor and the air is cleaned through a series of filters to remove any entrained water. The flow meter and pressure regulator control the amount of air that flows through the system and the air is heated by two inline fluid heaters. The erosive particles are fed into the air stream with a screw feeder to ensure constant feed rates. The particles and hot air are accelerated and may be impinged upon the sample at any angle between 0° and 90° and the particle velocity distribution prior to impact is directly measured with a Laser Doppler Velocometer (LDV). The erosion test conditions were as follows:

Eroded Sample Planar Dimensions = 1.27 cm x 1.27 cm

Sample Temperature = 400°C

Erodent Particle Velocity = 40 m/s ±5 m/s

Erodent Particles Flux = 8.56 mg/(mm^2/sec)

Impingement Angle = 90° and 30°

Erodent - angular alumina (Al_2O_3)

Erodent size range: 300-425 μm (average diameter=350 μm) and 300-600 μm (average diameter =450 μm) for wrought and weld alloys, respectively. The sample temperature was chosen to be 400°C,

4.3 Results and Discussion

Volume steady state erosion rates can be found in Table 4.1 for all overlays tested. The Fe-Al weld overlays had erosion rates comparable to that of the commercial alloys presently in use. Microhardness tests were performed to measure the size of the deformed region beneath the eroded surface, Fig 4.1. It was found that microhardness significantly increased near the eroded surface for most samples. These results show that, for all tested materials, a portion of the impacting particles kinetic energy is absorbed through plastic deformation with a subsequent increase in hardness at the eroded surface. The amount of plastic deformation attained is related to a number of material properties [Levin 1994, 1995]. Although hardness determines the materials resistance to plastic deformation, no correlation was found between the volumetric erosion rates of weld overlay coatings at 400°C and hardness at 400°C. Therefore, hardness is not the only material property that controls erosion resistance. The volumetric erosion rates for coatings can be seen plotted versus the plastic zone size, Fig 4.2. It can be seen that as the plastic zone size increased the volumetric erosion rate decreased. An increase in surface hardness due to erosion represents the material's ability to strain harden, while the plastic zone size shows the depth over which strain hardening occurs. These results show that, for all of the studied materials, the erosion involves significant plastic deformation and, therefore, erosion resistance is controlled by the ability to absorb impact energy through plastic deformation.

4.4 Erosion Conclusions

In general, the steady state volume erosion rate was found to be related to the depth of plastic deformation of the material at the eroded surface. Materials which dissipate particle impact energy through plastic deformation were found to exhibit low erosion rates. The erosion rate for the Fe-Al alloys were found to be comparable to other commercial overlays presently applied.

4.5 Erosion Tables

Table 4.1: Volume steady state erosion rates (in mm^3/min x 1000) for tested coatings [Levin, 1995]

Weld Overlay	90° impact angle	30° impact angle
Cobalt based		
Stellite-6	11.9	12.2
Ultimet	8.5	9.7
TS-2	10.4	12.5
Nickel base		
Inconel 625	9.4	9.5
Hastelloy-22	11.4	9.4
B-60	13.5	9.9
Iron based		
Iron aluminide	10.3	9.3
Armacor-M	22.2	20.3
High chromium iron	11.1	11.3
316L SS	10.0	9.2
420 SS	9.4	14.2

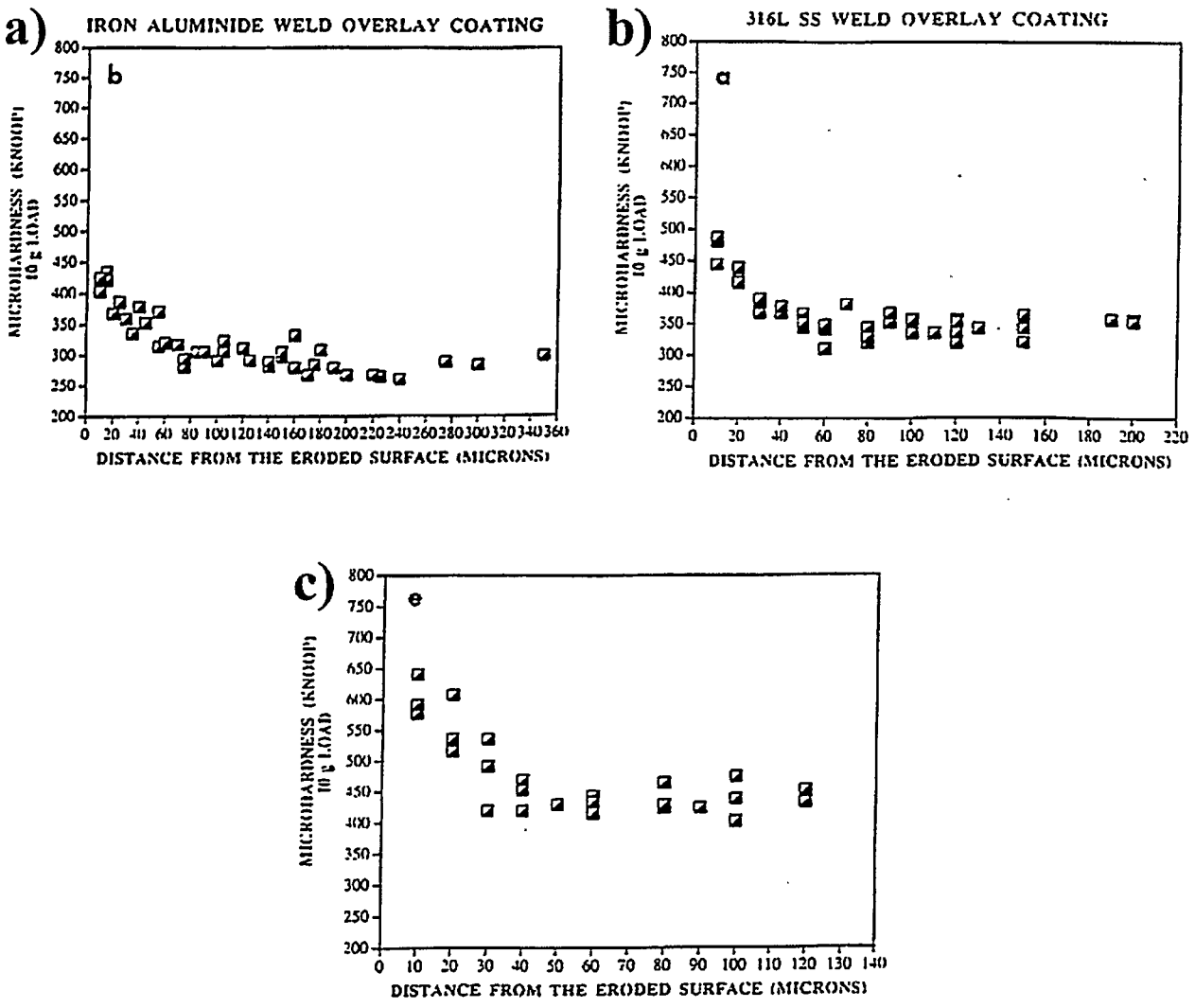

Figure 4.1: Variation of hardness as a function of distance from the eroded surface for weld overlay coatings. a) Fe-Al alloy, b) 316L SS, c) Inconel-625

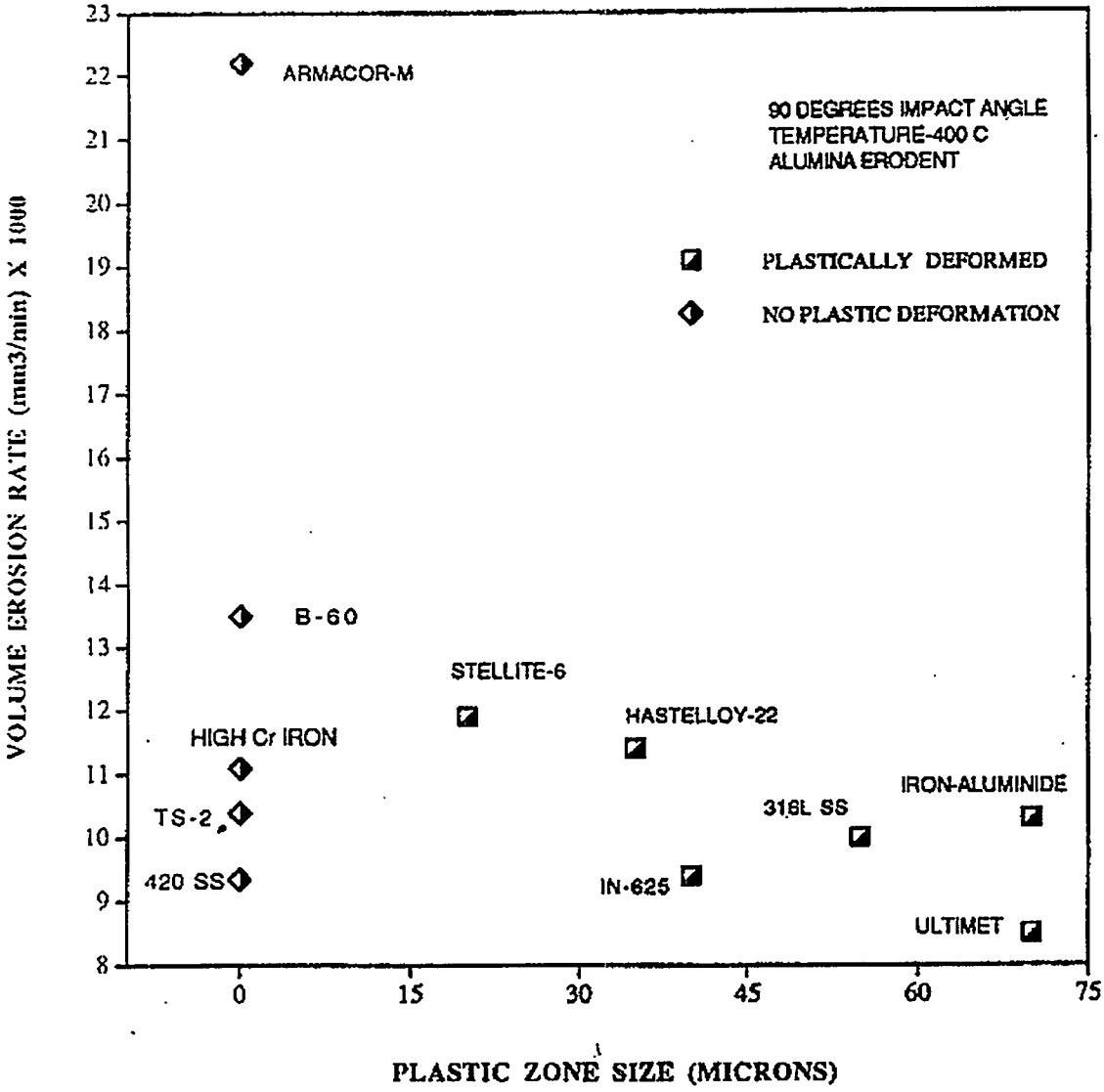

Figure 4.2: Volume steady state erosion rate of weld overlay coatings as a function of plastic zone size.

5.0 EROSION-CORROSION STUDIES

5.1 Introduction

In many fossil fuel-fired power plants, simultaneous erosion by solid particles and corrosion by chemically active compounds can produce accelerated wastage of metal surfaces. Typically, coal used for combustion contains hard erosive particles, such as alumina (Al_2O_3), and highly corrosive gases that can react with the metal to form surface scales. These two factors have separately been shown to degrade the material during exposure. This section will review the initial work started to determine the combined effect of erosion and corrosion on Fe-Al alloys.

5.2 Experimental Procedure

Oxidation of the Fe-Al alloys, with 0-12.5 wt% Al, was conducted using a Fisher Scientific box furnace. For these studies, only one face of the sample was ground to 600 grit and cleaned using methanol. The furnace was brought to temperature with zero grade compressed air flowing through the chamber for a minimum of 2 hours. Samples were then placed in the furnace, prepared side up, and held for 100 hours. They were subsequently removed and allowed to cool. The temperature was monitored using a thermocouple located next to the samples. Characterization of the corroded surfaces were similar to those described in Section 3.1.2.

Erosion tests were conducted using the automated erosion tester previously described in Section 4.2. The erosion test conditions were as follows:

Eroded Sample Planar Dimensions = 1.27 cm x 1.27 cm

Sample Temperature = 23 °C

Erodent Particle Velocity = 40 m/s ±5 m/s

Erodent Particles Flux = 8.56 mg/(mm^2/sec)

Impingement Angle = 90°

Erodent - angular alumina (Al_2O_3)

Erodent size range: 300-425 μm (average diameter=350 μm) and 300-600 μm (average diameter =450 μm) for wrought and weld alloys, respectively. The sample temperature was chosen to be 400°C,

5.3 Results and Discussion

The morphologies of the corroded surfaces was similar to that previously found in Section 3.2.3. A thin scale of gamma alumina (approximately 100nm) covered the surface of the 12.5Al sample, while thick iron oxide scales were found on the low carbon steel sample and the 5Al sample. Upon eroding the sample for 5 minutes, the scale was completely removed from the surface due to the large amounts of material degradation from the erosion process. Continued exposure to erodant particles resulted in the attainment of steady state corrosion rates similar to those found in Section 4.3. Therefore, due to the large mount of material removal from the erosion process and the thinness of the corrosion scale, the dominant mechanism this process was erosion.

5.4 Erosion-Corrosion Conclusions

The erosion-corrosion behavior of the Fe-Al alloys was conducted. After exposing iron-based alloys, with 0-12.5 wt% Al, in an oxidizing environment for a 100 hr exposure at 700°C, room temperature erosion testing was performed. Due to the thinness of the corrosion product that formed, as well as the large amount of material typically removed during erosion, the major mechanism for material degradation was found to erosion.

6.0 FIELD EXPOSURES

Fabrication of a co-extruded iron aluminide boiler tube was attempted at Oak Ridge National Laboratory. However, problems were incurred as the outer, iron aluminide portion of the tube was found to crack due to its low ductility. Work is presently in progress to fabricate an iron-aluminum weld overlay boiler tube at Lehigh University, as well as Welding Services, Inc. From the weldability and corrosion results of this work, a deposit with approximately 10 wt% Al is being attempted. Upon successful completion of a crack-free, coated tube, installation into a boiler will be conducted at the next scheduled shutdown.

7.0 CONCLUSIONS

From this study of evaluating the use of iron-aluminum weld overlays coatings for erosion/corrosion protection in fossil fired boilers with low NO_x burners, the following conclusions can be drawn.

1) The ability to produce consumable iron-aluminum wires for GMAW overlay applications was proven. Composite wires containing commercially pure aluminum wire wrapped in a low carbon steel sheath were produced that had iron a wide range of compositions, even those in the aluminide regions. The feasibility of additional alloying elements, such as Cr or Zr, was also shown by adding the element between the wire and sheath prior to the drawing process.

2) Using GTAW and GMAW processes, single and multiple pass claddings of Fe-Al were produced with aluminum contents ranging from 3 to 30 wt%. All claddings were found to have a columnar microstructure that was relatively homogenous on a microscopic scale throughout the bulk of the fusion zone. A partially mixed zone was located near the fusion line that increased in size as the nominal aluminum content of the cladding increased.

3) Under these processing conditions, cracking of the Fe-Al claddings, both inter- and transgranular, was found to be independent of the welding process and parameters. Instead, cracking was directly related to the amount of aluminum in the deposit. Above 10 wt% Al, cracking was seen to be prevalent throughout the cladding. This composition corresponds to the microstructural transition from the single phase disordered solid solution α to α + ordered Fe_3Al. It has previously been observed that the ordered structures (Fe_3Al, FeAl) are more susceptible to environmental embrittlement, which is the source of the cladding cracking problem.

4) The corrosion behavior of Fe-Al alloys in an oxidizing/sulfidizing atmosphere was found to be directly related to the aluminum content of the alloy. For high aluminum compositions,

protection was afforded due to the development of a thin, continuous gamma alumina scale that inhibited rapid degradation of the alloy. Increasing the aluminum content of the alloy was found to promote the formation and maintenance of this scale. For low aluminum alloys, thick scale growth of sulfide phases was found. Growth of these scales was diffusion controlled and the addition of aluminum 5 wt% Al was found to decrease the rate of the outer FeS scale growth by an order of magnitude when compared to pure iron at 700°C. Median aluminum contents saw the initial formation of the protective scale that encountered mechanical failure at later times and the subsequent growth of corrosion nodules.

5) According to which reaction product developed, the corrosion behavior of the alloys was found to exhibit one, if not more, of three stages of behavior: inhibition, breakdown, and steady state.

- The inhibition stage was characterized by growth of the gamma alumina scale that suppressed excessive degradation of the substrate at all temperatures. While relatively low weight gains were observed in this regime due to slow diffusion of cation species through the scale, it was also protective by the fact that internal sulfidation of the alloy did not occur.
- Localized mechanical failure of the initial passive scale, in combination with the inability to re-establish itself, led to the observance of the breakdown stage. The nodular growth of non-protective sulfide phases across the sample face was due to short circuit diffusion through the gamma alumina layer. This time period was labeled the breakdown stage as relatively fast weight gains replaced the transient low rates detected at early times. The morphologies observed were very complex as continued growth of the nodule did not depend solely upon the diffusion of species through the previously formed product (where $n = 0.5$), but rather, continued mechanical failure of the passive scale. This resulted in faster growth along a lateral direction ($n = 1$) with respect to the substrate surface instead of perpendicular to it. The corrosion rate observed during development of these morphologies was directly related to the density of the nodules on the surface and the exposure temperature.

- Steady-state behavior was encountered from the onset of exposure for all Fe-5 wt% Al alloys tested, or upon coalescence of the nodular growths. After initially high corrosion rates, the weight gains were found to increase at a steady rate as subsequent growth occurred via diffusion through the continuous scale.

6) Increasing the temperature for a given aluminum content was generally found to decrease the duration of the inhibition stage due to non-protective sulfide growth located at the corners and edges of the sample. However, this may be related to the geometry of the corrosion specimen, whether in reducing or oxidizing environments, and not indicative of the protective nature of the scale.

7) Regardless of alloy aluminum content, the thickness of the alumina scale was found to be relatively constant for a given time and temperature.

8) Nodular formations of corrosion products was found randomly distributed across the face of the samples. No relationship between the substrate grain boundaries and location of the nodules was found due to the rough surface finish of the corrosion sample, thus eliminating any effect from these microstructural features.

9) Determination of the corrosion product growth mechanism could not be directly obtained from the thermogravimetric data. For samples with relatively high weight gains, enhanced scale growth at the corners and edges of the sample, as well as the morphology of the multi-layered, multi-phase corrosion products, violated the assumptions necessary for data manipulation by this means. Instead, kinetic data was obtained by measuring the cross-sectional scale thickness for various times. Samples that developed gamma scale growth had weight changes that were within the noise level of the balance, thus rendering most of the calculations from the continuous weight gain data futile.

10) The corrosion product morphologies formed on Fe-Al alloys in an oxidizing environment were similar to those in the oxidizing-sulfidizing atmosphere, except with iron oxide phases as the non-protective corrosion product. The nodule growth mechanism in the oxidizing atmosphere was found to be different from that related to the growth of sulfide nodules. Instead of the mechanical failure of an initially passive scale, the co-development of two different cation oxides was observed according to the kinetic data. The difference in mechanisms between the two environments may lie in the relative growth rates of the non-protective corrosion products formed.

11) For Fe-Al alloys exposed in oxidizing environments, the formation of gamma alumina was promoted by increasing the temperature and aluminum content of the alloy.

12) The solid particle erosion resistance of Fe-Al weld overlay coatings at 400°C was comparable to other commercial overlays presently applied.

13) The erosion-corrosion behavior of the alloys was also conducted. Due to the thinness of the corrosion product that formed, as well as the large amount of material typically removed during erosion, the major mechanism for material degradation was found to erosion.

The results from this study indicate that weldable compositions of Fe-Al alloys (10 wt% Al) show excellent corrosion resistance to aggressive low NO_x gas compositions in the service temperature range (below 600°C). With the potential promise for applications requiring a combination of weldability and corrosion resistance in moderately reducing environments, these alloys are viable candidates for further evaluation for use as sulfidation resistant weld overlay coatings.

Acknowledgments

This research was sponsored by the Fossil Energy Advanced research and Technology Development (AR&TD) Materials Program, U.S. Department of Energy, under contract DE-AC05-96OR22464 with Lockheed Martin Energy Research Corporation. The authors wish to thank P.F. Tortorelli and B.A. Pint for helpful conversations and V.K. Sikka for the cast alloys used in corrosion testing. The authors also wish to thank A.O. Benscoter for his aid in metallographic preparation. In addition, S.W. Banovic thanks the National Science Foundation for financial support through the Graduate Traineeship Program in Materials Science and Engineering, DMR-9256332.

REFERENCES

Banovic, S.W., DuPont, J.N. and Marder, A.R. 1999a. Welding Journal, January, 23s-30s.

Banovic, S.W., DuPont, J.N., and Marder, A.R. 1999b. Corrosion Resistance of Weldable Fe-Al Alloys in Reducing Environments, Corrosion 99, Paper Number 59.

Boggs, W.E. 1971. J. Electrochem Soc, 118 (6), pp.906-12.

Boulam, M., Beranger, G., and Lambertin, M. 1993. In Microscopy of Oxidation 2, eds. S.B. Newcomb and M.J. Bennett, The Institute of Materials, Cambridge, England, pg 243.

Brumm, M. and Grabke, H.J. 1992. Corr. Sci, 33 (11), 1677-90.

Chou, S.F, Daniel, P.L., Blazewicz, A.J., and Dudek, R.F. 1984. Hydrogen Sulfide Corrosion in Low NOx Combustion Systems, presented to the Metallurgical Society of AIME, Detroit, Michigan, Sept 17-19, Babcock & Wilcox report # RDTPA 84-12.

Clark, J.B. 1963. Trans. AIME, 227,1250-1.

Condit, R.H., Hobbins, R.R., and Birchenall, C.E. 1974. Oxid. Met.. 8 (6), 409-55.

Cutler, 1970. I.B. In High Temperature Oxides, ed. A.M. Alper, Academic Press, New York, New York, pg 129.

Cutler, A.J. and Raask, E. 1981. Corrosion Science, 21 (12), pp. 789-800.

Danielewski, M., Mrowec, S., and Stoklosa, A. 1982. Oxid. Met. 17 (1-2), 77-97.

David, S.A., Horton, J.A., McKamey, C.G. Zacharia, T., and Reed, R.W. 1989. Welding Journal, Sept, pp. 372s-81s.

David, S.A. and Zacharia, T. 1991. In *Heat-Resistant Materials, Proceedings of the 1st International Conference*, pp. 169-73, Fontana, Wisconsin, Sept. 23-26.

DeVan, J.H. 1988. In Oxidation of High-Temperature Materials, eds. T. Grobstein and J. Doychak, The Minerals, Metals, and Materials Society, Cleveland, OH, 107-115.

DeVan, J.H., Hsu, H.S., and Howell, M. 1989 *Sulfidation/Oxidation Properties of Iron-Based Alloys Containing Niobium and Aluminum*, ORNL/TM-11176, Martin Marietta Energy Systems, Inc., Oak Ridge Natl. Lab., May 1989.

DeVan, J.H. and Tortorelli, P.F. 1992. High Temperature Corrosion of Iron Aluminides, Corrosion 92, Paper 127.

DeVan, J.H. and Tortorelli, P.F. 1993a. Corrosion Science, 35 (5-8), pp. 1065-71.

DeVan, J.H. and Tortorelli, P.F. 1993b. Mat. High Temp., 11 (1-4), 30-5.

DuPont, J.N. and Marder, A.R. 1995. Welding Journal, December, 406s-416s.

DuPont, J.N. and Marder, A.R. 1996. Welds, Metallurgical and Materials Transactions B, 27B, pp.481-9.

Fasching, A.A., Ash, D.I., Edwards, G.R., and David, S.A. 1995. Scripta Metallurgica et Materialia, 32 (3), pp. 389-94.

Fryt, E.M., Smeltzer, W.W., and Kirkaldy, J.S. 1979a. J. Electrochem. Soc., 126 (4), 673-83.

Fryt, E.M., Bhide, V.S., and Smeltzer, W.W. 1979b. J. Electrochem. Soc., 126, 683.

Gabrielson, J.E. and Kramer, E.D. 1996. In *1996 International Joint Power Generation Conference, Vol 1*, pp.19-23, ASME, EC-Vol. 4/FACT-Vol. 21.

Gaskell, D.R. 1981. Introduction to Metallurgical Thermodynamics, 2nd Edition, Hemisphere Publishing Corporation, New York, NY, 433-59.

Gittos, M.F. and Gooch, T.G. 1992. Welding Journal, December, pp. 461s-72s.

Gray, T.J. 1971. In High Temperature Oxides, Vol 5, ed. A.M. Alper, Academic Press, New York, New York, 77-81 and 97.

Hagel, W.C. 1965. Corrosion, 21, 316-26.

Hindam, H. and Whittle, D.P. 1982, Oxid. Met., 18 (5/6), 245-84.

HSC Chemistry for Window, Version 3.0. 1997. Outokumpu Research Oy, Finland, www.outokumpu.fi/hsc.

Hsu, H.S. 1986. Oxid. Met. 315-

Impey, S., Stephenson, D.J., and Nicholls, J.R. 1993. In Microscopy of Oxidation 2, eds. S.B. Newcomb and M.J. Bennett, The Institute of Materials, Cambridge, England, pg 323.

JANAF Thermochemical Tables, Third Edition, Journal of physical Chemical Reference Data, 14, Supplement 1, 1985.

Jellinek, F. 1968. In Inorganic Sulfur Chemistry, ed G. Nickless, Elsevier Publishing Company, New York, New York, 669-747.

Jordan, C.E. and Marder, A.R. 1997a. J. Mater. Sci., 32, 5593-602.

Jordan, C.E. and Marder, A.R. 1997b. J. Mater. Sci., 32, 5603-610.

Kai, W. and Huang, R.T. 1997a, Oxid. Met., 48 (1/2), 59-86.

Kai, W., Chu, J.P., Huang, R.T. and Lee, P.Y. 1997b. Mat. Sci. Engr., A239-240, 859-70.

Kattner, U.R. 1990. In Binary Alloy Phase Diagrams, Vol 1, ed. T.B. Massalski, ASM International, Materials Park, OH.

Kingery, W.D. 1959. In Kinetics of High Temperature Processess, Wiley, NY, NY, pp. 97.

Kingery, W.D., Bowen, H.K., and Uhlmann, D.R. 1976. Introduction to Ceramics, 2nd Edition, Wiley Publishing, NY,NY, pg 64.

Kofstad, P. 1988. High Temperature Corrosion. Elsevier Applied Science, New York, New York, 1-24.

Kubaschewski, O. 1990. In Binary Alloy Phase Diagrams, Vol 2, ed. T.R. Massalski, ASM International, Metals Park, OH.

Levin, B.F., DuPont, J.N., and Marder, A.R. 1994. In Proceedings of the TMS Symposium on High Temperature Coatings, Chicago, IL, Oct 2-6, 325-40.

Levin, B.F., DuPont, J.N., and Marder, A.R. 1995. Wear, 181-183, 810-20.

Liu, C.T., Lee, E.H., and McKamey, C.G. 1989. Scripta Metallurgica, 23, pp. 875-80.

Liu, C.T., C.G. McKamey, E.H. Lee, Scr. Metall. 24, 385-90 (1990).

Liu, C.T., C.L. Fu, E.P. George, and G.S. Painter, ISIJ International 31, pp. 1192 (1991).

Liu, Z., Gao, W., and Wang, F. 1998. Scripta Metall., 39 (11), 1497-502.

Maziasz, P.J., Goodwin, G.M., Liu, C.T., and David, S.A. 1992. Scripta Metallurgica et Materialia, 27 (12), pp. 1835-40.

Macintyre, J.E. (ed.) Dictionary of Inorganic Compounds, Vol 1, Chapman & Hall, NY, NY, 52.

McKamey, C.G. 1996. In Physical Metallurgy and Processing of Intermetallic Compounds, ed. N.S. Stoloff and V.K. Sikka, Chapman Hall, New York, New York, 351-91.

McKamey, C.G., DeVan, J.H., Tortorelli, P.F., and Sikka, V.K. 1991. J. Mater. Res., 6 (8), 1779-805.

McKee, R.A. and Druschel, R.E. 1983. J. Electrochem. Soc., 130 (4), 898-904.

McNallan, M.J. 1991. In *Chlorine in Coal*, eds. J. Stringer and D.D. Banerjee, Elsevier Science Publishers, NY, NY, 175-92.

Meier, G.H. and Pettit, F.S. 1985. In *High Temperature Corrosion in Energy Systems*, pp.161-75, TMS, Warrendale, PA.

Mrowec, S., Walec, T., and Werber, T. 1969. Oxid. Met. 1 (1), 93-120.

Mrowec, S. and Wedrychowska, M. 1979. Oxid. Met., 13 (6), 481-504.

Mrowec, S. 1995. Oxidation of Metals, 44 (1-2), pp. 177-209.

Narita, T. and Nishida, K. 1974. Trans. Jpn. Inst. Met., 15, 314-23.

Narita, T. Przybylski, K., and Smeltzer, W.W. 1984. Oxidation of Metals, 22 (3/4), 181-200.

Natesan, K. 1981. In High Temperature Corrosion, ed. R.A. Rapp, National Association of Corrosion Engineers, Houston, TX, 336-44.

Natesan, K. and Johnson, R.N. 1995. In Heat-Resistant Materials II. K. Natesan, P. Ganesan, and G. Lai (eds.), Materials Park, OH, ASM International, 591-9.

Nishida, K. and Narita, T. 1976, Hokkaido Daigaku Kogakubu Kenkyu Hokoku, (81), 99-109.

Orchard, J.P. and Young, D.J. 1986. J. Electrochem. Soc., 133 (8), 1734-41.

Patnaik, P.C. and Smeltzer, W.W. 1984. J. Electrochem. Soc., 131 (11), 2688-91.

Patnaik, P.C. and Smeltzer, W.W. 1985a. Oxidation of Metals, 23 (1-2), pp. 53-75.

Patnaik, P.C. and Smeltzer, W.W. 1985b. Journal of the Electrochemical Society, 132, pp 1226-32.

Pieraggi, B. 1987. Oxidation of Metals, 27 (3-4), pp. 177-85.

Pint, B.A. 1997. In Fundamental Aspects of High Temperature Corrosion. D.A. Shores, R.A. Rapp, and P.Y. Hou (eds.), Electrochemical Society, Pennington, NJ, 74-85.

Prasanna, K., Khanna, A., Chandra, R., and Quadakkers, W.J. 1996. Oxidation Of Metals, 46 (5/6), 465-80.

Prescott, R. and Graham, M.J. 1992a, Oxid. Met., 38 (3-4), 233-54.

Prescott, R. and Graham, M.J. 1992b. Oxidation of Metals, 38 (1-2), pp. 73-87.

Pruessner, K., Bruley, J., Salzberger, U., Zweygart, H., Schumann, E., and Ruhle, M. 1993. In Microscopy of Oxidation 2, eds. S.B. Newcomb and M.J. Bennett, The Institute of Materials, Cambridge, England, pg 435.

Przybylski, K. and Smeltzer, W.W. 1992a. Oxidation of Metals, 37 (5/6), 349-61.

Przybylski, K., Narita, T., and Smeltzer, W.W. 1992b. Oxidation of Metals, 38 (½), 1-33.

Quaddakers,W.J. and Bongartz, K. 1994. Werjst. Korros., 45, 232-8.

Quaddakers, W.J. and Bennett, M.J. 1994. Sci. Technol., 10, 126-31.

Quan, N.S. and Young, D.J. 1986. Oxid. Met., 25 (1-2), 107-19.

Raghavan, V. 1988a. In Phase Diagrams of Ternary Alloys, Pt 2, The Indian Institute of Metals, Calcutta, India, 5-9.

Raghavan, V. 1988b. In Phase Diagrams of Ternary Alloys, Pt 5, The Indian Institute of Metals, Calcutta, India, 5-8.

Renusch, D., Veal, B.M., Natesan, K., Koshelev, I., and Grimsditch, M. 1997. In Fundamental aspects of High Temperature Corrosion. D.A. Shores, R.A. Rapp, P.Y. Hou (eds.), Electrochemical Society, Pennington, NJ, 62-73.

Rybicki, G.C. and Smialek, J.L. 1989. Oxid. Met., 31 (3-4), 275-304.

Saegusa, F. and Lee, L. 1966. Corrosion, 22, 168-77.

Sakiyama, M., Tomsazewski, P., and Wallwork, G.R. 1979. Oxid. Met., 13 (4), 311-330.

Sikka, V.K., Viswanathan, S., Vyas, S. 1993. High Temperature Ordered Intermetallic Alloys V, in *Materials Research Society Symposium Proceedings, Vol 28,* , pp. 971-6, eds. I. Baker, R. Darolia, J.D. Whittenberger, and M.H. Yoo, Materials Research Society, Pittsburgh, PA.

Smith, P.J., Beauprie, R.M., Smeltzer, W.W., Stevanovic, D.V., and Thompson, D.A. 1987. Oxid. Met., 28 (5/6), 259-76.

Smith, P.J., Jackson, P.R.S., and Smeltzer, W.W. 1987a. J. Electrochem Soc, 134 (6), pp. 1424-1431.

Smith, P.J. and Smeltzer, W.W. 1987b. Oxidation of Metals, 28, pp. 291-7.

Speidel, M.P. 1977. In Hydrogen Damage, ed. C.D. Beachem, ASM Publication, 329-51.

Stoloff, N.S. and Duquette, D.J. 1993. Journal of Metals, Dec, pp. 30-5.

Strafford, K.N. and Datta, P.K. 1989. Mat Sci and Tech, 5, pp. 765-79.

Strafford, K.N. and Datta, P.K. 1993. Corrosion Science, 35 (5-8), pp. 1053-63.

Strafford, K.N. and Manifold. R. 1969. Oxidation of Metals, 1 (2), pp. 221-40.

Strafford, K.N. and Manifold, R. 1972. Oxidation of Metals, 5 (2), pp. 85-112.

Stringer, J. 1990. In *High Temperature Oxidation and Sulphidation Processes*, ed. J.D. Embury, Pergamon Press, Toronto, Ontario, pp. 257-75.

Tomaszewski, P. and Wallwork, G.R. 1978. Rev. High. Temp. Mater., 4 (1), 75-105.

Tomaszewski, P. and Wallwork, G.R. 1981. In High Temperature Corrosion, ed. R.A. Rapp, National Association of Corrosion Engineers, Houston, TX, 258-66.

Tomaszewicz, P., and Wallwork, G.R. 1983, Oxid Met., 19 (5/6), 165-85.

Tomaszewski, P. and Wallwork, G.R. 1986. In Alternate alloying for environmental resistance, eds. G.R. Smolik and S.K. Banerji, The Metallurgical Society, Metals Park, OH, 13-36.

Tortorelli, P.F. and DeVan, J.H. 1992. Mat Sci and Engr, A135 (1-2), pp. 573-7.

Tortorelli, P.F. and DeVan, J.H. 1994a, In *Processing, Properties, and Applications of Iron Aluminides*, pp. 257-70, TMS, Warrendale, PA.

Tortorelli, P.F., Devan, J.H., and Abdali, U.K. 1993. Cyclic oxidation of iron aluminides, Corrosion 93, Paper 258.

Tortorelli, P.F., DeVan, J.H., Goodwin, G.M., and Howell, M. 1994b. In *Elevated Temperature Coatings: Science and Technology I*, pp. 203-214, Rosemont, IL, Oct 3-6, 1994, TMS, Warrendale, PA.

Tortorelli, P.F., Goodwin, G.M., Howell, M., and DeVan, J.H. 1995. In *Heat-Resistant Materials II*, pp. 585-90, Gatlinburg, TN, Sept 11-14, 1995, ASM, Materials Park, OH.

Tortorelli, P.F. and Natesan, K. 1998. Mat. Sci. Engr., A285, 115-25.

Tortorelli, P.F., Wright, I.G., Goodwin, G.M., and Howell, M. 1996. In *Elevated Temperature Coatings: Science and Technology II*, pp. 175-86, Anaheim, CA, Feb 4-8, TMS, Warrendale, PA.

Urich, J.A. and Kramer, E. 1996. In *1996 International Joint Power Generation Conference, Vol 1*, pp.25-9, ASME, EC-Vol. 4/FACT-Vol. 21.

Viswanath, R.P., Rein, D., and Hauffe, K. 1980. Werkst. Korr., 31, 778-82.

Von Fraunhofer, J.A. and Pickup G.A. 1967. Corrosion Science, 1, 379.

S. Vyas, S. Viswanathan, and V.K. Sikka, Scripta Metall. 27, pp. 185 (1992).

Wang, C.R., Zhao, Z.B., Xia, S.K., and Zhang, W.Q. 1989, Oxid. Met., 32 (3/4), 241-72.

Wallwork, G.R. and McGirr, M.B. 1975. In Stress Effects and the Oxidation of Metals, ed. J.V. Carthcart, Metal Society of the American Institute of Mining, Metallurgical, and Petroleum Engineers, New York, New York, 263.

Wang, X.L., et al. Mat. Res. Soc. Symp. Proc. Vol 364, Materials Research Society, pp109-114.

Woodyard, J.R. and Sikka, V.K. 1993. Scripta Metallurgica, 29, pp. 1489-93.

Wriedt, H.A. 1985. Bulletin of Alloy Phase Diagrams, 6 (6), 548-53.

Yang, J.C., Schumann, E., Levin, I., and Ruhle, M. 1996. In Microscopy of Oxidation 3, eds., The Institute of Materials, Cambridge, England, pg 256.

Yurek, G.J. and Przybylski, K. 1987. Mat. Sci. and Engr., 87, 125-30.

NEW ALLOYS DISTRIBUTION

ALLISON GAS TURBINE DIVISION
P.O. Box 420
Indianapolis, IN 46206-0420
P. Khandelwal (Speed Code W-5)
R. A. Wenglarz (Speed Code W-16)

AMAX R&D CENTER
5950 McIntyre Street
Golden, CO 80403
T. B. Cox

BABCOCK & WILCOX
Domestic Fossil Operations
20 South Van Buren Avenue
Barberton, OH 44023
M. Gold

BETHLEHEM STEEL CORPORATION
Homer Research Laboratory
Bethlehem, PA 18016
B. L. Bramfitt
J. M. Chilton

BRITISH COAL CORPORATION
Coal Technology Development Division
Stoke Orchard, Cheltenham
Glocestershire, England GL52 4ZG
J. Oakey

CANADA CENTER FOR MINERAL & ENERGY TECHNOLOGY
568 Booth Street
Ottawa, Ontario
Canada K1A OG1
R. Winston Revie
Mahi Sahoo

COLORADO SCHOOL OF MINES
Department of Metallurgical Engineering
Golden, CO 80401
G. R. Edwards

DOE
DOE OAK RIDGE OPERATIONS
P. O. Box 2008
Building 4500N, MS 6269
Oak Ridge, TN 37831
M. H. Rawlins

DOE
Federal Energy Technology Center
3610 Collins Ferry Road
P.O. Box 880
Morgantown, WV 26507-0880
D. C. Cicero
F. W. Crouse, Jr.
R. A. Dennis
N. T. Holcombe
W. J. Huber
T. J. McMahon
J. E. Notestein

DOE
Federal Energy Technology Center
626 Cochrans Mill Road
P.O. Box 10940
Pittsburgh, PA 15236-0940
A. L. Baldwin
G. V. McGurl
U. Rao
L. A. Ruth
T. M. Torkos

DOE
OFFICE OF FOSSIL ENERGY
FE-72
19901 Germantown Road
Germantown, MD 20874-1290
F. M. Glaser

DOE
OFFICE OF BASIC ENERGY SCIENCES
Materials Sciences Division
ER-131 GTN
Washington, DC 20545
H. M. Kerch

ELECTRIC POWER RESEARCH INSTITUTE
P.O. Box 10412
3412 Hillview Avenue
Palo Alto, CA 94303
W. T. Bakker
J. Stringer

EUROPEAN COMMUNITIES JOINT RESEARCH CENTRE
Petten Establishment
P.O. Box 2
1755 ZG Petten
The Netherlands
M. Van de Voorde

FOSTER WHEELER DEVELOPMENT CORPORATION
Materials Technology Department
John Blizard Research Center
12 Peach Tree Hill Road
Livingston, NJ 07039
J. L. Blough

IDAHO NATIONAL ENGINEERING LABORATORY
P.O. Box 1625
Idaho Falls, ID 83415
R. N. Wright

LAWRENCE BERKELEY LABORATORY
University of California
Berkeley, CA 94720
Ian Brown

LAWRENCE LIVERMORE NATIONAL LABORATORY
P.O. Box 808, L-325
Livermore, CA 94550
W. A. Steele

LEHIGH UNIVERSITY
Materials Science & Engineering
Whitaker Laboratory
5 E. Packer Avenue
Bethlehem, PA 18015
J. N. DuPont

NATIONAL MATERIALS ADVISORY BOARD
National Research Council
2101 Constitution Avenue
Washington, DC 20418
K. M. Zwilsky

OAK RIDGE NATIONAL LABORATORY
P.O. Box 2008
Oak Ridge, TN 37831
M. P. Brady
P. T. Carlson
J. M. Crigger (4 copies)
R. R. Judkins
C. T. Liu
C. G. McKamey
M. L. Santella
J. H. Schneibel
V. K. Sikka
R. W. Swindeman
P. F. Tortorelli
I. G. Wright

PACIFIC NORTHWEST LABORATORY
P. O. Box 999, K3-59
Battelle Boulevard
Richland, WA 99352
R. N. Johnson

SHELL DEVELOPMENT COMPANY
WTC R-1371
P.O. Box 1380
Houston, TX 77251-1380
W. C. Fort

THE JOHNS HOPKINS UNIVERSITY
Materials Science & Engineering
Maryland Hall
Baltimore, MD 21218
R. E. Green, Jr.

THE MATERIALS PROPERTIES COUNCIL, INC.
United Engineering Center
345 E. Forty-Seventh Street
New York, NY 10017
M. Prager

THE TORRINGTON COMPANY
Advanced Technology Center
59 Field Street
Torrington, CT 06790
W. J. Chmura

THE UNIVERSITY OF LIVERPOOL
Liverpool, United Kingdom
L69 3BX
A. R. Jones

THE WELDING INSTITUTE
Abington Hall, Abington
Cambridge CB1 6AL
United Kingdom
P. L. Threadgill

UNION CARBIDE CORPORATION
Linde Division
P.O. Box 44
175 East Park Drive
Tonawanda, NY 14151-0044
Harry Cheung

UNIVERSITY OF CALIFORNIA
AT SAN DIEGO
Department of Applied Mechanics and Engineering Sciences
La Jolla, CA 92093-0411
B. K. Kad

UNIVERSITY OF WASHINGTON
Department of Materials Science and Engineering
101 Wilson, FB-10
Seattle, WA 98195
T. G. Stoebe

UNIVERSITY OF TENNESSEE AT KNOXVILLE
Materials Science and Engineering Department
Knoxville, TN 37996
P. K. Liaw

WEST VIRGINIA UNIVERSITY
Department of Physics
Morgantown, WV 26506-6315
B. R. Cooper

WESTERN RESEARCH INSTITUTE
365 N. 9th Street
P.O. Box 3395
University Station
Laramie, WY 82071
V. K. Sethi